Picosecond X-ray Diffraction from Shock-Compressed Metals: Experiments and Computational Analysis of Molecular Dynamics Simulations

Katarína K. Rosoľanková

St. Cross College, University of Oxford

Thesis Submitted for the Degree of Doctor of Philosophy

Hilary Term, 2005



Picosecond X-ray Diffraction from Shock-Compressed Metals: Experiments and Computational Analysis of Molecular Dynamics Simulations

Katarína K. Rosoľanková *St. Cross College, University of Oxford*

Thesis Submitted for the Degree of Doctor of Philosophy

Hilary Term, 2005

Abstract

In this thesis, Molecular Dynamics simulations of shocked single crystals of Copper and Iron are studied using simulated X-ray diffraction. Strains and volumetric compression in modeled Copper crystals shock-compressed on picosecond time-scales are found. By comparing the shifts in the second and fourth diffraction orders, the density of dislocations is calculated. In Iron, simulated X-ray diffraction is used to verify the modelling of the $\alpha - \epsilon$ phase transition induced by shock-compression on picosecond time-scales. No plastic deformation of Iron is found in the studied pressure range of ~ 15–53 GPa.

The results are then compared with data from *in situ* X-ray diffraction experiments of laser-shocked single crystals. Near-hydrostatic compression of shock-compressed Copper on nanosecond time-scales is confirmed using a new wide-angle film diagnostic capturing diffraction from multiple crystal planes. Also, the first *in situ* X-ray diffraction evidence of the onset of the $\alpha - \epsilon$ phase transition in laser-shocked single crystal Iron is shown. No plastic yield of the crystal lattice is found, which is in agreement with the simulation results.

Results from both the Molecular Dynamics simulations and experiments are used to suggest enhancements in computer modelling of shocked crystals, as well as future experimental studies. In particular, the need for a measurement of dislocation densities during the shock wave passage through a crystal is highlighted, and a method enabling such a measurement is proposed.

Venujem rodičom

Contents

1 Introduction **1**

1.1 Iron Is from Mars, Copper Is from Venus 1

1.2 Focus of this Thesis 5

1.3 Role of X-Ray Diffraction 8

1.4 Historical Development 9

1.5 Layout of Thesis 16

1.6 Role of the Author 17

2 Theory **18**

2.1 Crystal Structure 18

2.1.1 Lattice and Basis 18

2.1.2 Crystal Planes 20

2.1.3 Reciprocal Lattice 21

2.1.4 Hexagonal lattice 22

2.2 X-Ray Diffraction 24

2.2.1 Bragg Formulation of X-ray Diffraction 24

2.2.2 Laue Formulation of X-ray Diffraction 24

2.2.3 Ewald Sphere of Reflection 26

2.2.4 Kinematic and Dynamical X-Ray Diffraction Theories 27

2.3 Physical Properties of Crystalline Matter 29

2.3.1 Stress 29
2.3.2 Strain 31
2.3.3 Elasticity 36
2.4 Shock Waves 39
2.4.1 Shock Waves in Fluids 39
2.4.2 Rankine-Hugoniot Jump Condition Equations 41
2.4.3 The Shock Hugoniot 43
2.4.4 Shock Waves in Solids 45
2.4.5 Equations of State for a Shock Wave 50
2.5 Crystal Defects 51
2.5.1 Line, Planar, and Volume Defects 51
2.5.2 Dislocations – Line Defects 51
2.5.3 Movement of Dislocations 53
2.5.4 Partial Dislocations in FCC Crystals 57
2.5.5 Theoretical Models of Plastic Deformation 61
2.6 $\alpha - \epsilon$ Phase Transition in Iron 65
2.7 Diffraction from Imperfect Crystals 68

3 Computational Simulations **71**
3.1 Molecular Dynamics Simulations 71
3.1.1 Introduction 71
3.1.2 Potentials in MD Simulations 74
3.1.3 History of Molecular Dynamics Simulations 75
3.2 X-Ray Diffraction Post-Processor 80
3.2.1 Principle of X-Ray Diffraction Post-Processing Code 80
3.2.2 Extension of Code beyond 1-D 81

4 X-Ray Diffraction Post-Processor Results **83**
4.1 Copper 84
4.1.1 2×10^6 Atom MD Simulation 84

4.1.2 Call for Large-Scale MD Simulations 92
4.1.3 256×10^6 Atom MD Simulation 93
4.2 Iron 108
4.2.1 MD Simulations **A** – **D**: Results 111
4.3 Summary 130

5 Vulcan and OMEGA Experiments **132**
5.1 Vulcan Laser System 132
5.1.1 Beam Geometry and Set-up in TAE 133
5.2 Targets for Vulcan 136
5.3 X-Ray Generation 141
5.3.1 X-Ray Filters 141
5.4 Diagnostics for Vulcan 143
5.4.1 Wide-Angle Film Detector 143
5.4.2 Bragg and Laue Geometries 144
5.4.3 Image Plates 145
5.5 OMEGA Laser System 148
5.5.1 Beam Geometry and Set-up for OMEGA 149
5.6 Targets for OMEGA 151
5.7 Diagnostics for OMEGA 154

6 Experimental Analysis and Results **155**
6.1 Data Reduction 155
6.2 Copper Diffraction Results 158
6.3 Iron Diffraction Results 166
6.4 Summary 174

7 Summary and Further Work **177**
7.1 Computational Work 177
7.1.1 Copper 177
7.1.2 Iron 179

7.2 Experimental Work 180
7.3 Future Research 181

List of Figures

1.1 Metal Workshop in Ancient Egypt 2
1.2 Mars and Venus 4
1.3 Strain Rate v. Shock Stress 6

2.1 Hexagonal Lattice 22
2.2 Ewald Sphere 27
2.3 3-D Stress 29
2.4 1-D Strain 31
2.5 2-D Rotation 32
2.6 2-D Strain 33
2.7 Rotation and Strain in 2-D 34
2.8 Subsonic and Supersonic Regimes 39
2.9 Shock Propagation 41
2.10 Shock Hugoniot for a Fluid 44
2.11 Shock Wave Profile 46
2.12 Shock Hugoniot for a Solid 47
2.13 Burgers Circuit and Burgers Vector 52
2.14 Shear Stress 54
2.15 Dislocation Velocity Dependence on Stress 57
2.16 FCC Stacking 58

2.17 Stacking Faults in FCC Crystal 59
2.18 Dislocation Loops 60
2.19 Smith Model of Dislocations 62
2.20 Meyers Model of Dislocations 63
2.21 Fe: α and ϵ Phases 66
2.22 Fe: $\alpha - \epsilon$ Transformation 67

3.1 MD Simulation of Shock-Compressed Copper 78
3.2 Non-specular Diffraction 82

4.1 Small Cu MD: 1-D Diffraction 86
4.2 Strains in Large Cu MD – 2nd order 96
4.3 Strains in Large Cu MD – 4th order 98
4.4 Corrected Strains in Large Cu MD 100
4.5 Corrected Volumetric Strain in Large Cu MD 101
4.6 Dislocation Densities in Large Cu MD 103
4.7 Large Cu MD: Shear Strains 105
4.8 Large Cu MD: Rotations 107
4.9 Shock-Compressed Iron MD Simulations 110
4.10 Iron MD: 1-D Diffraction: $(00l)$ planes 112
4.11 Iron MD: 1-D Diffraction: $(00l)$ planes 113
4.12 Iron MD: 1-D Diffraction: $(h00)$ and $(0k0)$ planes 115
4.13 Iron MD: 1-D Diffraction: $(h00)$ and $(0k0)$ planes 116
4.14 Iron MD: 1-D Diffraction: $(h00)$ and $(0k0)$ planes 117
4.15 Iron MD: 1-D Diffraction: $(h00)$ and $(0k0)$ planes 118
4.16 Iron MD: 2-D Diffraction: (110) planes 120
4.17 Iron MD: 2-D Diffraction: $(1\bar{1}0)$ planes 121
4.18 BCC: 2-D Diffraction: (110) planes 122
4.19 HCP: 2-D Diffraction: (0001) planes 122
4.20 Density Rise with Pressure 127

5.1 Vulcan Beams 7 and 8 134
5.2 Vulcan Target Schematic Diagram 136
5.3 Vulcan Target Alignment 137
5.4 Vulcan Target Detail 138
5.5 Coatings on Vulcan Crystal Targets 139
5.6 Stepped Shock Profile 140
5.7 X-ray Transmission of Metal Foils 142
5.8 Schematic Diagram of Film-pack 143
5.9 Filtering on Film-packs 144
5.10 Schematic Diagram of Target and Film-packs 145
5.11 OMEGA Laser System 149
5.12 Omega Target Schematic Diagram 151
5.13 Coatings on OMEGA Crystal Targets 152
5.14 Omega Target Detail 153

6.1 Theoretical Diffraction Pattern 157
6.2 Cu Shot 130604 – Raw Data 160
6.3 Cu Shot 130604 – Detail 161
6.4 Cu Shot 130604 – Lineouts 163
6.5 Cu Shot 130604 – Hugoniot 164
6.6 Fe Shot 36185 – Beam Timing 167
6.7 Fe Shots 36194 and 36185 – Raw Data 168
6.8 Fe Shot 36185 – Theoretical Fit 170
6.9 Fe Shot 36185 – Hugoniot 172

Acknowledgements

Working towards and writing this dissertation has, without a doubt, been one of the most challenging experiences for me. Whilst the title page bears only one author's name, the work conducted towards the completion of this thesis would not have been possible without the help and support of a number of people. Here, I would like to mention at least some of them.

My thanks go firstly to my supervisor, Prof. Justin Wark, for giving me the opportunity to work in the group, and for his guidance throughout the course of my DPhil. It has been a privilege to participate in the research pursued in some of the most advanced institutions and facilities in the world.

The help of our collaborators at Lawrence Livermore National Laboratory and Los Alamos National Laboratory has been invaluable. In particular, I would like to thank Dr. Eduardo Bringa, Dr. Peter Lomdahl, and Dr. Kai Kadau, who provided the Molecular Dynamics simulations studied in this thesis. Numerous discussions, both in person and across long distances, have aided the progress documented in this work.

My sincere thanks also go to Dr. Dan Kalantar for the expertise with which he guided the experiments conducted on the OMEGA laser. I believe his methodical approach to scientific problems is something every researcher should aspire to.

I would also like to thank Dr. James Hawreliak, for his dedication and practical experimental skills employed at the Rutherford Appleton Laboratory, as well as

providing the software which enables a convenient and accurate data analysis.

My thanks also belong to the staff at the OMEGA and Vulcan lasers, who always endeavoured to fulfill our (often volatile) experimental requirements.

There are also a number of people to whom I would like to express my thanks on a more personal note.

Firstly, to my parents, for their tireless encouragement and support of all my academic pursuits over the last twenty-odd years, so much stronger than my occasional resistance.

Secondly, to my boyfriend Paul, for all along having the conviction—one I often lacked—that one day I would finish this thesis, and for the *enormous* amount of support and patience, not only in the worst of my DPhil times.

My gratitude also goes to: Peter, for his willingness to share his knowledge of Unix, Dynamical X-ray diffraction theory, and basic psychology, and for being a good friend and house-mate; Jim, for all the useful software tricks and tea-time jokes (I still don't know how you come up with either!), and preventing many a Rutherford disaster; Ben, who made it through the same long Oxford years as myself, for solving almost all IT problems I encountered during my DPhil, and for the calm approach to things, which I so often lacked; André, for the highly appreciated continental element; and Jon, for his willingness to help and to laugh, and for his immense knowledge of the film industry which made the experiments merrier. I am also very grateful for the opportunity I have had to travel during the course of my DPhil. In particular, I would like to thank Justin for the business-class upgrade on our San Francisco-London flight; definitely teaching me the right way to fly.

Other valued partners in crime include: Arthur, Claire, Dave, Fraser, Matt, Nicholas, Simon, Steve, Tom, and Tony. Thank you all for the atmosphere in the lab and in coffee-breaks, making it easier to keep sane and accept that there are times when, as someone once put it, *"there are no conquerors, only survivors"*.

Lastly, I would like to acknowledge the many truths and uplifting moments provided by the constantly updated *www.phdcomics.com* website.

Chapter 1

Introduction

1.1 Iron Is from Mars, Copper Is from Venus ...

For millennia, Copper and Iron have accompanied the progress of man- and womankind, whose development was spurred by the discovery of these two elements, and their subsequent use as constituents in tools, ornaments, and weapons.

Some of the oldest civilisations on record knew of and used Copper as long as 10,000 years ago. The era of Copper Age marks the beginning of the centuries-long period called the Bronze Age, which evolved on different time-scales in different parts of the world.

During this time, mining and metallurgy became extremely important industries in many ancient civilisations (Fig. 1.1). In Egypt, the exploitation of metals was solely the monopoly of the Court, with the management of the mines and quarries often entrusted to the highest officials or even the sons of the Pharaoh [1]. Indeed, it was in Egypt that the discovery of bronze (an alloy of Tin and Copper) followed shortly after the discovery of Copper. Brass (an alloy of Zinc and Copper) was known to the Greeks and later used extensively by the Romans.

Iron is known to have been used from around 4,000 BC by the ancient Sumerian and Egyptian civilisations. It was recovered from meteorites and used to make small items, such as tips of spears and ornaments. The production of Iron objects increased around 3,000 – 2,000 BC, when smelted Iron was used as well as meteoric Iron. Their



Figure 1.1: Illustration of an Egyptian metal workshop. The exploitation of metals was an important industry in ancient Egypt. Figure is taken from [1].

use, however, unlike that of Copper or bronze, was ceremonial: at this time, Iron was more expensive than Gold.

The period between the 12th and 10th centuries BC saw a rapid transition in the Middle East from the use of bronze to Iron for manufacturing tools and weapons. This was the dawn of the Iron Age.

The discovery of a number of processes enhancing the properties of Iron followed this transition. One of the most significant ones was carburisation, a process involving the addition of Carbon to Iron, resulting in sponge Iron (a mix of Iron and slag with some Carbon). This could be worked into wrought Iron by repeated hammering and folding over, thus freeing the slag and oxidising out the Carbon content.

The production of wrought Iron was soon improved in the Middle East by long-term heating on a bed of charcoal, and subsequent quenching in water or oil. This resulted in a harder and stronger material. In ancient China, temperatures exceeding 1,300 K were used to transform carburised Iron into a strong alloy, which could be cast into intricate shapes. Cast Iron was used in China for hundreds of years.

Cast Iron development lagged considerably in Europe, with the maximum smelting temperatures reaching only about 1,000 K. As a consequence, most manufacturers in medieval Western Europe used sponge Iron to produce wrought Iron.

The 18th century saw Abraham Darby's innovation of Iron smelting. Charcoal,

which was increasingly becoming scarce, was replaced by coal as the main fuel for brass and cast Iron manufactory. This step was a major factor in the success of the British Industrial Revolution.

As well as playing a huge role in the modernisation of technologies throughout our history, Copper and Iron, as well as other metals, have been closely linked to religions and mythologies.

From antiquity up until the mid-eighteenth century, there were seven known metals, all of which were associated with, and dominated by, one of the seven objects recognised in the Solar System, called the "seven planets" (Table 1.1).

Table 1.1: Seven planets and seven metals: ancient alchemy associated all known metals with objects recognised in the sky [2].

planet	metal
Sun	Gold
Moon	Silver
Mars	*Iron*
Mercury	Mercury
Jupiter	Tin
Venus	*Copper*
Saturn	Lead

The affiliation does not end there. In mythology, Copper was associated with Venus (Aphrodites), the goddess of love and beauty, probably owing to its lustrous appearance, as well as its ancient use in producing mirrors. The symbol for both the planet and the metal was a representation of the goddess's hand mirror: a circle with a small cross underneath (Fig. 1.2).

Coming from the skies in the form of meteorites, Iron was referred to as "the metal of heaven" by both the Egyptians and the Babylonians. Some linguists argue that the English word "Iron", as well as its similar-sounding equivalents in other northern and western European languages, derives from the Etruscan "aisar" meaning "the gods".

The mythological association of Iron is with Mars (Ares), the god of war, and

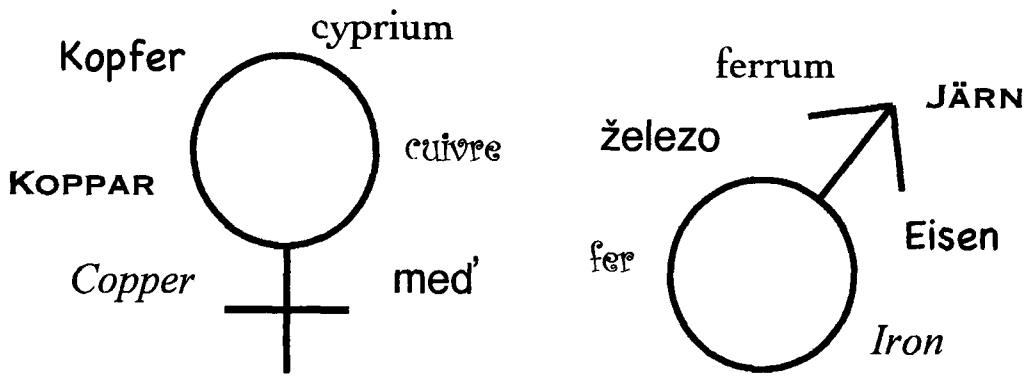


Figure 1.2: Iron is from Mars, Copper is from Venus: in the past, alchemy and mythology associated each of the seven known metals with an object in the Solar System, and a divinity. Symbols of the two elements are surrounded by their names in Latin and several modern languages.

its symbolic representation is therefore appropriately derived from Mars's shield and spear: a circle with an arrow (Fig. 1.2). It is interesting to note that the red colour of the planet Mars is due to an Iron oxide, the same one responsible for the colouring of blood.

It is clear that both Copper and Iron have rich and long histories, influencing many aspects of the human civilisation. As well as exploiting their properties, people have for millennia been captivated and fascinated by them. Deservingly, the two metals have for a long time been subjects of keen scientific research. Although a vast body of knowledge has been accumulated about them over the centuries, there are some attributes and features about them which we still do not fully understand.

1.2 Focus of this Thesis

This thesis focuses on a particular aspect of the behaviour of Copper and Iron under very specific conditions of *shock wave* regime. This corresponds to a very sharp and large rise in applied pressure over extremely short time-scales (10^{-9} s or less).

It is not surprising that the impact of a shock wave on the structure of a crystalline material can be very profound. When a solid is compressed beyond its threshold of reversible (elastic) behaviour, known under shock conditions as the Hugoniot Elastic Limit (HEL) [3], it stops behaving elastically and yields to a permanent plastic deformation.

The extent and character of the impact of a shock wave on a solid depends on the generated strain rate. Figure 1.3 shows the relationship, based on empirical data, between the peak shock wave stress and the resultant strain rate for a range of materials. The data for Copper and Iron are highlighted.

There is a broad range of strain rates experimentally attainable. Shock waves on sub-nanosecond time-scales with pressures ranging from approximately 1 GPa to 10's of GPa, and strain rates from 10^6 to $10^{10}\,\mathrm{s}^{-1}$ are an important area of scientific investigation. This thesis studies laser-induced shock waves generating such high strain rates.

Many of the fundamental properties of materials subject to these regimes are, however, presently not well understood. There is very little knowledge of how, on the atomic level, a material responds to uniaxial shock-compression, and flows towards the hydrostat in a way analogous to the behaviour of fluids, or undergoes polymorphic phase transitions.

Computationally, some light has been shed on the processes taking place under shock load conditions in crystals using multi-million atom Molecular Dynamics (MD) simulations [5, 6]. The field of MD simulations has soared in the recent years, owing to the rapid advance of fast computers with ever-expanding capacities.

One part of this thesis focuses on the mechanism of *plastic flow* in crystals subjected to a shock wave, which allows subsequent relaxation of the crystal structure



Figure 1.3: Relationship between strain rate and shock-induced stress for a range of materials. Figure is taken from [4].

towards the hydrostat. Such near-3-D compression on nanosecond time-scales has been experimentally verified in single crystal Copper using X-ray diffraction [7, 8]. However, the fundamental mechanism of plastic flow on these extremely short time-scales is not yet understood.

Theoretical models postulate that dislocations are generated and move within the crystal as a result of shock wave passage, thereby accommodating and relieving the deviatoric stresses at the shock front [9, 10]. Despite this, experimental studies have shown that there is generally an insufficient number of dislocations, both prior to the shock and in post-shock analysis, to account for the high plastic strain rates that the materials are subject to [8, 9, 11].

In this thesis, X-ray diffraction simulating computational post-processor is applied to MD simulations of shock-compressed single crystal Copper. Strains along the principal directions, as well as the volumetric compression, are measured and compared with experimental results. The relationship between defects present in a crystalline solid *prior to* shock wave passage and its subsequent tendency towards 3-D compression upon shock wave passage is then studied.

Additionally, a possible experimental method for measuring dislocation densities in a sample during shock loading is identified. This offers the potential for clarifying the fundamental, yet presently unresolved, questions of plastic deformation in shock wave physics.

The second part of this thesis focuses on the $\alpha-\epsilon$ phase transition in Iron. The phenomenon of phase transitions in crystals under pressure has been known for almost a century [12], and the $\alpha-\epsilon$ transition is the most well known, and indeed the most widely-studied of the shock-induced transformations in Iron. Despite this, it has up until now not been observed *in situ* during shock-loading. This thesis presents the first data of this kind. In addition, X-ray diffraction post-processing of MD simulations of this phase transformation is performed, and compared with the experimental results.

1.3 Role of X-Ray Diffraction

The above mentioned phenomena of plastic flow and phase transitions in crystalline solids under shock-compression can occur on extremely short time-scales. In order to understand them fully, a diagnostic method allowing the study of a material on nano- and sub-nanosecond time-scales is required.

In situ X-ray diffraction is an extremely powerful diagnostic for studying the structure of a crystalline material on very short time-scales (nanosecond and lower). Its main advantages are short wavelengths, comparable to lattice spacings in crystals, and its non-destructive nature. In addition, the advance in recent decades of high power lasers capable of generating pulses of sub-nanosecond lengths has enabled extremely high temporal resolutions in X-ray diffraction experiments. The main advantage of high power laser technology, in comparison with the traditional X-ray sources such as X-ray tubes and synchrotrons, is its ability to produce very high intensity pulses. In addition, using a laser source to generate both the shock wave in the crystal and the diffracting X-rays, enables a convenient and accurate timing of the diagnostic beam with respect to the shocking beam.

When a high energy, short laser pulse is focused on a tight spot ($\sim 100\,\mu$m in diameter) onto a low- to medium- Z material, producing an irradiation of $\sim 10^{14}$–$10^{16}\,\mathrm{Wcm}^{-2}$, most electrons in the outer shells of the atoms in this material will be stripped out. A hot plasma of Hydrogen- and Helium- like ions and electrons is thus created. When the ions and electrons subsequently recombine, X-rays are emitted from the plasma. The *characteristic* Hydrogen- or Helium-like X-rays used in diffraction experiments are due to the radiative decay of thermally excited electrons from higher to lower energy levels within an atom's shell. The low wavelengths of these X-rays are suitable to study interplanar spacings in crystals. Such extremely hot dense plasmas are therefore ideal sources of short lived, high intensity X-rays.

1.4 Historical Development

Although the behaviour of gaseous, fluid, and solid matter under pressure has been the subject of scientific investigation for centuries, the first solid foundations of shock wave physics were put down only in the 19th century by Rankine and Hugoniot, who derived the conservation equations governing a shock [13, 14].

In the early 20th century, Bridgman's systematic studies of solids under the influence of static pressure were the first ones to show the phenomenon of phase transformation in solids under pressure [12].

The early 1940's saw the first attempts to generate flash X-ray sources [15, 16]. It was not, however, until more than two decades later when X-rays produced in this way were bright enough to be used for diffraction from shocked materials. The first evidence of X-ray diffraction from crystalline matter under shock-compression was reported in 1969 by Q. Johnson *et al.* Diffraction images were obtained from (200) planes of shock-compressed Lithium Fluoride (peak pressure $\sim 13\,\mathrm{GPa}$), using X-ray pulses of $\sim 20\,\mathrm{ns}$ [17, 18]. This was the first conclusive evidence that crystals retained their crystalline identity upon shock wave propagation. Three years later, Johnson and Mitchell reported the first X-ray diffraction evidence of a phase transition in a crystalline solid, by recording X-ray images from shock-compressed crystals of Boron Nitride [19].

Scientific studies of Iron progressed in the second half of the 20th century. The first tentative evidence of the existence of the $\alpha - \epsilon$ transition in Iron under shock conditions came in 1954, when J.M. Walsh reported data on the propagation of high-pressure shock waves in Armco Iron [20]. These were in disagreement with an extrapolation of Bridgman's original static compressibility measurements, as they implied a compression up to 20% higher. Two years later, this discrepancy was resolved by Bancroft, Peterson, and Minshall, who found that three-wave shock structures can propagate within an Iron sample [21]. These different wave structures were identified as different phases present in the crystal, and the inferred threshold pressure for the existence of a polymorphic phase transition was $\sim 13\,\mathrm{GPa}$.

1962 brought the first crystallographic evidence of a phase transition in Iron at the same threshold pressure. A static X-ray diffraction study was conducted by Jamieson and Lawson, which indicated a phase transformation [22]. The transition associated with the multiple waves seen in shock experiments, and the one observed under static high-pressure conditions, has always been assumed to be one and the same phase transition. It has to be noted that despite this, no conclusive observation of the new phase (in the form of detailed *in situ* X-ray diffraction) during the passage of a shock wave has been reported to date.

Mao and co-workers determined the lattice parameters of the body-centred cubic (BCC) and hexagonal close-packed (HCP) phases of Iron as a function of static pressure up to 30 GPa using X-ray diffraction [23]. The ratio of the lattice parameters in the HCP phase was found to be pressure-independent up to 30 GPa.

Simultaneously, scientific work on Copper progressed. In 1962, Livingston studied dislocation densities in quasistatically deformed Cu single crystals. The study showed that prestraining annealed crystals prior to shock loading lead to dislocation densities of $\sim 10^9\,\mathrm{cm}^{-2}$ [24].

In 1967, Greenmann *et al.* made direct measurements of dislocation mobilities in single crystals of Cu for a range of dislocation velocities and shear stresses. The resultant data could be described by a phonon viscosity model with the exception of very large shear stresses [25]. This was resolved two years later by Gillis *et al.*, who extended the relationship between the dislocation velocity and shear stress to high shear stress regimes [26].

In 1969, Jones and Mote conducted a detailed study of Copper subjected to shock waves [27]. The material response to shocks up to 5 GPa generated by explosive plane-wave generators was studied along the [100], [110], and [111] crystallographic directions. The elastic yield points and plastic wave velocities for different shock propagation directions were measured. The effect of dislocation densities in the crystal on its response to a shock wave was also studied.

Anisotropy in material response to shock waves travelling along different crystal-

lographic directions was further explored by J. Johnson and co-workers in the early 1970's [28–31]. Dislocation dynamics were studied in a variety of FCC, BCC, and HCP crystals, and dislocation mobilities were measured. The dislocation densities found in experimental samples were two to three orders of magnitude lower than the theoretical predictions.

In the late 1970's, Gupta studied anisotropy in single crystals of LiF [32, 33]. Planar impacts induced by a gas gun were applied along the [100], [110], and [111] directions and the response of LiF to varied elastic impact stresses was observed.

Plate impact experiments were used to generate the $\alpha - \epsilon$ phase transition in Armco Iron by Barker and Hollenbach [34]. Shock waves up to 40 GPa were produced and highly accurate laser interferometry measurements were made. The phase transition was confirmed to occur at 13 GPa.

More studies of the ultrafast BCC to HCP phase transition in Iron under a shock wave impact were conducted by Forbes [35]. The transformation time inferred from the rise-time of applied shock waves was found to be under 50–100 ns.

An extensive study of phase transitions under shock wave loading was conducted by Duvall and Graham in 1977 [36]. Experimental observations of shock induced first-order polymorphic and second-order transitions, as well as melting and freezing were tabulated for a range of materials. A range of shock generating methods were employed, including explosives, flyer plates, projectile impact, and pulsed radiation.

More recently, Boettger and Wallace [37] studied the Hugoniot of the $\alpha - \epsilon$ Iron phase transition. The phase transition relaxation time was found to be dependent on the applied shock pressure, and decreased from 60 ns to 12 ns as the applied shock rose from 17 GPa to 30 GPa.

The 1980's saw a rapid progress in the development of high power laser technologies, enabling the generation of X-ray emitting hot dense plasmas. Their application was found in a number of scientific fields. The dramatic improvement in the temporal resolution of X-ray diffraction was also exploited in studies of crystalline matter under shock conditions. In 1987, Wark *et al.* used, for the first time, sub-nanosecond X-ray

pulses for direct observation of the spatial and temporal evolution of Silicon upon shock-compression in Bragg geometry [38]. The 100 ps pulse length meant a 500-fold increase in the temporal resolution in comparison with previous X-ray diffraction experiments. This study was later extended to using X-ray sources producing multiple wavelengths [39].

Furthermore, Woolsey, Wark and Riley conducted the first X-ray diffraction measurements on *powder* samples, using 600 ps X-ray pulses to diffract from shocked LiF [40]. The added advantage of these experiments was the application of lasers as the source of shock waves in the materials; this improved the synchronisation of the laser-produced X-rays with the shock-inducing laser beam.

A further improvement in the temporal resolution of X-ray diffraction experiments was achieved by Wark *et al.* in the early 1990's. 1 ns X-ray pulses were diffracted from shocked (111) planes of single crystal Silicon, and time-resolved diffraction data were obtained by replacing the previously used static X-ray diagnostics with a streak camera with temporal resolution of 50 ps [41, 42]. This was a direct measurement of compressive and tensile components of strain during shock breakout. Shock waves causing crystal compression of $\sim 6\%$ were observed.

In the mid-90's, Whitlock and Wark studied the behaviour of single crystal LiF subjected to laser-induced shock waves with peak pressure of 6 GPa. The shock propagation direction was [100] and 0.25 ns long X-ray pulses were simultaneously diffracted from the (200) and (020) planes [43]. Crystal compression in the direction normal to the shock propagation direction was recorded, indicating the onset of a plastic lattice deformation.

In 1998, Rigg and Gupta [44] conducted plate impact experiments on single crystal LiF, in which X-ray diffraction was used to measure the elastic and elastic-plastic deformation of the crystal subjected to shock waves of pressure in the range 2–4 GPa along the [111] and [100] directions. The probing X-ray pulses were 50 ns long and the results showed purely uniaxial compression of the crystal upon shock wave propagation along [111], whilst isotropic 3-D compression of the unit cell occurred when the

shock propagated along [100]. This was in agreement with previous measurements by Whitlock and Wark.

In 1999, Kalantar *et al.* enhanced the time-resolved X-ray diffraction technique by increasing the time window available on the streak camera, whilst maintaining a high temporal resolution [45]. Single crystal Si was subjected to a laser-induced shock along the [111] direction and X-ray diffraction from the free surface was recorded over a period of 4 ns. Information was recorded about the uncompressed and compressed crystal, as well as the shock breakout and subsequent lattice relaxation.

The new millenium saw further progress in the field of X-ray diffraction from shock-compressed matter. Loveridge *et al.* measured the lattice parameters in shock-compressed crystals of Silicon and Copper [7]. Despite compressing the Si lattice uniaxially along [100] by as much as 11% (more than twice the originally accepted HEL of Si), no compression in the lateral directions was detected, proving that Silicon behaves elastically on nanosecond time-scales. In contrast, it was found that under similar conditions, the Copper crystal was readily compressed towards the hydrostat. This finding agreed with previously obtained values of mobile dislocation velocities in the two materials. It should be stressed that plasticity in crystals is directly linked to the presence of mobile dislocations in them, since they are the mediators of shear stress relaxation, leading to 3-D compression [9, 10].

As well as continually improving the temporal resolution of the X-ray diffraction measurements, the next challenge in diffraction experiments was to record information from various planes in the crystal, with different (hkl) indices. In 2003, Zaretsky designed a method which allowed the recording of X-ray diffraction information from multiple planes by rotating the crystal sample around its [200] axis [46]. Crystals of NaCl were shocked using the planar impact of a projectile along the [100] direction and X-rays from shocked (200) and (220) planes were recorded.

Shock-compressed single crystals of Silicon and Copper have been the subject of subsequent X-ray diffraction experiments. In 2003, Kalantar *et al.* studied both materials' responses to shock-induced pressures above their published HEL [47, 48].

As well as recording temporally resolved diffraction, these experiments employed, for the first time, the static detection method of a wide-angle film-pack, which is also the diagnostic used in the work conducted for this thesis. Diffraction from planes both parallel and normal to the shock propagation was recorded, as well as from a number of other planes with different orientations. Near-3-D compression of Copper on nanosecond time-scales was confirmed by diffraction from multiple atomic planes. The author took part in these experiments, and the studies of single crystal Copper presented in this thesis are related to them.

In this thesis, X-ray diffraction is also used as a computational tool. Post-processing of MD simulations of shock-compressed Copper crystals is presented and discussed. It is shown that existing MD simulations, carried out on time-scales shorter than $\sim 10\,\text{ps}$ and with no finite ramp on the applied shock wave, do not emulate the close-to-hydrostatic compression of Copper achieved under experimental shock conditions on nanosecond time-scales. As a result of this study, larger MD simulations incorporating realistic features such as pre-existing defects and ramped shock waves were generated. It will be shown that these simulations provide a far better understanding of and insight into how Copper responds to shock conditions.

Furthermore, a possible experimental method for a direct *in situ* X-ray diffraction measurement of dislocation densities is identified. Observations of dislocations in a solid *during* shock-compression have not yet been made, although they are believed to be key to the mechanism of plastic flow in crystals. The new method suggested in this thesis therefore opens up the possibility to resolve one of the most fundamental questions remaining in shock wave physics.

In addition, this thesis presents the first *in situ* X-ray diffraction evidence of the $\alpha - \epsilon$ phase transition in Iron, which is one of the most important and widely-studied phase transitions known to man (and woman). Single crystal Iron subjected to laser-induced shock-compression on nanosecond time-scales is shown to undergo the transformation from its BCC (α) phase to the HCP (ϵ) phase at pressures above the transformation threshold value. Significantly, no evidence of a plastic deformation

of the crystal structure is found.

The X-ray diffraction post-processing tool is also applied to MD simulations of this phase transition and compared with the experimental results. Clear evidence of the onset of the $\alpha - \epsilon$ transformation is found, and no plastic deformation of the crystal is detected for the studied pressure range of $\sim$ 15–53 GPa. This is in agreement with the experimental results.

1.5 Layout of Thesis

This thesis is divided into seven chapters. Their contents are as follows:

Chapter 2 outlines the physics relevant to this work. It is divided into separate sections covering the following topics: basics of crystal structure (primarily focusing on cubic crystals); X-ray diffraction, with emphasis on the Kinematic Theory; physical properties of materials; shock waves; defects and imperfections in crystalline matter.

Chapter 3 is an introduction to the computational work relevant to this thesis. The concept and history of MD modelling is outlined, and the principle of the X-ray diffraction post-processing used to analyse MD simulations is described.

In **Chapter 4**, the results of the X-ray diffraction post-processor are discussed. MD simulations of Copper and Iron are presented.

Chapter 5 provides a description of the experiments carried out. This includes an introduction to the laser facilities used, as well as a detailed description of the particular experimental set-ups, targets, and the diagnostic methods employed.

Chapter 6 describes the experimental data analysis. Results obtained from *in situ* X-ray diffraction from single crystal Copper and Iron are discussed, and compared with the post-processed MD simulation results from Chapter 4.

Chapter 7 summarises the work accomplished in this thesis, and outlines possible directions for future research.

1.6 Role of the Author

The computational work on simulated X-ray diffraction presented in this thesis is solely the work of the author, with the help and guidance of Prof. Justin Wark. The computer programs simulating X-ray diffraction, as well as other programs relevant to the analysis, were developed by the author, and the post-processing of the MD simulations was also carried out by the author alone. The collaborators who provided the MD simulations studied are acknowledged in the relevant parts of the thesis.

Large experimental facilities such as the Vulcan and OMEGA lasers, which were used for the work described in the thesis, by necessity require the collaboration of a number of people. The author actively participated in the planning of the experiments conducted on the Vulcan laser at the Rutherford Appleton Laboratory, and played a major role in their setting up and realisation. The author also took part in the planning and realisation of the experiments conducted on the OMEGA laser at the University of Rochester, under the help and guidance of Dr. Daniel Kalantar.

The analysis of the experimentally acquired data is the work of the author. The software used for the data analysis was developed by Dr. James Hawreliak and used by the author to obtain the results presented in this thesis.

Chapter 2

Theory

This chapter details the underlying theory crucial to the work conducted for this thesis. It is subdivided into separate sections covering crystal structure, X-ray diffraction, physical properties of materials, the physics of shock waves, crystal defects, and the effects of imperfections in crystalline matter on the resultant X-ray diffraction patterns.

2.1 Crystal Structure

This section outlines the theory of crystalline matter. Definitions of basic quantities used to describe crystals are given. The concept of the reciprocal lattice, crucial in the study of X-ray diffraction from crystals, is introduced.

2.1.1 Lattice and Basis

An infinite periodic array of points in space is called a *lattice*. The repetition scheme of the lattice is given by its *translation vector* $\mathbf{T}$,

$$\mathbf{T} = u_1\mathbf{a}_1 + u_2\mathbf{a}_2 + u_3\mathbf{a}_3\,, \tag{2.1}$$

where u_1, u_2, u_3 are arbitrary integers and $\mathbf{a}_1, \mathbf{a}_2, \mathbf{a}_3$ are the fundamental translation vectors of the lattice. In 3-D, they form three adjacent edges (axes) of a paral-

lelepiped.

The volume enclosing one or more lattice points is called a *unit cell.* A unit cell can fill out the entire space solely by repeating itself. A unit cell whose volume encloses only one lattice point is called a *primitive unit cell*, and in 3-D it is spanned by the three primitive vectors $\mathbf{a}_1, \mathbf{a}_2, \mathbf{a}_3$. The primitive unit cell volume V_a is then given by

$$V_a = \mathbf{a}_1 \cdot (\mathbf{a}_2 \times \mathbf{a}_3)\,. \tag{2.2}$$

Lattices are categorised according to the symmetry operations that can be performed on them. If a lattice remains invariant under a certain subset of symmetry operations, it belongs to a special lattice type. Such a distinct lattice type is commonly described as a *Bravais lattice.* Three-dimensional lattices are divided into a total of fourteen different Bravais lattice types.

Both the theoretical and experimental work conducted for this thesis deals with face-centred (FCC) and body-centred (BCC) cubic crystals. This chapter therefore primarily focuses on the analysis of these types of crystals.

It is possible to describe both the body-centred cubic and face-centred cubic lattices by their primitive unit cells, which contain one lattice point each, and are the smallest possible parallelepipeds that can span the entire crystal. The disadvantage of this definition is that the primitive unit cells do not easily display the cubic symmetry of the BCC and FCC lattices. It is therefore more convenient to use the non-primitive, or *conventional*, unit cell, in which the cubic symmetry of the lattices can easily be visualised.

The conventional cubic unit cell of FCC lattice is such that it contains four lattice points whose positions, with respect to three mutually perpendicular axes are

$$\mathbf{0},\ \frac{a}{2}(\hat{\mathbf{x}}+\hat{\mathbf{y}}),\ \frac{a}{2}(\hat{\mathbf{x}}+\hat{\mathbf{z}}),\ \frac{a}{2}(\hat{\mathbf{y}}+\hat{\mathbf{z}})\,, \tag{2.3}$$

where a is the side length of the cube and $\hat{\mathbf{x}}$, $\hat{\mathbf{y}}$, and $\hat{\mathbf{z}}$ are the unit vectors along the

three Cartesian axes. The volume of the conventional FCC unit cell is hence four times the volume of the primitive FCC unit cell.

Similarly, the conventional unit cell of the BCC lattice will contain two lattice points whose positions are

$$\mathbf{0},\ \frac{a}{2}(\hat{\mathbf{x}}+\hat{\mathbf{y}}+\hat{\mathbf{z}})\,. \tag{2.4}$$

The conventional cell volume is twice that of the primitive BCC unit cell.

A *basis* is an arrangement of atoms situated on each lattice point. The number of atoms in a basis can vary from a single atom to many atoms or molecules. The position of the jth atom within a basis relative to the lattice point with which it is associated is given by

$$\mathbf{r}_j = x_j\mathbf{a}_1 + y_j\mathbf{a}_2 + z_j\mathbf{a}_3\,, \tag{2.5}$$

where x_j, y_j, z_j give the fractional positions of the jth atom in terms of the dimensions of the unit cell.[1]

In this way, the crystal structure can be defined as the *convolution* of the lattice and the basis.

2.1.2 Crystal Planes

A *crystal plane* is defined by three non-collinear lattice points. It is conventional to define a crystal plane using the *Miller indices* h, k, l. These are the reciprocals of the intercepts of a given plane with the axes of the unit cell of the lattice, reduced to the simplest integers.

The spacing d_{hkl} between two adjacent planes is the perpendicular distance between them. In a cubic lattice, it is given by

$$d_{hkl} = \frac{a}{(h^2+k^2+l^2)^{1/2}}\,, \tag{2.6}$$

[1]The vectors $\mathbf{a}_1, \mathbf{a}_2, \mathbf{a}_3$ now refer to the conventional unit cell, and are not limited to the primitive unit cell.

where a is the lattice constant and h, k, l are the Miller indices of the plane.

2.1.3 Reciprocal Lattice

For the purpose of studying crystals using diffraction, it is convenient to refer to a specific crystal structure in terms of its *reciprocal lattice*. The fundamental vectors of the reciprocal lattice $\mathbf{A}_1$, $\mathbf{A}_2$, and $\mathbf{A}_3$ are given by

$$\mathbf{A}_1 = 2\pi \frac{\mathbf{a}_2 \times \mathbf{a}_3}{\mathbf{a}_1 \cdot (\mathbf{a}_2 \times \mathbf{a}_3)}\,,\ \mathbf{A}_2 = 2\pi \frac{\mathbf{a}_3 \times \mathbf{a}_1}{\mathbf{a}_1 \cdot (\mathbf{a}_2 \times \mathbf{a}_3)}\,,\ \mathbf{A}_3 = 2\pi \frac{\mathbf{a}_1 \times \mathbf{a}_2}{\mathbf{a}_1 \cdot (\mathbf{a}_2 \times \mathbf{a}_3)}\,. \tag{2.7}$$

It can be seen that each reciprocal vector is perpendicular to the plane defined by the two crystal axes with different indices. For a cubic lattice, these equations simplify to

$$\mathbf{A}_1 = 2\pi \frac{\hat{\mathbf{x}}}{a_1}\,,\ \mathbf{A}_2 = 2\pi \frac{\hat{\mathbf{y}}}{a_2}\,,\ \mathbf{A}_3 = 2\pi \frac{\hat{\mathbf{z}}}{a_3}\,. \tag{2.8}$$

The *reciprocal lattice vector* $\mathbf{G}$ is then given by

$$\mathbf{G} = v_1 \mathbf{A}_1 + v_2 \mathbf{A}_2 + v_3 \mathbf{A}_3\,, \tag{2.9}$$

where v_1, v_2 and v_3 are integers. If they are equal to the Miller indices h, k, l of a certain set of planes, then the reciprocal lattice vector $\mathbf{G}_{hkl}$ is perpendicular to those planes and the interplanar spacing is related to it as

$$d_{hkl} = \frac{2\pi}{|\mathbf{G}_{hkl}|}\,. \tag{2.10}$$

The unit cell in the reciprocal, or inverse, space is then defined by

$$\mathbf{G}_{hkl} = h\mathbf{A}_1 + k\mathbf{A}_2 + l\mathbf{A}_3\,. \tag{2.11}$$

The next section outlining the theory of X-ray diffraction shows the usefulness of this notation in describing crystals.

2.1.4 Hexagonal lattice

The hexagonal close-packed (HCP) lattice is also relevant to this thesis. Indexing of hexagonal lattices, which differs from that of cubic lattices, is explained below.

Figure 2.1 shows the basal plane of a primitive hexagonal unit cell. Part (a) shows x and y axes with respective unit vectors $\mathbf{a}_1$ and $\mathbf{a}_2$, at 120°, with z axis pointing out of the plane of the paper. Part (b) shows the more convenient notation using an extra u axis at 120° to both x and y axes. The new x, y, u, and z axes with respective unit vectors $\mathbf{a}_1$, $\mathbf{a}_2$, $\mathbf{a}_3$, and $\mathbf{c}$ are the *Miller-Bravais* axes. The corresponding Miller-Bravais plane indices are $(hkil)$.

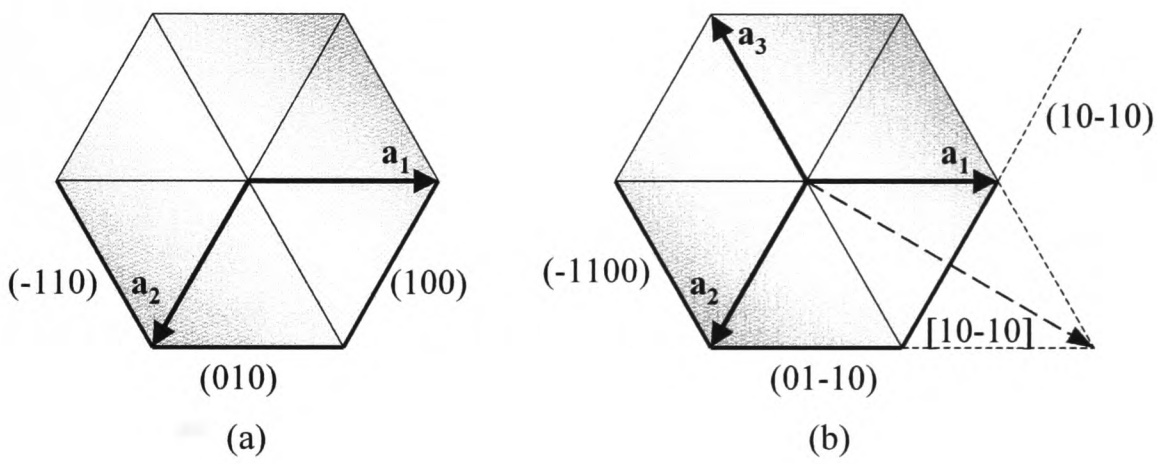


Figure 2.1: Primitive hexagonal unit cell, plane (0001). Conventional three-index $\{hkl\}$ indexing of planes (a), and Miller-Bravais four-index indexing $\{hkil\}$ (b). Dashed arrow indicates the $[10\bar{1}0]$ direction, normal to the $(10\bar{1}0)$ plane.

When labelling planes using the four-index system, each plane must satisfy the condition that $h + k + i = 0$. It can be seen that the planes indicated in the figure satisfy this condition. The crystallographic directions corresponding to the Miller-Bravais planes are referred to as the *Weber* symbols $\langle UVTW \rangle$. The components of a vector have to be such that $U + V + T = 0$. Below are the relationships between the three-index directional symbols and four-index directional symbols:

$$U = \frac{1}{3}(2u - v)\,, \qquad V = \frac{1}{3}(2v - u)\,, \qquad T = -(U + V)\,, \qquad W = w\,. \tag{2.12}$$

Using these identities, the directions for the x, y, u, and z axes are $[2\bar{1}\bar{1}0]$, $[\bar{1}2\bar{1}0]$, $[\bar{1}\bar{1}20]$, and $[0001]$, respectively.

2.2 X-Ray Diffraction

This section outlines the theory of X-Ray Diffraction. Bragg and Laue formulations are given, as well as the rationale behind limiting this thesis to the simpler *Kinematic* form of X-Ray Diffraction.

2.2.1 Bragg Formulation of X-ray Diffraction

When beams diffracted from different parts of the crystal are in phase, they produce an intensity maximum. The condition for such a diffraction maximum is given by the well-known *Bragg's law*,

$$\lambda = 2d_{hkl} \sin \theta_B \,, \tag{2.13}$$

where λ is the X-ray wavelength, θ_B is the Bragg angle, i.e. the glancing angle of incident and diffracted X-ray beams with respect to the planes defined by indices (hkl), and d_{hkl} is the inter-planar spacing, as before. The diffraction signal found for values of incident and reflected angles both equalling to θ_B corresponds to constructively interfering waves reflected from the given set of planes (hkl).

2.2.2 Laue Formulation of X-ray Diffraction

A more sophisticated approach to X-ray diffraction considers X-rays scattered from all the electrons in the crystal. The scattering vector of the radiation is defined as

$$\Delta \mathbf{k} = \mathbf{k}' - \mathbf{k} \,, \tag{2.14}$$

where $\mathbf{k}$ and $\mathbf{k}'$ are the wavevectors of the incident and reflected radiation, respectively. Their magnitudes are such that $|\mathbf{k}| = |\mathbf{k}'| = (2\pi)/\lambda$. This is because X-ray scattering is predominantly elastic (Thomson scattering).

Each electron in the crystal is considered as a diffuse cloud of negative charge [49]. X-ray diffraction is therefore scattering from the electron density in the entire crystal.

The total amplitude of the scattered wave from the entire crystal is then given by

$$F_{crystal}(\Delta\mathbf{k}) \propto \int_{crystal} \rho(\mathbf{r})\, e^{-i(\Delta\mathbf{k}\cdot\mathbf{r})}\, d^3\mathbf{r}\,, \tag{2.15}$$

where $\mathbf{r}$ is the position of an electron in the crystal, and $\rho(\mathbf{r})$ is the electron density. In other words, the amplitude of the diffracted wave from a crystal is proportional to the 3-D Fourier Transform (FT) of the electron density in that crystal. Equation (2.15) can be separated into the form

$$F_{crystal}(\Delta\mathbf{k}) = \overbrace{\sum_{\substack{\mathbf{r}_i \\ \text{crystal}}} e^{-i(\Delta\mathbf{k}\cdot\mathbf{r}_i)}}^{lattice\ points\ in\ crystal} \overbrace{\left[\sum_{\substack{\mathbf{r}_j \\ \text{atoms in basis}}} \left(\overbrace{\int_{atom} \rho_j(\mathbf{r})\, e^{-i(\Delta\mathbf{k}\cdot\mathbf{r})}\, d^3\mathbf{r}}^{electrons\ in\ one\ atom} \right) e^{-i(\Delta\mathbf{k}\cdot\mathbf{r}_j)} \right]}^{basis}, \tag{2.16}$$

where $\mathbf{r}_i$ are the lattice translation vectors, $\mathbf{r}_j$ are the positions of the atoms in the basis, and $\rho_j(\mathbf{r})$ is the electron density of the jth atom in the basis.

Since the crystal is defined as the convolution of the lattice and the basis, by convolution theorem, the amplitude of the scattered X-ray radiation will be the product of the FT's of the lattice and the basis.

The condition for a strong reflection in eqn. (2.16) is that all individual $e^{-i(\Delta\mathbf{k}\cdot\mathbf{r}_i)}$ add up in phase. Since the product of a reciprocal lattice vector $\mathbf{G}_{hkl}$ with any direct space lattice translation vector $\mathbf{r}_i$ is always a multiple of 2π (see eqn. (2.7)), the following relation holds:

$$e^{-i(\mathbf{G}_{hkl}\cdot\mathbf{r}_i)} = 1\,.$$

The diffraction condition, also known as the *Laue condition*, is therefore given by

$$\Delta\mathbf{k} = \mathbf{k}' - \mathbf{k} = \mathbf{G}_{hkl}\,, \tag{2.17}$$

where $\mathbf{G}_{hkl}$ is given by eqn. (2.10). Constructive interference therefore occurs when

the change in the X-ray wavevector equals a vector of the reciprocal lattice. When the Laue diffraction condition is satisfied, the amplitude of the wave scattered from one unit cell is given by

$$S_{hkl} = \overbrace{\sum_{\substack{\mathbf{r}_j \\ \text{unit cell}}} \left(\underbrace{\int_{atom} \rho_j(\mathbf{r})\, e^{-i(\mathbf{G}_{hkl}\cdot\mathbf{r})}\, d^3\mathbf{r}}_{\text{Atomic form factor}} \right) e^{-i(\mathbf{G}_{hkl}\cdot\mathbf{r}_j)}}^{\text{Geometric structure factor}}, \tag{2.18}$$

which in the case of cubic crystals can be written as

$$S_{hkl} = \sum_j f_j e^{-i(\mathbf{r}_j\cdot\mathbf{G}_{hkl})} = \sum_j f_j e^{-i2\pi(hx_j+ky_j+lz_j)}, \tag{2.19}$$

where $\mathbf{r}_j = (x_j, y_j, z_j)$ is the position of jth atom in the unit cell, and $\mathbf{G}_{hkl}$ is the diffraction wavevector, as before. The quantity f_j is called the *Atomic form factor*, and represents the scattering power of the jth atom in the unit cell [50]. S_{hkl} is referred to as the *Geometric structure factor*. This is the scattering power of a unit cell. It is a very important quantity for structure determination of crystalline matter using X-ray diffraction. The total diffracted *intensity* from a crystal, being the square of the total amplitude, will be a multiple of $|S_{hkl}|^2$.

2.2.3 Ewald Sphere of Reflection

A very useful illustration of the Laue diffraction condition (eqn. (2.17)) is that due to Ewald. It is called the *Ewald sphere* and is illustrated in two dimensions in Fig. 2.2. The origin of the wavevector $\mathbf{k}$ of the incident beam is chosen to be such that $\mathbf{k}$ terminates on a reciprocal lattice point. The sphere is centred on the origin of $\mathbf{k}$ and has a radius of $|\mathbf{k}|$. Any other reciprocal lattice point which happens to lie on the surface of the sphere represents a set of planes (hkl), which give rise to constructive interference.

Referring back to eqn. (2.10), it can be seen that the Ewald sphere representation is equivalent to the Bragg law (2.13):

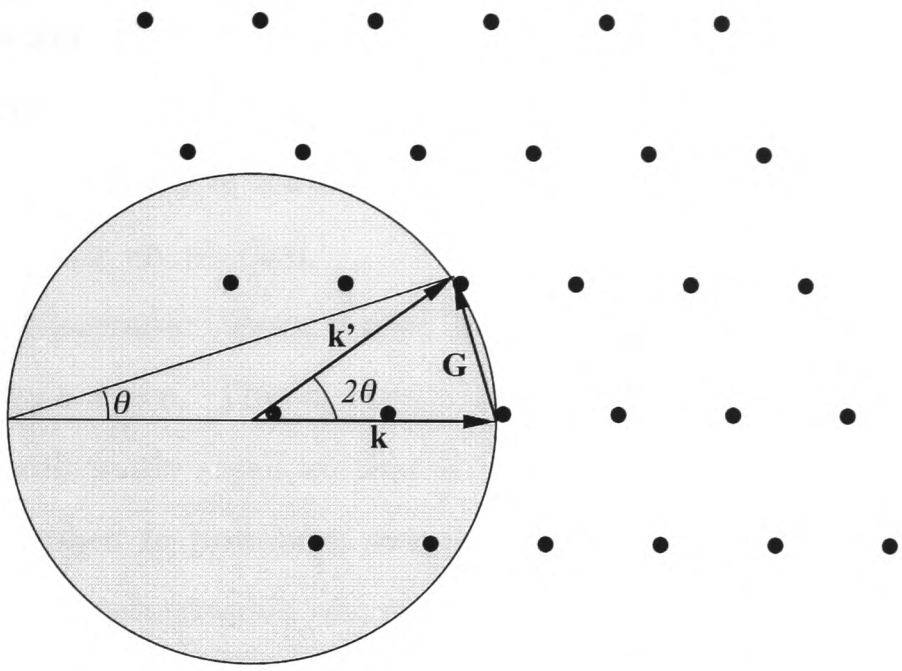


Figure 2.2: Two-dimensional diagram of the Ewald Sphere. The surface of the sphere intercepts two reciprocal lattice points, on one of which the incident wavevector $\mathbf{k}$ terminates. The reciprocal lattice vector $\mathbf{G} = \mathbf{k}' - \mathbf{k}$ represents the diffraction vector which satisfies the Bragg diffraction condition.

$$sin\theta_B = \frac{|\mathbf{G}_{hkl}|}{2|\mathbf{k}|} = \frac{\lambda}{2d_{hkl}} \qquad \Rightarrow \qquad \lambda = 2d_{hkl}sin\theta_B \,.$$

2.2.4 Kinematic and Dynamical X-Ray Diffraction Theories

The theory of X-ray diffraction described above is known as the *Kinematic* X-ray diffraction theory. This definition is a simplified version of the full *Dynamical* X-ray diffraction theory, developed by Darwin in 1914 [51,52], and independently by Ewald.

The Kinematic X-ray diffraction theory treats X-ray scattering from each volume element of a crystal independently, and considers the same amount of intensity incident on all scattering planes, thus ignoring the effects of both *absorption* and *extinction*. Absorption is the reduction in the beam intensity as a consequence of the energy in the beam being deposited in the material the beam passes through. The intensity therefore undergoes an exponential decay as a function of depth. Extinction is specific to crystalline matter and is the weakening of the incident beam in favour of the stronger-growing diffracted beam. Extinction is thus a direct consequence of

energy conservation. Essentially, it is a decay of the incident beam intensity due to efficient scattering. Both absorption and extinction are fully treated by the more complex Dynamical theory of X-ray diffraction, which must be applied in cases when large, perfect crystals are studied.

The simpler Kinematic theory, whilst ignoring these two phenomena, is, however, sufficient in certain cases. This applies when the individual scattering elements in the crystal are sufficiently small, so that no significant beam interaction takes place. It can also be applied to powdered samples, mosaic crystals with a high degree of misalignment of crystallographic planes, as well as to highly strained crystals [53].

Previous work conducted by the group [53, 54] involved studies of single crystals of Silicon, Germanium, and Lithium Fluoride. These pure materials required the use of the Dynamical theory of X-ray diffraction.

Crystal models used for computational simulations in this thesis are small (up to 0.8 μm thick), therefore absorption and extinction can both be safely ignored. Materials studied experimentally are single crystals of metals of thickness in the range 10–200 μm. Previous experimental tests show that carefully grown and handled single crystals of Copper contain dislocation densities between 10^6–$10^9\,\mathrm{cm}^{-2}$ [27, 55], and this number rises rapidly when a crystal is subjected to a shock wave. Recent shock experiments measured post-shock dislocation densities in the range 10^{10}–$10^{11}\,\mathrm{cm}^{-2}$ [8]. Such high densities of impurities mean that beam interaction within the crystals (up to the X-ray absorption and extinction depth) can safely be ignored. Therefore, X-ray scattering from each small volume element can be treated as independent, whilst absorption may still need to be accounted for.

2.3 Physical Properties of Crystalline Matter

This section introduces the matrix representation of two physical quantities, which are crucial to any discussions of shock wave propagation through solid materials: stress and strain.

2.3.1 Stress

A body which is acted upon by external, or internal, forces is said to be in a state of stress. In 3-D, *stress* σ is defined as the force per unit area on a body. A complete description of a stress acting on a body requires a specification of its direction and magnitude, as well as the orientation of the surface on which it is acting. The state of stress in a three-dimensional body is therefore completely specified by nine stress components. This is illustrated in Fig. 2.3 below.

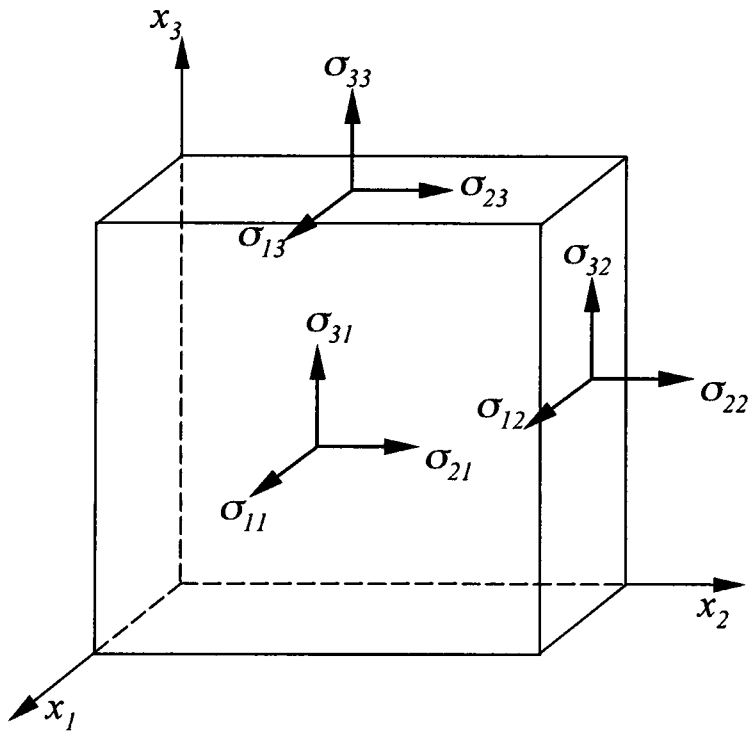


Figure 2.3: Components of the stress tensor in a 3-D body.

All the components of stress acting upon the cube form a second-rank tensor, or

a matrix, which represents the total stress in 3-D:

$$\begin{pmatrix} \sigma_{11} & \sigma_{12} & \sigma_{13} \\ \sigma_{21} & \sigma_{22} & \sigma_{23} \\ \sigma_{31} & \sigma_{32} & \sigma_{33} \end{pmatrix} . \tag{2.20}$$

The notation convention is such that σ_{ij} denotes the component of force per unit area along the positive x_i direction, acting on the face of the cube perpendicular to the x_j axis. The sign convention is such that, for example, σ_{12} is the force per unit area exerted in the positive x_1 direction on the face normal to x_2, exerted by the material outside the cube upon the material inside the cube.

The diagonal components of $[\sigma_{ij}]$, σ_{11}, σ_{22}, and σ_{33} are called the *normal* components of stress. The off-diagonal components σ_{12}, σ_{13}, and σ_{23} represent the *shear* components of stress. By considering moments of force around the three axes x_1, x_2, and x_3, it can be shown [56] that the rotational equilibrium of the volume element requires that

$$\sigma_{12} = \sigma_{21} , \qquad \sigma_{13} = \sigma_{31} , \qquad \sigma_{23} = \sigma_{32} . \tag{2.21}$$

The stress matrix (2.20) is therefore symmetric and there are only six independent stress components: three for normal stress and three for shear stress.

Any stress state can be split up into a *shear* (or deviatoric) component, which causes distortion and yielding and a *hydrostatic* stress component, which causes dilation (volume change) only.

This thesis uses the convention in which a *positive* normal stress results in *tension* and a *negative* normal stress results in *compression.* The pressure acting on one volume element is therefore

$$P = -\frac{1}{3}(\sigma_{xx} + \sigma_{yy} + \sigma_{zz}) . \tag{2.22}$$

2.3.2 Strain

Strain is defined as the extent to which a body is deformed when it is subjected to a stress.

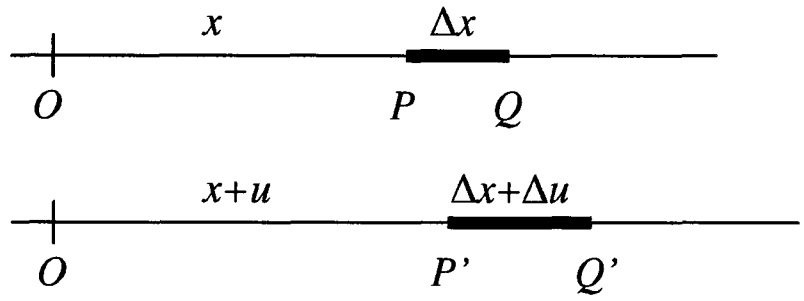


Figure 2.4: Illustration of 1-D strain on an extendible string. Line segment PQ with original length Δx stretches to a new length $\Delta x+\Delta u$.

The simplest case of a strain is in a one-dimensional body. This is illustrated in Fig. 2.4. An extendible string with origin O and an arbitrary point P, with a position x, is subject to tension. As the string is stretched, point P shifts a distance u to P', and a small line segment PQ, with original length Δx, stretches to $P'Q'$, which has a new length $\Delta x + \Delta u$. Since strain is not concerned with actual displacement of points, but with their *relative* displacements, the strain of the section PQ is defined as

$$\frac{P'Q' - PQ}{PQ} = \frac{\Delta u}{\Delta x}\,, \tag{2.23}$$

and strain e at point P is defined as

$$e = \lim_{\Delta x \to 0} \frac{\Delta u}{\Delta x} = \frac{du}{dx}\,. \tag{2.24}$$

This is the definition of strain in one dimension. An extension of this definition of strain to 2-D and 3-D is more complex. The total *deformation matrix* $[e_{ij}]$ can be separated into a *strain matrix* $[\epsilon_{ij}]$ and a *rotation matrix* $[\omega_{ij}]$, such that

$$e_{ij} = \epsilon_{ij} + \omega_{ij}\,, \tag{2.25}$$

where

$$\epsilon_{ij} = \frac{1}{2}(e_{ij} + e_{ji})\,, \tag{2.26}$$

and

$$\omega_{ij} = \frac{1}{2}(e_{ij} - e_{ji})\,. \tag{2.27}$$

The four components e_{ij} of the general deformation matrix are defined as:

$$e_{ij} = \frac{\partial u_i}{\partial x_j} = \frac{\Delta u_i}{\Delta x_j}\,, \tag{2.28}$$

where $i, j = 1, 2$. This definition is the 2-D equivalent of strain in 1-D, defined in eqn. (2.24).

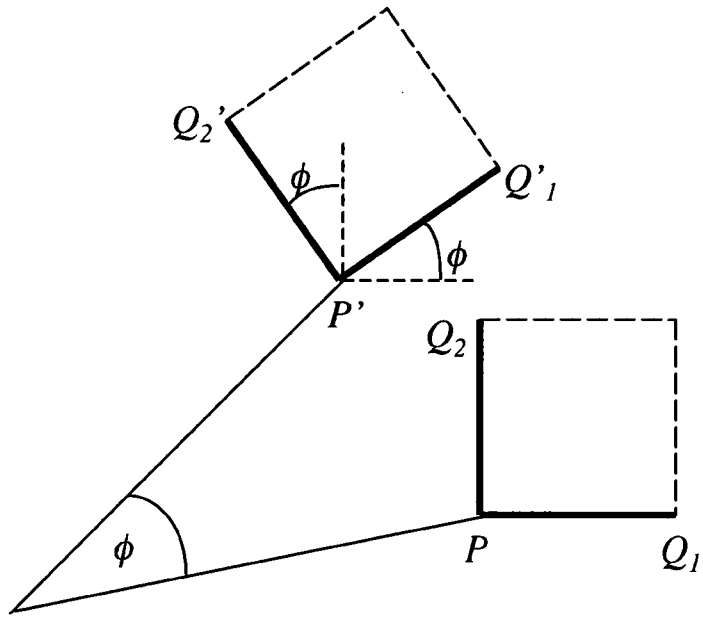


Figure 2.5: A rigid body rotation of a 2-D sheet in its own plane, through a small angle ϕ.

It is important to distinguish between a pure strain and a pure rotation in a 2-D body. Figure 2.5 is an illustration of a pure rotation. A 2-D sheet is rotated through a small angle ϕ. As a result, line $\mathbf{PQ}_1$ is rotated anti-clockwise by an angle ϕ to $\mathbf{P'Q'}_1$, and similarly line $\mathbf{PQ}_2$ is rotated to $\mathbf{P'Q'}_2$. This operation can be expressed

in a matrix form as

$$[\omega_{ij}] = \begin{bmatrix} 0 & -\phi \\ \phi & 0 \end{bmatrix} . \tag{2.29}$$

The sign convention is such that the element ω_{12} of the matrix represents a *clockwise* rotation of line segment $\mathbf{PQ}_2$, and element ω_{21} represents an *anti-clockwise* rotation of line segment $\mathbf{PQ}_1$, causing the matrix (2.29) to be antisymmetric. This is in accordance with the definition of rotation given in eqn. (2.27).

It can be seen that even if an object is subjected to rotation only, and strain components $\epsilon_{ij} = 0$, the total deformation matrix will contain some nonzero elements. In this case, and $[e_{ij}] = [\omega_{ij}]$.

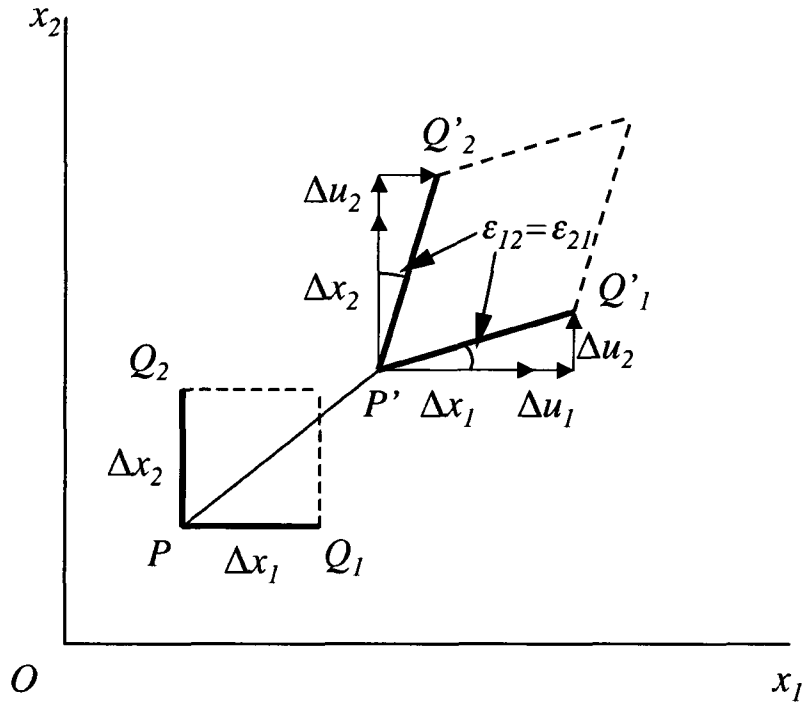


Figure 2.6: Strain of a 2-D body. ϵ_{11} and ϵ_{22} are changes in the horizontal and vertical displacements Δu_1 and Δu_2, respectively. $\epsilon_{21} = \epsilon_{12}$ represent the small angular rotations of $\mathbf{PQ}_1$ anti-clockwise and $\mathbf{PQ}_2$ clockwise.

Pure strain in a 2-D body is illustrated in Fig. 2.6. An extendible plane sheet undergoes a deformation, such that line $\mathbf{PQ}_1$ moves to $\mathbf{P'Q'}_1$ and $\mathbf{PQ}_2$ to $\mathbf{P'Q'}_2$. The quantity $\Delta u_1/\Delta x_1$ is a measure of extension per unit length of $\mathbf{PQ}_1$ along Ox_1, whilst $\Delta u_2/\Delta x_1$ measures the *anti-clockwise* rotation of $\mathbf{PQ}_1$ to $\mathbf{P'Q'}_1$. The exact

angle of this rotation is given by

$$\tan\theta = \frac{\Delta u_2}{\Delta x_1 + \Delta u_1},$$

but since displacements Δu_1 and Δu_2 are $\ll \Delta x_1$, and $\theta \ll 1$, this can be rewritten as

$$\theta = \frac{\Delta u_2}{\Delta x_1}. \tag{2.30}$$

Similarly, for the segment $\mathbf{PQ}_2$, $\Delta u_2/\Delta x_2$ is a measure of extension per unit length of $\mathbf{PQ}_2$ along Ox_2, whilst $\Delta u_1/\Delta x_2$ measures the *clockwise* rotation of $\mathbf{PQ}_2$ to $\mathbf{P'Q'}_2$, as shown in the figure.

In a matrix form, this operation can then be expressed as

$$[\epsilon_{ij}] = \begin{bmatrix} \epsilon_{11} & \epsilon_{12} \\ \epsilon_{21} & \epsilon_{22} \end{bmatrix}. \tag{2.31}$$

The small and equal angular distortions $\epsilon_{12} = \epsilon_{21} = \frac{1}{2}(e_{12} + e_{21})$ are due to pure strain only. For this reason, the matrix in eqn. (2.31) is always symmetric. This is also in accordance with the definition of strain given in eqn. (2.26).

The above results are subject to the assumption that $e_{ij} \ll 1$ [56]. For the calculations relevant to this thesis, this condition holds.

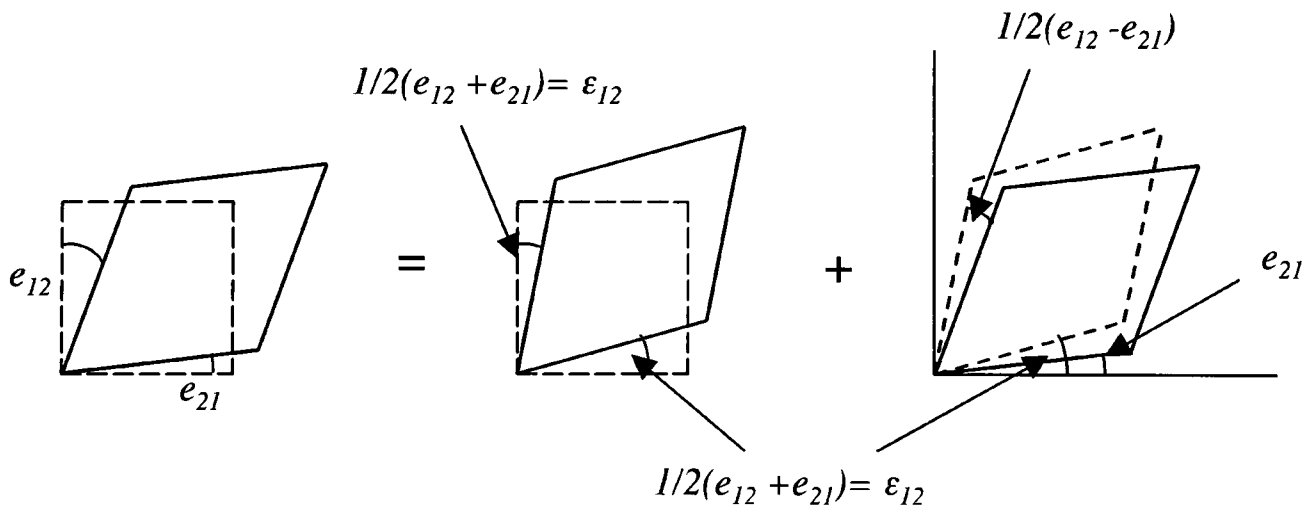


Figure 2.7: Deformation of a 2-D object: the total deformation (left) is a sum of strain (centre) and a rotation (right).

A general deformation of a 2-D body, combining rotation and strain, is illustrated in Fig. 2.7. The total deformation, shown on the left in the figure, can be decomposed into a strain operation, and a rotational operation. The new angle between two originally perpendicular lines due to strain is $\frac{\pi}{2} - (e_{12} + e_{21})$. Pure rotation is responsible for a clockwise angular shift of the originally vertical component by $\frac{1}{2}(e_{12} - e_{21})$, and an anti-clockwise angular shift of the originally horizontal component by $\frac{1}{2}(e_{21} - e_{12})$, as shown on the right in the figure. The sum of these two deformations gives a clockwise angular shift of the originally vertical component by e_{12} and an anti-clockwise angular shift of the originally horizontal component by e_{21}, as illustrated on the left-hand side of the figure.

Extending the above definition of strain and rotation to a three-dimensional solid body subjected to a stress, the 3-D second rank tensors can be written as:

$$\left.\begin{pmatrix} e_{11} & e_{12} & e_{13} \\ e_{21} & e_{22} & e_{23} \\ e_{31} & e_{32} & e_{33} \end{pmatrix}\right\} \quad \text{total deformation}$$

$$= \left.\begin{pmatrix} e_{11} & \frac{1}{2}(e_{12}+e_{21}) & \frac{1}{2}(e_{13}+e_{31}) \\ \frac{1}{2}(e_{21}+e_{12}) & e_{22} & \frac{1}{2}(e_{23}+e_{32}) \\ \frac{1}{2}(e_{31}+e_{13}) & \frac{1}{2}(e_{32}+e_{23}) & e_{33} \end{pmatrix}\right\} \quad \text{strain}$$

$$+ \left.\begin{pmatrix} 0 & \frac{1}{2}(e_{12}-e_{21}) & \frac{1}{2}(e_{13}-e_{31}) \\ \frac{1}{2}(e_{21}-e_{12}) & 0 & \frac{1}{2}(e_{23}-e_{32}) \\ \frac{1}{2}(e_{31}-e_{13}) & \frac{1}{2}(e_{32}-e_{23}) & 0 \end{pmatrix} \cdot\right\} \quad \text{rotation}$$

The separate strain tensor can therefore be rewritten as

$$\begin{pmatrix} \epsilon_{11} & \epsilon_{12} & \epsilon_{13} \\ \epsilon_{21} & \epsilon_{22} & \epsilon_{23} \\ \epsilon_{31} & \epsilon_{32} & \epsilon_{33} \end{pmatrix} = \begin{pmatrix} e_{11} & \frac{1}{2}(e_{12}+e_{21}) & \frac{1}{2}(e_{13}+e_{31}) \\ \frac{1}{2}(e_{21}+e_{12}) & e_{22} & \frac{1}{2}(e_{23}+e_{32}) \\ \frac{1}{2}(e_{31}+e_{13}) & \frac{1}{2}(e_{32}+e_{23}) & e_{33} \end{pmatrix} . \qquad (2.32)$$

The diagonal components of $[\epsilon_{ij}]$, ϵ_{11}, ϵ_{22}, and ϵ_{33} are called the *normal* strains, and are sometimes referred to as *tensile* strains or *stretches*. They are defined as

$$\begin{aligned} \epsilon_{11} = e_{11} &= \frac{\partial u_1}{\partial x_1}, \\ \epsilon_{22} = e_{22} &= \frac{\partial u_2}{\partial x_2}, \\ \epsilon_{33} = e_{33} &= \frac{\partial u_3}{\partial x_3}. \end{aligned} \tag{2.33}$$

They represent the fractional changes in the length of the elements parallel to x_1, x_2, and x_3 axes, respectively. It should be noted that a *tensile* strain is equivalent to a *compressive* strain of the same magnitude and opposite sign, in that direction.

The symmetric off-diagonal components represent the *shear* strains. They are defined as

$$\begin{aligned} \epsilon_{12} = \epsilon_{21} &= \frac{1}{2}\left(\frac{\partial u_1}{\partial x_2} + \frac{\partial u_2}{\partial x_1}\right), \\ \epsilon_{13} = \epsilon_{31} &= \frac{1}{2}\left(\frac{\partial u_1}{\partial x_3} + \frac{\partial u_3}{\partial x_1}\right), \\ \epsilon_{23} = \epsilon_{32} &= \frac{1}{2}\left(\frac{\partial u_2}{\partial x_3} + \frac{\partial u_3}{\partial x_2}\right). \end{aligned} \tag{2.34}$$

The strain matrix, like the stress matrix in the previous section, therefore has only six independent components: three for tensile strains and three for shear strains. The quantities $2\epsilon_{12}$, $2\epsilon_{13}$, and $2\epsilon_{23}$ from eqn. (2.34) can also be referred to as the *engineering* strains γ_{12}, γ_{13}, and γ_{23}, respectively.

2.3.3 Elasticity

In the linear elasticity regime of materials, the relationship between stress and strain is given by *Hooke's law*. This states that, within the elastic limit for any solid, the stress applied to a material is proportional to the strain it produces.

For a one-dimensional body, this is written as

$$\epsilon = s\sigma\,, \tag{2.35}$$

$$\sigma = c\epsilon\,, \tag{2.36}$$

where s and c are the *elastic compliance constant* (or just *compliance*), and *elastic stiffness constant* (or *stiffness*), respectively. c is also called the *Young's Modulus of elasticity.*

In 3-D, the linear relationship between the stress and strain tensors is more complicated, and can be expressed in a concise form as

$$\epsilon_{ij} = s_{ijkl}\sigma_{kl}\,, \tag{2.37}$$

$$\sigma_{ij} = c_{ijkl}\epsilon_{kl}\,. \tag{2.38}$$

Here, s_{ijkl} and c_{ijkl} represent fourth-rank tensors relating stress and strain in 3-D bodies. A 3-D fourth-rank tensor has 3^4 components. It can be shown that for cubic crystals, this reduces to three independent components [57]. Considering only the six independent components in the stress (eqn. (2.20)) and strain (eqn. (2.32)) matrices, the equation relating these components of the stress and the strain tensors can be written as

$$\begin{array}{c} \\ \epsilon_{11} \\ \epsilon_{22} \\ \epsilon_{33} \\ \gamma_{12} \\ \gamma_{23} \\ \gamma_{13} \end{array} \begin{array}{c} \begin{array}{cccccc} \sigma_{11} & \sigma_{22} & \sigma_{33} & \sigma_{12} & \sigma_{23} & \sigma_{13} \end{array} \\ \begin{pmatrix} s_{11} & s_{12} & s_{12} & 0 & 0 & 0 \\ s_{12} & s_{11} & s_{12} & 0 & 0 & 0 \\ s_{12} & s_{12} & s_{11} & 0 & 0 & 0 \\ 0 & 0 & 0 & s_{44} & 0 & 0 \\ 0 & 0 & 0 & 0 & s_{44} & 0 \\ 0 & 0 & 0 & 0 & 0 & s_{44} \end{pmatrix} \end{array}\,, \tag{2.39}$$

where s_{11}, s_{44} and s_{12} are the independent components of the compliance tensor.

Similarly, the relationship for stiffness c_{ijkl} is reduced to

$$\begin{array}{c} \\ \sigma_{11} \\ \sigma_{22} \\ \sigma_{33} \\ \sigma_{12} \\ \sigma_{23} \\ \sigma_{13} \end{array} \begin{array}{c} \begin{array}{cccccc} \epsilon_{11} & \epsilon_{22} & \epsilon_{33} & \gamma_{12} & \gamma_{23} & \gamma_{13} \end{array} \\ \begin{pmatrix} c_{11} & c_{12} & c_{12} & 0 & 0 & 0 \\ c_{12} & c_{11} & c_{12} & 0 & 0 & 0 \\ c_{12} & c_{12} & c_{11} & 0 & 0 & 0 \\ 0 & 0 & 0 & c_{44} & 0 & 0 \\ 0 & 0 & 0 & 0 & c_{44} & 0 \\ 0 & 0 & 0 & 0 & 0 & c_{44} \end{pmatrix} \end{array} . \tag{2.40}$$

The stiffness (or compliance) constants are directly related to the *shear modulus* G of a crystal, also known as the *rigidity modulus*, which is a measure of its strength. For cubic crystals, this is given by

$$G = \frac{1}{s_{44}} = c_{44} . \tag{2.41}$$

2.4 Shock Waves

This section details the theory underlying shock wave propagation in a material. Conservation equations for a shock wave are derived, as is the shock Hugoniot. A comparison of shock waves in fluids and solids is given, and the types of shock waves which occur in crystalline solids are outlined.

2.4.1 Shock Waves in Fluids

A wave is a disturbance propagating through a medium. The medium can be gaseous, liquid, or solid, or a field, and the disturbance can be mechanical or electromagnetic.

An important quantity characterising a medium when discussing waves is the propagation of sound in it. A sound wave is defined as an oscillatory motion of a small amplitude in a compressible fluid, which causes alternate compressions and rarefactions at each point in the fluid [58], and its speed c is defined by

$$c^2 = \left(\frac{\partial P}{\partial \rho}\right)_S = -V^2\left(\frac{\partial P}{\partial V}\right)_S, \tag{2.42}$$

where P is the pressure in the fluid, ρ is its density, S is entropy, and V is the fluid specific volume (i.e. volume per unit mass) [59]. The significance of the speed of a sound wave is illustrated in Fig. 2.8 below.

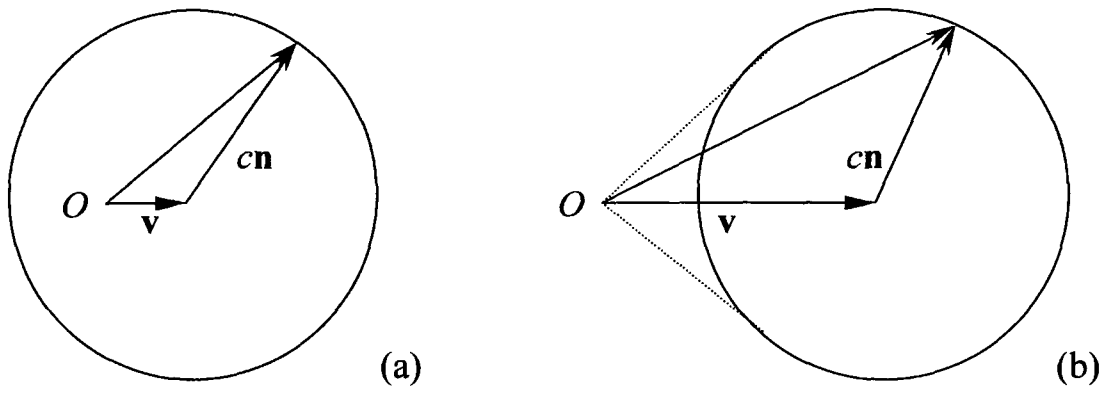


Figure 2.8: Difference between subsonic and supersonic waves propagating through a fluid medium. Disturbance in (a) will propagate through the whole medium continuously. In (b), the disturbance will only propagate within the characteristic surface enclosed by the cone.

A disturbance at a point O in a compressible fluid, moving with a velocity $\mathbf{v}$, causes a wave to propagate through the medium. The velocity with which the perturbation will propagate from O will be $\mathbf{v} + c\mathbf{n}$, where $\mathbf{n}$ is the unit vector in any direction. If $|\mathbf{v}| < c$, the wave will propagate through the entire medium, which is able to respond to the disturbance smoothly and the transition between the disturbed and undisturbed regions of the material will be continuous. This is illustrated in part (a) of the figure. This is the regime of *subsonic flow.*

If, however, the disturbance causing the wave propagating through the medium is such that $|\mathbf{v}| > c$, the medium will not be able to respond as quickly as the perturbation itself and the disturbance will not propagate through the entirety of the medium. The directions of the vector $\mathbf{v} + c\mathbf{n}$ can only lie on a cone with its vertex at O, which touches the sphere of radius c centred at the other end of the vector $\mathbf{v}$. This is shown in part (b) of Fig. 2.8. This is the regime of *supersonic flow.*

The surface enclosing the region reached by the disturbance starting from point O is called the *characteristic surface*, or the *characteristic.* There is a sharp discontinuity at the surface, separating the perturbed and unperturbed regions of the medium. Since the disturbance only affects regions within the characteristic, the discontinuity is stable. This is the regime of shock waves, and a medium in this state can be described as *shocked.*

A *shock wave* is therefore defined as a discontinuity in pressure, temperature (or internal energy), and density.

The concept of shock propagation in a fluid is illustrated in Fig. 2.9. A fluid is compressed in a cylinder which has a unit cross-section area by a piston moving from left to right. When the piston is at rest, the initial pressure, density, and internal energy per unit mass of the material are P_0, ρ_0, and E_0, respectively. The piston is then pushed into the material at a velocity u_p, referred to as the *piston velocity*, or *particle velocity.* After time t, the compressed region ahead of the piston has moved a distance $u_s t$, where u_s is the *shock velocity*, whilst the piston has moved a distance $u_p t$. The compressed region is separated from the stationary, undisturbed material

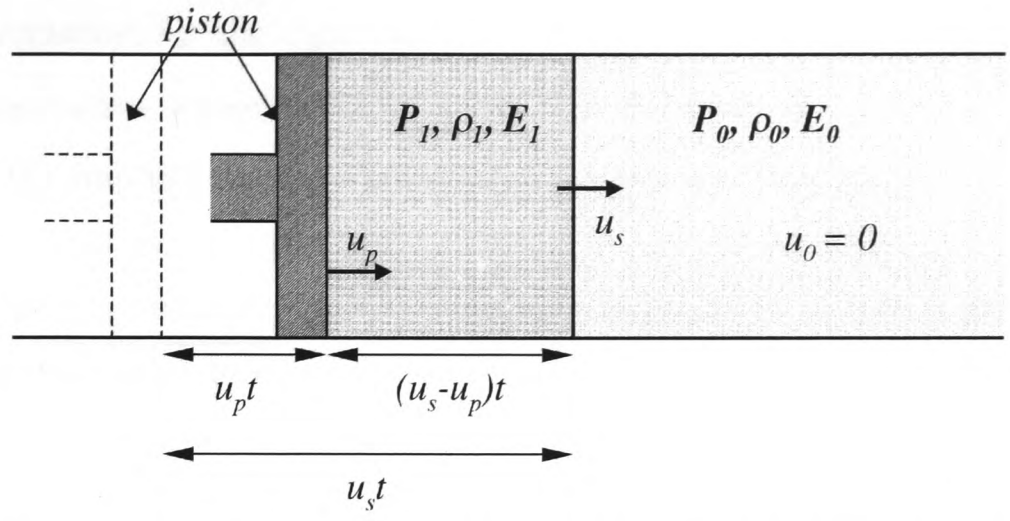


Figure 2.9: Illustration of shock propagation in a fluid enclosed in a cylinder. In time t, the piston moves a distance $u_p t$, compressing some of the material, whose total mass is now $\rho_1(u_s - u_p)t$. The uncompressed material ahead of the shock front is moving at a velocity $u_0 = 0$.

by the *shock front*, which is moving at u_s. At time t, the total mass of the compressed region between the piston and the shock front is $\rho_1(u_s - u_p)t$. As the piston moves further inwards, more material is continuously added to the compressed region. It follows that for a shock wave, $u_s > u_p$.

2.4.2 Rankine-Hugoniot Jump Condition Equations

The compressed and uncompressed regions in a fluid are related via conservation equations for mass, momentum, and energy. These are derived under the so called *hydrodynamic* treatment of shocks, which can be applied to fluids. One crucial assumption is that the shear modulus of the material is taken to be zero.

For mass conservation, the mass moving towards the shock front per unit time and the mass moving away from the shock front per unit time are equal. This yields the expression

$$\underbrace{\rho_0(u_s - u_0)dt}_{\text{mass ahead of shock front}} = \underbrace{\rho_1(u_s - u_p)dt}_{\text{mass behind shock front}} ,$$

which can be reduced to

$$\boxed{\rho_0 u_s = \rho_1(u_s - u_p)\,.} \tag{2.43}$$

This is the equation for the conservation of mass.

The conservation of momentum requires that the total change in momentum must be equal to the impulse that the material is subject to. This gives

$$\underbrace{\rho_1(u_s-u_p)u_p dt}_{\text{momentum behind shock front}} - \underbrace{\rho_0(u_s-u_0)u_0 dt}_{\text{momentum ahead of shock front}} = \underbrace{(P_1-P_0)dt}_{\text{impulse}} .$$

Taking $u_0 = 0$ and using eqn. (2.43), this can be rewritten as

$$\boxed{\rho_0 u_s u_p = P_1 - P_0 ,} \tag{2.44}$$

which is the equation for the conservation of momentum.

To derive the equation for the energy conservation, the total work done on the material ΔW is equated to the total change in kinetic ΔE_k plus internal ΔE_i energies of the system. This is formulated as

$$\underbrace{P_1 u_p dt - P_0 u_0 dt}_{\Delta W} = \overbrace{\frac{1}{2}\left[\rho_1(u_s-u_p)dt\right]u_p^2 - \frac{1}{2}\left[\rho_0(u_s-u_0)dt\right]u_0^2}^{\Delta E_k} + \underbrace{E_1\rho_1(u_s-u_p)dt - E_0\rho_0(u_s-u_0)dt .}_{\Delta E_i}$$

Taking $u_0 = 0$ and using eqn. (2.43) again, this can be rewritten in a simpler form

$$\boxed{P_1 u_p = \frac{1}{2}\rho_0 u_s u_p^2 + \rho_0 u_s (E_1 - E_0) ,} \tag{2.45}$$

where E represents the internal energy per unit mass. This is the equation for the conservation of energy in a shock wave.

Equations (2.43), (2.44), and (2.45) are the *Rankine-Hugoniot* conservation equations for a shock wave [13, 14], also known as the *jump condition* equations. They relate the variables on either side of the discontinuity represented by the shock front.

Rearranging the jump condition equations yields further useful formulae describing the behaviour of shock waves. By substituting specific volume V (i.e. volume per unit mass) for the inverse of density $1/\rho$, eqn. (2.43) and (2.44) give an expression for the shock velocity:

$$u_s^2 = V_0^2 \frac{P_1 - P_0}{V_0 - V_1} \,. \tag{2.46}$$

Similarly, the particle velocity u_p of the fluid behind the shock front is given by

$$u_p^2 = (P_1 - P_0)(V_0 - V_1) \,. \tag{2.47}$$

Dividing eqn. (2.47) by eqn. (2.46) and taking the positive root of the equation gives a useful expression relating the compressive volumetric strain to the shock velocity and the particle velocity:

$$\frac{\Delta V}{V_0} = \frac{u_p}{u_s} \,. \tag{2.48}$$

Also, substituting eqn. (2.46) and (2.47) back into eqn. (2.45) gives the *Hugoniot energy equation*,

$$\boxed{E_1 - E_0 = \frac{1}{2}(P_1 + P_0)(V_0 - V_1) \,.} \tag{2.49}$$

This relates the change in the internal energy per unit mass of the system to the initial and final pressures and specific volumes across the shock discontinuity.

2.4.3 The Shock Hugoniot

A graphic form of the eqn. (2.49) is illustrated in Fig. 2.10. It is referred to as the *Hugoniot* and is defined as the locus of all possible shocked states in a material. It is important to note that when a shock is applied and the material changes its state from $\mathrm{A}(P_0, V_0)$ to a final state $\mathrm{B}(P_1, V_1)$, the changes in pressure and volume that the material undergoes do not follow the Hugoniot curve; rather, they change

discontinuously from P_0, V_0 to P_1, V_1.

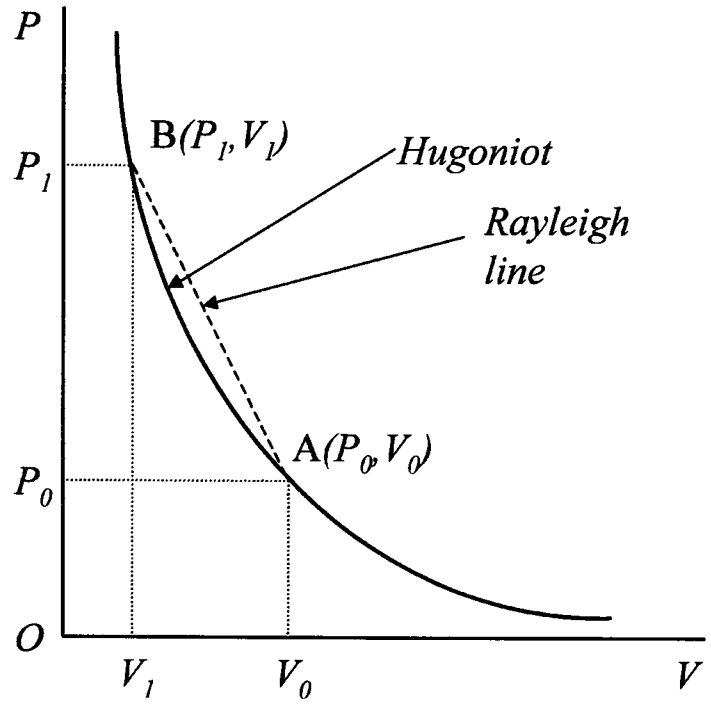


Figure 2.10: Illustration of a shock Hugoniot for a fluid. The Rayleigh line is a straight line connecting an initial state A and a final state B separated by the shock discontinuity. The gradient of the line, given by $(P_1 - P_0)/(V_1 - V_0)$, is directly related to the speed of the shock, u_s.

The straight line joining the initial state $\mathrm{A}(P_0, V_0)$ with a final state $\mathrm{B}(P_1, V_1)$ is called the *Rayleigh line*. The gradient of the Rayleigh line, $(P_1 - P_0)/(V_1 - V_0)$, is directly related to the square of the shock velocity in the material and, using eqn. (2.46), is given by

$$\frac{P_1 - P_0}{V_1 - V_0} = -\frac{u_s^2}{V_0^2}\,. \tag{2.50}$$

The general condition for shock stability is also related to the slope of the Rayleigh line. In order for a shock to be stable, the rate of change of a Hugoniot must increase with compression, i.e. $\partial^2 P/\partial V^2 > 0$. This causes the shock to steepen and overcome any dispersive effects in the material. The gradient of the Rayleigh line linking any initial and final states A and B must be higher than that of the tangent of the

Hugoniot at the initial state A which, by (2.42), is

$$\left(\frac{\partial P}{\partial V}\right)_S = -\left(\frac{c}{V}\right)^2, \tag{2.51}$$

hence directly determining the speed of sound in the fluid. This means that the shock speed is greater than the sound speed, and the shock is stable.

2.4.4 Shock Waves in Solids

The previous discussion of shock waves was based on shocks in fluids. A fluid cannot support any shear (deviatoric) stresses and the compression in it will therefore be *hydrostatic.* This means that the off-diagonal components in the stress tensor (2.20) will be zero, and the diagonal elements will be such that

$$\sigma_{xx} = \sigma_{yy} = \sigma_{zz} = -P\,, \tag{2.52}$$

where P is the hydrostatic pressure in the fluid.

The primary difference between fluids and crystalline solids in relation to shock propagation arises from the fact that a crystal structure can support shear stresses. This results in an anisotropic behaviour and usually the component of stress along the shock propagation direction σ_{zz} will be greater than the transverse components σ_{xx} and σ_{yy}. However, when the shear stresses in a solid become negligible with respect to hydrostatic stresses, the shear stress component can be ignored and, in this approximation, the same treatment as for fluids can be applied.

A shock wave travelling through a solid, whose amplitude does not exceed its elastic threshold, called the *Hugoniot Elastic Limit* (HEL), will be an elastic wave. The material will respond elastically, obeying Hooke's law (2.37), and the compression caused by the shock wave will be uniaxial in the direction of the wave propagation, and reversible.

When the amplitude of a wave travelling through a solid exceeds the HEL, the material yields to plastic flow and plastic deformation sets in. In terms of the material

strength, this is when the shear stress exceeds the dynamic yield shear stress of the solid [3]. The wave travelling through the solid decomposes into its *elastic* and *plastic* components.

A simplified configuration for a shock wave travelling in a solid is illustrated in Fig. 2.11.

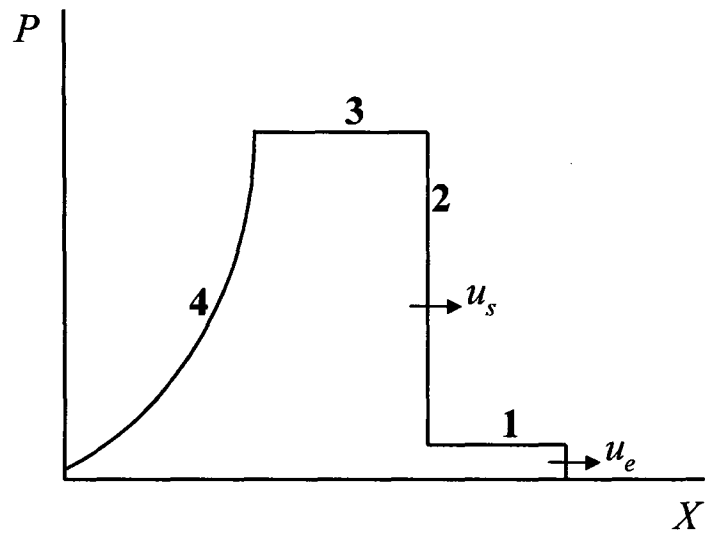


Figure 2.11: Illustration of an idealised shock wave in a solid. The elastic precursor (1) precedes the plastic shock front (2). The pressure remains at its peak (3) for a length depending on the duration of the impact pulse, and decreases in the release part of the wave (4).

Ideally, a shock wave consists of a shock front, a flat top, and a release part. The elastic precursor (1) has an amplitude equal to the HEL of the material. When the solid gives way, a steep discontinuity in the form of the shock front (2) is created, which travels at the shock velocity u_s. In real crystals, the discontinuity is not vertical, but its slope has been shown to increase with increasing initial pressure (or particle velocity u_p) [4, 60]. The shock wave beyond the discontinuity initially has a square shape. This has a flat top (3), whose length depends on the length of the impact pulse propagating through the material. In the case of the experiments conducted for this thesis, the maximum length of (3) is equivalent to the length of the laser pulse used to shock the crystal. The part of the wave where the pressure returns to zero (4) is called the *release*, or *rarefaction* part of the wave. This rarefaction wave, closely following the shock wave as it propagates into the bulk of the crystal, results

in a gradually decaying shock wave, shortening the duration of its peak pressure (3), and decreasing its magnitude [48].

In the region of strong plastic deformation, when the shear stresses in a solid can be neglected in comparison with the compressive hydrostatic components, the solid can be approximated as a fluid with zero shear stress. The jump condition equations (2.43)–(2.45) derived earlier can therefore be applied to shocks in solids as well as fluids, so long as the shock wave propagating through the material is stable.

The Hugoniot curve for a shock wave in a solid will differ from that in a fluid shown in Fig. 2.10. A simplified $P - V$ relationship is shown in Fig. 2.12.

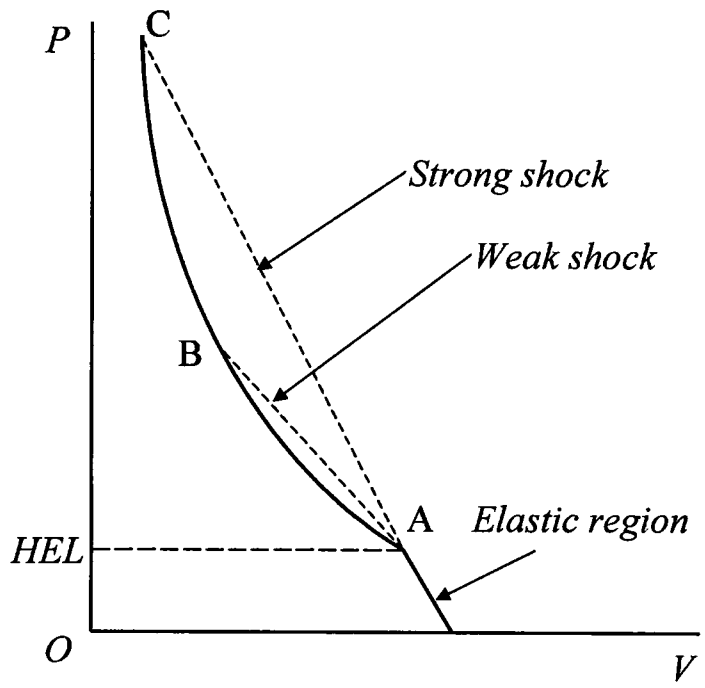


Figure 2.12: Illustration of a shock Hugoniot in a solid. The linear elastic region below HEL is shown, as are two shock regimes. For a weak shock, the gradient AB of the Rayleigh line is lower than the slope of the line of the elastic region, so $u_e > u_s$. For a strong shock, the Rayleigh line gradient AC exceeds this value, so $u_s > u_e$.

In the elastic region below the HEL, the $P - V$ Hugoniot is approximately linear. When the material yields to plastic flow, the rate of change of the Hugoniot decreases with respect to that in the elastic region. As the pressure increases further, the gradient of the Hugoniot will typically rise again.

There are two types of shocks in the plastic deformation region, depending on the magnitude of the shock wave peak pressure: a *weak shock* and a *strong shock*.

In the strong shock case, the peak amplitude of the shock wave greatly exceeds the HEL (typically by orders of magnitude). In this regime, the slope of the Rayleigh line for the plastic part of the Hugoniot will be steeper than the gradient of the linear elastic line below the HEL. The speed of the plastic component of the shock wave will therefore exceed that of the elastic component, and the plastic wave will overtake the elastic one, resulting in a single wave.

In the weak shock case, the peak amplitude of the shock wave will usually be several times larger than the HEL of the solid. The gradient of the Rayleigh line will be smaller than that of the corresponding elastic part, and the elastic precursor will propagate faster than the plastic wave.

The work conducted for this thesis deals mainly with shocks in the weak shock regime, where the speed of the plastic component of the wave does not exceed that of the elastic component.

A plastic wave satisfying the above description is said to be in a state of *purely uniaxial strain*. This allows the build-up of the hydrostatic component of stress to high levels [3]. The total *transverse* strain in the material is therefore zero and any volumetric change in the material is solely due to the *longitudinal* strains:

$$\epsilon_T = \epsilon_T^p + \epsilon_T^e = 0\,, \tag{2.53}$$

$$\epsilon_L = \epsilon_L^p + \epsilon_L^e = \frac{\Delta V}{V_0} \neq 0\,, \tag{2.54}$$

where ϵ_L and ϵ_T are the total longitudinal and transverse strains, with the superscripts p and e corresponding to their plastic and elastic components, respectively.

It is also assumed that the total sum of all *plastic* strains (one in the longitudinal direction and two in the transverse directions) in the material is zero:

$$2\epsilon_T^p + \epsilon_L^p = 0\,. \tag{2.55}$$

This is called the *zero dilation assumption* for a shock wave [61]. It should be noted that this implies that plastic flow, i.e. shear deformation in response to the shear

stress, is not compressive.

Combining equations (2.53)–(2.55), it can be seen that the total volumetric change (i.e. compression or dilation) in the crystal is purely due to the elastic component of the strain, and is reversible; when the load is removed, the volume returns to its initial value. The fractional volume change is given by

$$\frac{\Delta V}{V_0} = 2\epsilon_T^e + \epsilon_L^e \,. \tag{2.56}$$

By diffracting from a number of crystal planes, it is possible to measure the longitudinal and transverse components of the elastic strain.[2] X-ray diffraction therefore provides a measure of the volumetric compression of the crystal. Furthermore, by rearranging equations (2.53)–(2.55), we find that

$$\epsilon_T^p = -\epsilon_T^e \,, \tag{2.57}$$

$$\epsilon_L^p = 2\epsilon_T^e \,. \tag{2.58}$$

The extreme usefulness of X-ray diffraction therefore lies in the fact that it is capable of measuring both transverse and longitudinal components of elastic and plastic strains in a crystal, and hence determine the size and shape of the unit cell.

In a real material with non-negligible shear strength, the nonhydrostatic components of the stress have to be considered. The hydrostatic pressure in a solid is defined as

$$P = -\frac{1}{3}(\sigma_{xx} + \sigma_{yy} + \sigma_{zz}) = -\frac{1}{3}(2\sigma_{xx} + \sigma_{zz}) \,, \tag{2.59}$$

assuming that the shock propagation direction is along the z axis and that the two transverse components of the stress are equal. The maximum value of the shear stress

[2]The effect of stacking faults and dislocations on the position of the diffracted intensity peak is discussed in section 2.7.

τ_{max} is defined as half the difference between the longitudinal and transverse stresses:

$$\tau_{max} = \frac{1}{2}(\sigma_{zz} - \sigma_{xx})\,. \tag{2.60}$$

This gives the final expressions for the longitudinal σ_{zz} and transverse $\sigma_{xx} = \sigma_{yy}$ components of stress as

$$\sigma_{zz} = -P + \frac{4}{3}\tau_{max}\,, \qquad \sigma_{xx} = \sigma_{yy} = -P - \frac{2}{3}\tau_{max}\,. \tag{2.61}$$

It can be seen that in the case of fluids, where the shear stress is relieved by viscous flow, this equation yields the relationship for stress components in a fluid as shown in eqn. (2.52).

2.4.5 Equations of State for a Shock Wave

A further equation describing the behaviour of shock waves in a large number of solid materials is an empirical equation relating the shock velocity u_s and the particle velocity u_p. Its general form is a polynomial and is given by

$$u_s = c_0 + S_1 u_p + S_2 u_p^2 + \ldots\,,$$

where c_0 is the sound speed in the material at zero pressure, and parameters S_1 and S_2 have to be experimentally determined.

For most metals, $S_2 = 0$ and the equation takes the linear form

$$\boxed{u_s = c_0 + S_1 u_p\,.} \tag{2.62}$$

This is known as the *Equation of State* (EOS) of a material. This linear relationship is a good description of a material subject to a shock wave, so long as it does not undergo a phase transition. In that case, the form of the EOS changes [3].

2.5 Crystal Defects

This sections covers the theory of defects in crystals. Fundamental definitions of various physical quantities related to different types of defects are provided, and the important concept of movement of dislocations is related to shear stress release upon shock loading.

2.5.1 Line, Planar, and Volume Defects

A defect is a discontinuity, or imperfection, in a crystal. Defects may be point (0-D), line (1-D defects), surface or planar (2-D), and volume (3-D).

Point defects are *vacancies* and *interstitial atoms*. The former is an absence of an atom in its lattice site. The latter is the presence of an atom in a non-lattice site. If the interstitial atom is of the same element as the main body of the crystal, this is then called an *intrinsic* defect. Vacancies and interstitials can be produced by plastic deformation. Additionally, point defects appear in perfect crystals as a result of thermal vibrations; all crystals at temperatures above $0K$ have a nonzero concentration of point defects [56].

Impurity atoms in a crystal are called *extrinsic* defects. These can either be *interstitial*, or *substitutional*, i.e. replacing an intrinsic atom in its atomic site.

One dimensional defects in crystals are called *dislocations*. They can be *perfect* or *partial*, the latter resulting in 2-D planar defects called *stacking faults*. Both these defects are covered in greater detail below in sections 2.5.2–2.5.4.

Volume defects in crystals include imperfections such as precipitates, voids, and bubbles. These are not relevant to the work in this thesis, and their theory is not covered in this chapter.

2.5.2 Dislocations – Line Defects

A dislocation is defined as the boundary between the slipped and unslipped regions in a crystal. A slipped region is one where the atoms have been displaced from their

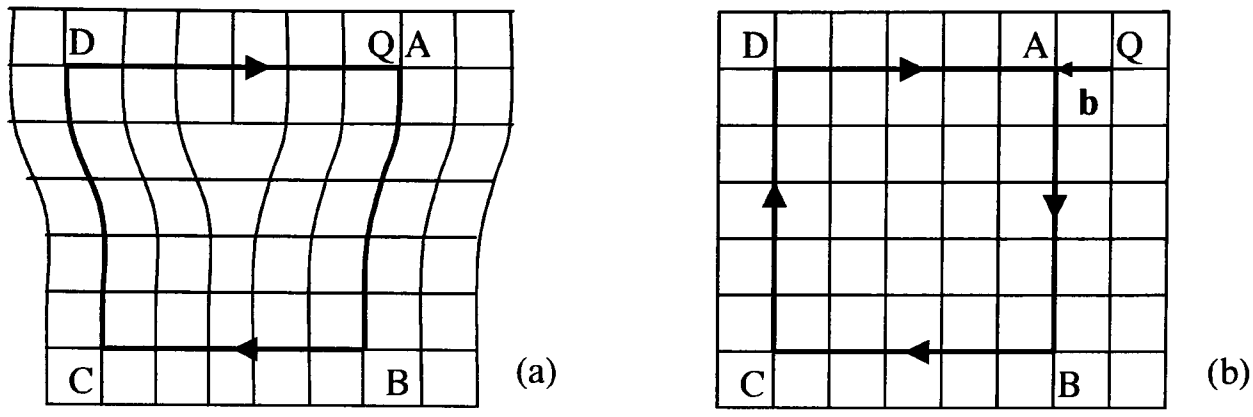


Figure 2.13: Illustration of the Burgers circuit around an edge dislocation. The dislocation in (a) is enclosed by the Burgers circuit ABCD. Point A coincides with Q. In (b) the circuit passes through the same part of the crystal, but without the dislocation. The circuit is now shorter by the path **QA**, which is the Burgers vector of the dislocation. It is perpendicular to the line of the edge dislocation.

original positions by more than a half of the lattice constant.

Burgers Vector

There are two main types of dislocations, the *edge* dislocation and the *screw* dislocation. An edge dislocation is an extra half-plane of atoms inserted in between two atomic planes. A screw dislocation occurs when a crystal is displaced in such a way that two sides of the crystal, separated by an atomic plane, move along the plane in directions opposite with respect to one another.

An important parameter for describing a dislocation is its *Burgers vector.* This is illustrated on an edge dislocation in Fig. 2.13. An atom-to-atom path is taken around the dislocation in question. The loop completely encloses the dislocation, so that its path only passes through unperturbed parts of the crystal. This is called a *Burgers circuit.* The path is compared to a closed loop in the same region of the crystal, but without any dislocations. The difference in the two paths is the Burgers vector of the dislocation.

The line of an edge dislocation is normal to its Burgers vector. The line of a screw dislocation is parallel to its Burgers vector.

Perfect Dislocations

A dislocation whose Burgers vector is a lattice translation vector is known as a *perfect*, or *unit* dislocation.

Density of Dislocations

The *dislocation density* ρ_d is defined as the number of dislocations intersecting a unit area, and is given by

$$\rho_d = l/V\,, \tag{2.63}$$

where l is the total line of dislocations in volume V. (Here, ρ is unrelated to the electronic density described in section 2.2, or the fluid density described in section 2.4.) The units of dislocation density are usually cm^{-2}.

As mentioned earlier in this chapter, the initial dislocation densities in metals tend to be several orders of magnitude higher than those in non-metallic crystals; prior to shock-compression this is in the range 10^6–$10^9\,\mathrm{cm}^{-2}$. Shock wave propagation through metallic crystals increases the values of ρ_d up to 10^{11}–$10^{13}\,\mathrm{cm}^{-2}$ [8]. In this thesis, values of dislocation densities in simulations of shocked crystals are also calculated, and this is described in Chapter 4.

2.5.3 Movement of Dislocations

Plastic deformation of a crystalline solid requires a *critical shear stress*, τ_c. Work on shear stress modelling was pioneered by Frenkel [62], and his model of shear stress in a crystalline solid is illustrated in Fig. 2.14.

The periodic shearing force per unit area, τ_{th}, required to move the top row of atoms across the bottom row is given by

$$\tau_{th} = \frac{Gb}{2\pi a} \sin \frac{2\pi x}{b}\,,$$

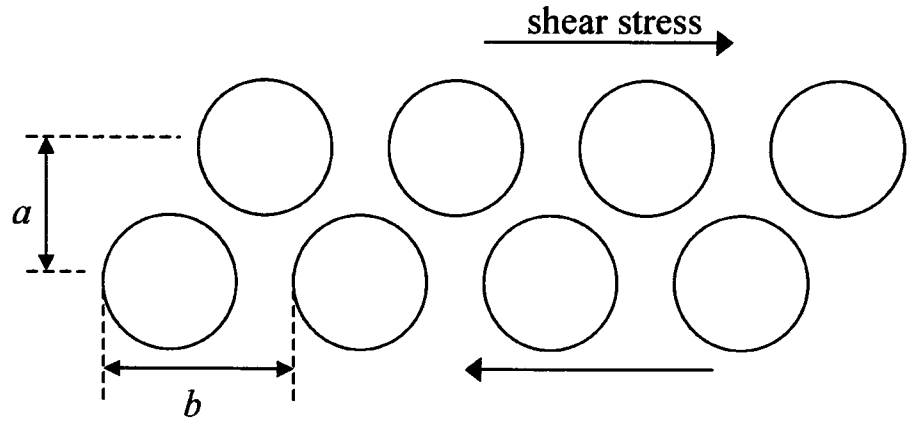


Figure 2.14: Illustration of applying shear stress in a material. When the applied stress exceeds the threshold value τ_c, regions of the crystal shear, and atomic planes on the interface move in opposite directions to one another.

where G is the shear modulus, b is the interatomic spacing in the direction of the applied shear force, a is the spacing between the atomic rows, and x is the translation of the two rows from their equillibrium positions. The critical shear stress of a material, τ_c, is given by the maximum value of this expression which, using $a \approx b$, can be written as

$$\tau_c \simeq \frac{G}{2\pi} . \tag{2.64}$$

In real materials, however, the value of the critical shear stress required for plastic deformation has been shown to be several orders of magnitudes lower than the values given by eqn. (2.64), in the region of 10^{-4}–10^{-8} G [27]. This discrepancy was first linked to the presence of mobile dislocations in crystals independently by Orowan, Taylor, and Polanyi in 1934 [63–65]. It is the *movement* of the dislocations present in crystals which significantly reduces the critical shear stress.

In a region where a dislocation is present, a much smaller shear stress is required to cause a slip of atomic planes, and hence plastic deformation. This reduced stress is called the *Peierls-Nabarro stress*, and is much smaller than the theoretical shear stress of a perfect lattice. In perfect regions far away from dislocations, where atoms are close to or at their ideal atomic sites, large stress is required to move them from these sites. In the vicinity of a dislocation, atoms are not in their ideal atomic

sites, and a relatively small change in the position of a few atoms is required for a dislocation to move. The Peierls-Nabarro stress is sensitively dependent on the nature of interatomic bonding, i.e. the force-distance relation between individual atoms [56].

Glide and Climb

The two basic types of dislocation movement are *glide* and *climb*. Glide occurs when the motion is in the plane containing both the dislocation line and its Burgers vector. It is also called *conservative motion*, meaning that the total number of atoms and lattice sites is conserved when this motion occurs [66]. Dislocations able to move in this way are called *glissile*, those that cannot are *sessile*. Climb, or *nonconservative motion*, involves movement normal to the Burgers vector of the dislocation.

Glide of many dislocations is called a *slip*. This is the most common type of dislocation movement, and hence the most common type of plastic deformation in crystalline solids. When a slip occurs, a plane of atoms slides in a certain *slip direction* over another plane. The slip direction is always parallel to the Burgers vector of the dislocation responsible for the slip. The plane in which the motion occurs is called the *slip plane*. From the definition of climb given above, a slip plane must contain both the line and the Burgers vector of the dislocations undergoing the motion. A slip direction and slip plane together define a *slip system*.

Slip planes are generally planes with the highest density of atoms. The direction of a slip usually corresponds to one of the shortest possible translation vectors in the lattice. In FCC crystals, slip therefore mostly occurs on $\{111\}$ planes, in $\langle 110 \rangle$ directions. Each of the four $\{111\}$ planes contains three possible $\langle 110 \rangle$ directions. FCC crystals therefore have twelve $\{111\}$ $\langle 110 \rangle$ slip systems.

Orowan Equation

Dislocation movement is directly related to the plastic deformation a crystal undergoes. This is in addition to the *elastic strain*, which is simply related to the external stress by Hooke's law. The relationship between the *plastic strain* in a crystal and

dislocation motion is given by

$$\epsilon^p = b\rho_m\langle x\rangle\,, \tag{2.65}$$

where ϵ^p is the total plastic strain, b is the magnitude of the Burgers vector of the moving dislocations, ρ_m is their density, and $\langle x\rangle$ is the average distance moved by one dislocation. If N is the total number of mobile dislocations, $\langle x\rangle$ is given by

$$\langle x\rangle = \frac{1}{N}\sum_{i=1}^{N} x_i\,. \tag{2.66}$$

This relationship is for slip of edge or screw dislocations. It follows that the plastic *strain rate*, $\dot{\epsilon^p}$, which is the measure of how fast a plastic deformation in a material propagates through it, is therefore

$$\dot{\epsilon^p} = \frac{d\epsilon^p}{dt} = b\rho_m\langle v\rangle\,, \tag{2.67}$$

where $\langle v\rangle$ is the mean speed of the mobile dislocations. Equation (2.67) is known as the *Orowan equation*, as the dependence of plastic shear strain rate on dislocation motion was first formulated by Orowan in 1940 [67].

The stress dependence of dislocation velocity varies strongly between materials. This is shown in Fig. 2.15. The relationship for Copper has been highlighted. In comparison with other materials, the onset of dislocation movement is at relatively low shear stresses, and their velocities are high.

In FCC metals such as Cu, the dislocation mobility decreases with increasing temperature. When the temperature in such a crystal rises, lattice vibrations, called phonons, become the dominant damping factor of mobile dislocations.

It is apparent from the Orowan eqn. (2.67) that a crucial part in measuring the shear strain rate in materials subjected to shock waves is the measurement of the mobile dislocation density. As will be discussed in section 4.1, one of the key results of this thesis is showing that X-ray diffraction offers a non-perturbing method for

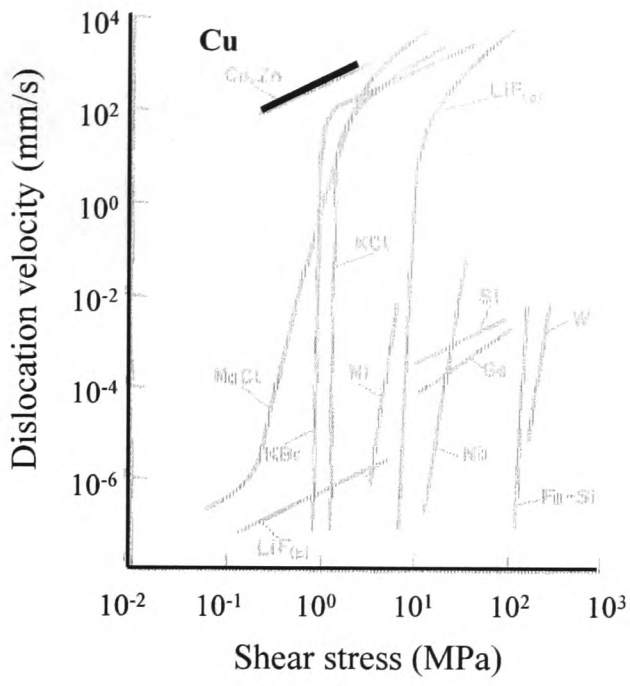


Figure 2.15: Dislocation velocity as a function of shear stress. Figure is taken from [56].

measuring dislocation density on nanosecond time-scales relevant to shock-loading in metals.

2.5.4 Partial Dislocations in FCC Crystals

As mentioned earlier in this chapter, the Burgers vector of a perfect dislocation is a lattice translation vector. If a dislocation is formed in such a way that its Burgers vector is not a lattice translation vector, it is called a *partial* dislocation, or a *partial.*

When a perfect (or unit) dislocation undergoes glide, it leaves behind an unperturbed crystal; the stacking of the atomic planes in the crystal remains perfect. On the other hand, the movement of a partial dislocation leaves behind an imperfect crystal containing a *stacking fault*, i.e. a region in the crystal where the regular atomic stacking sequence has been interrupted. When this stacking fault ends inside a crystal, the perfect crystal region is separated from the faulted one by the partial dislocation.

Stacking faults play a role in the plasticity of crystals. It is postulated that the spontaneous generation of partial dislocations resulting in stacking faults within

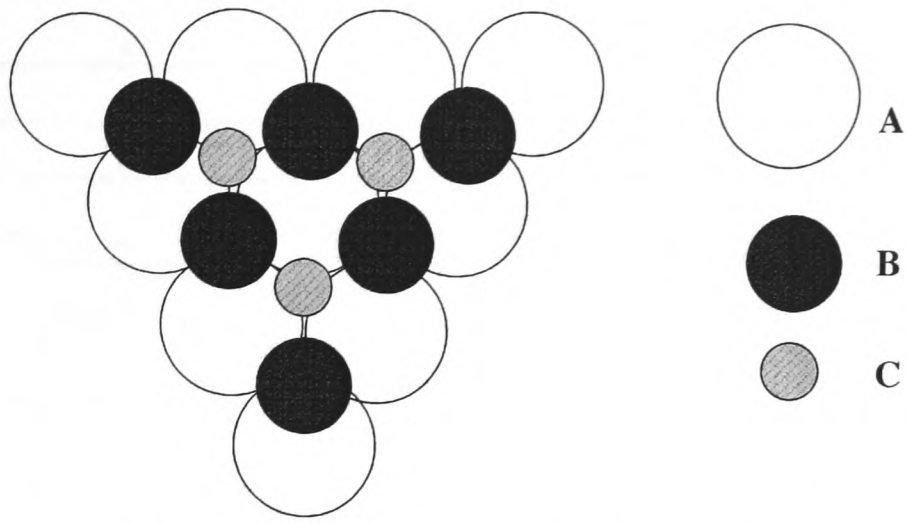


Figure 2.16: Stacking of atoms in a perfect FCC crystal along the [111] direction (normal to the plane of diagram). Layers of atoms form a repetitive sequence ABCABCABC.

materials subject to shock loading is responsible for the relaxation and subsequent plastic flow of the lattice.

Stacking of atoms in a perfect FCC crystal along the [111] direction is shown in Fig. 2.16. A layer of atoms situated in position A is followed by a layer in position B and this is followed by a layer in position C, resulting in a sequence ABCABC. Such stacking of the {111} planes is characteristic for FCC crystals.

Shockley and Frank Partials

Formation of partial dislocations is a very common phenomenon in FCC crystals. Usually, they are formed in such a way that the resultant stacking faults occur on the {111} planes, which are energetically most favoured.

The two most important partial dislocations that can be found in FCC crystals are the *Shockley partial* and the *Frank partial.* A Shockley partial dislocation is associated with slip. Part of an atomic layer in the crystal slips by a vector which is not a lattice translation vector, resulting in a stacking fault. The Burgers vector of a Shockley partial is *in the plane* of the stacking fault formed. Shockley partial dislocations are therefore glissile, which means they can move via slip (or glide).

A Frank partial dislocation is caused by the *removal* or *addition* of a layer of

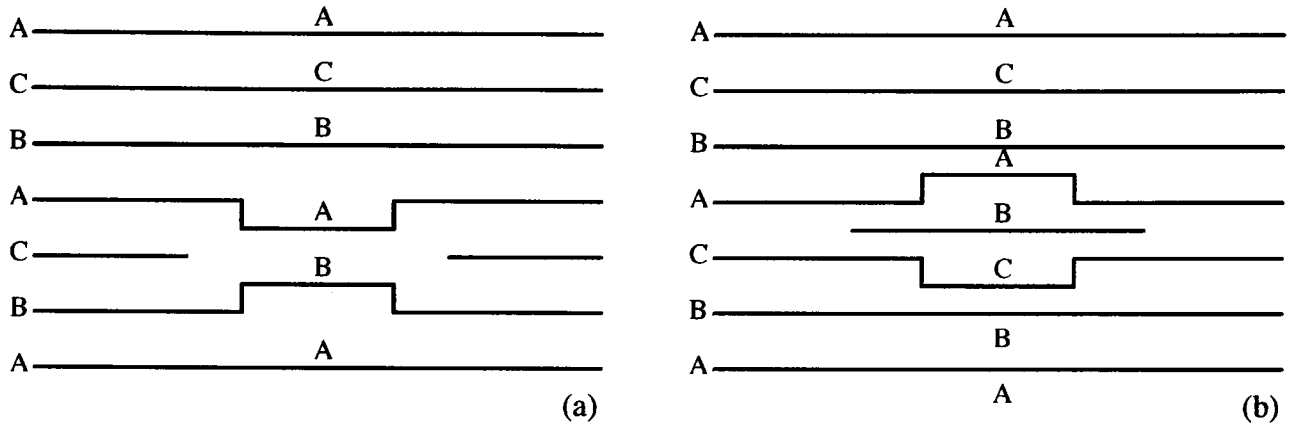


Figure 2.17: Two possible types of stacking faults on the {111} planes (normal to the plane of diagram) in FCC lattice. An intrinsic stacking fault (a) results in sequence ABCABABC... An extrinsic stacking fault with an extra layer of atoms in B position (b) results in the atomic sequence ABCBABCA...

atoms in the crystal. The removal of a layer of atoms from the stacking sequence results in an *intrinsic* stacking fault. The addition of an extra layer of atoms results in an *extrinsic* stacking fault. These two types of stacking faults are illustrated in Fig. 2.17.

The extra (or missing) atomic layer associated with a Frank partial dislocation creates a stacking fault whose plane is normal to the Burgers vector of the dislocation. (In the diagram, the stacking fault plane is *normal* to the plane of the diagram, whilst the Burgers vector is *in* the plane of the diagram.) This type of dislocation is sessile, which cannot move via glide and can only move via climb.

Dislocation Loops

An excess concentration of vacancies or interstitials in a region of a crystal can result in the formation of a platelet of point defects concentrated on a close-packed plane [56]. When such supersaturation occurs, it is then energetically favourable for this disc to collapse and form a *dislocation loop*.

A dislocation loop of Frank partials due to vacancies is called a *negative* Frank dislocation loop, and one due to interstitials is called a *positive* Frank dislocation loop. These two types of Frank dislocation loop are illustrated in parts (a) and (b)

of Fig. 2.17, respectively.

Depending on the size of a partial dislocation loop, it may be favourable for it to undergo glide resulting in the removal of the stacking fault. It can be shown [56] this leads to a perfect dislocation loop, such that its Burgers vector is a translation vector of the lattice. The required movement for this dislocation reaction corresponds to the glide of a Shockley dislocation. This is because Frank dislocations are sessile and cannot glide. A vacancy loop requires the glide of one Shockley dislocation to remove the intrinsic stacking fault, and hence for the dislocation loop to become perfect. An interstitial loop requires the glide of two Shockley dislocations in order for the extrinsic stacking fault to be removed.

Perfect dislocation loops formed in this way contain no stacking faults and are glissile. Because their Burgers vector is not in the plane of the loop, the glide surface is defined by the line of the loop, and the Burgers vector of the dislocation. This usually results in a cylindrical glide surface. In contrast, a dislocation loop formed by a slip of atomic planes forming Shockley partial dislocations, has its Burgers vector in the plane of the loop. Its glide surface is a plane. This is shown in Fig. 2.18.

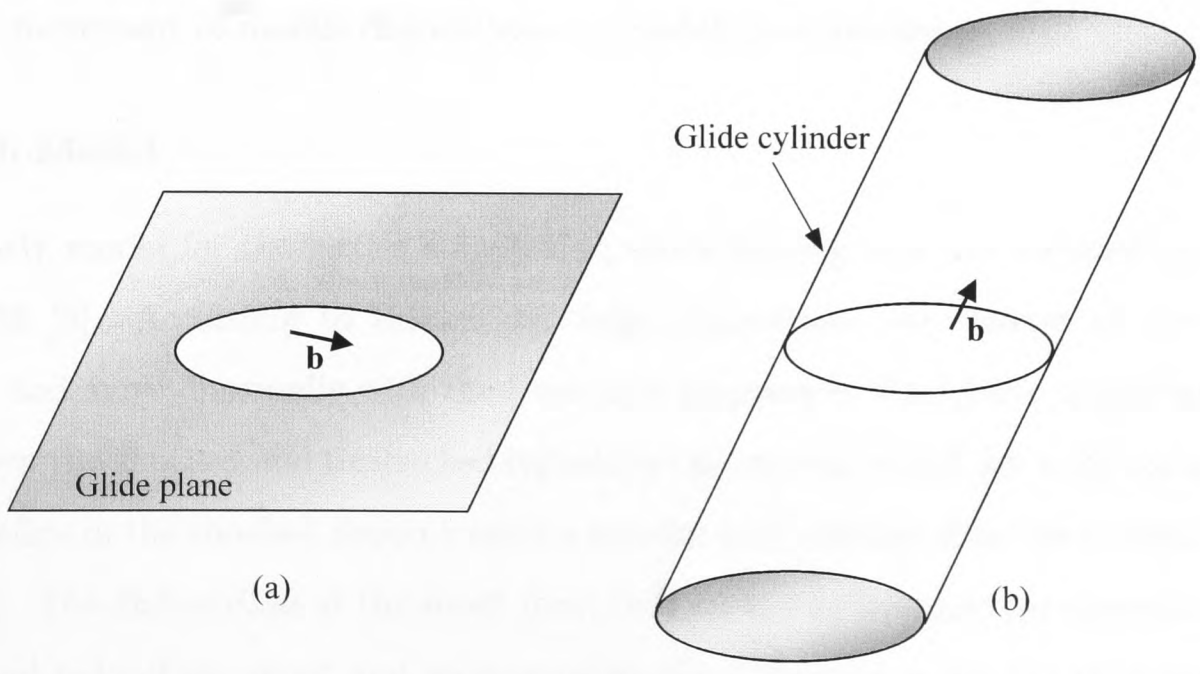


Figure 2.18: Dislocation loop with Burgers vector in the plane of the loop (a), and not in the plane of the loop (b). In (b), conservative motion of the loop is confined to the cylindrical surface. The loop can expand or shrink via climb.

When more vacancies (or interstitials) are added to the loop, it expands via climb, i.e. in the direction normal to its Burgers vector. Similarly, by emitting vacancies (or interstitials), a loop can shrink via negative climb.

It will be shown in Chapter 4 that the presence of pre-existing defects in a crystal, such as dislocation loops, has a major impact on the outcome of shock wave modelling in crystals.

2.5.5 Theoretical Models of Plastic Deformation

Crystal defects such as those described in the previous section are common in experimental crystal samples. Their formation in a material can also be induced by shock wave propagation through it. Exactly how this process takes place on such short time-scales has been addressed by various theoretical models developed in the last half-century.

It has to be stressed that a plastic deformation in a crystal is directly related to the concentration of *mobile* dislocations in it (eqn. (2.67)). The theoretical models therefore focus on determining the correct mechanism of the generation and subsequent movement of mobile dislocations in crystalline materials.

Smith Model

An early model for the lattice response to shock loading was put forward by Smith in 1958 [9]. According to this model, edge dislocations are created at the shock front, and move diagonally with the front as it progresses. They form a thin interface between the shocked and unshocked regions in the crystal, which are both cubic, with the lattice in the shocked region having a smaller unit cell size than the original cubic lattice. The dislocations at the shock front thus enable hydrostatic compression of the material behind the shock and accommodate the difference in the lattice parameters of the two regions. This is illustrated in Fig. 2.19.

The main difficulty of this model was its requirement that dislocations move at supersonic velocities, since they move at a 45° angle with respect to the direction of

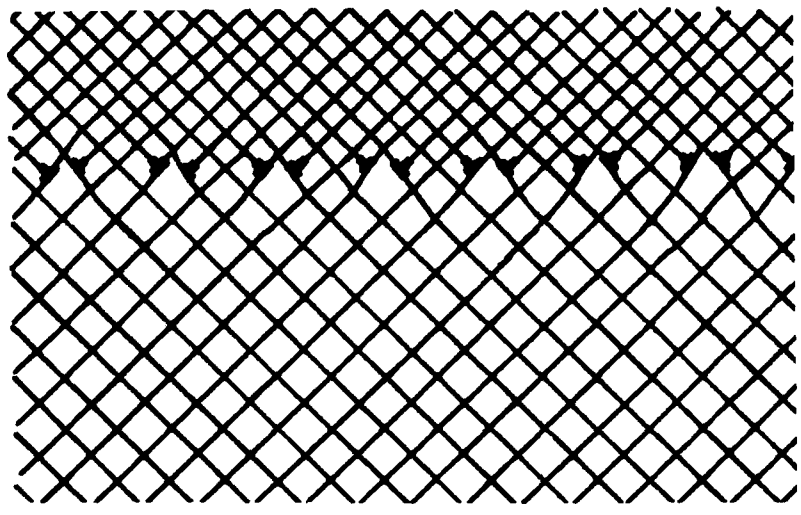


Figure 2.19: Interface formed by dislocations at the shock front, moving from top to bottom in the figure, as modeled by Smith [9]. The formed dislocations relieve shear stress in the material and a cubic lattice with a reduced unit cell size is formed behind the shock front.

the shock front movement. Supersonic dislocations have experimentally never been observed. Despite this shortcoming, the model has been used as the basis of many subsequent theories since [11, 27, 68].

Meyers Model

One significant modification of the Smith model was due to Meyers [10,69]. The model proposes that the shocked material is first compressed elastically in one dimension. When the threshold for a plastic deformation is reached in the uniaxially compressed region, dislocations are homogeneously nucleated, relieving the shear stress and allowing a hydrostatic compression of the lattice in this region. They move short distances and need not move with the shock front, so supersonic velocities are not required. New dislocations are generated as the shock front propagates through the material. This is shown in Fig. 2.20.

The significant shortcoming of both models outlined above is that the proposed dislocation densities required in order to satisfy the Orowan relationship (eqn. (2.67)) exceed, by a factor of 10^3–10^4, the density values found in crystals retrieved from shock-loading experiments [8, 11, 70].

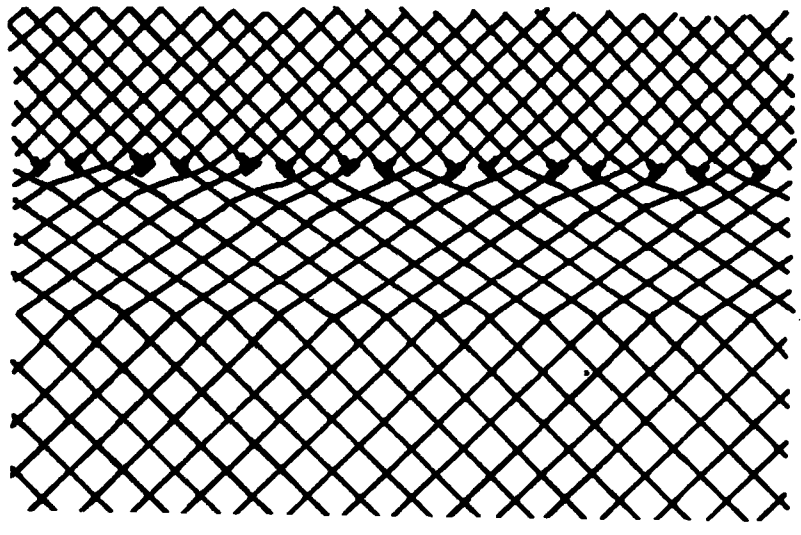


Figure 2.20: The Meyers [10, 69] model of dislocations. As the shock propagates through the material (from top to bottom), pairs of dislocations form when the plastic deformation threshold is reached, allowing a hydrostatic compression of the material behind the shock front. The next layer of the crystal is compressed elastically as the shock front progresses.

The model proposed by Meyers tries to resolve this discrepancy. It suggests that dislocations with equal and opposite Burgers vectors are created simultaneously, and subsequently annihilate upon rarefaction. This would reduce the final concentration of dislocations as found in *post mortem* studies of crystals. To date, however, no experimental data providing dislocation densities *during* shock loading is available, which could verify this proposal. One of the main achievements of this thesis, outlined in section 4.1, is the proposal of a method for measuring dislocation densities in shock-compressed crystals, using *in situ* X-ray diffraction.

Zaretsky Model

Another model of shear stress release in shock-compressed materials is one by Zaretsky [71,72]. The model proposes a fast source of dislocations, based on stacking faults and partial dislocations surrounding them, which can be activated at high strain rates (up to $\sim 10^{10}\,\mathrm{s}^{-1}$) typical for shock wave experiments. It is postulated that a segment of partials encompassing a stacking fault area will readily induce the formation and emission of fresh partial dislocation loops and stacking fault structures. Partial dislocations, which typically have a smaller Burgers vector than perfect dislocations,

will have a higher mobility and hence be a better source of further dislocations and shear stress release.

The post-shock dislocation concentration estimated on the basis of this model is 10^{11}–$10^{12}\,\mathrm{cm}^{-2}$, i.e. still 1–2 orders of magnitude higher than that found in release experiments [8, 11, 70]. To resolve this, the model takes into account the fact that the formed partial dislocation loops will naturally have lateral branches in opposing directions, which will eventually annihilate. The model thus accounts for the discrepancy in dislocation concentrations calculated and found experimentally, whilst avoiding the condition of simultaneous generation of dislocations with opposite signs proposed by Meyers.

These basic models of plastic deformation in crystals through generation and movement of dislocations remain fundamental in our attempts to understand the processes that crystalline matter undergoes in shock-loading conditions. The direct measurement of dislocation densities during the passage of a shock wave is therefore of high importance. A potential method for obtaining such a measurement is outlined in Chapter 4.

2.6 $\alpha-\epsilon$ Phase Transition in Iron

This section describes the $\alpha-\epsilon$ transition in Iron. It belongs to a group of structural transformations known as *martensitic transformations*, after Adolph Martens, who pioneered work in this field in the 19th century.

Martensitic transformations are characterised by a collective movement of atoms across distances typically shorter than the nearest neighbour distance, as a combination of a homogeneous lattice-distortive *strain*, followed by a *shuffle*. A shuffle is defined as a coordinated movement of atoms producing no lattice distortive deformations, but altering the symmetry and structure of the crystal.

The proposed mechanism of the shock-induced phase transition described here is based on the work of Wang and Ingalls described in [73]. A compression of the BCC lattice along [001] (or [00$\bar{1}$]) by 18.35% forces the (110) and (1$\bar{1}$0) BCC planes to form perfect hexagons, with the side of the hexagon, $\tilde{a}$, equal to $\sqrt{(2/3)}a$, where a is the side of the original BCC cubic cell. The relevant crystallographic planes and directions in both phases are illustrated in Fig. 2.21.

It is proposed that the uniaxial compression is accompanied by a shuffle of alternate (110) (or (1$\bar{1}$0)) planes along the [1$\bar{1}$0] (or [110]) direction. This forms a pseudo-HCP lattice, by establishing ABAB... ordering of the (110) (or (1$\bar{1}$0)) BCC planes, which transform into HCP (0002) close-packed planes. The c axis of the new phase corresponds to the original [1$\bar{1}$0] (or [110]) directions, with the $c:\tilde{a}$ ratio equal to $\sqrt{3}$.

The crystallographic relationship between the two phases in this arrangement is illustrated in Fig. 2.22. The shuffle of alternate (110) or (1$\bar{1}$0) BCC planes accommodates the required position of the second atom in the basis of the HCP unit cell, and the correct separation of the HCP (0002) planes.

Since atoms participating in the $\alpha-\epsilon$ phase transition do not move far enough from their original sites, it is a *diffusionless* transformation, i.e. no atomic mixing occurs [74]. The consequence of this diffusionless nature is that the parent and product lattices are closely related via *orientation relations*. These relationships specify

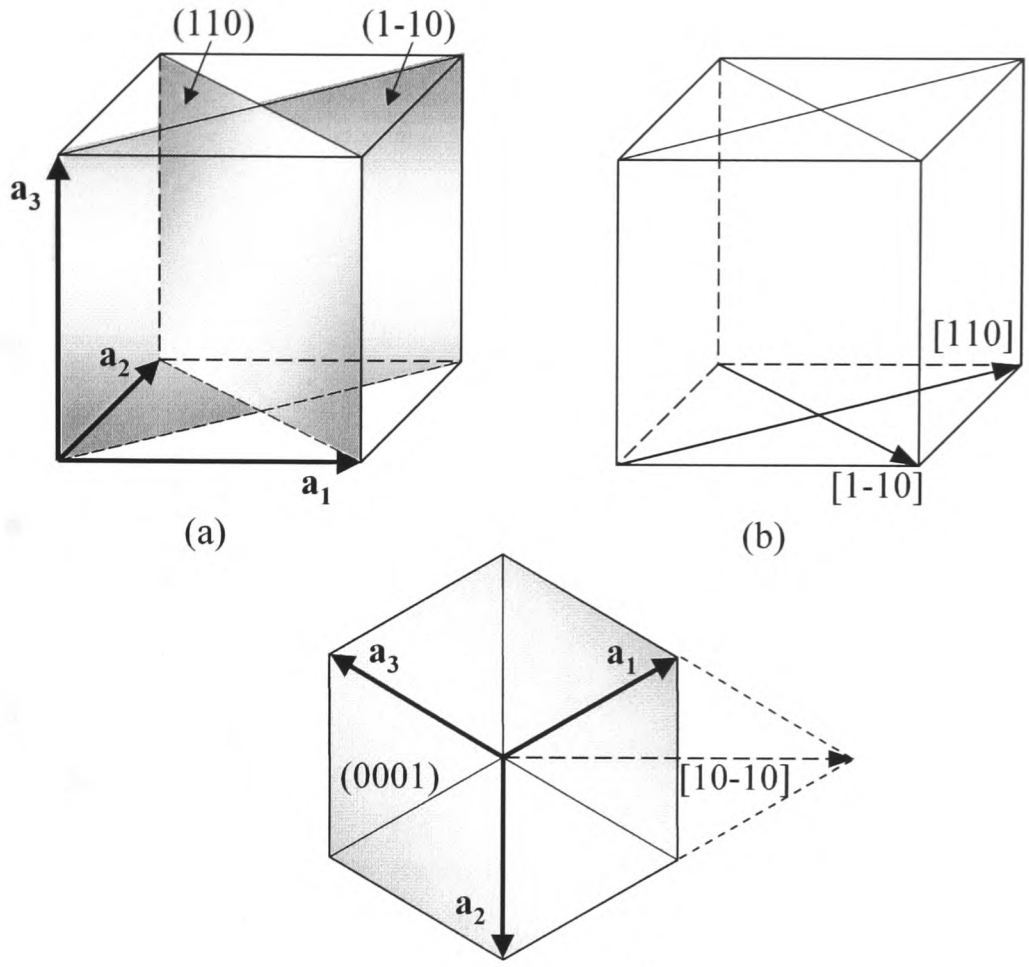


Figure 2.21: Orientation of (110) and $(1\bar{1}0)$ planes (a), and [110] and $[1\bar{1}0]$ directions in BCC lattice (b). (0001) plane of hexagonal lattice, transformed from (110) (or $(1\bar{1}0)$) BCC planes (c).

a parallelism between the planes and directions in the parent and product lattices. The orientation relation for the two possible orientations of the $\alpha-\epsilon$ transition is as follows:

$$\begin{aligned} &(0001)_{HCP} \parallel (110)_{BCC}\,, \qquad [10\bar{1}0]_{HCP} \parallel [1\bar{1}0]_{BCC}\,, \\ &(0001)_{HCP} \parallel (1\bar{1}0)_{BCC}\,, \qquad [10\bar{1}0]_{HCP} \parallel [110]_{BCC}\,. \end{aligned} \tag{2.68}$$

The two orientations of the new phase are energetically equally preferred, which results in the formation of close-packed grains of HCP, separated by grain boundaries, or twinned regions of HCP.

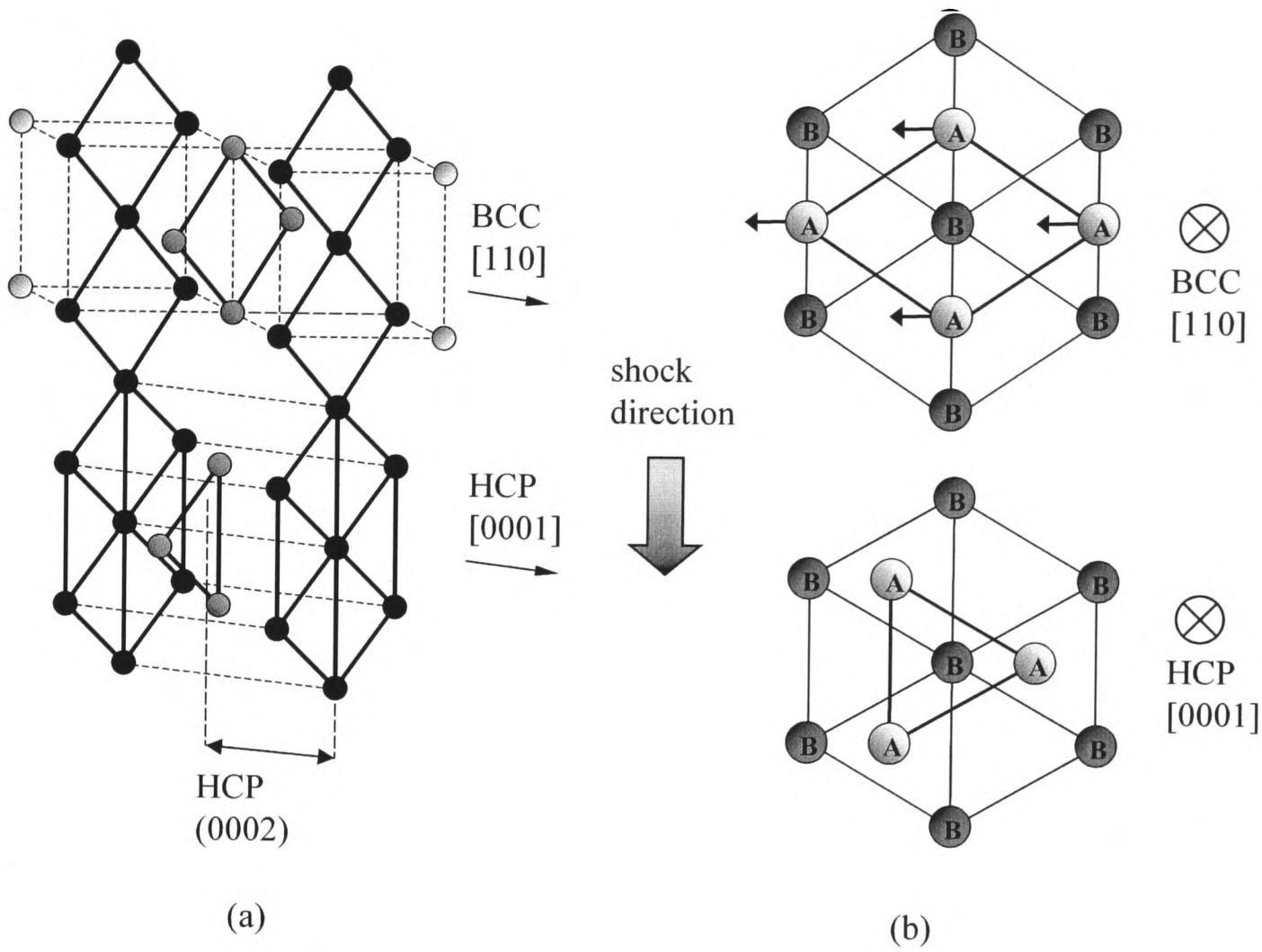


Figure 2.22: (a) Crystallographic relationship between α and ϵ phases in Iron (figure adapted from [75]). Only one of the two possible orientations of the new HCP phase is illustrated: BCC [110] direction becomes HCP [0001] direction. (b) View along BCC [110] (top) and HCP [0001] (bottom) directions. A shuffle of atoms in the A (110) plane in the BCC lattice (marked by arrows) results in the correct position and separation of the (0002) planes in the new phase. The shock propagation direction is $[00\bar{1}]$.

2.7 Diffraction from Imperfect Crystals

The defects embedded in experimental crystal samples prior to a shock, as well as those generated under the influence of a shock wave, can have an effect on the resultant X-ray diffraction patterns. It will be shown in Chapter 4 that this feature of X-ray diffraction can be used to infer further information about the studied material. This section outlines some of the effects that imperfections in crystalline matter have on the resultant diffraction patterns.

Planes Compression

Atomic planes compressed uniaxially will give rise to a shift in the Bragg peak in the diffraction pattern. Referring to Bragg's law of diffraction, the compression is related to the difference $\Delta\theta$ between two diffraction angles:

$$\frac{\Delta d}{d_o} = 1 - \frac{\sin\theta_B}{\sin\theta_B \cos\Delta\theta + \cos\theta_B \sin\Delta\theta}, \tag{2.69}$$

where θ_B is as before, d_o is the plane separation of the uncompressed planes, $\Delta d = d_o - d_{compressed}$ is the difference between the plane separation of the uncompressed and the compressed planes, and $\Delta\theta$ is the angular separation between the diffraction peaks arising from the uncompressed and the compressed planes of the crystal.

In the experiments conducted for this thesis, the diffraction geometries were such that X-rays scattered from multiple planes were captured on the wide-angle film diagnostic. In this way, both longitudinal and transverse strains in the crystal could be detected.

Stacking Faults

Stacking faults and dislocations in FCC crystals are believed to be closely related to the plastic flow under shock loading in these materials. Their presence also has an effect on the resultant diffraction patterns. A fault in the stacking of the {111} planes in a FCC lattice (Fig. 2.17) introduces a phase shift in the scattered X-rays,

which leads to a shift of the Bragg peak position. The magnitude and sign of the shift depends on the Miller indices (hkl) of the diffracting planes. As will be shown later, this particular feature of X-ray diffraction is extremely useful, as comparing the positions of the diffraction peaks corresponding to different Miller indices can provide the density of stacking faults, and hence dislocations, in the crystal.

The detailed theory of this effect is derived by Warren [49], and the following expression represents the Bragg peak shift for Bragg reflections from planes {200}, {400}, {111}, and {222} in a FCC crystal:

$$\begin{aligned} \Delta(2\theta)^{o}_{200} &= -\frac{90\sqrt{3}\alpha\tan\theta_{200}}{2\pi^2}, \qquad \Delta(2\theta)^{o}_{400} = +\frac{90\sqrt{3}\alpha\tan\theta_{400}}{4\pi^2}, \\ \Delta(2\theta)^{o}_{111} &= +\frac{90\sqrt{3}\alpha\tan\theta_{111}}{4\pi^2}, \qquad \Delta(2\theta)^{o}_{222} = -\frac{90\sqrt{3}\alpha\tan\theta_{222}}{8\pi^2}. \end{aligned} \tag{2.70}$$

Here, α is the inverse of the average number of planes between two consecutive stacking faults.

Since all quantities apart from α in eqn. (2.70) can be readily evaluated, the probability of the occurrence of a stacking fault between any two consecutive planes, α, can be determined. This will be exploited in Chapter 4.

Debye-Waller Factor

The integrated intensity of a Bragg reflection is influenced by the crystal temperature. This is due to the thermal motion which can be described at any one time by a small random displacement z representing a distortion of the perfect lattice periodicity. The integrated intensity of the scattered radiation from cubic crystals with identical atoms, such as the ones relevant to this thesis, is then given by

$$I = I_0 \exp\left(-\frac{1}{3}\langle z^2\rangle G^2_{hkl}\right), \tag{2.71}$$

where I_0 is the scattered intensity from the rigid lattice at $T = 0$, $\langle z^2\rangle$ is the mean square displacement of an atom from its atomic site, and G_{hkl} is the magnitude of the reciprocal lattice vector. An increase in temperature causes the integrated intensity

of the diffracted Bragg peaks to decrease, while their sharpness is not affected, at least in the Kinematic X-ray diffraction model. The exponential factor in eqn. (2.71) is referred to as the *Debye-Waller factor.* It can be seen that the higher the order of a reflection (i.e. the larger the magnitude of the diffraction wave vector), the more significant the effect of thermal vibrations will be.

Chapter 3

Computational Simulations

This chapter describes the computational work relevant to this thesis. This work involves Molecular Dynamics (MD) models of shocked crystals, provided by collaborators, and X-ray diffraction computer simulations applied to these models, designed and performed by the author. When compared with existing experimental results, these simulations have proved to be extremely useful in assessing the applicability of MD modelling to real experiments. They also elucidate the unique capability of *in situ* X-ray diffraction in determining the properties of shock-compressed crystals. A brief introduction to the nature and history of MD simulations is followed by a description of the diffraction code.

3.1 Molecular Dynamics Simulations

3.1.1 Introduction

Molecular Dynamics is a computer simulation technique in which equations of motion of a set of N particles are solved and integrated over a period of time. In the simulations relevant to this thesis, the particles obey classical mechanics, and use Newton's formulation, where the equation of motion is given by

$$\mathbf{F}_i = m_i \frac{\partial^2 \mathbf{r}_i}{\partial t^2} , \tag{3.1}$$

where $\mathbf{r}_i$ is the position of the ith particle, m_i is its mass, and $\mathbf{F}_i$ is the force acting upon it. The force is determined by a potential V through which all particles interact within the system:

$$\mathbf{F}_i = -\nabla_i V(\mathbf{r}_1, \mathbf{r}_2, \ldots, \mathbf{r}_i, \ldots, \mathbf{r}_N)\,. \tag{3.2}$$

In more pictorial terms, the particles "move" in the computer, oscillating and interacting with their neighbours, in a way similar to how atoms and molecules in a real substance would.

The basic features of any Molecular Dynamics code are: an algorithm for integration of the equations of motion; an interatomic potential; boundary conditions and constraints. When modelling a crystalline solid, the original positions of all atoms in the lattice are first defined. The energy and forces on each atom are then calculated, using the chosen interatomic potential. Finally, the equations of motion are integrated to obtain the next values of positions and velocities of the atoms. In this way, for a system containing N atoms, the computer calculates a trajectory in a $6N$-dimensional space: $3N$ positions and $3N$ velocities [76].

This thesis deals with systems generated via *non-equilibrium* MD (NEMD) simulations, in which energy, temperature and volume are not constant. NEMD simulations were pioneered by Hoover and Ashurst in 1975 [77]. One of the main motivations for this type of computer modelling was directly to examine the response of systems to large perturbations [76].

Shock wave propagation has been the subject of MD simulations for several decades. In NEMD simulations, there are three principal ways to generate a shock wave [5]. The first method is one in which a flyer plate is hurled towards a stationary target at a velocity $2u_p$, which is equivalent to two plates colliding at $\pm u_p$. Two shock waves then move out from the interface, travelling at the shock velocities $\pm u_s$. The shock wave travelling in the stationary target is then studied. This method is analogous to the experimental use of flyer plates to generate shock waves in a solid.

A second way to model a symmetric impact is by inhomogeneously shrinking the

longitudinal dimension of the system. This method is used particularly for fluid shock wave simulation [78].

The third main way to generate a shock wave is by using a piston. This is the method used in the MD simulations studied in this thesis. At a given initial temperature, the crystal travels at a uniform velocity $-u_p$ towards a stationary, infinitely massive piston which specularly reflects any atoms reaching it. A shock wave then moves away from the piston at velocity $u_s - u_p$, where u_s is the planar shock velocity and u_p is the piston velocity [5]. An alternative to the constant-velocity piston is a constant-force piston [79]. Details are provided later in this chapter.

Appropriate boundary conditions (BC's) are another fundamental feature of MD simulations. Simulations presented in this thesis use *periodic* BC's in the lateral directions with respect to the shock propagation direction. These are chosen to minimise the surface effects and thereby model an infinite material in the transverse directions, consisting of identical crystal blocks [5]. When periodic boundary conditions are used, the simulation block is replicated throughout space to form an infinite lattice. When an atom moves inside the central block during the course of the simulation, its periodic image in every one of the other blocks moves with exactly the same orientation in exactly the same way. When an atom exits the central block, one of its images will enter through the opposite face. The boundary of the central block has no walls, and hence the system has no surface in the transverse directions. Along the shock propagation direction, the surface at the end of the sample far from the piston is free.

In MD simulations, the equations of motion for all the particles are solved numerically. In order to simplify the calculations and shorten the computation time, certain approximations can be used. These inevitably lead to errors associated with the calculation of the final states of each atom. In principle, the approximation (and hence error) can be made as small as possible, depending solely on the memory and speed of the computer used.

There are a number of codes used for MD modelling at present. The ones used

to generate the MD simulations studied in this thesis are SPaSM [80], and MD-CASK [81].

3.1.2 Potentials in MD Simulations

Various types of potentials can be used in MD simulations. The most commonly used ones are the Lennard-Jones 6-12 pair potential and the Embedded Atom Method potential and its modifications. These two widely used potentials are described below.

Lennard-Jones Potential

The Lennard-Jones (LJ) 6-12 *pair* potential describes the interaction between two atoms, and is given by

$$\phi_{LJ}(r) = 4\epsilon \left[\left(\frac{\sigma}{r}\right)^{12} - \left(\frac{\sigma}{r}\right)^{6} \right], \tag{3.3}$$

where r is the distance between two atoms. $\epsilon = A^2/4B$ and $\sigma = (B/A)^{1/6}$, where A and B are empirically obtained positive constants.

In order to save computer power, it is customary to use a *truncated* LJ potential, where interactions between particles at a distance beyond a certain cutoff radius r_c from each other are neglected, so that

$$V(r) = \begin{cases} \phi_{LJ}(r) - \phi_{LJ}(r_c) & \text{if } r \leq r_c \\ 0 & \text{if } r > r_c\,. \end{cases} \tag{3.4}$$

In MD modelling of metals, usually $\phi_{LJ}(r_c)$, as well as at least the first two derivatives of the potential, are made equal to zero.

Embedded Atom Model

The most commonly used *many-body* potential is the Embedded Atom Method (EAM) potential [82, 83]. In this method, each atom is treated as an impurity in a host of the remaining identical atoms in the system. The total energy of the system is then

given by

$$E_{tot} = \frac{1}{2}\sum_{ij} V(r_{ij}) + \sum_{i} F(\bar{\rho}_i)\,, \tag{3.5}$$

where $V(r_{ij})$ is a pair potential, such as the LJ 6-12 potential described above, and $F(\bar{\rho}_i)$ is the *embedding energy* induced at the site of atom i by all other atoms in the system. The host electron density, $\bar{\rho}_i$, is given by $\bar{\rho}_i = \sum_{i \neq j} \rho(r_{ij})$, where $\rho(r)$ is the electron density function.

The MD simulations studied in this thesis use the EAM potential and its modifications.

3.1.3 History of Molecular Dynamics Simulations

One of the very first publications reporting MD simulations was written by Alder and Wainwright in 1957 [84]. This was a study of a hard sphere system containing up to 100 particles. In the subsequent years, MD simulations were used mainly to study liquids. Amongst the first ones to extend the method to solids were Dickey and Paskin in 1969 [85]. Thermodynamic and phonon properties of approximately 1,000 atoms were studied using the Lennard-Jones potential, which was the interatomic potential used in most of the early MD work. Paskin and Rahman [86] showed that other potentials could also be used in simulations of atomic interactions in metals.

In the following years, MD simulations began to be used as a tool to study one-, two-, and three-dimensional atomic systems. The issue of applicability of the Rankine-Hugoniot (RH) jump conditions (2.43)–(2.45) to shock waves in solids was questioned in 1966, when Tsai and Beckett found that shock waves in a 3-D solid displayed non-steady behaviour [87]. It is known that the validity of RH jump conditions depends on the conservation of mass, energy and momentum, and the existence of a steady wave, as detailed in section 2.4. It was therefore concluded that they could not be used to analyse data in impact planar experiments.

The finding of Tsai and Beckett was, however, in contrast to that of Paskin and

Dienes in 1972 [88]. The LJ 6-12 potential was used in a simulation of approximately 3,600 atoms in a rare-gas solid. Pressure, volume, and temperature were monitored, and reasonable agreement was found between the simulation results and high-pressure measurements on Neon. In addition, Paskin and Dienes reported observation of steady waves, with no significant deviations from the RH relations.

These conflicting findings were partially resolved by Holian and Straub in 1979 [89]. Shock wave propagation through perfect 3-D FCC crystals, also using a LJ 6-12 potential, was simulated. It was shown that in systems with initial temperature $T_0 = 0$, the shock wave remained unsteady, irrespective of the initial shock strength, and no stress relaxation was detected. For $T_0 > 0$, however, at sufficiently high initial shock strengths (determined by the piston velocity), steady shock waves were found to be propagating within the material. The Rankine-Hugoniot relations were thus shown to be appropriate for describing atoms in MD simulations of crystalline solids subjected to shock waves.

As in many other MD studies conducted during this period and before, the major limitation of these simulations was the small number of atoms used, which in this case did not exceed 1,800. Until recent advances in computer technology, which have enabled simulations of much larger atomic systems, limited computer power was a major problem in the MD field.

In the 1980's, shock loading in Copper was modeled by Mogilevsky [90–92]. Uniaxial compression up to a certain value in a perfect lattice resulted in elastic lattice behaviour. For compressions above 18.6%, nucleation of defects causing subsequent shear was observed. This finding was in agreement with the Meyers model of dislocation generation outlined in section 2.5 [10, 69]. Furthermore, models of single crystal Copper with embedded interstitials showed that, in the vicinity of embedded defects, lattice rearrangement occured for values of compression lower than the perfect crystal threshold by a factor of ~ 5. The main weakness of this model, however, besides its small size, was the fact that the sample was subject to a *uniform compression* followed by a release, thus not simulating shock wave propagation through the crystal.

In 1988, Holian accomplished a significantly larger MD simulation in comparison with those conducted earlier [93]. Up to 10,000 atoms in an FCC lattice, interacting via a truncated LJ potential, were subject to shock waves of various strengths. Three different regimes, in increasing order of shock wave strength, were found: an *unsteady elastic wave*, a *steady plastic wave* preceded by an unsteady elastic precursor, and a *steady overdriven plastic wave*. It was also found that in solids, the region of atomic slippage allowing the release of shear stress is very small, only several atomic planes wide.

One of the first MD simulations containing more than one million atoms was performed by Hoover *et al.* in 1990 [94]. A two-dimensional crystal with a triangular close-packed lattice was modeled. Atoms interacted through a truncated LJ potential, both with and without added embedded-atom contributions. The simulation was designed to mimic Copper and Nickel behaviour. Its main success lied in the fact that its size approached a magnitude comparable with real-life nanometer technology systems. The limitation was its two-dimensional nature and, as the authors themselves pointed out, the next important step was performing a multimillion 3-D MD simulation.

The end of the 20th century saw the advance and development of massively parallel supercomputers enabling multimillion-atom 3-D MD simulations. Holian and Lomdahl [5] ran non-equilibrium MD simulations of $100\times100\times250$ FCC unit cells (10^7 atoms) interacting under a Lennard-Jones spline potential [95, 96]. Shock wave passage through the crystal in the [001] direction initiated random atomic slippage, forming Shockley partial dislocations and arrays of stacking faults. This is illustrated in Fig. 3.1.

It should be noted that this simulation used considerably larger cross-sections (100×100 unit cells) in comparison with the previous ones [93]. In the new simulations, stacking faults were created randomly along all four available {111} slip systems. Viewed at an arbitrary {100} plane, they formed a randomly spaced pattern (as seen in Fig. 3.1). Previously conducted simulations with smaller cross-sections

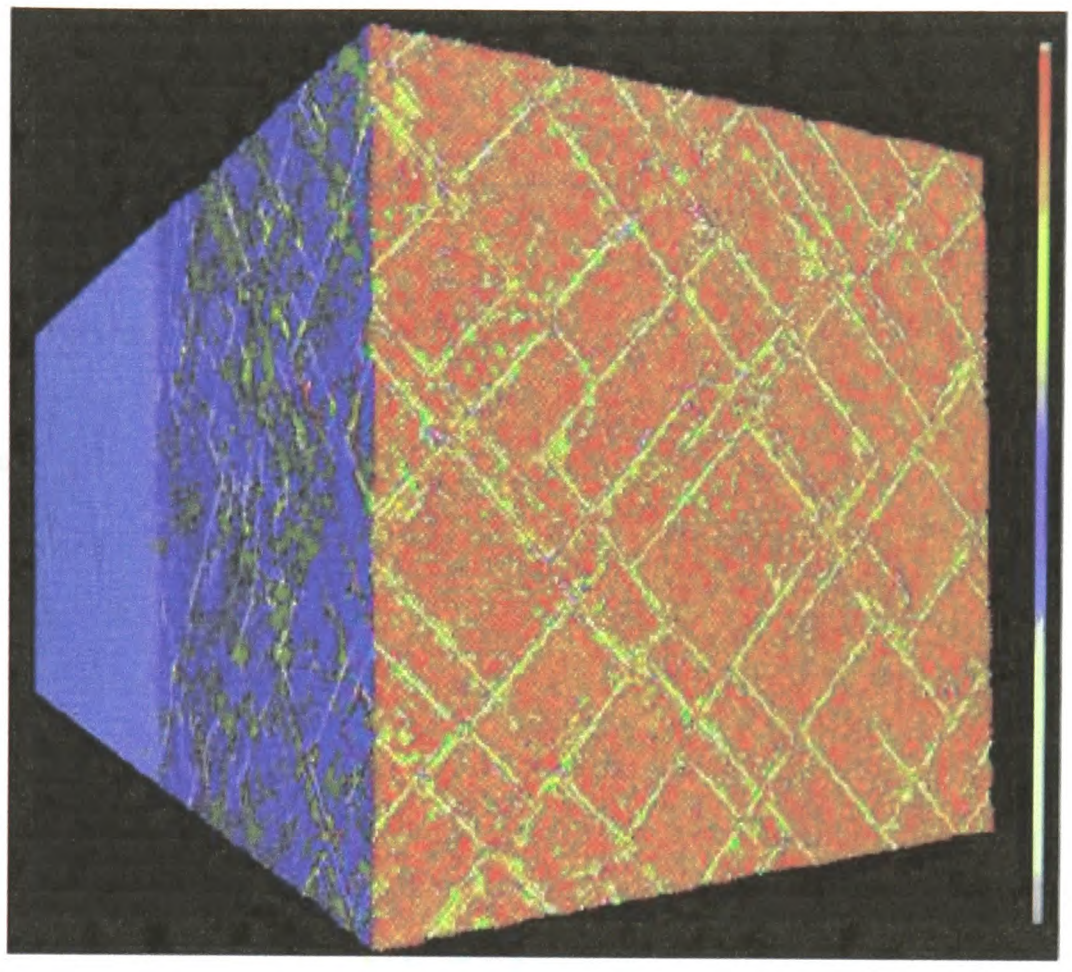


Figure 3.1: Stacking fault generation following shock wave passage through a 10^7-atom FCC crystal, as modeled in [5]. Atoms slip along all four {111} planes, relieving shear stress.

showed a considerably smaller number of created stacking faults, which were not distributed randomly and were therefore believed to be directly related to the periodic BC's used [5, 93].

The results of these large MD simulations therefore disputed the possibility that the slippage of atoms was merely an artifact of the periodic boundary conditions used. Furthermore, the presence of inhomogeneities in the crystal was mimicked by warping the shape of the piston. This proved that pre-existing defects in the crystal aid nucleation of stacking faults at shock strengths below the perfect crystal yield limit; the dislocation nucleation was, in this case, not homogeneous, as expected in a perfect crystal, but inhomogeneous.

Such multimillion-sized MD simulations of crystalline solids subject to shock wave propagation showed that the formation and subsequent movement of dislocations relieves shear stress. According to atomic models of material behaviour upon shock-compression outlined in section 2.5.5, this was expected to lead to a near-hydrostatic 3-D compression, as shown experimentally using *in situ* X-ray diffraction in single crystals of Copper [7]. Evidence of dislocation generation in MD simulations hence resulted in an apparent agreement of MD modelling with both theory and experiment, which caused the general MD community to accept that hydrostatic compression of crystalline solids was correctly simulated using Molecular Dynamics.

For this thesis, simulated X-ray diffraction was applied to MD simulations of FCC metals in order to compare the resultant diffraction patterns with experimental data. The MD simulation results showed that whilst uniaxial compression of the lattice in the direction of the shock propagation was dominant, compression along the transverse directions remained relatively insignificant. This crucial and surprising finding suggested that the scale and complexity of the existing MD simulations had to be enhanced in order for them correctly to mimic the real crystal behaviour occuring on longer time-scales.

Details of the X-ray diffraction simulator are presented in the following section.

3.2 X-Ray Diffraction Post-Processor

3.2.1 Principle of X-Ray Diffraction Post-Processing Code

The principle of the X-ray diffraction post-processor of MD simulations, generating patterns comparable with experimental data, is conceptually simple. Recalling, from section 2.2, that the diffracted X-ray intensity is proportional to the FT of the lattice, the intensity, I, of the diffracted radiation is given by

$$I = |\sum_j f_j \exp[-i\,(\mathbf{r}_j \cdot \Delta\mathbf{k})]|^2\,, \tag{3.6}$$

where f_j is the atomic form factor of the jth atom, $\mathbf{r}_j$ its position, and $\Delta\mathbf{k} = \mathbf{k}' - \mathbf{k}$ is the difference between the wavevectors of the scattered ($\mathbf{k}'$) and incident ($\mathbf{k}$) radiation, i.e. the diffraction vector. This expression is equivalent to eqn. (2.19). The sample sizes used in the MD simulations are sufficiently small that, even in the absence of dislocations, the Kinematic diffraction theory is applicable.

The X-ray diffraction post-processor inputs the atomic x, y, and z positions of the atoms in the MD simulation. In this way, X-rays "diffract" from the entire crystal. (It is, of course, possible to select a smaller section of a simulation for post-processing; this, however, has to be done prior to applying the X-ray diffraction routine.) For simplicity, the initial unit cell size of the crystal is always normalised to unity and $\Delta\mathbf{k}$ is normalised to the length of the relevant reciprocal lattice vector, along which the diffraction calculation is conducted. In this way, the diffraction peaks corresponding to a constructive interference appear for integer values of $\Delta\mathbf{k}$.

It can be seen from eqn. (3.6) that the code does not use any specific values of X-ray wavelength, or atomic plane spacing. The resultant diffraction pattern is, therefore, not directly comparable to an experimental diffraction pattern based on the Bragg formula (2.13). Rather, it is a direct FT of the lattice, effectively allowing one to view the inverse space of the crystal studied. In its simplest (1-D) form, the code is performed in such a way that a *line* in the reciprocal space is mapped out,

along the direction of the chosen diffraction vector $\Delta\mathbf{k}$.

The value of the atomic form factor, f_j, is made equal to one. As shown in eqn. (2.18), its precise value is given by the 3-D FT of the electron density within an atom. It will sharply decrease with the scattering vector $\Delta\mathbf{k}$ and for $\Delta\mathbf{k} = \mathbf{0}$, f_j will equal the number of electrons in a specific atom, Z. This element-specific dependence can easily be incorporated into the diffraction results if necessary, such as when actual diffracted intensities are quantitatively compared with experimentally obtained ones. However, there is no particular need for this calculation to be part of the main diffraction code. Additionally, due to the sharp decrease of f_j with $\Delta\mathbf{k}$, the higher orders of diffraction would be harder to discern, which would impede the advantages this code provides.

Equation (3.6) for the diffracted intensity neglects the effects of absorption within the sample. Absorption can easily be taken into account by keeping track of the path length traversed by the X-rays scattered from a given atom, but current simulated sample sizes make this unnecessary.

3.2.2 Extension of Code beyond 1-D

The 1-D post-processing outlined above is performed under the assumption that X-rays undergo solely specular reflection.

The code is amenable to extending to 2-D and 3-D. This is equivalent to mapping out a *plane* (2-D), or a *volume* (3-D), in k-space. This computation is more elaborate and requires more computer power and calculation time. The latter effectively maps out the inverse k-space of a given crystal in 3-D. This version, although highly demanding in terms of computer power and speed, has proved to be essential for determining the 3-D strain matrix derived in section 2.3.2 and summarised in eqn. (2.32), relating the shocked and unshocked parts of the crystal.

An intermediate 1-D version of the code was also developed, wherein some diffuse (non-specular) scattering is captured. This is done by allowing the tip of $\Delta\mathbf{k}$ (the diffraction vector) to map out a segment on the Ewald sphere (in 3-D) or Ewald circle

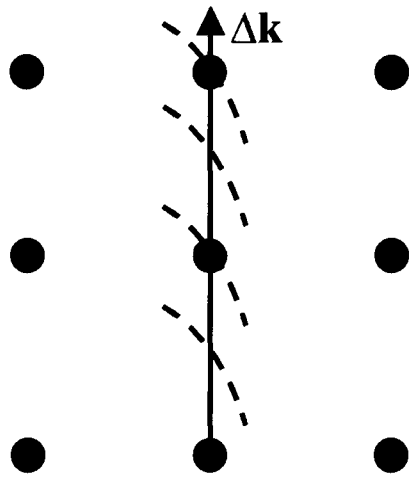


Figure 3.2: A schematic diagram illustrating non-specular diffraction as accounted for by the extended code. The arrow represents a 1-D diffraction vector in 2-D k-space. Whilst specular diffraction maps out k-space *along* this vector only, diffuse diffraction is captured by the non-specular code, illustrated by segments of the Ewald circle, shown by dashed lines intersecting $\Delta\mathbf{k}$.

(in 2-D) (Fig. 2.2) in the vicinity of the reciprocal lattice vector in question. For this purpose, a specific value of X-ray wavelength has to be chosen in the calculation, as this determines the radius of the arc of the circle (sphere) in k-space. A schematic diagram of this extension of the code to capture diffuse scattering is illustrated in Fig. 3.2.

As will be presented later, these extensions of the post-processor do pay off in terms of the information provided about the crystals in question.

The code is written in the C programming language.

Chapter 4

X-Ray Diffraction Post-Processor Results

In this chapter, MD simulations of single metallic crystals are post-processed using the computational tool described in the previous chapter. In particular, results from MD simulations of Copper and Iron are studied.

The outcome of the work on the Copper MD simulations presented here has called into question the basic picture of material deformation upon shock loading on picosecond time-scales, as presented by previous MD studies. This consequently led to attempts to perform more accurate MD simulations on far longer time-scales than those conducted previously. Post-processing of such large MD simulations is presented, highlighting the achieved improvements. Additionally, a new experimental method to measure dislocation densities in crystals during shock loading is proposed. This has the potential to resolve one of the most pressing questions remaining in shock wave physics, regarding the mechanism of shock-induced plastic deformation in crystals.

The post-processing of Iron MD simulations serves to verify the modelling of the $\alpha - \epsilon$ transition in single crystal Iron on picosecond time-scales. It is also extremely useful for a direct comparison with the X-ray diffraction data from shock experiments subsequently discussed in Chapter 6 which, for the first time, give direct structural

information on the most widely studied shock-induced phase transformation.

4.1 Copper

4.1.1 2×10^6 Atom MD Simulation

The results presented in this section are from X-ray post-processing of a MD simulation of a single Copper crystal containing 2×10^6 atoms.

This MD simulation was conducted using the "MDCASK" code ("Molecular Dynamics Code for Radiation Damage") at Lawrence Livermore National Laboratory (LLNL) [97], adapted to simulate shocks. Periodic boundary conditions were applied in the lateral [100] and [010] directions, and the shock was launched along the [001] direction. The end of the sample that was on the far side with respect to the shock-inducing piston was a free surface.

The shock was generated by applying a force to $\sim$2–4 planes of atoms on one side of the sample. This thin atomic layer then represented the piston. The force was kept constant throughout the entire simulation, the duration of which was $\sim$8 ps. This arrangement gave a fixed Hugoniot pressure. The piston responded to the pressure applied to it by moving at a velocity u_p and generating a shock with velocity u_s. The advantage of the atomically rough piston is that it is more realistic than a perfectly smooth one. The constant force piston can only be used for relatively short runs (<10–20 ps), as it deforms considerably for runs on longer time-scales. For those cases, a constant velocity piston, also consisting of $\sim$2–4 atomic layers, can be used [98].

All atoms moved under a modified EAM potential, altered to model the behaviour of Copper. Its exact form is described in [99]. Interactions between atoms extended up to the fourth nearest neighbours (54 interacting atoms in total for each atom) at the equilibrium density.

The spatial ($\leq$100 nm) and temporal ($\leq$10 ps) scales of this MD simulation are representative of the limits achieved by most MD studies up to the present. It should

be noted that in comparison, typical experimental scales are of micrometers and nanoseconds, i.e. 2–3 orders of magnitude higher in both spatial and temporal sense. The purpose of applying the X-ray diffraction post-processor was also to find out whether this difference in scales affects the relevance of previous MD modelling of Copper behaviour.

A pressure of ~ 50 GPa was applied to a crystal sample sized $50\times50\times200$ FCC unit cells. This exceeds the HEL of the system simulated here, 32 ± 2 GPa [79], so plastic deformation was expected to occur. The unit cell size of Cu is 3.615 Å, so prior to the shock-compression, the length of the system was ~ 72.3 nm. The shock rise-time was ≤ 1 ps, i.e. very sharp. A snapshot of the MD simulation was taken 7.81 ps after the start of the simulation, before the shock reached the rear surface. Approximately half of the atoms were in the shocked region, the rest remaining unperturbed.

It was expected that a high density of dislocations would be generated by homogeneous nucleation at the shock front, which should allow the lattice to rearrange towards the hydrostat, according to the model outlined in section 2.5.5.

1-D FT Results: Diffraction Order Discrepancies

Figure 4.1 shows the X-ray diffraction signal, in 1-D, from this MD simulation. The diffracted intensity is plotted as a function of the diffraction vector Δk for the three directions [100], [010], and [001], which are normal to planes $(h00)$, $(0k0)$, and $(00l)$, respectively. For clarity, the contribution to the diffraction from the unshocked part of the crystal has not been included.

Diffraction peaks appear at Δk values corresponding to the FCC-allowed Miller indices, i.e. for even values of Δk. A noticeable shift in the diffraction signal, corresponding to lattice compression along the shock propagation direction (compression of the $(00l)$ planes), can clearly be seen. In contrast, no significant shift can be seen in the diffraction from the orthogonal planes in the second order, although some shift is seen in the fourth order.

Compression of the crystal in the three principal directions can be inferred from



Figure 4.1: Diffracted intensity as a function of Δk, normalized to the length of the [001] reciprocal lattice vector. Compression of $(00l)$ planes is noticeably more significant than that of planes $(0k0)$ and $(h00)$. The figure is taken from [100], published by the author.

shifts in the intensity peaks. The weighted centre of each diffraction peak was calculated, which subsequently yielded the lattice compression in the given direction. For the second order, the compression is 13.4±1.5% along [001], and 0.6±1.0% and 0.1±1.0% along [100] and [010] directions, respectively. For the fourth order the inferred compression values are 11.9±2.0% along [001], and 3.0±2.0% and 2.7±2.0% along [100] and [010] directions, respectively.

Under the assumption of zero plastic dilation (eqn. (2.55)), the total sum of the elastic strains should equal the total volumetric compression. This is equal to the increase of the atomic density in the compressed part of the crystal, which was found to be $\sim 16.7\%$.

The total volumetric strain given by the X-ray diffraction post-processing is 14.1±3.5% from the second order, and 17.8±6.0% from the fourth order calculation. Although these results are consistent (within the error-bars) with the $\sim 16.7\%$

atomic density increase, the errors associated with them are relatively large, and there is a notable discrepancy between the two final figures. Additionally, very little lateral compression is detected, especially in the second order, which is inconsistent with the experimental results obtained to date [7].

3-D FT Results: Detailed Analysis

In order to resolve this discrepancy, as well as to obtain more accurate information about the crystal, the 1-D post-processing was extended to 3-D. A high resolution (step size $=0.005$) 3-D FT was performed on the shocked part of the crystal. The range of k-vectors probed was such that the weighted centre of mass of each peak corresponded to the position of a corner of the unit cell in the inverse space of the crystal, i.e. (2,0,0), (0,2,0), and (0,0,2) for the second order diffraction, etc. By comparing the coordinates of a perfect inverse unit cell with one in the shocked crystal region, the total deformation matrix in 3-D, as outlined in section 2.3.2, can be deduced. This calculation is extremely useful, as it yields the tensile strains along the three principal axes, the total volumetric strain, shear strains, and the rotations of xy, zx, and yz planes within the crystal.

Table 4.1: Tensile and volumetric strains inferred from second and fourth order 3-D FT calculations. The volumetric change is compared with the atomic density increase. Error values (%Δ) are the standard deviations on each of the strains inferred in the three principal directions. The total error on the volumetric strain is %ΔV.

order	% x	% y	% z	%Δ	% volume	%ΔV	% at. density rise
2^{nd}	2.0	2.0	8.6	$\pm$0.5	12.2	$\pm$1.5	16.7
4^{th}	4.3	4.3	9.9	$\pm$1.0	17.5	$\pm$3.0	16.7

Table 4.1 compares the tensile strains and the volumetric compression given by the 3-D X-ray diffraction post-processor using the second and fourth order diffraction, and the atomic density increase in the shocked part of the crystal. As in the 1-D calculations, the results show that there is a large discrepancy between the second and fourth order. As the 3-D calculation is more accurate, this discrepancy could

no longer be ascribed to errors alone. Instead, the trend in the results was identified as that described by Warren [49] and stated in Chapter 2, eqn. (2.70), for shifts in Bragg reflection peaks due to dislocations and stacking faults in FCC crystals.

Warren Formula Revisited

The above mentioned eqn. (2.70) provides a quantitative measure of the angular shifts of the second and fourth order Bragg diffraction peaks as a result of the presence of stacking faults and dislocations in the system. In order to use it, both expressions in eqn. (2.70) were first converted into radians, resulting in

$$\Delta\,(2\theta)_{200} = -\frac{\sqrt{3}\alpha\tan\theta_{200}}{4\pi}\,, \qquad \Delta\,(2\theta)_{400} = +\frac{\sqrt{3}\alpha\tan\theta_{400}}{8\pi}\,. \tag{4.1}$$

Further, the diagram in Fig. 2.2 relates the diffraction angle θ and the magnitude of the diffraction vector G as

$$\sin\theta = \frac{G}{2k}\,.$$

Dividing this expression by its first derivative gives an expression for $d\theta$,

$$d\theta = \frac{dG}{G}\tan\theta\,. \tag{4.2}$$

Equating $\Delta(2\theta)$ with $2d\theta$ for each diffraction peak, and combining (4.1) and (4.2) gives shifts in the second and fourth order peaks in k-space, respectively, as

$$dG_{200} = -\frac{\sqrt{3}\alpha G_{200}}{8\pi}\,, \qquad dG_{400} = +\frac{\sqrt{3}\alpha G_{400}}{16\pi}\,. \tag{4.3}$$

Here, G_{200} and G_{400} represent the second and fourth order diffraction peaks, respectively, unaffected by the presence of dislocations, i.e. solely dependent on the interplanar spacing in the crystal. It should be noted that this expression is one-dimensional, i.e. the shift of the peak corresponding to point (2,0,0) in k-space will be along x direction only, and similarly for the other two peaks probed.

The diffraction peaks in k-space, affected by the presence of stacking faults and

dislocations, can then be rewritten in the following form:

$$|200| = 2A - \frac{A\sqrt{3}\alpha}{4\pi}, \qquad |400| = 4A + \frac{A\sqrt{3}\alpha}{4\pi}. \tag{4.4}$$

Here, |200| and |400| are the second and fourth order peaks, respectively, as detected by the simulated X-ray diffraction post-processor. $A = G_{200}/2 = G_{400}/4$ represents the *theoretical* first order diffraction peak, in reality forbidden in FCC crystals, discounting the dislocations-induced shift of the X-ray diffraction peaks. In other words, the values of A inferred from eqn. (4.4) for points (1,0,0), (0,1,0), and (0,0,1) in k-space are the corners of the "corrected" first-order inverse unit cell. The resultant volumetric strain they yield should agree with the atomic density rise.

Rearranging eqn. (4.4) gives an expression for α, the probability of finding a stacking fault between two consecutive planes in the crystal:

$$\alpha = \frac{8\pi(|400| - 2|200|)}{\sqrt{3}(|400| + |200|)}. \tag{4.5}$$

Lattice Compression and Dislocation Densities

The values of A for the shocked region of the crystal were calculated from eqn. (4.4) and (4.5). These provide the post-shock positions of the corners of the inverse unit cell of the crystal. Using the matrix representation of 3-D strain outlined in section 2.3.2, the tensile and volumetric strains in the crystal can be inferred, which should no longer be spuriously affected by the presence of dislocations and stacking faults. The results are shown in Table 4.2.

Table 4.2: Tensile and volumetric strains corrected for the presence of dislocations and stacking faults in the crystal. The volumetric change is now in very good agreement with the atomic density rise. Errors on the individual strains and on the total volumetric strain are provided.

strain	% x	% y	% z	%Δ	% volume	%ΔV	% at. density rise
	3.5	3.5	10.3	$\pm$1.0	16.5	$\pm$3.0	16.7

The table shows much better agreement between the corrected value of volumetric strain and the atomic density increase, indicating that the discrepancy shown in Table 4.1 was indeed caused by the dislocations in the system.

The results also show that the compression along z is approximately three times larger than the compression in the lateral directions x and y. This means that, contrary to experimental results [7, 8], the rearrangement of the atoms in the crystal structure under the influence of the applied shock wave was not such as to cause a near-hydrostatic compression. Clearly the predominant compression was along the shock propagation direction.

The above derived equations also enable the calculation of the dislocation density in the shocked part of the crystal. Since $1/\alpha$ is the average number of atomic planes between two consecutive stacking faults, this is related to dislocation density, ρ_d, via the relation

$$\rho_d = (\alpha/l)^2 \,, \tag{4.6}$$

where l is the separation of two consecutive planes in the crystal.

For the case of the Copper crystal analysed here, the value of l was taken as 3.615 Å. Using eqn. (4.6), the resultant dislocation density in this MD simulation was found to be $\sim 3\times10^{13}\,\mathrm{cm}^{-2}$.

In order to obtain the values of dislocation densities directly from the MD simulations, a *centrosymmetry deviation* (CSD) filter [101] was used. This technique exploits the *centrosymmetric* property of materials such as FCC metals.

Under homogeneous elastic deformation, these materials remain centrosymmetric, i.e. each atom has pairs of equal and opposite bonds with its nearest neighbours. Upon distortion, these bonds change in direction and/or length, but remain equal and opposite. However, when a defect is introduced nearby, this equal and opposite relation no longer holds for all nearest-neighbour pairs. It is therefore possible to define a *centrosymmetry parameter*. This is zero for a centrosymmetric material under any homogeneous elastic deformation, and nonzero for a plastic deformation.

Using a CSD filter, it is the possible to identify atoms which are associated with a plastic deformation of the crystal structure.

Using this method, dislocation densities were inferred directly from the MD model, giving $\rho_d \sim 10^{13}\,\mathrm{cm}^{-2}$ [98]. This result is in very good agreement with the value calculated using the X-ray diffraction post-processor. It can be seen that the dislocation concentrations are relatively high, implying that a sufficient number of dislocations was generated as a result of the shock wave. The fact that the compression of the lattice was only partially hydrostatic suggests, however, that the dislocations did not move to relieve shear stress sufficiently for a significant 3-D compression, as has previously been surmised.

Can We Measure Dislocation Densities during Shock Loading?

Besides providing the strains in the crystal in the three principal directions, the post-processing analysis presented in the previous section has led to a method of calculating the dislocation densities in a MD simulation, by comparing the second and fourth orders of X-ray diffraction, and applying the Warren formula, eqn. (2.70).

This result opens up new possibilities for the applicability of experimental *in situ* X-ray diffraction. By designing an experiment where both second and fourth order diffraction signals from a shock-compressed crystal can be recorded, it should be possible to measure the dislocation densities in a material on the extremely short time-scales (nanosecond and sub-nanosecond) relevant to the processes of plastic flow and hydrostatic compression under shock loading. Recalling the attempts of the theoretical models to emulate the phenomenon of plastic flow, outlined in section 2.5.5, it is clear that this measurement could be key to our understanding of how a crystal responds to a shock wave and yields to plastic deformation, obeying the Orowan equation (2.67).

The importance that such a measurement would afford to the field of shock wave physics can hardly be overstated. Measured plastic strain rates compel us to conclude that far higher dislocation densities are present in shocked materials than have ever

been found in recovered samples [8, 9, 11]. However, since no quantitative measurement of dislocation concentrations in a crystal under shock conditions exists to date, this assumption has never been experimentally verified. The technique proposed here offers the first prospect of such a verification.

4.1.2 Call for Large-Scale MD Simulations

Another important result described in the previous section is the contradiction between the resultant strain inferred from simulated shocked single crystals, and those from experimental X-ray diffraction where the found compression was much more hydrostatic [7]. This difference suggests that shear stress relaxation could occur on considerably longer time-scales than $\sim 10\,\text{ps}$. To this end, it was necessary to conduct a substantially larger MD simulation, whose spatial and temporal scales would be comparable to those in a typical experiment. Indeed, it was these X-ray diffraction post-processor results which motivated collaborators at LLNL to conduct MD simulations on larger scales.

Experimental samples of single Copper crystals are known to have a dislocation density of $\sim 10^6$–$10^8\,\text{cm}^{-2}$ and dislocation sources with a length of $\sim 1\,\mu\text{m}$. These are believed to allow the multiplication of dislocations at a reduced HEL of ~ 0.01–$2.6\,\text{GPa}$ [8, 27]. In contrast, most MD simulations to date use perfect crystals, where the HEL is given solely by the threshold for homogeneous nucleation of dislocations. It was therefore necessary to incorporate pre-existing defects in the simulations.

Additionally, experimental laser-induced shock waves in crystals are known to have finite rise-times, ranging from picoseconds to several nanoseconds [102]. Currently, most MD simulations almost exclusively employ a zero rise-time pulse since they span no more than $\sim 10\,\text{ps}$ in their entirety. In order to distinguish whether different shock wave rise-times have a discernible effect on the final state of the crystal, the new MD simulation was to include a finite linear ramp on the shock, analogous to experimental ones.

The massively parallel MDCASK code was employed again to generate these new

MD simulations. It was run on the Multi-programmic Capability Resource (MCR) Linux Cluster with a capacity of 11 teraflops (see http://www.top500.org), using 500–2000 Central Processing Units (CPU's) at LLNL.

The samples had free surfaces along the shock propagation direction [001], and periodic boundary conditions were used in the transverse [100] and [010] directions. As previously, the EAM potential for Copper due to Mishin *et al.* [99] was used.

Pre-existing dislocation sources incorporated in the MD simulations were prismatic dislocation loops with a length of $\sim 7\,\text{nm}$ each. The crystal regions in their proximity were found to have a reduced HEL of $\sim 10\,\text{GPa}$ [102]. The prismatic loops were oriented in such a way that the partial dislocations associated with them were in the energetically favoured $\{111\}$ planes. They were sufficiently far apart ($>400\,a_0$) that any interaction between them was negligible. The resulting dislocation density prior to the shock was $\sim 10^9\,\text{cm}^{-2}$.

The shock was launched in a manner analogous to that used in the first MD simulation. A force was applied to typically ~ 2–4 planes of atoms on one side of the sample, which then comprised the piston. Because these simulations were conducted on relatively long time-scales ($\sim 100\,\text{ps}$), a constant-velocity piston was chosen instead of a constant-force one, in order to avoid piston deformation [98].

The results of X-ray diffraction post-processing are presented in the following section.

4.1.3 256×10^6 Atom MD Simulation

A single Copper crystal MD simulation containing 256×10^6 atoms is studied. Its dimensions prior to shock launch were $200\times200\times1600$ unit cells, with the long side of the sample along the shock propagation direction [001], and the unperturbed unit cell size $a_0 = 3.615\,\text{Å}$, as before. The simulation thus spanned $\sim 0.6\,\mu\text{m}$ in length, an increase in size by two orders of magnitude with respect to the simulations analysed in section 4.1.1. The added advantage of this rapid increase in the simulation size is that the effects of the periodic BC's, applied in the directions normal to the shock

propagation direction, on the behaviour of the sample in its response to a shock load, are minimised [5].

In terms of the unit cell positions, the location of the centre of the crystal prior to shock launch was at (0,0,0) along the three primary axes. In other words, the limits of the crystal, in terms of the unit cells, were –100 and +100 for both [100] and [010] directions, and –800 and +800 for the [001] direction.

This extremely large computation was processed on 1440 parallel CPU's, producing a total of ~ 20 TB compressed data.

The shock wave launched in the crystal had a 50 ps long linear ramp. The peak pressure generated was 35 GPa, thus exceeding the threshold for the onset of homogeneous, as well as inhomogeneous dislocation generation (~ 32 and ~ 10 GPa, respectively [79]). The total duration of the simulation was ~ 130 ps and the simulation was stopped before the shock propagated to the end of the crystal.

Two prismatic loops were incorporated into the crystal prior to shock launch. The first one was located at $\sim 0.18\,\mu$m and the second one at $\sim 0.4\,\mu$m along the z axis, corresponding to unit cell positions of ~ -320 and ~ 230, respectively.

For the purposes of the X-ray diffraction post-processing, the resultant crystal was divided into eight parts, each consisting of data processed by 180 CPU's, and corresponding to a cube of 200×200×200 original FCC unit cells. The final data is contained in seven of the eight parts, as the piston pushed the atoms forward during the shock-compression.

The high-resolution 3-D X-ray diffraction post-processor was applied to cubic segments from the simulation, whose size was equivalent to 50×50×50 perfect FCC unit cells. The segments were chosen from the centre of the simulation with respect to the x and y axes. Their relatively small size in comparison with the 200×200 unit cells large cross-section available was chosen due to unfeasibly long computer times required to process samples of such scale at the required resolution.

Second Order 3-D FT Results

The resultant tensile and volumetric strains as yielded by the second order 3-D X-ray diffraction post-processing are presented in Fig. 4.2. The shock wave propagates from left to right, so the crystal regions on the left side of the sample have been subjected to the shock for the longest time. The original positions of the two prismatic loops present in the sample are marked by two vertical lines in the figure.

The atomic density rise in different crystal sections is also indicated. It should be noted that the 8% atomic density rise near the leading edge of the compression wave (furthest from the piston) is significantly lower because this segment is in the region of the 50 ps rise-time and is only partially shock-compressed.

It is expected that in the region between the first prismatic loop and the piston (i.e. $z < -320$), the dislocation generation will be homogeneous, and the onset of inhomogeneous dislocation generation will only be in the vicinity of the loop. The figure shows that the part of the crystal between the piston and the first prismatic loop remains primarily uniaxially compressed, with the compression in the lateral directions, x and y, remaining below 4%. As the shock propagates to the loop-containing region, the compression along the two lateral directions increases, whilst that along z remains approximately the same. This results in more hydrostatic-like compression of the crystal.

Once the shock wave reaches the first prismatic loop and the pressure exceeds the threshold of ~ 10 GPa, dislocations are generated inhomogeneously, aided by the embedded sources. Dislocation movement and subsequent shear stress relaxation can occur more promptly than in the crystal region between the piston and the first loop, which relies solely on homogeneous dislocation generation. This is because at lower threshold pressures, lower concentrations of dislocations are generated; these do not inhibit each other's movement and are hence more capable of shear stress release than dislocations created in a region which was previously a perfect crystal. Lattice compression in the vicinity of the prismatic loops is therefore more hydrostatic.

As will be shown later, once the activation threshold of the embedded sources has

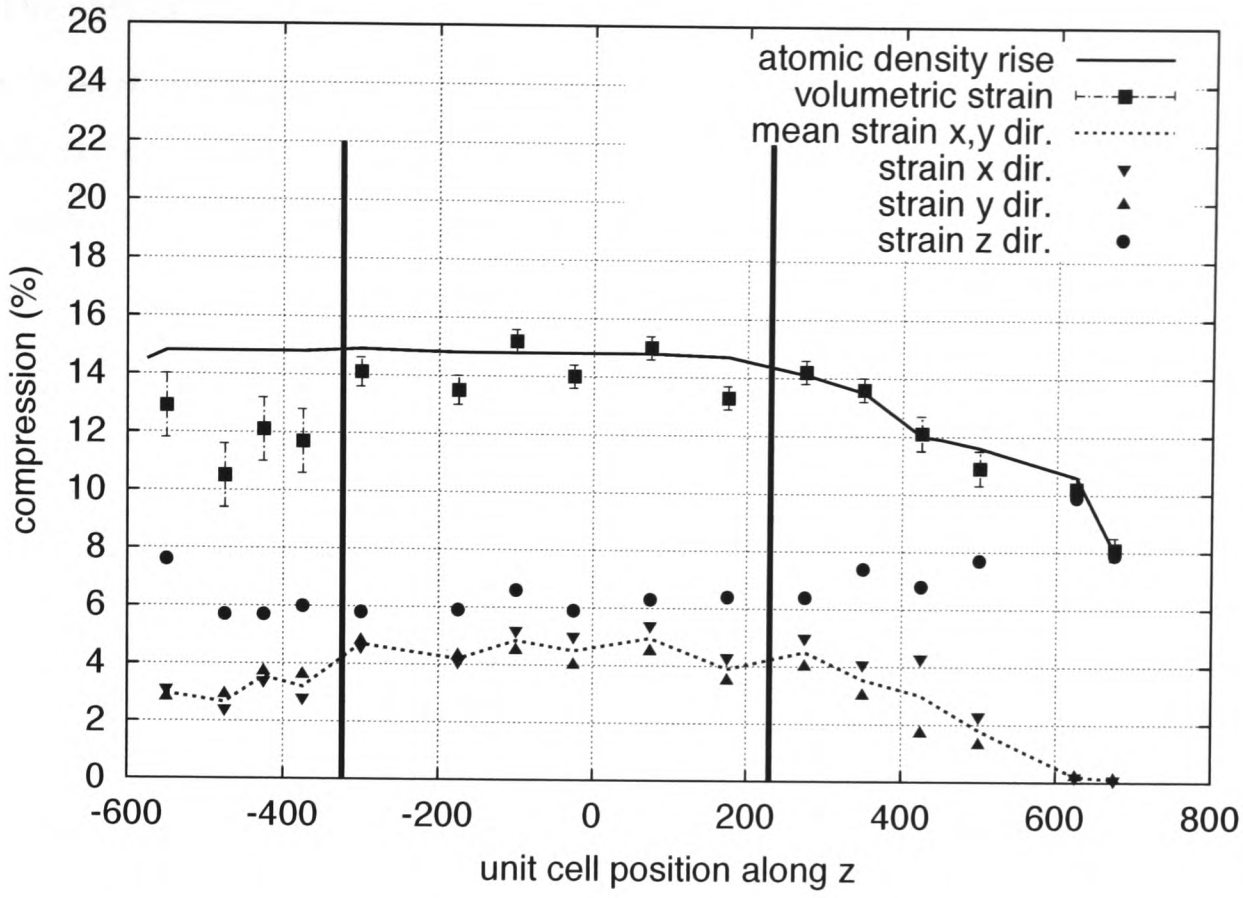


Figure 4.2: Second order diffraction results: Volumetric compression and compression along the principal axes of the crystal, of sampled cubic sections in the MD simulation. The corresponding rise in atomic density is shown for comparison. The two prismatic loops present in the sample are indicated by vertical lines. The shock moves from left to right, with the shock front at $z \sim +675$.

been reached, mobile dislocations are generated at relatively low pressures at and near the first prismatic loop [102]. It is therefore expected that the region between the two prismatic loops will contain lower dislocation densities in comparison with the region nearest the piston.

The region around the second prismatic loop at $z \sim 230$ behaves similarly to that near the first one; the compression is nearly hydrostatic, accounting for a successful shear stress release in the crystal. Material up to unit cell position $z \sim 400$ is thus more hydrostatically compressed. Such near-3-D compression can be accounted for by a high mobility of the dislocations nucleated in the region between the two loops. These mobile dislocations alleviate shear stress, resulting in lateral compressions and plastic flow.

The part of the crystal furthest from the piston, well beyond the second prismatic loop, is predominantly uniaxially compressed. As the simulation was stopped before the shock wave could propagate to the end of the crystal, the applied pressure at $z>+600$ is relatively low, and hence the compression in this region is primarily elastic.

The region in the vicinity of unit cell position $z=+500$ still displays some lateral compression, with tensile strain along x an y being $\sim 2\%$. This suggests that some shear stress has been released, although not sufficiently to allow a significant 3-D compression of the lattice. Notably, the value of the volumetric strain calculated for this part of the crystal is below the atomic density rise value, unlike regions immediately ahead of or behind it. In this way, this region is similar to that between the piston and the first prismatic loop, which relied solely on homogeneously generated dislocations.

The material centered at $z\sim +675$ is uniaxially compressed by $\sim 8\%$ along the shock propagation direction, remaining uncompressed in the lateral directions. Due to the 50 ps rise-time of the shock, the applied piston pressure is still rising and not at its peak value. For this reason, it is only sufficient to generate an elastic compression of the lattice.

The error bars indicate the standard deviation in the values detected by probing five different segments sized $50\times50\times50$ unit cells at the same z position along the crystal. It can be seen that there is a clear disagreement between the volumetric strain as obtained using the post-processing code and the atomic density rise, in the region between the piston and the first prismatic loop. This discrepancy decreases in the region between the loops, and disappears in the part of the crystal farthest from the piston (with the exception of the region near unit cell $z=+500$), where the shock pressure is still rising and the compression is more uniaxial.

This disagreement appears to be similar to the discrepancy in the results in section 4.1.1. In order to investigate its trend and cause, the same calculation was performed in the fourth order. This is presented in the following section.

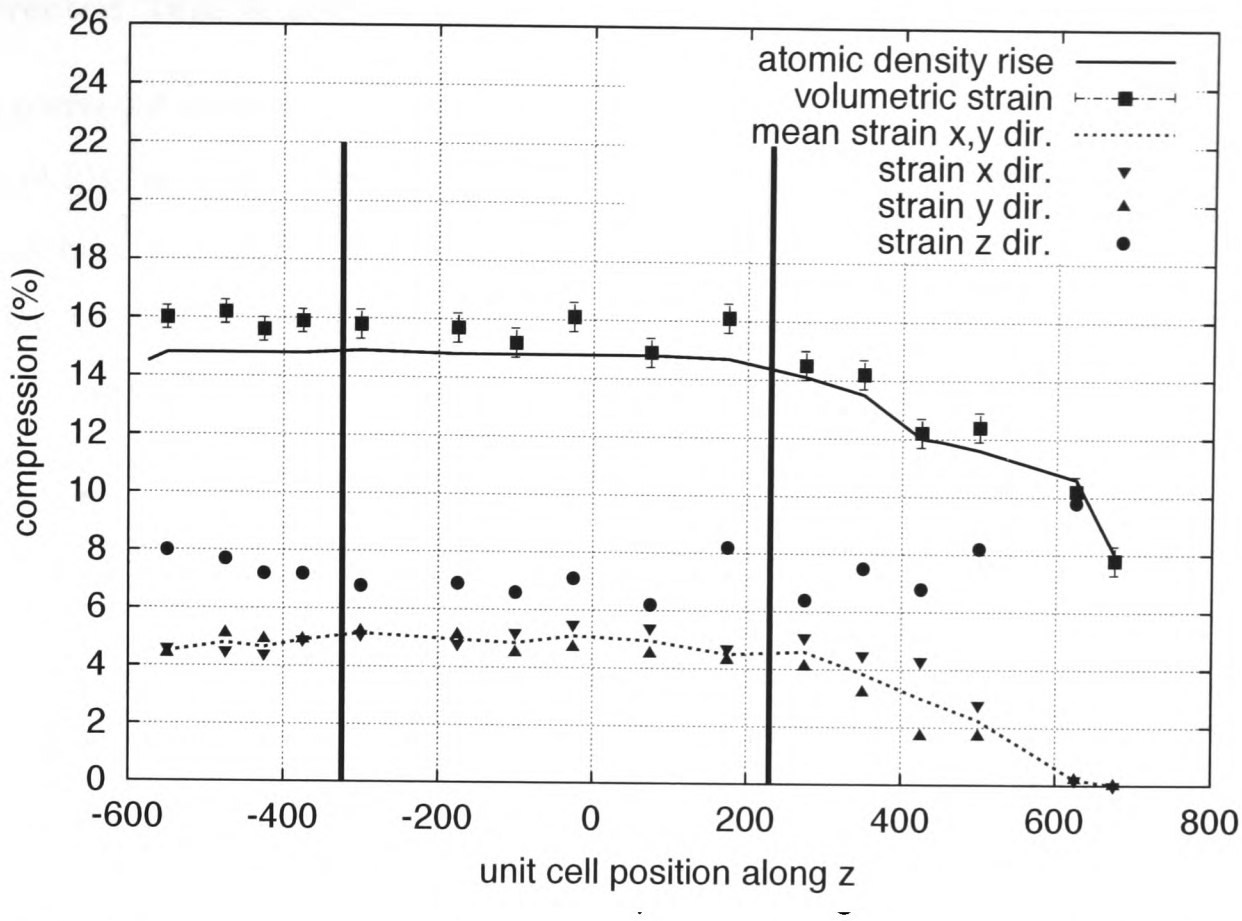


Figure 4.3: Fourth order diffraction results: Volumetric compression and compression along the principal axes of the crystal. The shift in the resultant volumetric compression in the first region of the crystal is visibly in the opposite direction to that given by second order diffraction.

Fourth Order 3-D FT Results

Figure 4.3 shows the tensile and volumetric strains in the crystal, obtained from the fourth order X-ray diffraction calculation.

Whilst qualitatively, the behaviour of the crystal as depicted in the fourth order post-processing corresponds well to the behaviour inferred from the second order diffraction calculation, the discrepancy in the volumetric strain has the opposite tendency; the detected values are above those given by the increase in the atomic density. These findings support the formula due to Warren, used earlier. The same method was used again to calculate the corrected strains in the crystal.

Corrected Tensile and Volumetric Strains

The corrected strains in the three principal directions (using the method involving eqn. (4.5)), as well as the corrected volumetric strains, are plotted in Fig. 4.4. It should be noted that these values ignore any peak shifts in the directions perpendicular to the primary directions they represent. The errors introduced by this are, however, within the standard deviations on the peaks, and one can see that the agreement between the X-ray diffraction results and the atomic density rise is excellent.

A snapshot of the MD simulation, taken from [102], is also shown, illustrating the character of the different parts of the crystal. Only atoms forming dislocations, identified using the CSD filter [101], are highlighted. Three distinct regions can be identified. The region labeled "homogeneous" is between the piston and the first embedded source. It can be seen that high dislocation densities are generated here, as was postulated earlier. Despite this, the shear stress release in this region did not result in much 3-D compression, as the mobilities (and hence velocities) of the dislocations were hindered.

Nonetheless, it can be seen that this region shows a more 3-D compression than the small MD simulation studied in section 4.1.1. Here, the compression along z is ~ 1.7 times larger than the compression along x or y. This tendency towards the hydrostat even in the homogeneous crystal region can be explained by the use of a finite ramp on the shock, as well as the long time-scale of the MD simulation. Both these factors render the model closer to an experimental laser-induced shock in a crystal.

This first region is followed by the "mixed" region in the centre of the MD simulation, where the compression in the two lateral directions can be seen to increase by $\sim 1\%$. This causes the overall crystal compression to approach 3-D, with the strain along z only ~ 1.3 times larger than that along x or y. This is a significant improvement in the modelling of near-3-D compression of shocked crystals. It should also be noted that the dislocation concentration is lower than in the homogeneous region without the pre-existing sources. This shows that the dislocations generated here are

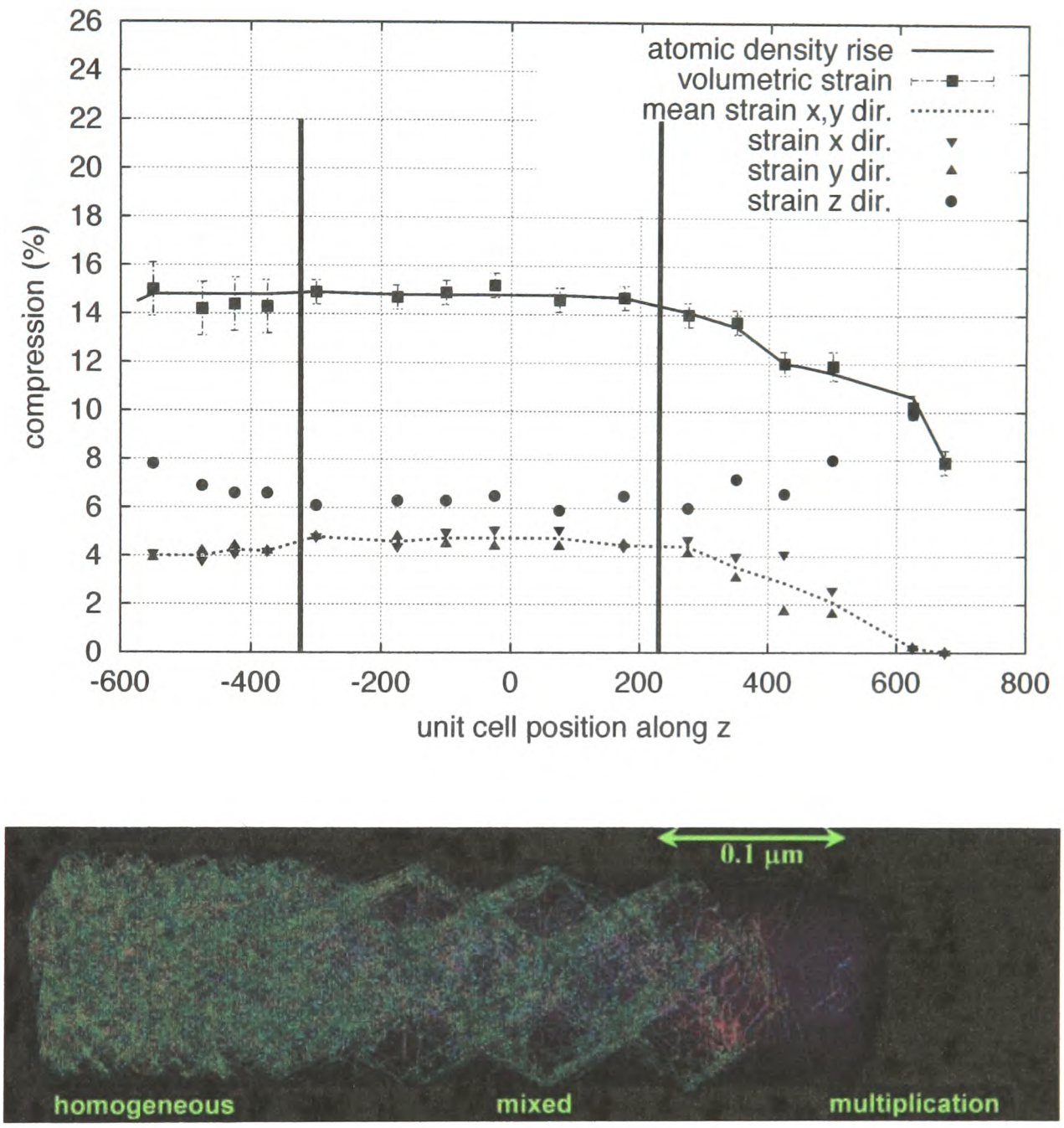


Figure 4.4: Corrected tensile and volumetric strains in sampled cubic sections of Cu simulation (top) and a snapshot of the corresponding MD simulation (bottom). The region between the prismatic loops, displaying compression closest to the hydrostat, is seen to contain lower dislocation densities than the region nearest the piston.

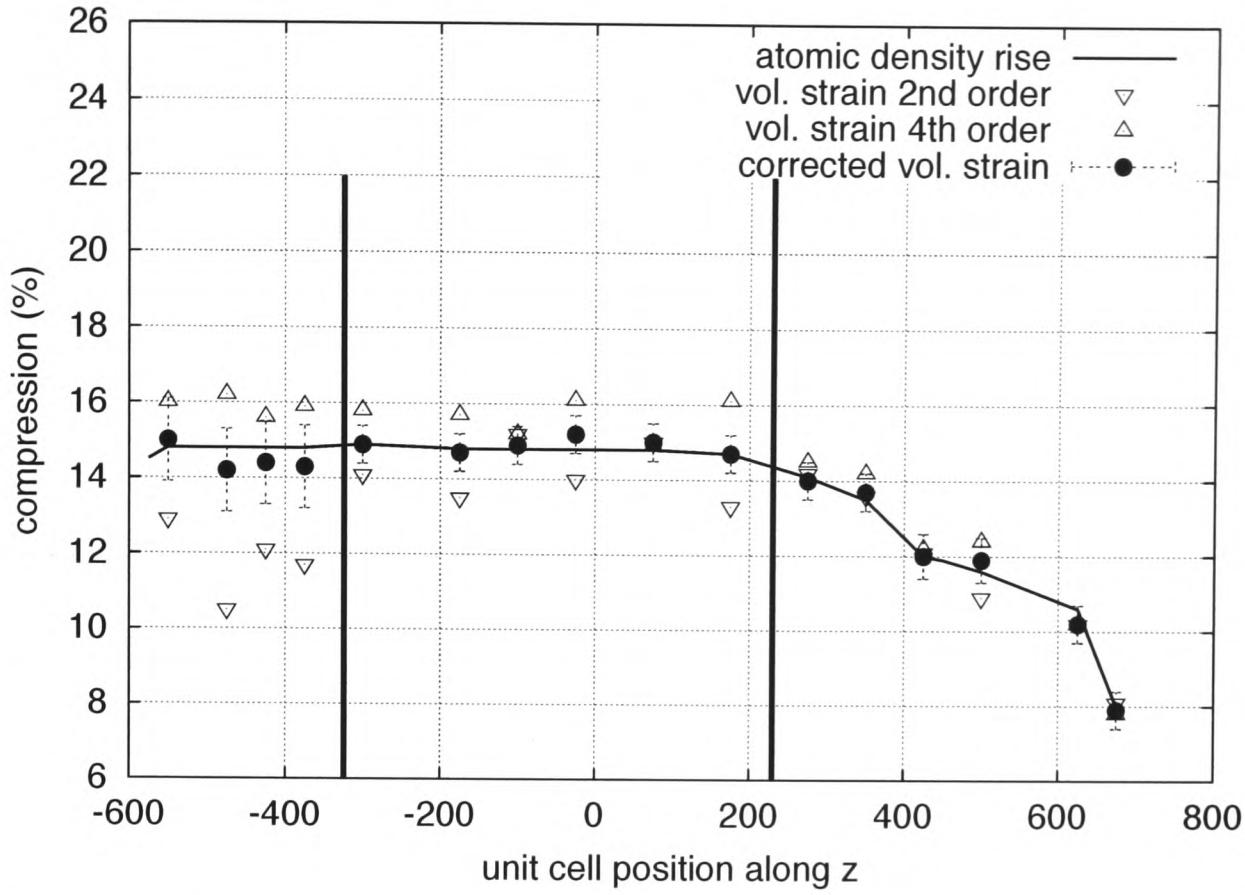


Figure 4.5: Volumetric strain in sampled cubic sections in the MD simulation. Results obtained from second and fourth order diffraction are shown, as well as the corrected values, which are in excellent agreement with the atomic density rise.

more mobile, and hence readily enabling plastic flow in the crystal. Recalling the Orowan equation (2.67), the plastic strain rate is determined by the concentration of *mobile* dislocations only, since they alone are responsible for it. Clearly the presence of pre-existing defects is a catalyst in this process.

Lastly, the part of the simulation furthest from the piston can be seen to contain a small concentration of dislocation lines. These are a consequence of dislocation multiplication from the second prismatic loop, where the applied pressure has exceeded the activation threshold of the pre-existing sources. This region is therefore labeled "multiplication". The partial 3-D compression seen here (up to and including unit cell position $z \sim +500$) can be accounted for by these sparse mobile dislocations.

The crystal region far from the piston, near the leading edge of the shock, is predominantly elastically compressed along the z direction, as expected and shown

previously. Only uniaxial compression is detected in this part of the crystal.

Figure 4.5 compares the values of the volumetric strain obtained from the second and fourth order diffraction with the final values corrected for the presence of dislocations. The final results are in excellent agreement with the atomic density rise in all regions of the crystal. This verifies the X-ray diffraction method of strain calculations, as well as the assumption that the second and fourth order peaks were shifted due to the dislocations present in the crystal.

Dislocation Densities

The calculated values of α were used to infer dislocation densities in different parts of the crystal. Figure 4.6 shows the obtained results.

As expected, the calculated dislocation densities in the homogeneous crystal region between the piston and the first prismatic loop are the highest. It should, however, be stressed that merely a high dislocation concentration does not necessarily result in a successful shear stress release which leads to near-3-D compression of the lattice. As shown earlier, the compression of the lattice in this crystal region is primarily along the shock propagation direction. The dislocation density result is in very good agreement with that inferred directly from the MD simulation, $\sim 10^{13}$–$10^{14}\,\mathrm{cm}^{-2}$ [102].

The parts of the crystal beyond the first prismatic loop have a concentration of dislocations approximately three times lower than those in the homogeneous region. This is also expected, and in very good agreement with the direct calculations from the MD simulation [102]. The pressure required for inhomogeneous dislocation generation is only $\sim 10\,\mathrm{GPa}$, so dislocations were generated more readily at lower pressures. It was predicted earlier that their mobilities are higher than those of the dislocations in the homogeneous crystal region, resulting in a more hydrostatic-like compression of the lattice, seen in Fig. 4.4. Indeed, direct observations of the MD simulation showed that the mean dislocation velocity, v_d, decreased from its peak value of $\sim 0.3\,c_0$, where $c_0 \simeq 4\,\mu\mathrm{m\,ns}^{-1}$ is the sound velocity in Copper, as their den-

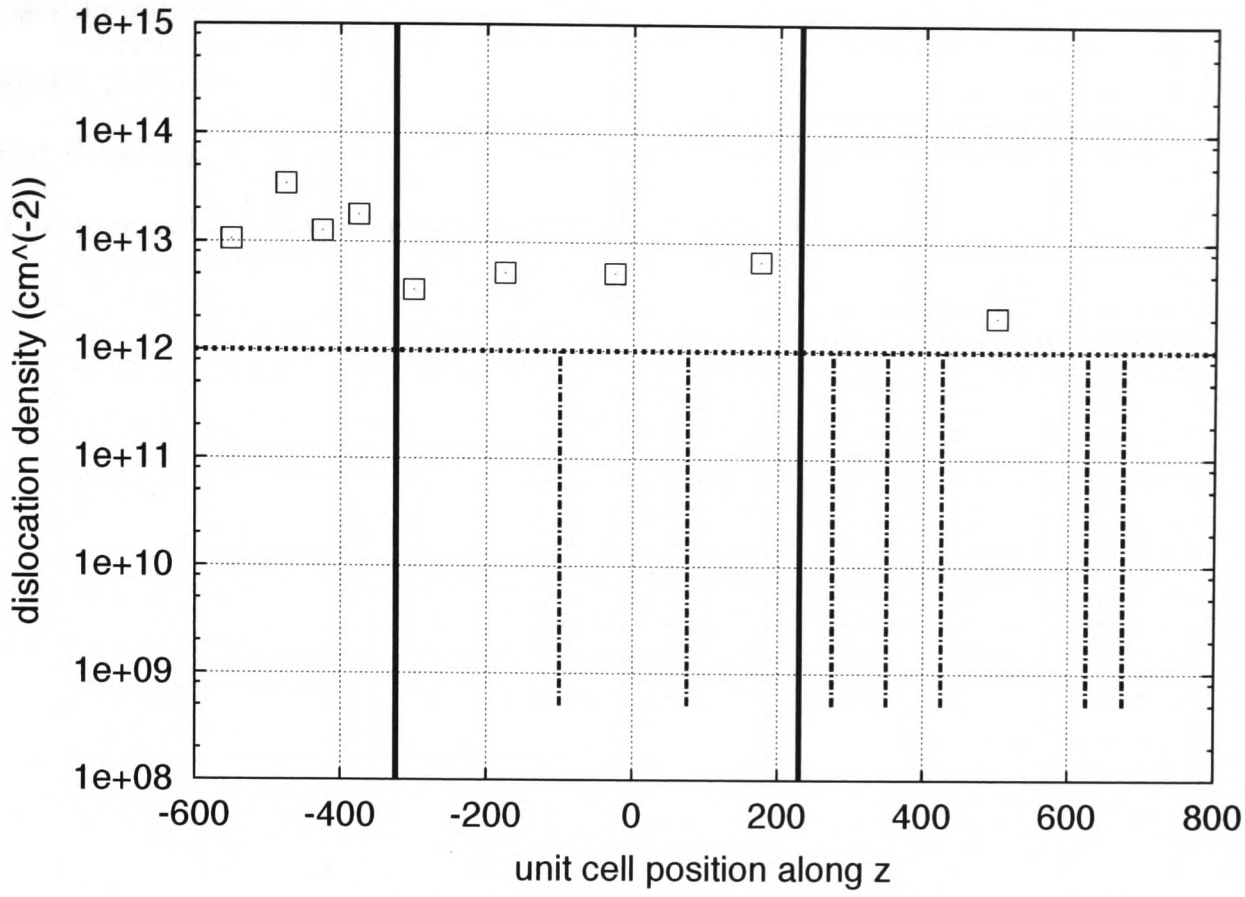


Figure 4.6: Dislocation densities in different regions of the MD simulation. Positions of the prismatic loops are indicated. Density values with too high errors are omitted and replaced by dashed vertical lines representing the range of their possible values.

sity increased [102]. This shows the sensitivity of v_d to the population of obstacles in the crystal, and explains their lowered mobility in the homogeneous region.

Certain parts of the crystal between the prismatic loops have significantly lower dislocation densities than regions ahead of and behind them. These are in the vicinity of unit cell positions z=–100 and +75. Referring back to Fig. 4.2 and 4.3, the diffraction post-processing for these regions yielded volumetric compressions which, for both second and fourth order calculations, coincide with the atomic density rise. This means that the stacking fault densities are too low to induce any significant shifts in the diffraction peaks. Any shifts which do occur are therefore within the error-bars on the peaks. As such, the errors on the inferred values of α and dislocation densities are too large for the results to have any quantitative validity. For this reason, Fig. 4.6 omits the values of dislocation density at these points, and the range

of possible values is marked by dashed vertical lines. The horizontal line marked on the graph indicates the cut-off dislocation density value, which can still be considered quantitatively accurate.

The dislocation densities in the regions furthest from the piston are mainly also omitted, since the peak shifts in the second and fourth order diffraction calculations are negligible. The only exception is the region located near unit cell z=+500, where the detected dislocation density is $\sim 2\times 10^{12}\,\mathrm{cm}^{-2}$, i.e. an order of magnitude lower than in the homogeneous crystal region nearest the piston. This is in accordance with the sparse population of dislocations in this part of the crystal.

The dislocation concentration in the region farthest from the piston is expected to drop rapidly, since the shock pressure significantly decreases. The compression on the end far from the piston is therefore predominantly uniaxial and elastic, as shown earlier in Fig. 4.4.

Plane Shears and Rotations

In addition to the tensile and volumetric strains, the 3-D FT yields the shear strains and rotations in the crystal. These provide further information about the processes that the material undergoes whilst subject to shock-compression.

Figure 4.7 shows the shears which the three principal planes in the unit cell undergo as a consequence of the shock wave passage. Both figures show that relatively little shear strain occurred throughout the entire sample. It is expected that, within small deviations, the shock wave should not result in a shear of the crystal planes.

It can be seen that some regions of the crystal, especially one between the piston and the first prismatic loop, and the region near the unit cell position z=+500, display a planar shear of almost $\pm 1°$. As this is the only study of a MD simulation of this kind, further post-processing of MD models with similar features would be required to assess whether these deviations represent a real physical phenomenon in the material.

The shear strain values can be seen to approach zero particularly in the region

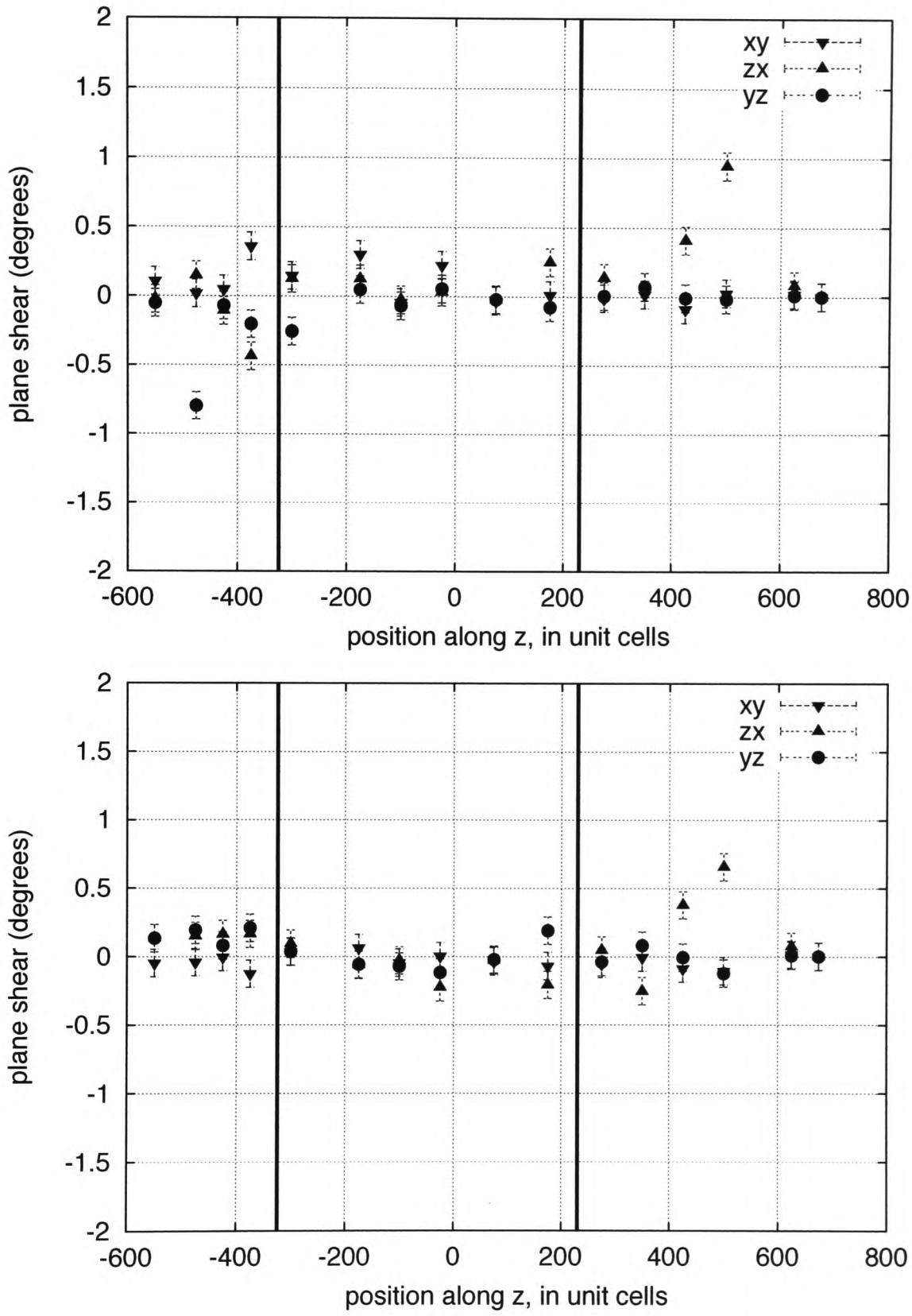


Figure 4.7: Shear strains of the xy, zx, and yz planes in the sample given by the second (top) and fourth (bottom) order 3-D X-ray diffraction post-processing. Relatively little plane shear is found, with the exception of the homogeneous crystal region, and the region in the vicinity of unit cell position z=+500.

beyond unit cell position z=+600, which was subjected to elastic compression along [001] only. Since no plastic deformation occurred in this part, this lack of planar shear is not surprising.

Figure 4.8 shows rotations of the three principal planes. Very good agreement between the results from the second and fourth diffraction orders is found. It can be seen that the region of the crystal closest to the piston displays a gradually increasing rotation of the yz planes. Beyond the first prismatic loop, however, a rotation of the zx planes sets in, with that of the yz planes remaining at $\sim -1°$. It is assumed that this could be caused by the positioning and orientation of the prismatic loops in the sample, which may have resulted in an asymmetry of the crystal's response to the applied shock wave. However, further analysis of large MD simulations with pre-existing prismatic loops would be required to verify this assumption.

The regions beyond unit cell position z=+600 show a minimal planar rotation. This is in accordance with the elastic, reversible deformation of the crystal here.

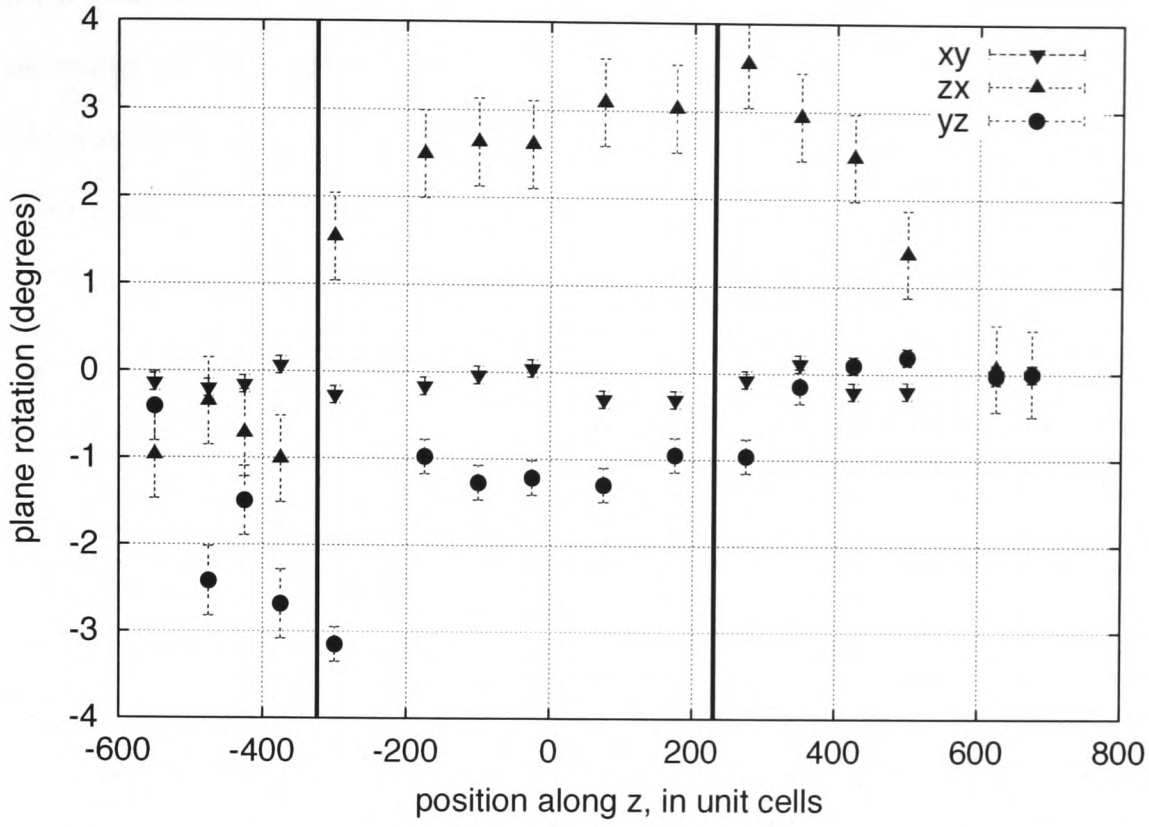


Figure 4.8: Rotations of the xy, zx, and yz planes given by the second and fourth order diffraction calculation.

4.2 Iron

The second part of the computational work conducted for this thesis analyses the post-processing of MD simulations of single crystals of Iron, which were performed in Los Alamos National Laboratory (LANL), and are presented in [6].

The simulations studied in this section were generated using a massively parallel MD code "SPaSM" ("Scalable Parallel Short-range Molecular Dynamics") [80], running on a 12-processor shared-memory Sun Enterprise 4000. Each simulation modeled 7.84×10^6 atoms in samples of dimensions $140\times140\times200$ BCC unit cells. The unit cell size of uncompressed Iron is 2.8665 Å, so the samples spanned ~ 57.4 nm along the shock propagation direction [001] (or z), and 40.2 nm in the lateral directions.

The shock was generated using the momentum mirror method described in section 3.1.1 [5]. Atoms were specularly reflected by an infinitely massive, perfectly flat piston, moving at piston velocity u_p, generating a shock wave moving at shock velocity u_s. Periodic BC's were applied in the lateral directions [100] and [010]. The duration of each simulation was <10 ps.

Modified EAM potentials [103, 104] were used, adapted to simulate high-pressure experiments in BCC metals. The Voter-Chen EAM Fe potential [103], giving the $\alpha-\epsilon$ transition pressure of 15 GPa, proved to be in better agreement with experimentally measured threshold pressures for the onset of this transformation in Iron, ~ 13 GPa [21, 34].

Four simulations were studied (**A** – **D**), with gradually increasing values of u_p. The shock velocity u_s was also provided. Using these two quantities, and the momentum conservation eqn. (2.44), it was possible to calculate the pressure applied to the crystal in all four MD simulations. The values of u_p in the simulations were $362\,\mathrm{ms}^{-1}$, $471\,\mathrm{ms}^{-1}$, $689\,\mathrm{ms}^{-1}$, and $1087\,\mathrm{ms}^{-1}$, and the respective pressures along the shock propagation direction were 15.0 GPa, 19.6 GPa, 28.7 GPa, and 52.9 GPa.

A snapshot of all four MD simulations is illustrated in Fig. 4.9. In simulation **A**, the crystal is elastically compressed along the shock propagation direction; the applied piston pressure is at the threshold of plastic deformation, however this is

not sufficient to induce the phase change on the time-scale of several picoseconds covered by the simulation. Simulations **B** and **C**, with gradually increasing values of u_p, show a two-wave shock structure: an elastic precursor precedes a slower phase transformation wave from BCC (or α) phase to HCP (or ϵ) phase.

It should be noted that the intermediate elastic-plastic transition wave which exists in real engineering crystal samples does not appear in these simulations. Experimental crystals contain defects and are often polycrystalline, which lowers their HEL to only $\sim 1\,\text{GPa}$. At pressures above this threshold, a slower plastic wave follows the elastic precursor and this is followed by an even slower phase transformation wave at higher pressures [6]. In *perfect* single crystals, such as the system modeled here, the three-wave shock structure does not exist; the phase transformation takes place at the threshold pressure and there is no elastic-plastic transition wave.

As the applied piston velocity increases, so does the velocity of the phase transformation wave. Simulation **D** shows a single, over-driven phase transformation wave. Here, the applied piston pressure is well above the threshold for plastic deformation, and the elastic precursor is overtaken by the faster transformation wave. It is postulated that the BCC (α) lattice of Iron has transformed into a HCP (ϵ) phase, as described in Chapter 2.

It is surmised that with increasing piston velocities, the higher temperatures reached in the crystal aid the annealing process, leading to a mergence of smaller grains into fewer larger ones [6]. In addition, the grains are expected to grow larger at later times.

The aim of studying these simulations using the post-processing code was to verify all these findings using simulated X-ray diffraction and, importantly, to determine the most appropriate way to detect the $\alpha - \epsilon$ phase transformation in Iron upon shock-compression experimentally.

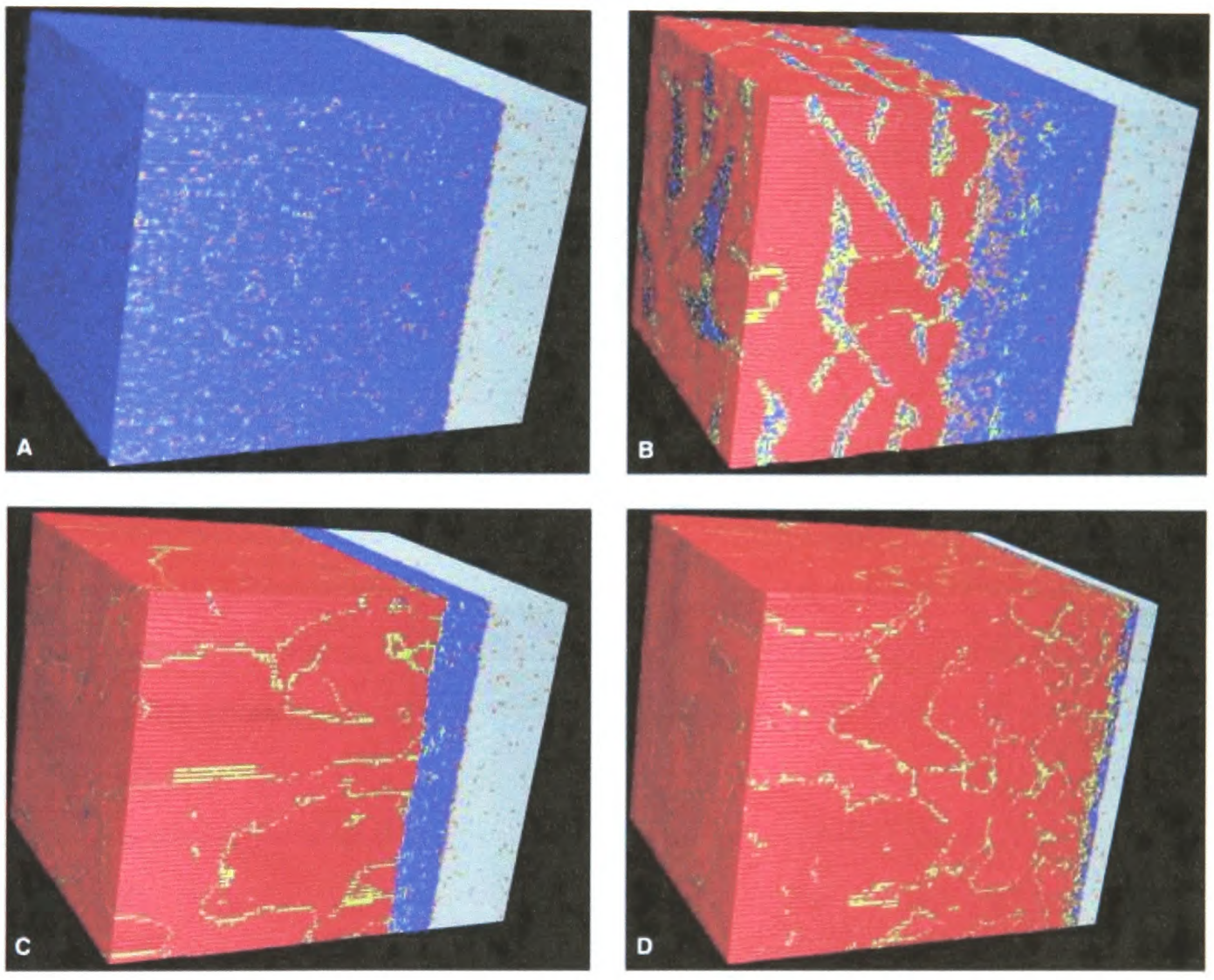


Figure 4.9: MD simulations of shock-compressed single crystal Iron [6]. u_p increases from **A** through to **D**. Colour legend: grey = unshocked BCC (α phase); blue = uniaxially compressed BCC; red = transformed ϵ phase (quasi-HCP); yellow = grain boundaries (e.g. twin boundaries).

4.2.1 MD Simulations A – D: Results

1-D FT Results: Detecting Structural Changes

Figures 4.10 and 4.11 show results of simulated 1-D X-ray diffraction applied to all four MD simulations. The diffraction is from the $(00l)$ planes, i.e. those normal to the shock propagation direction.

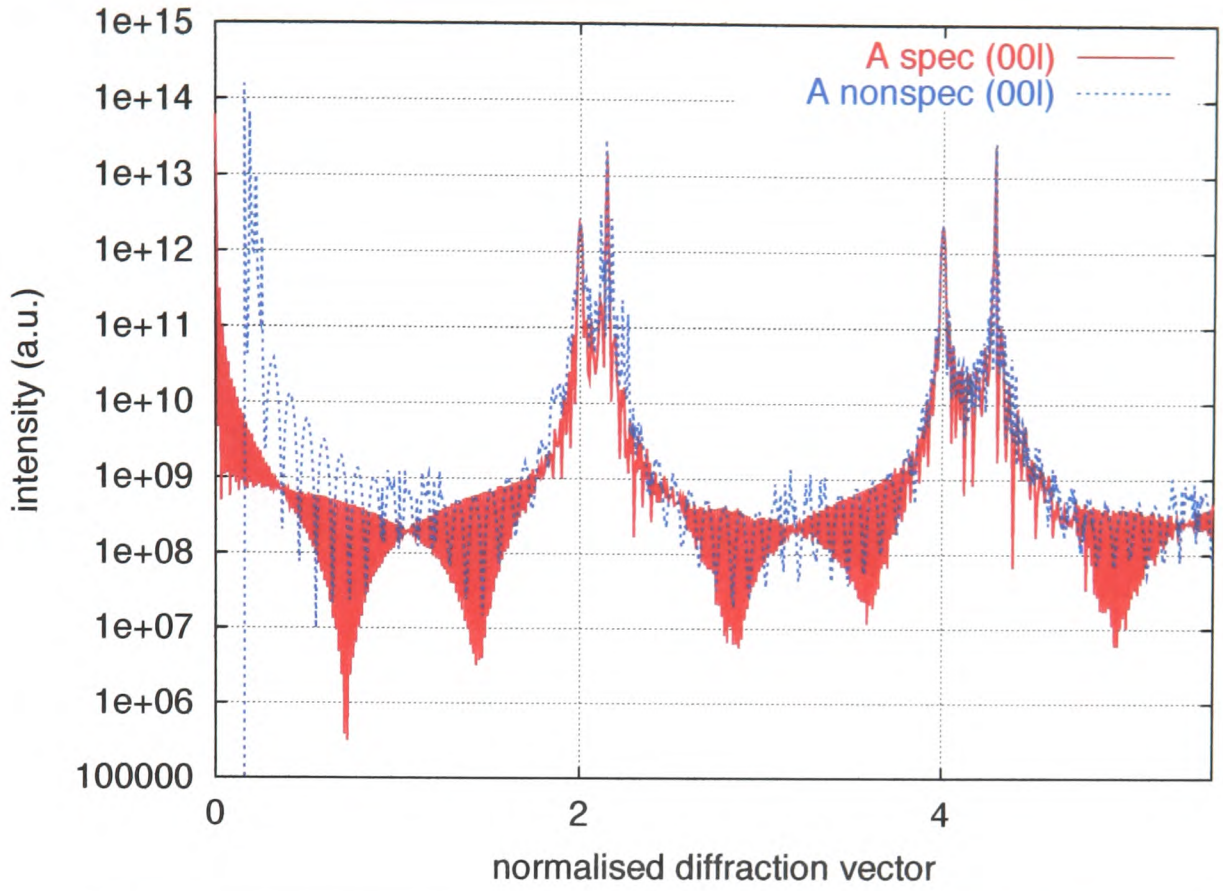
Diffraction peaks from the unshocked material appear at normalised Δk values corresponding to the BCC-allowed Miller indices, i.e. 2 and 4 for the range of Δk probed here. A second, shifted intensity peak in part **A** in Fig. 4.10 indicates that a larger proportion of the crystal has been compressed along z. Detailed analysis showed that the elastically compressed region of the crystal spanned the length of ~ 145 original BCC unit cells along z.

Simulation **B** also shows a relatively sharp second peak corresponding to a uni-axial compression, and a further peak, of lower intensity and greater breadth. This is believed to correspond to the phase-changed part of the crystal. The region of the crystal nearest the piston, spanning ~ 90 BCC unit cells along z, has been phase-changed, with the subsequent crystal region spanning ~ 55 BCC unit cells along z compressed elastically.

As the piston velocity rises (simulation **C**), this third diffraction peak increases in intensity, suggesting a larger proportion of the crystal has been phase-changed. In this MD simulation, the region nearest the shock-inducing piston spanning ~ 115 BCC unit cells along z has been phase transformed, with only the ~ 20 unit cells long region adjacent to it compressed elastically.

In simulation **D**, only a single peak besides the diffraction signal from the virgin material is distinguishable. The phase-transformation wave has now overcome the elastic wave, and there is no purely elastic response from the crystal. The shock has propagated the length equivalent to ~ 155 original BCC unit cells along z, and this entire part of the crystal has undergone a phase transition.

It is interesting to note that non-specular diffraction yields broader peaks for what



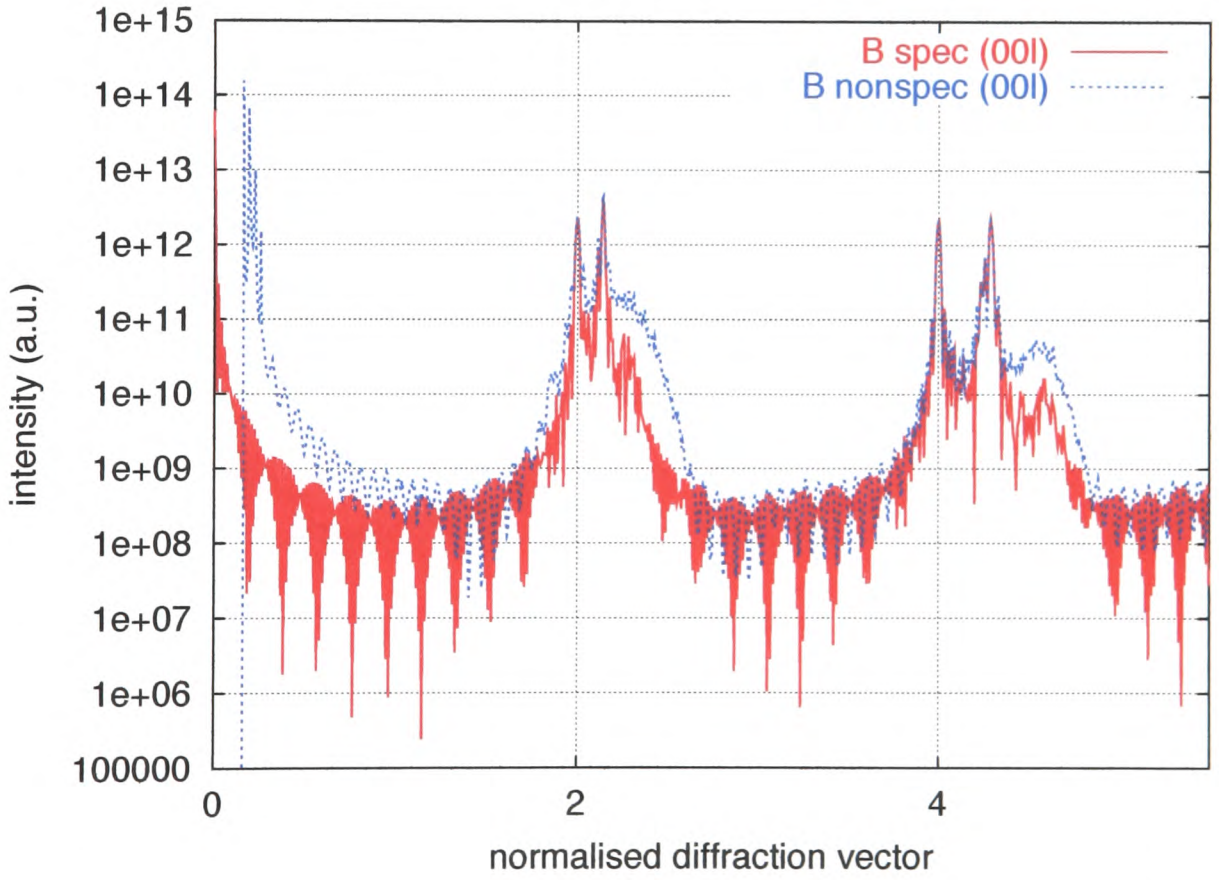
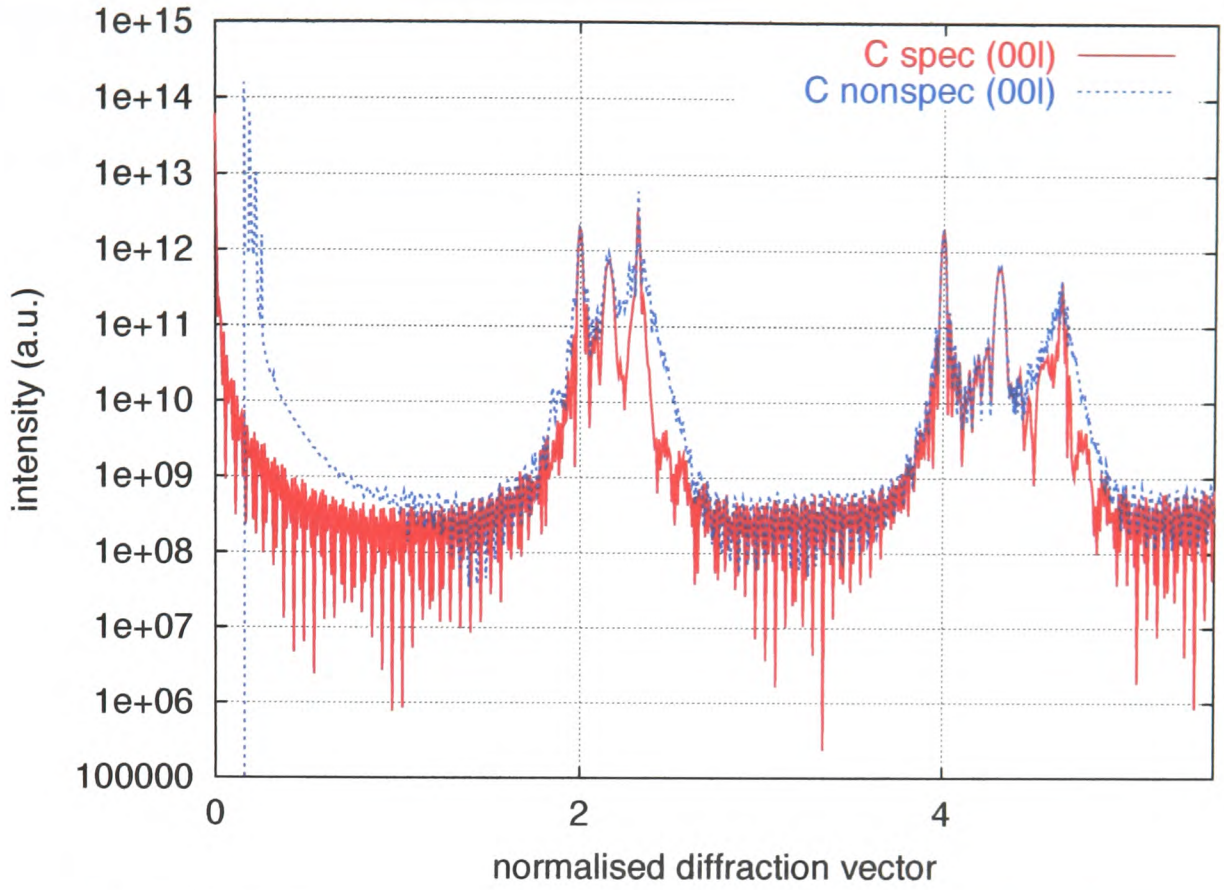


Figure 4.10: 1-D diffraction from planes normal to the shock propagation direction in MD simulations **A** and **B**. Non-specular diffraction captures diffuse scattering, resulting in a broader secondary peak corresponding to the phase-changed region in simulation **B**, whilst the pattern for **A** remains unchanged.



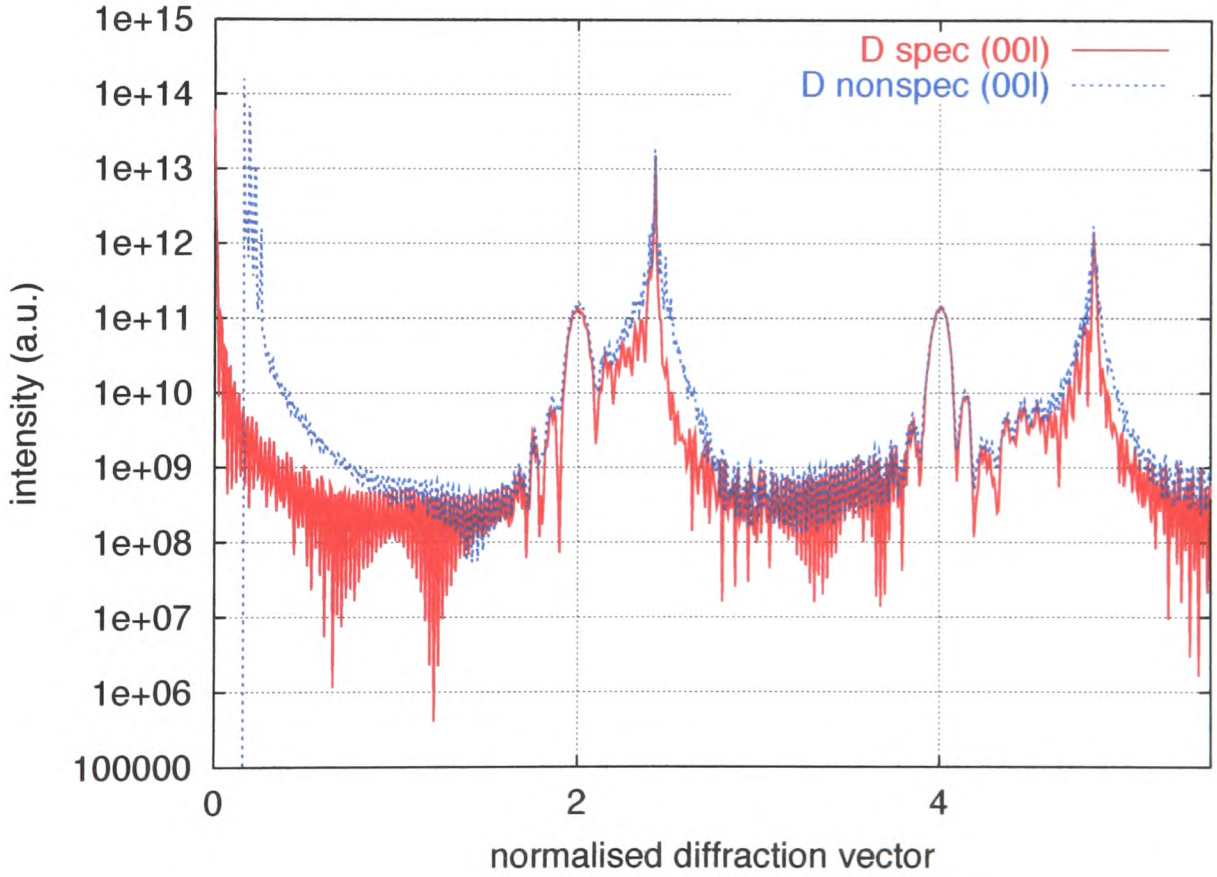


Figure 4.11: 1-D diffraction from planes normal to the shock propagation direction in MD simulations **C** and **D**. Peaks due to phase-changed parts of the crystal increase in intensity whilst diffraction from the uniaxially compressed lattice weakens for simulation **C**, and completely disappears for simulation **D**.

is assumed to be the evidence of the phase change, whilst the signal from the elastically compressed material remains unbroadened. It is believed that diffuse radiation, diffracted at a small range of angles near the Bragg angle, is caused by imperfections in the lattice which are a consequence of the BCC – HCP phase transition. In different regions in the crystal, the transformation will result in a range of lattice sizes of the new unit cell, and their slightly differing orientations. This is due to the anisotropic nature of shock waves in solids. Additionally, as stated above, BCC planes (110) and $(1\bar{1}0)$ can *both* transform to the HCP (0001) planes with equal probabilities and energetic preferences. Although these two orientations are symmetric with respect to the $(h00)$ planes, and as such will not cause peak broadening, the grain boundaries and defects separating them will have a broadening effect on the resultant non-specular diffraction signal from the $(00l)$ planes.

As before, compression of the crystal along z was calculated from the positions of the shifted intensity peaks. In MD simulations **A** – **C**, where elastically compressed BCC material was discernible, this was found to be 6.6±1.0%.

Figures 4.12–4.15 show the resultant 1-D diffraction patterns from planes parallel to the shock propagation direction. It can be seen that the position of the diffraction peaks does not differ from those for a perfect crystal, indicating that compression in the lateral directions did not occur and that the crystal has not undergone a plastic deformation. Despite this, the peak widths as depicted by the non-specular diffraction, and the shape of the pattern between the peaks, suggest that the crystal has undergone a structural change.

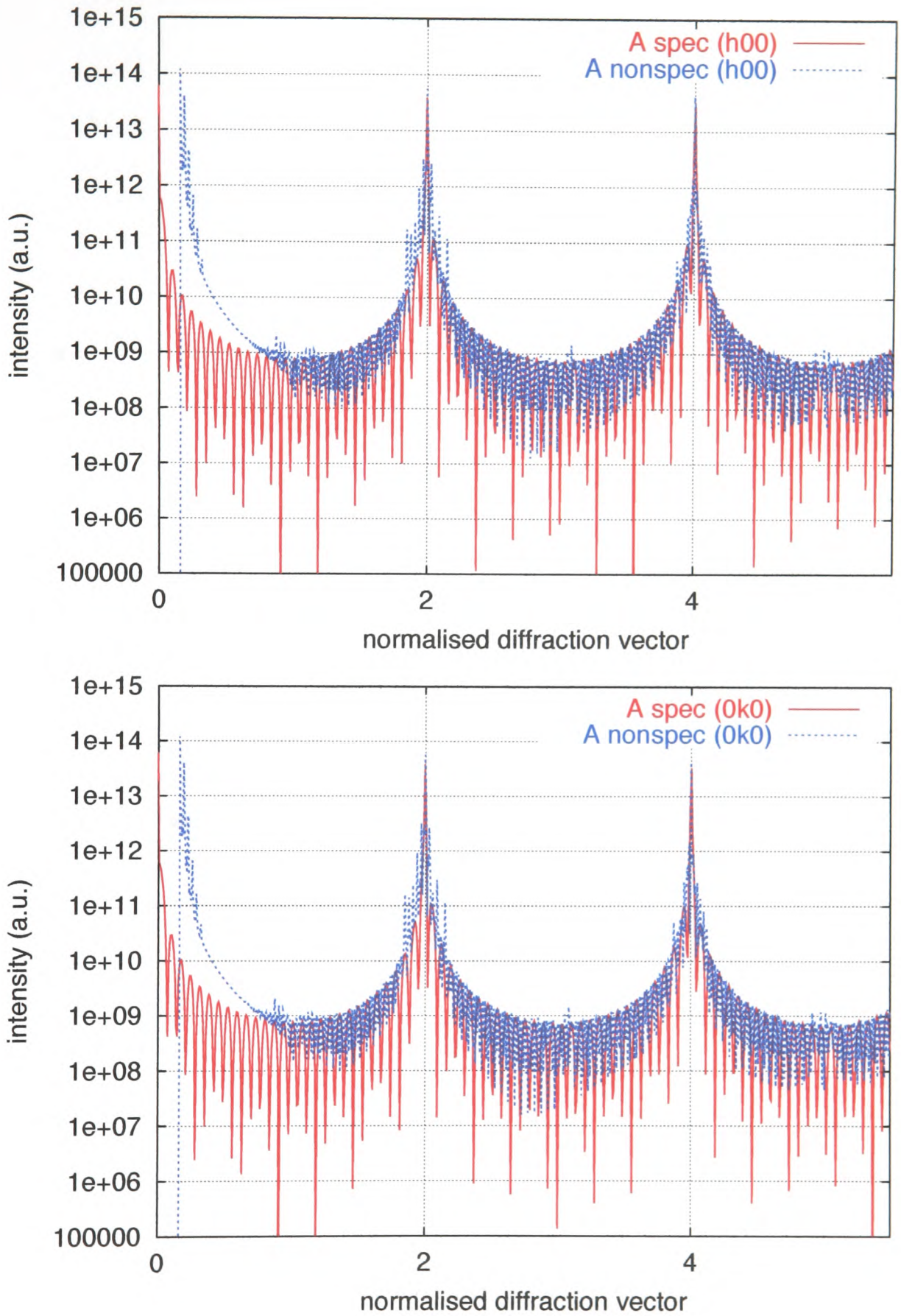
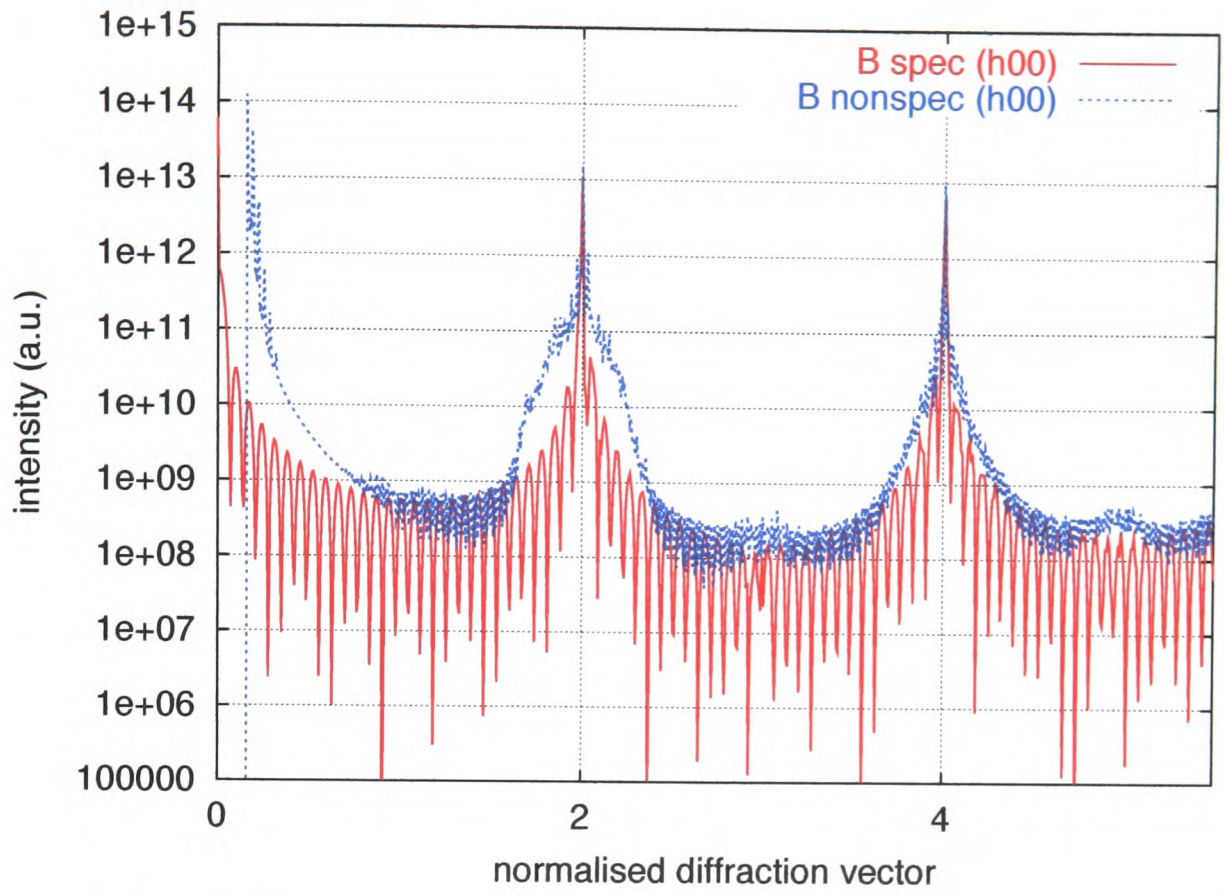


Figure 4.12: 1-D diffraction results from $(h00)$ and $(0k0)$ planes in MD simulation **A**. The peak position and width do not change, suggesting no atomic movement in the directions normal to the shock propagation direction.



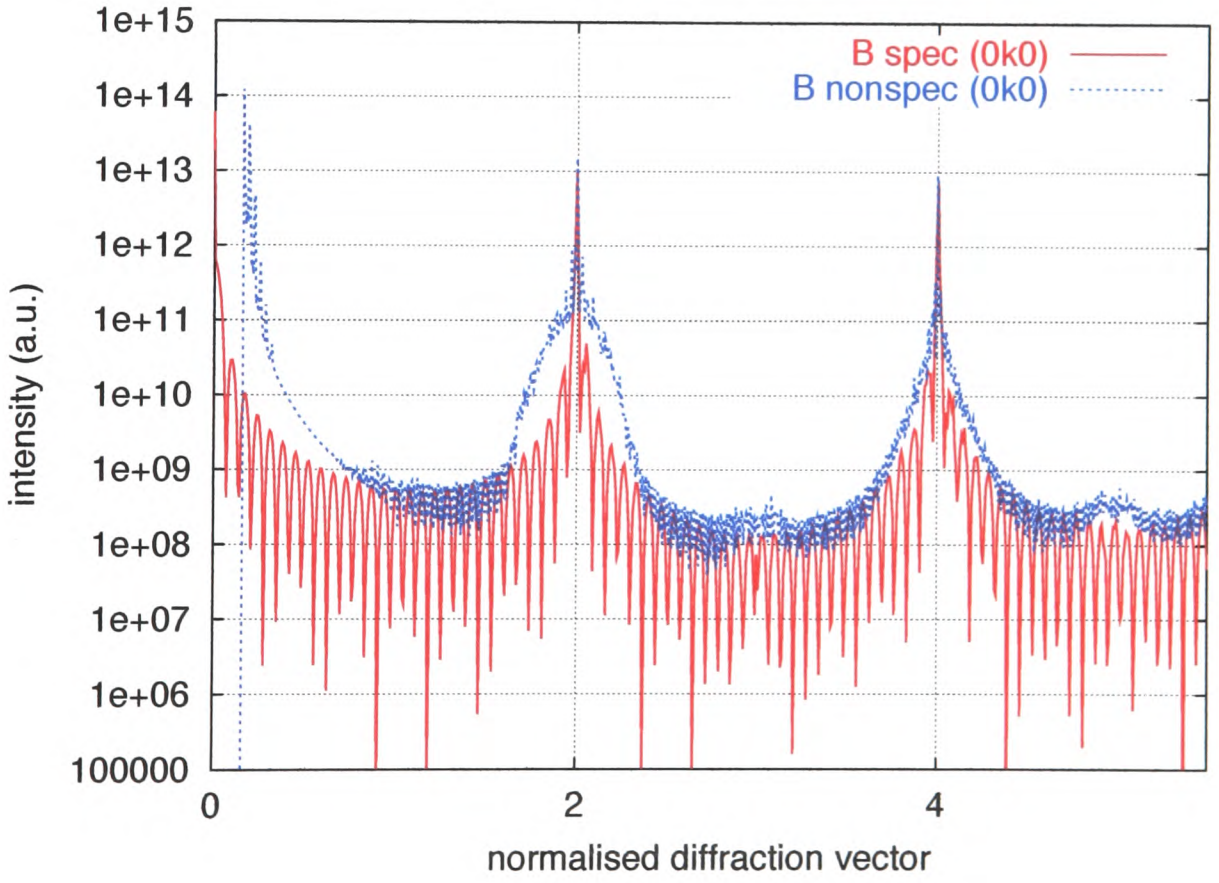


Figure 4.13: 1-D diffraction results from (h00) and (0k0) planes in MD simulation **B**. Although the position of the intensity peaks does not alter, their difference in breadth suggests a change in the crystal has taken place.

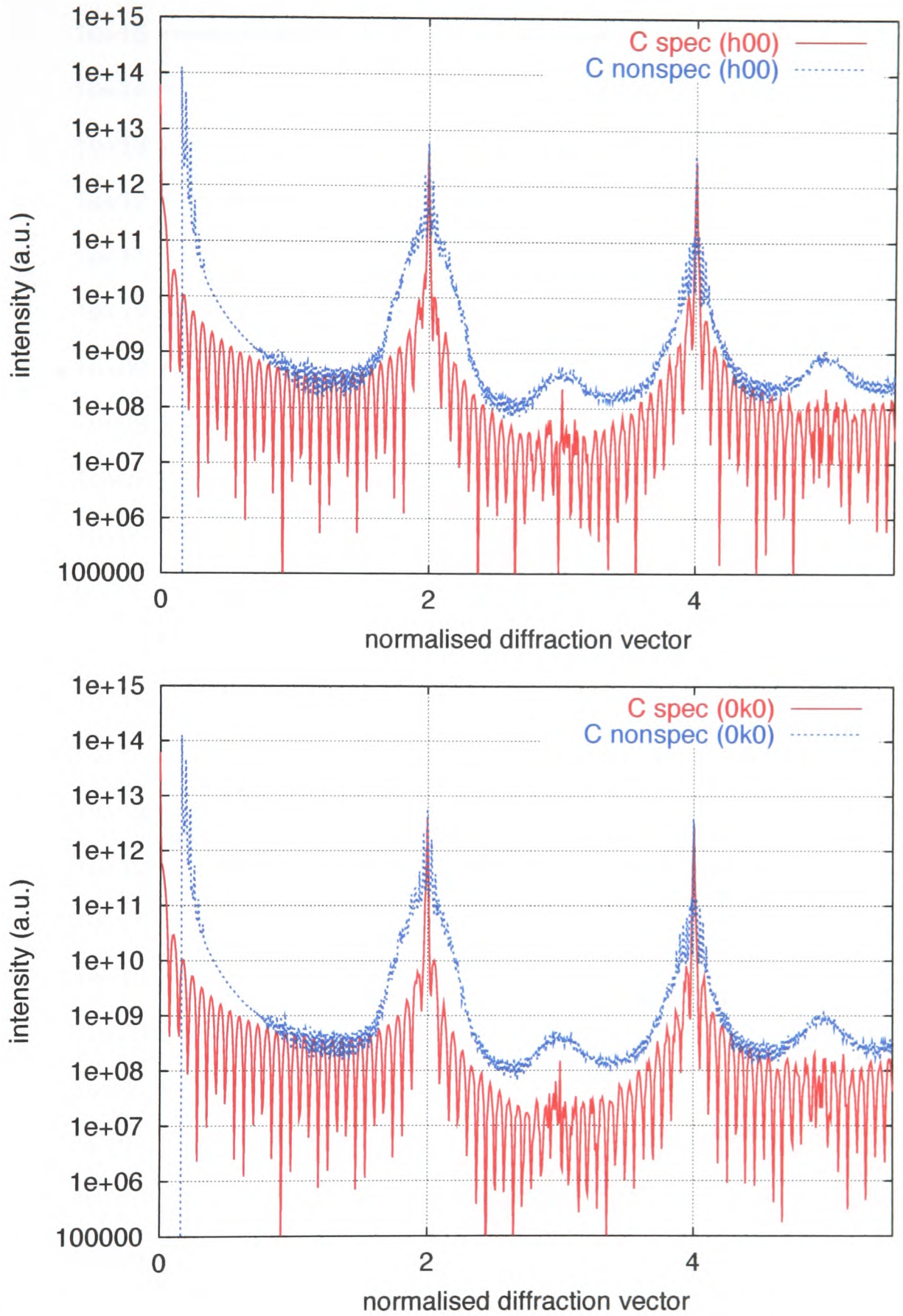
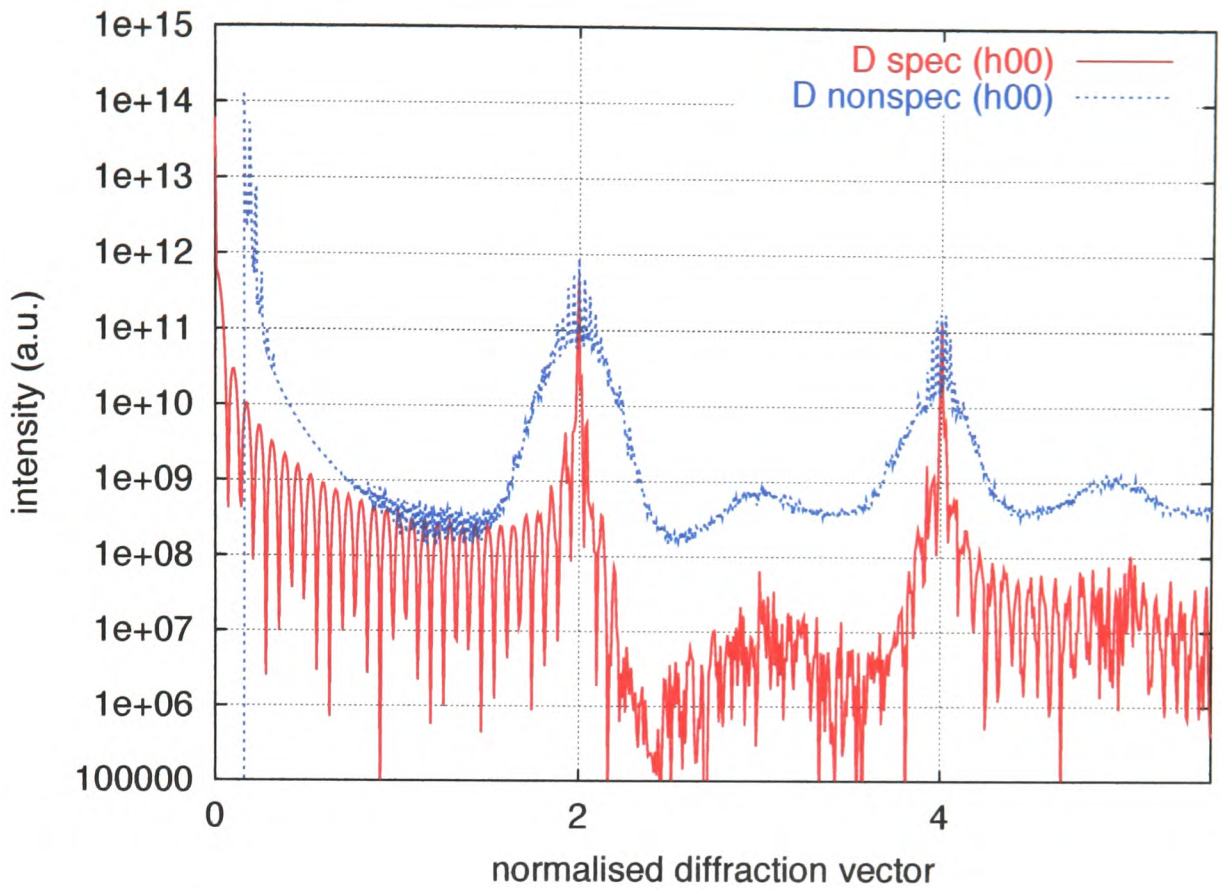


Figure 4.14: 1-D diffraction results from (h00) and (0k0) planes in MD simulation **C**. The peak breadth as depicted by non-specular diffraction, as well as the shape of the pattern between the principal diffraction peaks, indicate that a structural change in the crystal has taken place.



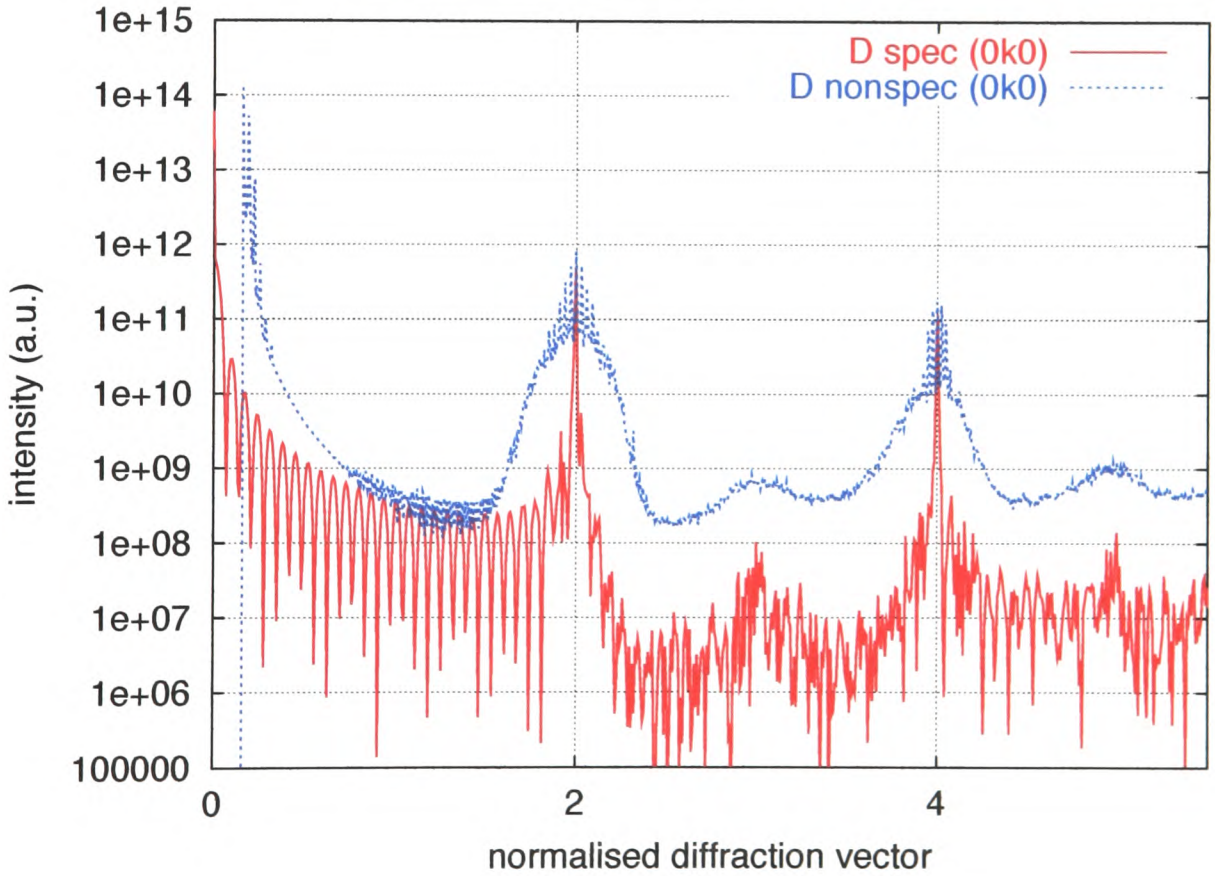


Figure 4.15: 1-D diffraction results from (h00) and (0k0) planes in MD simulation **D**. Further alteration of the X-ray diffraction pattern occurs; the principal peaks' intensities drop and their breadths increase.

2-D FT Results: Evidence of $\alpha-\epsilon$ Phase Change

A 2-D FT of the lattice was also performed on all four simulations. In order to map out a plane in the reciprocal space, two diffraction vectors have to be chosen. Vectors along $[1\bar{1}0]$ and [001] mapped out the original BCC (110) plane in the reciprocal space, and another set of vectors [110] and [001] mapped out the original BCC $(1\bar{1}0)$ plane (normal to (110) plane) in the reciprocal space. This was in order to verify that the (110) and $(1\bar{1}0)$ BCC planes transform into the (0001) HCP planes, thus proving the onset of the $\alpha-\epsilon$ phase transition according to eqn. (2.68). Figures 4.16 and 4.17 show the results.

In both figures, the patterns from the first simulation (**A**), which is not expected to have undergone a phase change, differ from those of the other three MD simulations (**B**–**D**). For comparison, a 2-D FT on a *perfect* BCC crystal in plane (110) was also performed, and is shown in Fig. 4.18.

For the perfect BCC crystal, the positions of the diffraction peaks along the [00l] direction are at -2 and 2, as expected. The pattern from the MD simulation **A** (Fig. 4.16 (a)–4.17 (a)) shows evidence of elastically compressed material. The diffraction peaks corresponding to shock-compressed crystal regions have been displaced from their original positions. As the unit cell in real space becomes smaller due to the compression along z, it expands correspondingly in k-space. A range of elastic strains can be seen, with the maximum of $7.0\pm0.5\%$ along z. This is in agreement with the previously obtained result from 1-D FT of $6.6\pm1.0\%$.

Post-processing of the remaining simulations **B**–**D** in both Fig. 4.16 and 4.17 shows hexagonal patterns in place of the original BCC (110) and $(1\bar{1}0)$ planes. Compared with 2-D post-processing of a perfect HCP crystal performed in plane (0001) (Fig. 4.19), it can be seen that the shape of the patterns, as well as their orientations, coincide. This proves that the $\alpha-\epsilon$ phase transition indeed occurs upon shock-compression of the material in the two equally preferred orientations. (In Fig. 4.19, the lower intensity peaks correspond to the weaker $(h0\text{–}h0)$, $(0k\text{–}k0)$, etc. reflections, and the higher intensity peaks correspond to the stronger $(hh\text{–}2h0)$, $(2h\text{–}h\text{–}h0)$,

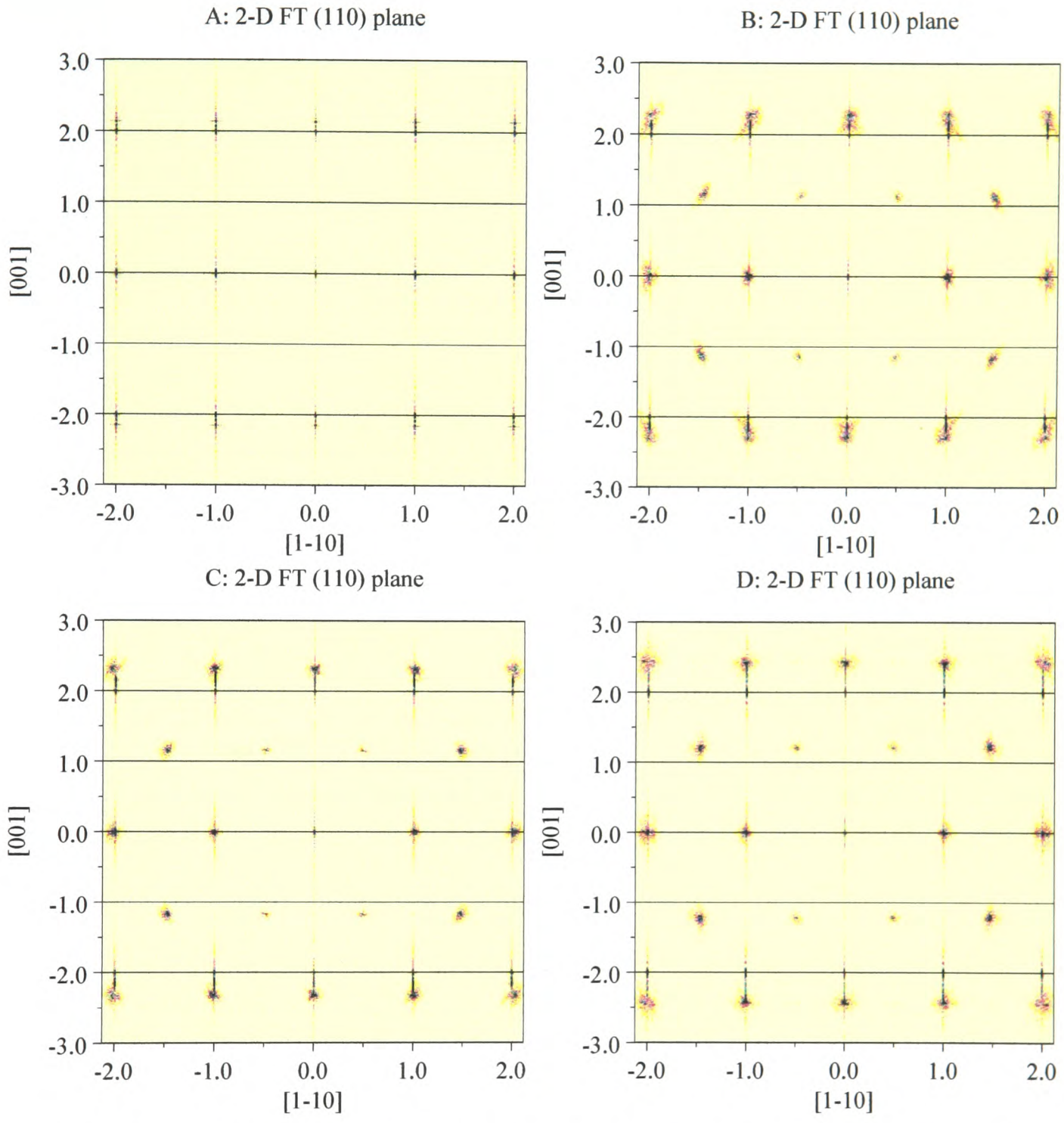


Figure 4.16: 2-D diffraction from (110) BCC planes in Iron MD simulations. Both $[1\bar{1}0]$ and [001] vectors are normalised. Elastically compressed simulation **A** does not display a hexagonal inverse lattice, whilst simulations **B** – **D** show a clear hexagonal basis in the original BCC (110) plane.

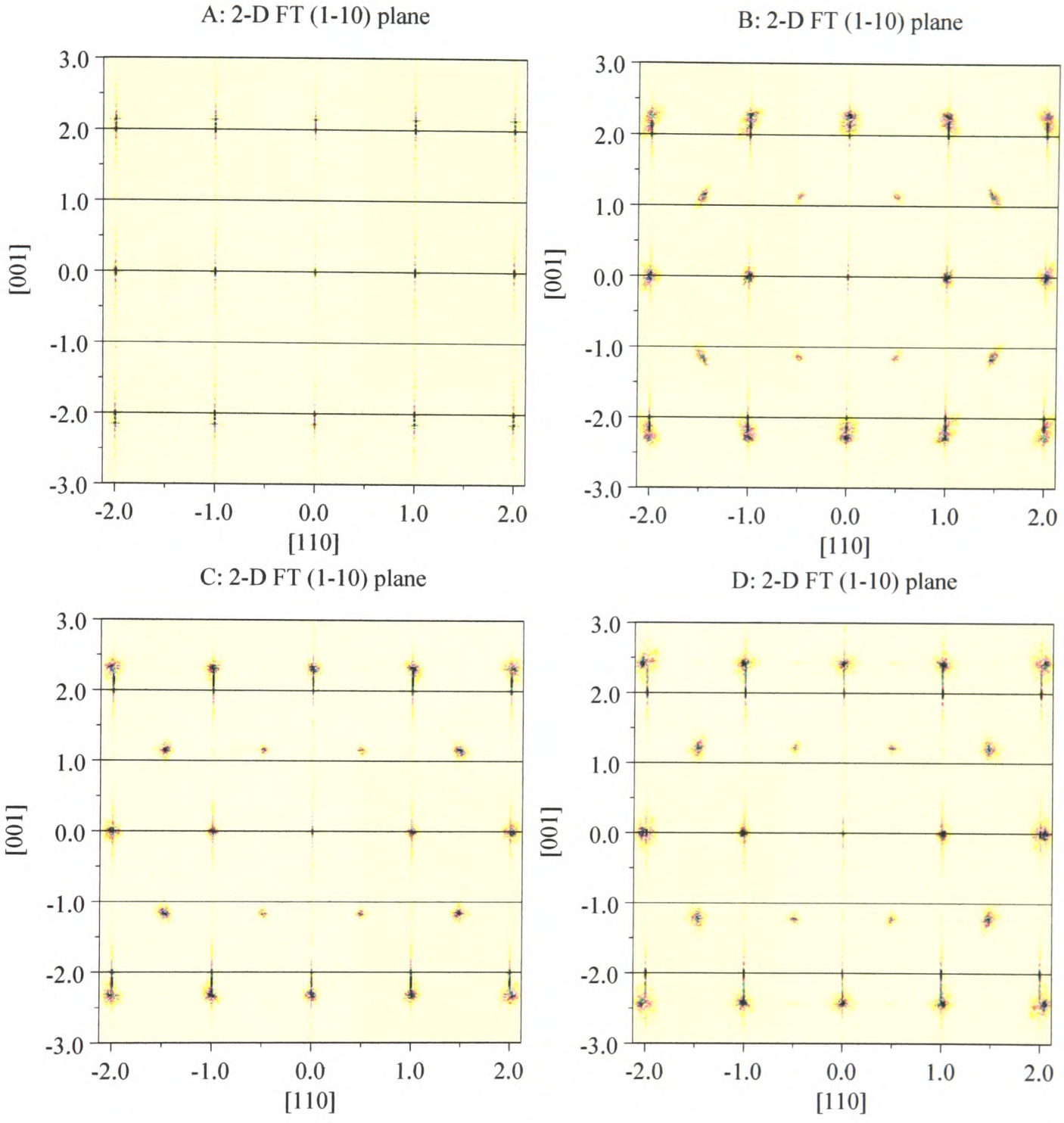


Figure 4.17: 2-D diffraction from $(1\bar{1}0)$ BCC planes in Iron MD simulations. [110] and [001] vectors are normalised. Patterns are analogous to diffraction results from orthogonal (110) planes, confirming the existence of two equally preferred orientations of the ϵ phase in Iron.

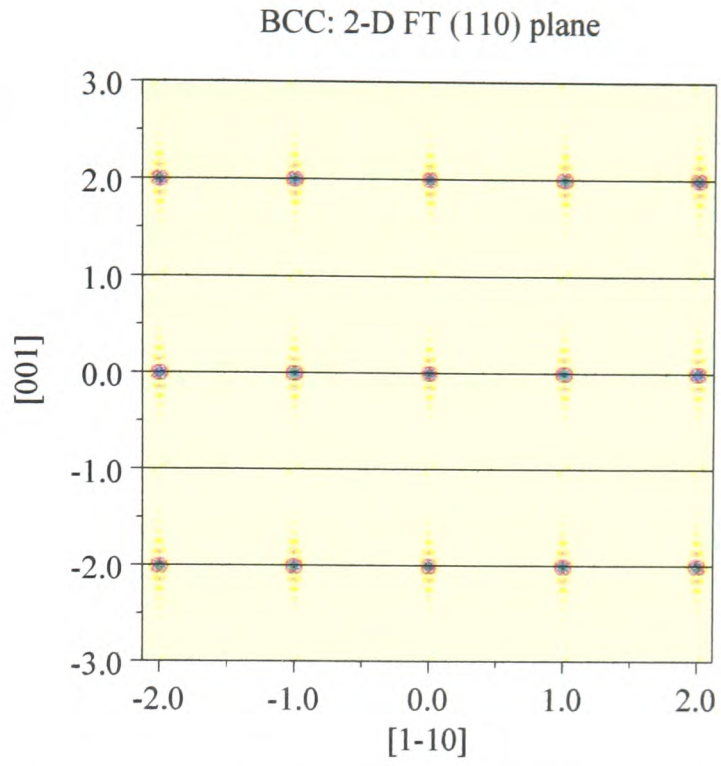


Figure 4.18: 2-D diffraction results from perfect BCC crystal. The secondary maxima surrounding the intensity peaks, sometimes called *Laue oscillations* [105], are due to the finite number of scattering planes the crystal. Axes are labeled as directions in a conventional cubic lattice.

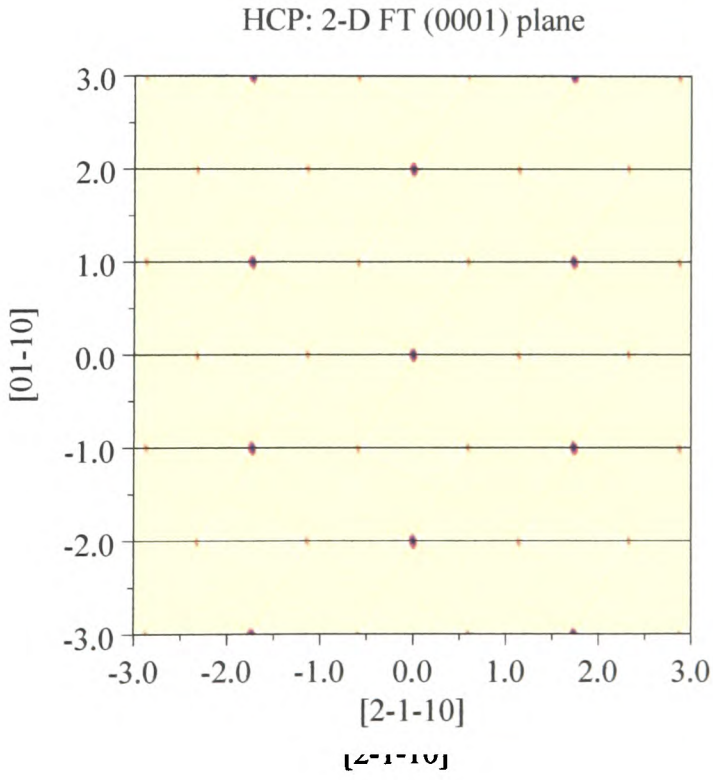


Figure 4.19: 2-D diffraction results from a perfect HCP crystal, depicting the (0001) plane in k-space. Axes are labeled as directions in a hexagonal lattice. The hexagonal pattern depicted in the inverse space is rotated by 30° with respect to the real space.

etc. reflections.)

Simulations **B** – **D** also show compression of the shocked crystal along [001]. Inferring the shifts of the peaks from their original positions gives compressions along the shock propagation direction of 11.5±0.5%, 13.8±0.5%, and 17.4±0.5% for simulations **B**, **C**, and **D**, respectively. In comparison with the BCC phase of the crystal, which was not compressed beyond $\sim 7\%$, the compression of the HCP phase clearly increases with pressure. The original BCC crystal compresses elastically up to the limiting threshold, above which no further uniaxial compression occurs. Rather, it undergoes a phase transformation, and the resultant HCP phase is further compressed, depending on the applied pressure.

Another important point which has to be stressed is the number of points per unit area in k-space, detected by the 2-D FT calculations presented above. The HCP phase has a two-atom basis, which means a doubling of the unit cell size in comparison with the BCC phase, which can be represented by a mono-atomic primitive unit cell. This doubling of the unit cell size corresponds to an increase, by a factor of two, of the number of points per unit volume in the inverse space of the new phase. It can be seen in Fig. 4.16–4.17, parts (b)–(d), that the number of points per unit area corresponding to the new phase is twice that corresponding to the original BCC phase. This effect is sometimes referred to as "*period doubling*". In Chapter 6, it will be seen that experimentally, this results in the detection of extra diffraction lines corresponding to the new phase.

Compression in directions [110] and $[1\bar{1}0]$ normal to the shock propagation direction was not detected, as was the case in 1-D diffraction analysis. No plasticity was therefore detected.

In order to confirm this result and achieve higher accuracy, detailed 3-D post-processing was performed, yielding tensile, shear, and volumetric strains of the crystals, and rotations of the principal planes.

3-D FT Results: Can We See Lateral Lattice Compression?

3-D FT post-processing was performed on three different sections in each MD simulation, so that together, they spanned most of each crystal sample along z. (With respect to the z axis, they were approximately centred on original unit cell positions 25, 75, and 125.) Their dimensions were chosen in such a way that the phase-changed regions were not mixed with the elastically compressed regions. Where possible, the segments were sized $50\times50\times50$ perfect BCC unit cells, although some segments were made shorter along z; this is detailed below. As before, they were selected from the centre of each simulation with respect to the x and y axes. This analysis is similar to the one applied to the Cu MD simulations (section 4.1). Second order X-ray diffraction calculation yielded the tensile and volumetric strains the samples were subjected to, as well as shear strains and rotations.

Table 4.3 summarises the results of the post-processing. The centroid of each segment with respect to the z axis is indicated in the second column. The following sections deviate in length (along z) from the standard cubic segment of $50\times50\times50$ BCC unit cells: the third section in simulation **A** spans 40 unit cells; the second section in **B** spans 40 unit cells; the third section in **C** spans 20 unit cells.

The results confirm that, within the errors, there is no evidence of lateral compression of the lattice in any of the four MD simulations. The inferred lattice compression values along the shock propagation direction are in agreement with those inferred from the 1-D and 2-D FT analyses above, the 3-D results are, however, more accurate. Comparison of the volumetric compression inferred from the X-ray diffraction post-processing with the rise in the atomic density in each segment shows very good agreement between the two results.

The apparent lack of plasticity in Iron under shock conditions in the given pressure range is remarkable. It is interesting to recall that simulated single crystal Copper under similar conditions (piston pressure 50 GPa, time-scale of MD simulation < 10 ps) analysed in section 4.1.1, underwent a lateral compression of $\sim 3.5\%$ and compression along the shock propagation direction of $\sim 10.3\%$. On the other

hand, a pressure of $> 50\,\mathrm{GPa}$ applied to Iron resulted in a uniaxial compression of $\sim 7\%$ of the parent phase, and a phase transformation.

Recalling the Orowan eqn. (2.67), it is clear that the plastic strain rate is directly related to the mobility of the dislocations generated in a material. Extrapolating the data from Fig. 2.15, one can see that the dislocation velocities in Copper induced by shear stresses in the range 10–100 GPa, are $\sim 10^6\,\mathrm{mm\,s^{-1}}$. Taking the magnitude of the Burgers vector as b=2.56 Å [70], and the mobile dislocation density as $\rho_m = 3\times10^{12}\,\mathrm{cm^{-2}}$, as calculated in section 4.1.3, yields the time-scale on which a plastic deformation of Copper is expected to take place as $\sim$10–100 ps. This is in agreement with the results inferred from the large MD simulation analysed in section 4.1.3.

Iron and other BCC metals differ from Copper, in that stacking faults have never been observed in them [56]. Nevertheless, experimental evidence exists that screw dislocations are generated in Iron by shock wave passage even at pressures below the $\alpha-\epsilon$ transition threshold of $\sim 13\,\mathrm{GPa}$ [11]. The apparent lack of plasticity found in the post-processing analysis shown here suggests that their mobilities, and hence their mean velocities, are too low for any plastic flow to occur on picosecond time-scales probed by the MD simulations.

The results of X-ray diffraction post-processing performed on these four MD simulations were compared with the density rise in other, similar MD simulations performed by collaborators at LANL [6]. Figure 4.20 shows the increase in the density of the crystal as a function of the applied pressure, as inferred from the X-ray diffraction results of the four MD simulations studied here, as well as calculated directly in a number of MD simulations of shock-compressed single crystal Iron for a range of pressures. Excellent agreement is reached.

Table 4.3: Tensile and volumetric strains inferred from second order 3-D FT calculations performed on all four MD simulations of shocked Iron. Error values (%Δ) in the sixth column refer to the standard deviations on each of the strains inferred in the three principal directions, x, y, and z. Error values (%ΔV) in the eighth column refer to the combined error on the volumetric strain values.

MD	z position	% x	% y	% z	%Δ	% volume	%ΔV	% density rise
A	25	0.0	0.0	6.8	$\pm$0.1	6.8	$\pm$0.3	7.4
A	75	0.0	0.0	6.8	$\pm$0.1	6.8	$\pm$0.3	6.5
A	120	0.0	0.0	6.8	$\pm$0.1	6.8	$\pm$0.3	7.0
B	25	0.3	0.5	11.1	$\pm$0.3	11.9	$\pm$0.9	10.8
B	70	0.1	0.1	10.9	$\pm$0.3	11.0	$\pm$0.9	10.0
B	120	0.0	0.0	6.6	$\pm$0.1	6.6	$\pm$0.3	6.6
C	25	0.0	0.1	13.6	$\pm$0.2	13.8	$\pm$0.6	14.0
C	75	-0.1	-0.3	14.0	$\pm$0.2	13.7	$\pm$0.6	13.8
C	130	0.0	0.0	7.1	$\pm$0.1	7.1	$\pm$0.3	7.0
D	25	-0.1	-0.3	17.7	$\pm$0.3	17.3	$\pm$0.9	18.0
D	75	0.3	-0.4	17.5	$\pm$0.3	17.4	$\pm$0.9	17.4
D	125	-0.0	-0.2	17.3	$\pm$0.3	17.1	$\pm$0.9	17.3

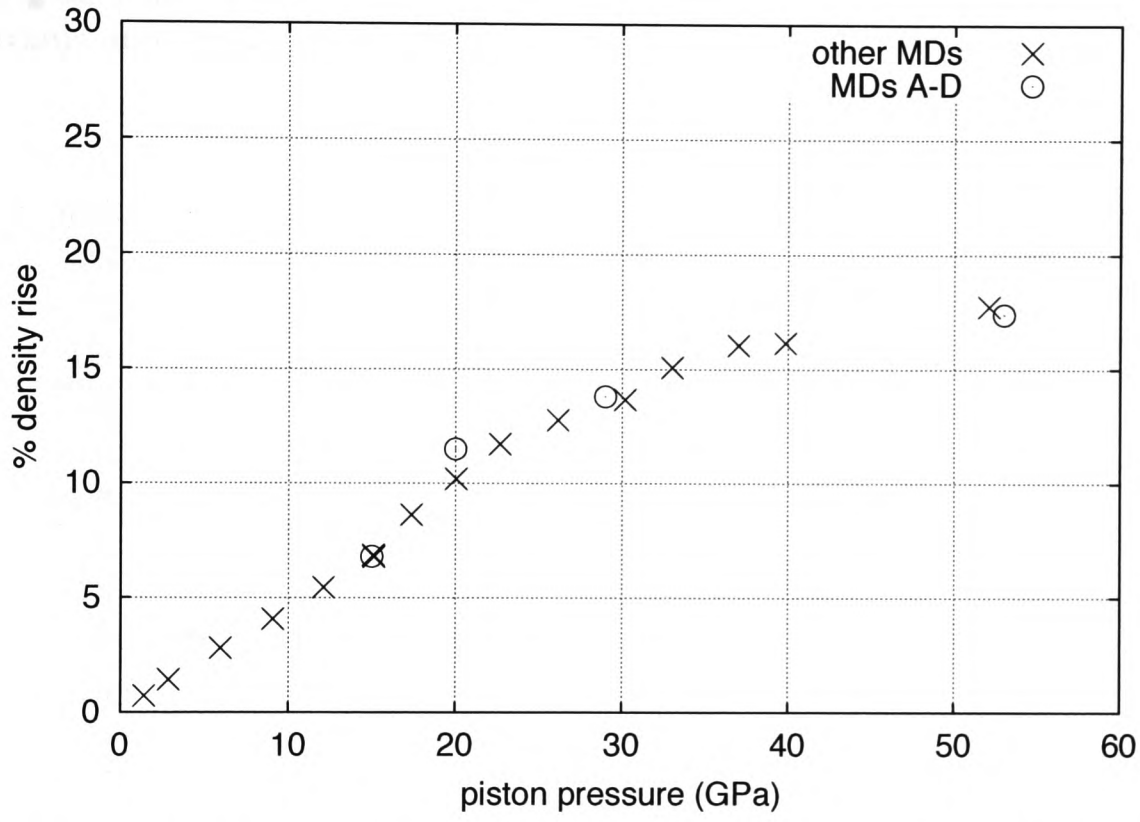


Figure 4.20: Rise in atomic density in MD simulations, calculated for a range of pressures by collaborators at LANL [6], compared with 3-D FT results from simulations **A** – **D**. Excellent agreement is reached. (For simulations **B** – **D**, the plotted density increase is for the phase-transformed regions only.)

Plane Shears and Rotations

The shear strains and rotations that the xy, zx, and yz planes were subjected to due to the passage of the shock wave were also calculated, and are shown in Table 4.4. As before, no planar shear or rotation is expected merely as a consequence of the shock wave passage.

Table 4.4: Shear strains and rotations of three principal crystal planes, in degrees, inferred from 3-D FT calculations of MD simulations of shocked Iron. The error on both strains and rotations, in degrees, is ± 0.1.

		shear strain			rotation		
MD	z position	xy plane	zx plane	yz plane	xy plane	zx plane	yz plane
A	25	0.0	0.0	0.0	0.0	0.0	0.0
A	75	0.0	0.0	0.0	0.0	0.0	0.0
A	120	0.0	0.0	0.0	0.0	0.0	0.0
B	25	0.1	0.0	0.0	-0.3	0.2	-0.1
B	70	0.0	0.0	0.0	-0.2	-0.1	0.1
B	120	0.0	0.0	0.0	0.0	0.0	0.0
C	25	0.1	-0.1	0.1	-0.3	0.1	-0.1
C	75	0.0	0.0	0.0	0.1	0.0	0.1
C	130	0.0	0.0	0.0	0.0	0.0	0.0
D	25	-0.3	0.0	0.1	0.1	0.1	0.1
D	75	-0.1	0.1	0.1	0.4	-0.1	-0.1
D	125	0.1	0.0	0.0	0.1	0.0	0.0

It can be seen that the crystal planes of elastically compressed BCC material (all of MD simulation **A**, section centred at z=120 of simulation **B**, and section centred at z=130 of simulation **C**) display no shear strain or rotations. This is expected, since uniaxial elastic compression is reversible, and causes relatively little perturbation to the crystal.

Some shear strains and rotations were detected for crystal regions which underwent the phase change. No general trend could be detected, as the values vary between different crystal regions within a single MD sample. It is believed that detailed X-ray diffraction analysis of larger sections of the MD simulations, as well as

a similar study of other MD simulations of shocked Iron, would reveal any possible trend as a function of increasing pressure.

4.3 Summary

This chapter presents detailed X-ray diffraction post-processing of MD simulations of shocked single crystals of Copper and Iron.

The post-processing analysis showed that temporally and spatially small (i.e. spanning $\leq$10 ps and $<$0.1 μm) MD simulations of *perfect* Cu do not adequately model the processes occurring in real experimental samples under shock conditions on nanosecond time-scales. The compression of the crystal along the shock propagation direction was found to be approximately three times larger than that along the two lateral directions, despite the high concentration of dislocations found in the crystal. This finding did not agree with experimental results, which indicated a hydrostatic-like behaviour of shock-compressed Copper on nanosecond time-scales [7].

This led to the generation of new MD simulations, with both temporal and spatial scales increased by over an order of magnitude. They also incorporated realistic features, such as pre-existing defects, and a finite ramp on the induced shock wave. X-ray diffraction post-processing presented in this chapter has shown that more hydrostatic-like compression of the crystal was reached, leading to a better agreement with experimental results. The finite ramp on the shock wave meant that the regions containing pre-existing defects were activated at their lower threshold pressures, readily producing new dislocations. These were more mobile than dislocations in previously perfect crystal regions, thus enabling successful shear stress alleviation, which leads towards a 3-D compression of the crystal lattice. The dislocation densities measured in the regions containing these defects were approximately three times lower than those in the previously perfect crystal regions, proving that it was the mobility of these lower-concentration dislocations which resulted in a better 3-D compression. The lattice compression along the shock propagation direction was only $\sim$1.3 times larger than that along the two lateral directions.

Additionally, it was found that X-ray diffraction enables the calculation of dislocation densities in various crystal regions, by comparing the results from the second and fourth diffraction orders. Identifying a possible method of experimental measure-

ment of dislocation densities in crystals during shock loading is of high significance. The generation and subsequent movement of dislocations in crystals subjected to a shock wave are key to the plastic yield of the lattice, resulting in its 3-D, or near-3-D, compression. To date, no experimental results exist which would quantitatively determine the concentration of dislocations in a crystal under shock loading. This finding therefore opens up new possibilities for experimental X-ray diffraction to clarify one of the most fundamental and pressing questions remaining in shock wave physics.

The post-processing also provided information about the rotations and shear strains the lattice was subjected to as a consequence of shock wave passage through it.

X-ray diffraction post-processing of MD simulations of shock-compressed single crystals of Iron has verified the modelling of the important $\alpha-\epsilon$ phase transition. Shock-compression of the lattice along the [001] direction was shown to lead to the onset of the HCP (ϵ) phase in Iron when the threshold pressure of $\sim 15\,\text{GPa}$ was exceeded.

In the MD simulations where the $\alpha-\epsilon$ phase transition was found, the applied piston pressure ranged between $\sim$ 20–53 GPa, with the resultant uniaxial compression of the new phase ranging between $\sim$ 11.5–17.3$\pm$0.9%. Uniaxial elastic compression of the parent BCC phase was also detected, ranging between 6.6–7.1$\pm$0.3%. Furthermore, 3-D FT analysis showed no lateral compression of the parent phase in the given pressure range, indicating that plastic deformation in Iron does not occur on time-scales below $\sim 10\,\text{ps}$. It is assumed that conducting and analysing MD simulations of longer temporal dimensions would clarify whether the onset of plasticity in Iron occurs at later times.

Detailed 2-D FT analysis confirmed that the ϵ phase occurs in two different orientations: both (110) and $(1\bar{1}0)$ planes of the BCC phase transform into the (0001) planes of the new HCP phase.

Chapter 5

Vulcan and OMEGA Experiments

This chapter provides a description of the experimental work conducted for this thesis. X-ray diffraction experiments were carried out in the Vulcan laser facility at the Rutherford Appleton Laboratory, and in the OMEGA laser facility at the University of Rochester, USA. The laser parameters, beam geometry, targets, target set-up and diagnostic methods are detailed separately for each of the two laser facilities used.

5.1 Vulcan Laser System

Vulcan is one of the high power lasers operated by the UK Central Laser Facility at the Rutherford Appleton Laboratory. It is an eight-beam Nd:Glass laser system capable of delivering up to 2.6 kJ of laser energy in nanosecond pulses at its fundamental wavelength of 1054 nm. Frequency conversion to the second harmonic can give an energy of 1 kJ at a wavelength of 527 nm. The Vulcan laser delivers beamlines into three separate target areas: Target Area West (TAW), Target Area East (TAE), and the new Target Area Petawatt (TAP). The pulse lengths available. in various geometries, are in the range of 500 fs and 5 ns. Sub-picosecond pulses achieved using the Chirped Pulse Amplification technique are available in TAW and TAP [106]. The highest attainable intensity delivered in TAP is $\sim 10^{21}\,\mathrm{Wcm}^{-2}$, which is equivalent

to 500 J in a 500 fs laser pulse with a spot size of $\sim 10\,\mu$m.

The experiment described in this chapter was carried out in TAE. The Vulcan laser is capable of delivering up to eight beams into this target area. They are commonly referred to as the "*main six*", and beams 7 and 8. The main six use one oscillator and rod amplifier chain, and beams 7 and 8 (also called the backlighter beams) use a separate oscillator. The main six can, but need not, use the same seed pulse as 7 and 8. For the experiments presented in this thesis, a single seed pulse was used for all eight beams. The final stage of beam amplification takes place in the disc amplifiers. The diameter of the main six upon exiting the final disc amplifiers is ~ 110 mm. The final diameter of beams 7 and 8 is ~ 150 mm.

On a full-shot experiment, the repetition rate of the Vulcan laser is a maximum of three pulses per hour. This is because it takes approximately 20 minutes for the system to cool down sufficiently to allow the next pulse to be generated without any risk of optics damage. As the Vulcan laser facilitates experiments in two target areas, for two simultaneously running experiments, the repetition rate per target area on full laser shots is 40 minutes.

Vulcan users are responsible for the beam alignment and target set-up of the experiments; this gives one the flexibility to use as many of the available beams as necessary and in the most advantageous arrangement.

5.1.1 Beam Geometry and Set-up in TAE

Up to three of the main six beams were frequency-doubled (λ=527 nm) in this experiment, and used in a cluster geometry to drive the backlighter. The X-rays generated were used as a diagnostic. Between two and three of the main six beams were used per shot. The beams were chosen according to the quality of their profiles (as determined on burn shots) and the favourability of their orientation with respect to the position of the backlighter.

The remaining two beams available (7 and 8) were used to drive the crystal, i.e. to create a shock. They were set up in such a way that beam 7 was driving the

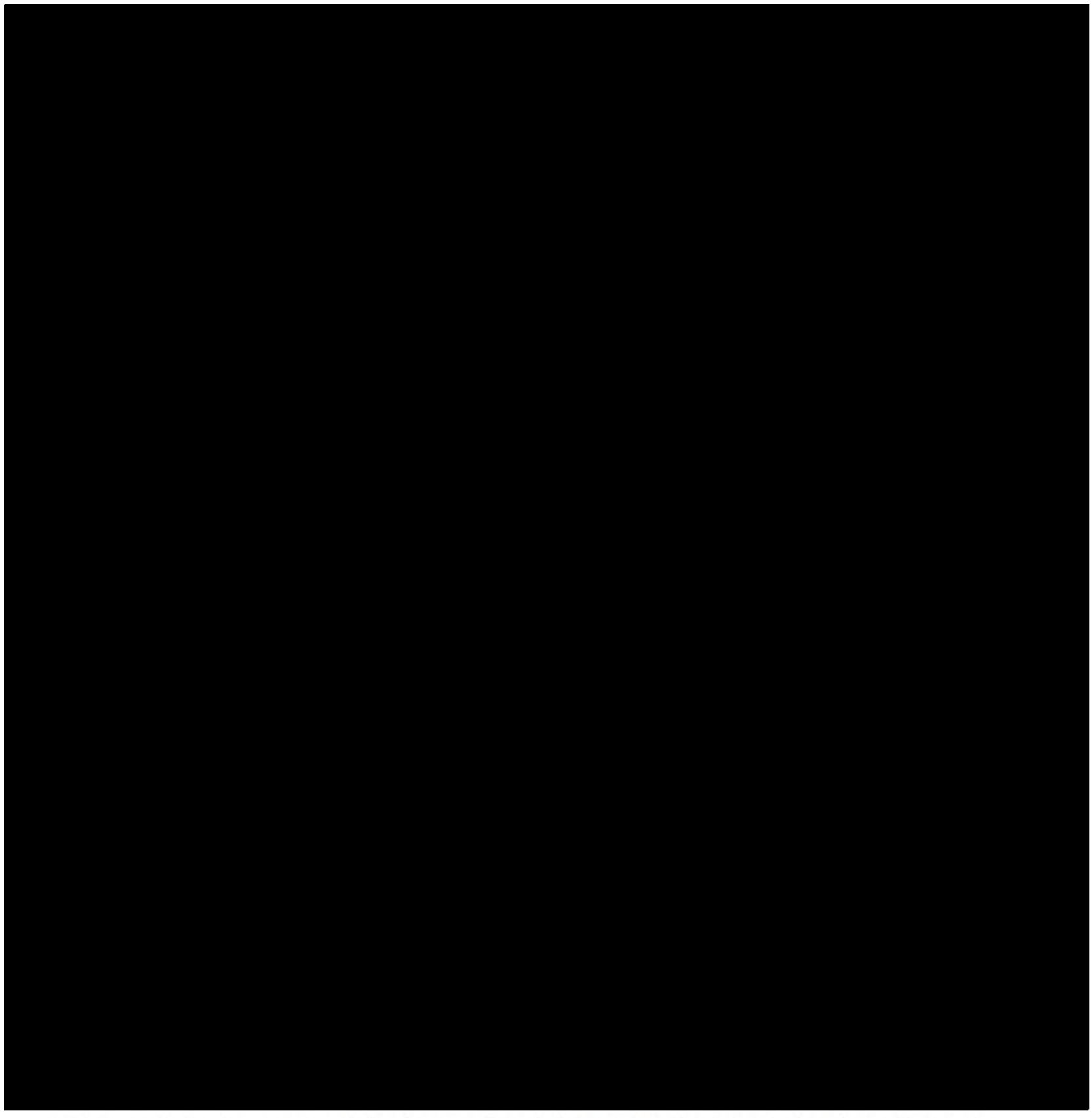


Figure 5.1: Arrangement for beams 7 and 8 to enter the target chamber. Beam 7 enters via an upper port, and beam 8 enters via a side port.

front side of the crystal (the side from which X-rays were diffracted) and beam 8 was driving the rear side of the crystal. Beams 7 and 8 could be used either separately or simultaneously. The most successful shots were those for which the driven side of the crystal was the rear side (i.e. only beam 8 was used). Each shocking beam pulse had a 100 ps linear rise-time, a 1.8 ns long constant intensity duration, and a 100 ps linear fall-time, effectively forming a 2 ns pulse. The fundamental wavelength of 1054 nm was used. The energy of the shocking beams was in the range 20–30 J. The beams were defocused to a spotsize of ~ 3 mm in order to illuminate the whole of the crystal.

Beam 8 entered the vacuum chamber through a side port. In order not to interfere with the diagnostics and the alignment system in the chamber, beam 7 was made to enter the chamber from a top port. This arrangement is shown in Fig. 5.1.

For diagnostic purposes, a delay was introduced between the shocking beams and the backlighter-driving beams. To determine the delay length, it was necessary to consider whether an unshocked, as well as a shocked, region of the crystal should be probed, and how far the shock should have propagated within the crystal at the time when the X-rays diffracted from it. The crucial factors were the crystal material and thickness (if shocked on its rear side). For the crystals used in this experiment, the delay of the probing beam with respect to the shocking beams (as measured from the leading edges of their respective pulses) was between 1.7–4.0 ns.

5.2 Targets for Vulcan

The targets used in these experiments all consisted of two parts: a backlighter and a crystal. A schematic diagram of the target is shown in Fig. 5.2.

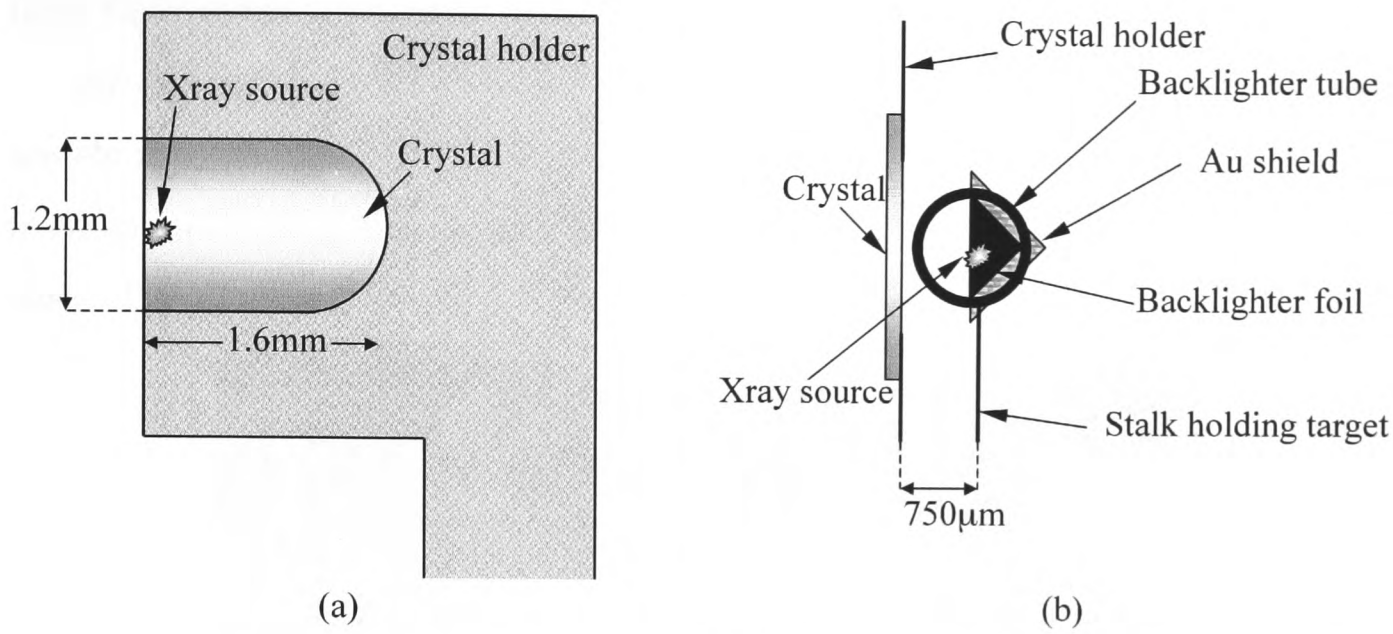


Figure 5.2: A schematic diagram of the Vulcan target assembly. View normal (a) and parallel (b) to the plane of the crystal. The sparkle indicates the approximate position ($\sim 750\,\mu$m from crystal surface) of the X-ray source, generated by the laser beams incident on the backlighter foil.

The crystals were cut 3×3 mm in size, with thicknesses varying from 10 to 30 μm. Each was mounted in an Aluminium holder, which allows an area of $\sim 1.2\times1.6$ mm of the crystal to be probed.

The backlighter consists of a cylindrical tube made of a Silver-Palladium alloy, with an outer diameter of 1000 μm and an inner diameter of 800 μm and a length of 1000 μm, open at each end. A backlighter foil is attached at one end. The foil is an equilateral triangle with a 1000 μm base and a 500 μm height. The base of the triangular foil vertically bisects the end of the cylindrical tube. The backlighter-driving beam enters the tube through the other (open) end, and hits the foil, thereby creating a plasma.

The positioning of the backlighter with respect to the crystal is such that the edge of the cylindrical tube is in line with the edge of the crystal. The end of the tube

with the backlighter foil attached to it is closer to the crystal, and the focal point of the backlighter-driving beams is approximately 750 μm from the crystal surface, as illustrated in Fig. 5.2.

To prevent a direct exposure of the detectors by X-rays, a semi-conical, 25 μm thick Gold shield is attached at 45° with respect to the tube.

For the purposes of the target alignment, the crystal and backlighter were separately mounted, each having three independent, mutually perpendicular degrees of freedom on the alignment stage. This allowed sufficient flexibility on a shot-to-shot basis. The photograph in Fig. 5.3 shows this arrangement.



Figure 5.3: Two components of the target in their separate mounts in the target alignment stage: the crystal is held in the left-hand-side mount, and the backlighter is mounted on a stalk in the right-hand-side mount. One of the three cameras used for the alignment is seen in the background.

Detailed photographs of the targets can be seen in Fig. 5.4.

In order to improve the shock stability within the crystal, the targets were coated with a 300 Å layer of Aluminium and a 1 μm layer of CH plastic, as shown in Fig. 5.5. This arrangement was pioneered by Wark *et al.* in the late 1980's, before very high intensity lasers were available [38,39,53]. The laser irradiation incident on the target



Figure 5.4: Detailed photographs of the target (clockwise from top left): (1) Crystal and backlighter target assembly with crucial parts labeled. The slanted edges of the crystal mount minimise the shadow of the mount on the detector. (2) A magnified image of the backlighter tube as seen on a monitor used for alignment. The crystal, held in its mount, is seen on the left side of the monitor. The cross marked on the screen indicates the position of the focal spot of the backlighter beams. The correct position of the crystal is also drawn on the screen for reference. (3) View at an angle; the backlighter tube, through which the X-ray generating laser beams enter, is clearly seen. (4) View at an angle; a reflection of the backlighter from the crystal surface can be seen.

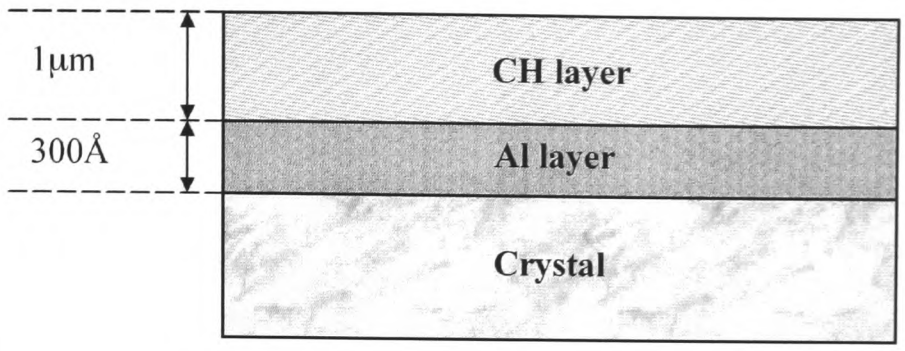


Figure 5.5: Coatings on the crystal targets used for the Vulcan experiment. Shock is created by laser produced Al plasma, which is driven into the crystal. The plastic layer provides confinement for better shock stability.

creates an Aluminium plasma, which becomes confined between the plastic and the crystal. The plasma then expands and this drives the shock into the crystal. This arrangement improves the shock strength and stability even for relatively low incident laser intensities.[1]

For most of the shots, a varied shock pressure profile on the crystal was generated. This is achieved by placing two types of filter in the near field of the beam, thus blocking a certain proportion of the incident laser energy. Such a stepped shock profile is used to compare the extent to which varying shocking pressure distorts the crystal. The region in the crystal which remains unshocked provides a diffraction pattern from an unperturbed lattice. This is used as a reference. The relative intensities at the target are shown in Fig. 5.6.

[1]It will be shown later that a different, more desirable arrangement can be chosen when laser intensity is not the limiting experimental factor.

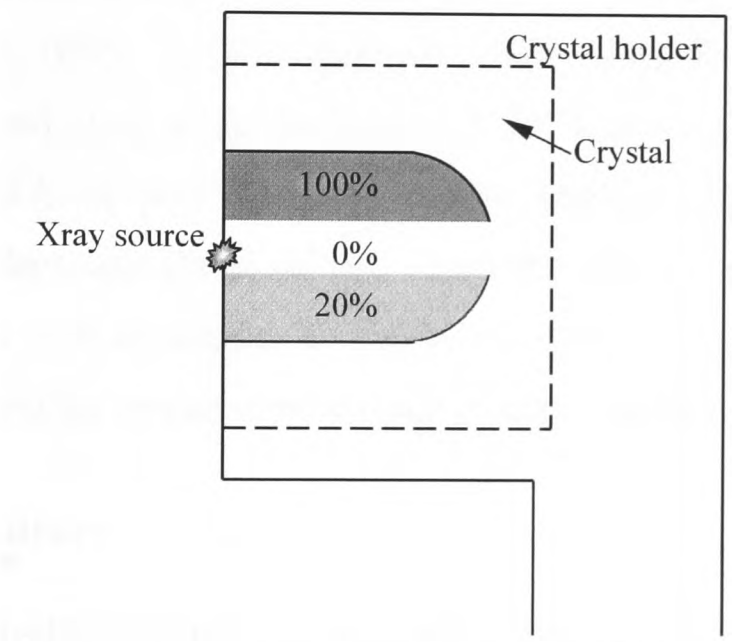


Figure 5.6: Schematic diagram of the shock intensity profile incident onto the crystal, showing the outline of the crystal holder and the location of the backlighter. The central part of the crystal remained unshocked, whilst the top and bottom parts were shocked with 100% and 20% of the shocking beam energy, respectively.

5.3 X-Ray Generation

The beams chosen to drive the backlighter were focused using f/10 lenses to a tight focal spot ($\sim 150\,\mu$m in diameter) onto the backlighter foil in the cylinder. Their combined energy was up to 200 J in the green, and the pulse length was 1 ns. This is equivalent to up to $\sim 10^{15}\,\mathrm{Wcm}^{-2}$ irradiance on the target.

When a laser pulse of such intensity hits a metal target, a high temperature (up to 1 keV) plasma is created, consisting of electrons and Helium-like ions (with two innermost electrons remaining). Such a laser-produced plasma is a bright source of line X-ray radiation [107]. In this experiment, 5 μm thick Copper and Iron backlighter foils were used, generating Cu lines at 1.478 Å and 1.485 Å, and Fe lines at 1.8503 Å and 1.8553 Å. In each case, the two wavelengths correspond to the transitions between the electronic states $1s^2\,{}^1S_0$ – $1s2p\,{}^1P_1$ and $1s^2\,{}^1S_0$ – $1s2p\,{}^3P_1$. This is referred to as the L → K transition, or the "He-α" lines.

The X-ray generating beams were smoothed using random phase plates.

5.3.1 X-Ray Filters

To protect the diagnostics from X-ray backlighter radiation of unwanted X-ray wavelengths, thin metallic foil filters were placed inside the film-packs. The material and thickness used depended on the backlighter material and on the X-ray intensity generated by the backlighters. Figure 5.7 shows wavelength dependence of X-ray transmission in the four different materials that were used as filters [108]. Iron and Copper He-α wavelengths [109, 110] are also indicated.

It can be seen that Copper and Iron are transparent to the He-α lines of their respective elements, but they attenuate X-rays of shorter wavelengths. Copper and Iron filters were therefore used as primary filters for shots with backlighter made of the same material, to block out harder X-rays. Nickel and Titanium were used as additional filters to reduce the overall X-ray intensity incident on the diagnostics. Filter thicknesses used were 7.5 and 15 μm Ni, 12.5 and 25 μm Ti and Fe, and $\sim 25\,\mu$m Cu tape.

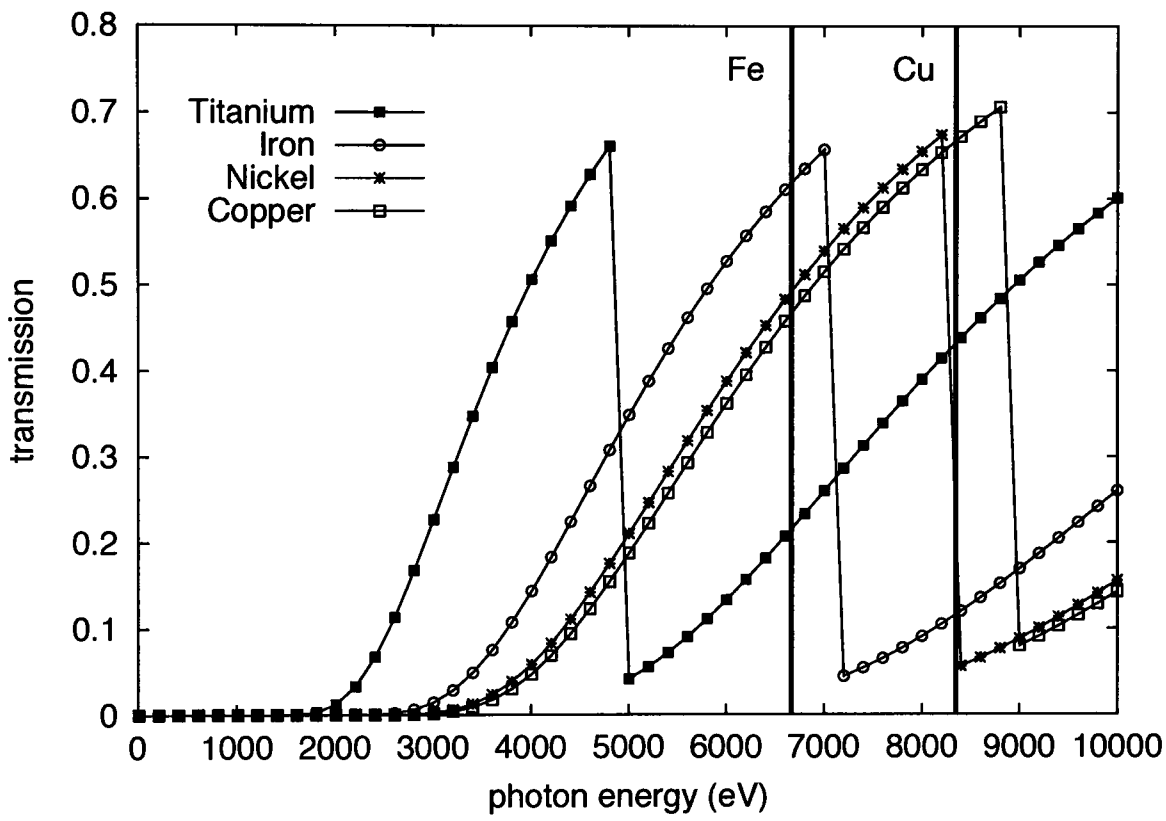


Figure 5.7: Transmission of radiation through 10 μm of material. The two vertical lines indicate the positions in the spectrum of Fe and Cu He-α doublets.

5.4 Diagnostics for Vulcan

5.4.1 Wide-Angle Film Detector

The primary diagnostic used in the experiments conducted for this thesis was a novel film-based wide-angle detector developed to collect X-rays diffracted from multiple lattice planes of a crystal [47, 48]. A diagram of the target and the film-pack, as arranged inside the target chamber, is illustrated in Fig. 5.8.

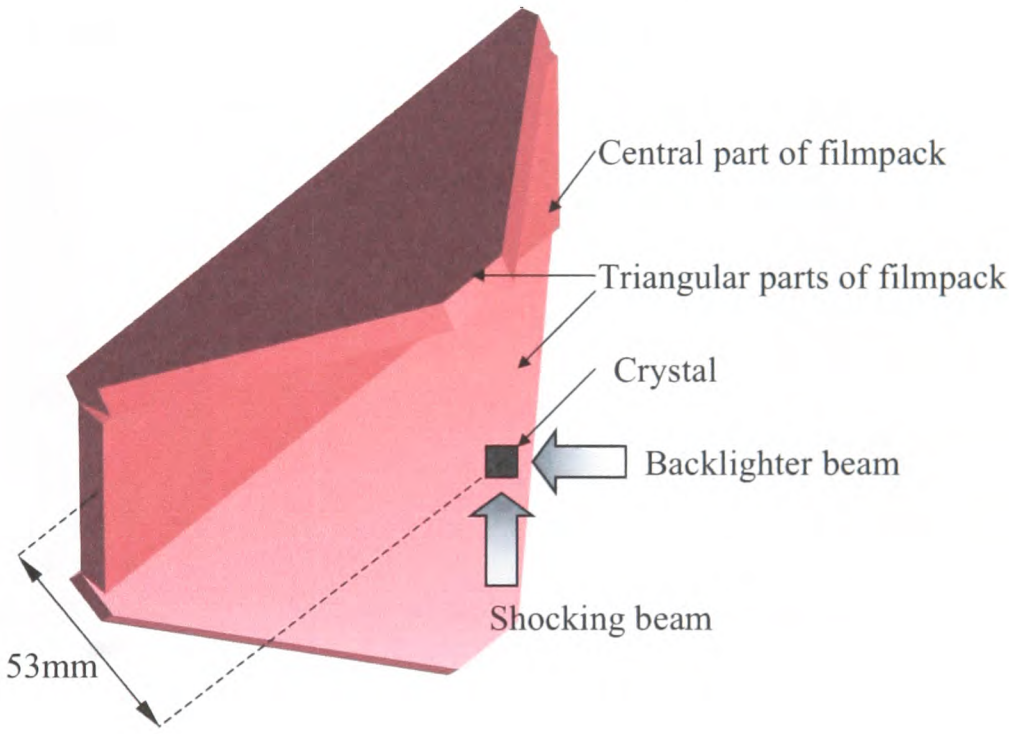


Figure 5.8: A schematic diagram of the film-pack diagnostic and the crystal target. The film-pack subtends an angle of 90° horizontally and 180° vertically at the crystal.

The detector consisted of three separate parts: one rectangular one (71×142 mm), and two triangular ones. The two equilateral triangles with a base of 142 mm and a height of 71 mm were bolted to the sides of the rectangle. When aligned in the target chamber, the entire assembly of the filmpack covered approximately π steradians of solid angle from the crystal, i.e. $\sim 90°$ in the horizontal direction and $\sim 180°$ in the vertical direction. The three film planes were all at a distance of ~ 53 mm from the target chamber centre where the crystal was placed. Each film-pack component consisted of a front and a rear part. When assembled together, they provided a

light-tight cover for the X-ray sensitive diagnostic inside.

Each film holder was covered with a 0.75 mm thick Beryllium light shield used to prevent any optical wavelengths from reaching the detector, whilst remaining X-ray transparent. For the Vulcan experiments, the film-packs were covered with an extra 20 μm layer of mylar and 6 μm of aluminised mylar to protect the film from stray laser light and the Be shield from target debris. The Al-mylar was replaced after every shot. The layers of filtering used are shown in Fig. 5.9.

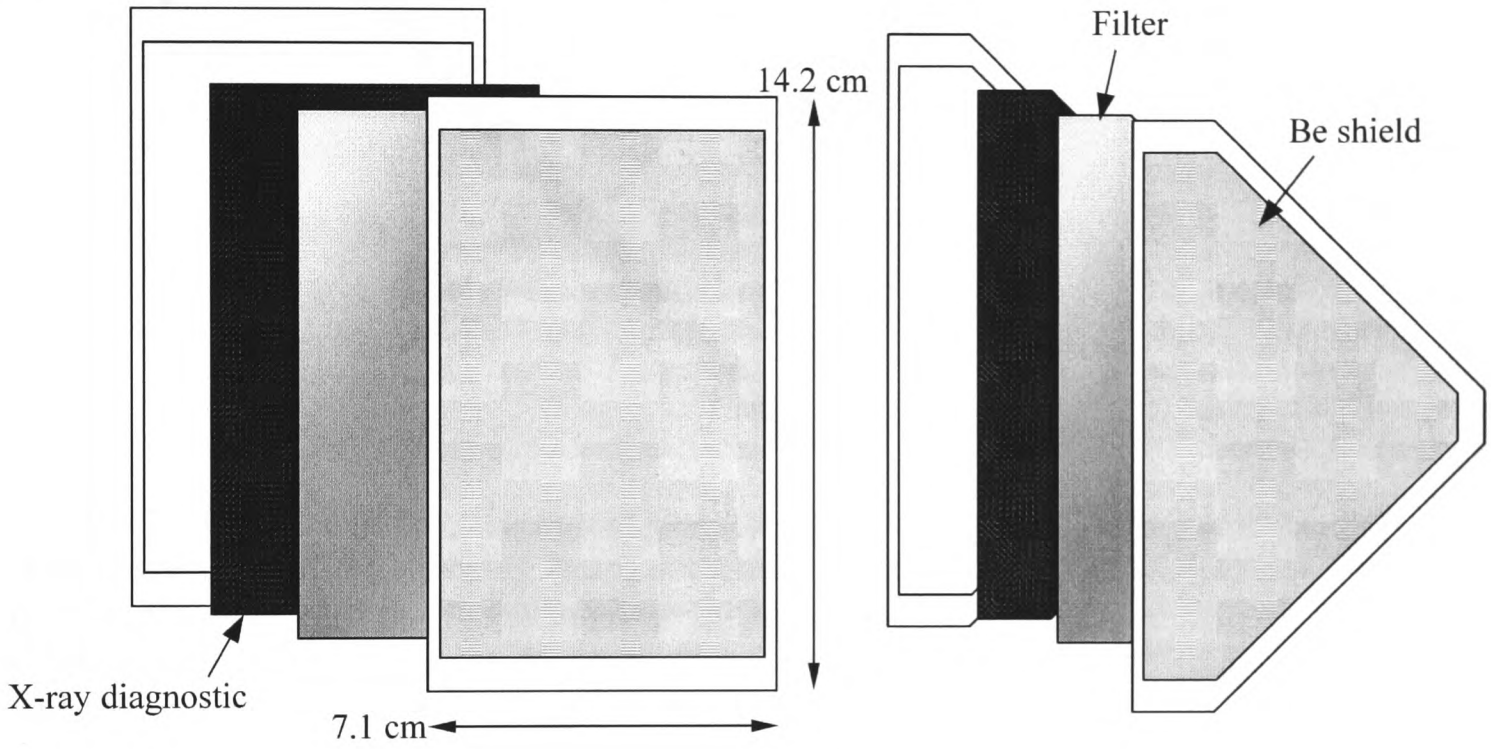


Figure 5.9: Layers of protective filtering contained in the film-packs. Before X-rays hit the diagnostic, they pass through a Beryllium shield, followed by an appropriate filter, depending on the backlighter material used (e.g. Fe filter for Fe backlighter).

5.4.2 Bragg and Laue Geometries

For most of the experiments conducted on the Vulcan laser, two film-packs facing each other were used to capture both the Bragg (reflection) and the Laue (transmission) diffracted X-rays from the crystal. This enabled the investigation of planes with various orientations to the shock propagation direction in the crystal. The set-up is illustrated in Fig. 5.10.

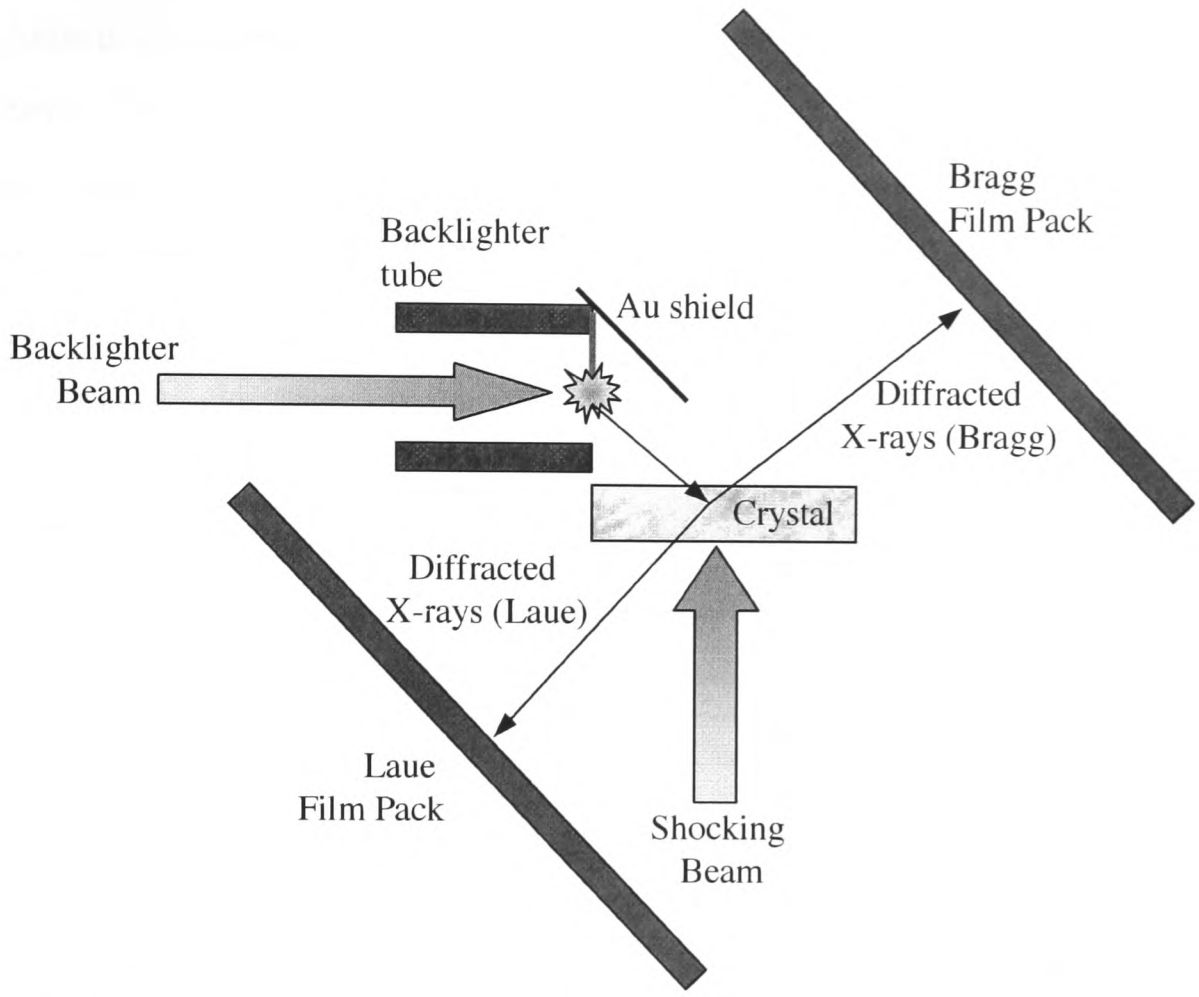


Figure 5.10: A schematic diagram of the cross-section of the target and the diagnostics (plane view). The shocking beam is incident on the rear side of the crystal. The plasma generated by the beam incident on the backlighter produces X-rays, which subsequently diffract from the crystal target. Both Bragg and Laue diffraction occurs and the scattered radiation is captured on the two film-packs.

On the Vulcan experiments, the targets and all diagnostics were positioned in the chamber manually. Precise determination of the target chamber centre using visible lasers, and beam pointing and focusing onto the chamber centre were necessary for a correct positioning of all components.

5.4.3 Image Plates

The X-ray sensitive diagnostic inside the film-pack was a Fuji BAS-MS 206 image plate (IP). The principle behind image plates is based on *photo-stimulated luminescence* (PSL) [111, 112]. This phenomenon is achieved in photo-stimulable materials, commonly called *phosphors*. The phosphor with the best storage and read-out prop-

erties known at present is Eu^{2+} doped BaFBr [113]. When a phosphor is irradiated by X-rays, electrons and holes are generated in it. They are stored separately at different trap sites, thereby forming and maintaining a latent image of the applied X-ray exposure which is, in this case, the diffraction image. Upon secondary stimulation with visible light (i.e. light with a longer wavelength than that of the primary stimulation), the electrons are released from their meta-stable states and recombine with the holes. This recombination energy is transferred to the activator ion Eu^{2+}, which consequently emits at 390 nm. This secondary emission of light upon stimulation by radiation of a longer wavelength than the wavelength of the first stimulation is the process of photo-stimulated luminescence.

In the image plates used in this experiment, small crystal grains ($\sim 5\,\mu$m in size) of BaFBr:Eu^{2+} were uniformly coated on a polyester support film and covered by a protective layer. An exposed IP was kept in a light-tight container and scanned with a He-Ne laser (λ=633 nm). The 390 nm blue light emitted via PSL was collected to produce a digitised image of the diffracted X-rays. The pixel size chosen for scanning the digitised image was 50 μm. The reading sensitivity could also be selected. This experiment used a dynamic range of 5 orders of magnitude (16 bits). The image plate is reusable after erasing the residual latent image with uniformly irradiated visible light.

IP reading was always carried out approximately 20 minutes after exposure. This is because the decay of the excited electrons from their meta-stable states can be induced not only via optical radiation, but also thermally. This phenomenon is called *fading* [114]. The higher the temperature at which the IP is maintained, the faster the detected values decrease. Also, the shorter the primary exposure time, the faster the decay rate. In the first ten minutes after the exposure, rates of fading therefore vary considerably, depending on the time between the exposure and the reading.

Extracting the data from an IP during this period could potentially cause an unevenness in the final data. For this reason, the IP's were kept in a light-tight cassette at room temperature for approximately 20 minutes after the exposure, for

data stabilisation. At this point, the fading rate was sufficiently low that it did not affect the reading process, which took approximately two minutes per IP.

5.5 OMEGA Laser System

The OMEGA laser system is also known as the National Laser Users' Facility (NLUF) and is located at the University of Rochester's Laboratory for Laser Energetics (LLE) in Rochester, New York, USA. It is a 60-beam, Nd:Glass laser system. It is used for experiments requiring very high-intensity laser beams, and is capable of producing intensities of up to $10^{17}\,\mathrm{Wcm}^{-2}$. The fundamental wavelength is 1054 nm, and target irradiation occurs at its third harmonic, i.e. 351 nm (UV). The diameter of the focal spot is a few tens of wavelengths of light. The maximum energy that can be delivered at 351 nm is 30 kJ, depending on the pulse length and shape. Pulse lengths vary between 115 ps and several nanoseconds. Any subset of the 60 available beams can be transported into the target chamber, depending on the specific demands of an experiment. Individual beams can be timed separately with delays of up to several nanoseconds, and a timing resolution of ± 10 ps.

A diagram of the OMEGA laser system is shown in Fig. 5.11. The entire system is installed in two bays separated by a neutron-absorbing shield wall. It rests on a bed of gravel which is structurally independent of the laboratory building enclosing it. The western (left) bay contains the laser amplifiers and the eastern (right) bay contains the target chamber.

Light is injected into the main system through laser drivers providing smooth seed pulses. The initial laser beam is spatially filtered and then split into three. There are six further amplifier stages (four rod amplifiers and two disk amplifiers), which also split the light into the total 60 beams. After the final disk amplifier stage, the diameter of each beam is 200 mm. Each beam is then transported into the chamber via two mirrors, which provide the pointing and centring controls. Optional distributed phase plates can be used for beam smoothing. The standard focusing optics used on OMEGA are f/6.2 lenses. The repetition rate of the laser system is 1 shot/hour.

The OMEGA laser system is a much larger and more complex one in comparison with the Vulcan laser system. The target chamber has a diameter of 3.3 m and is

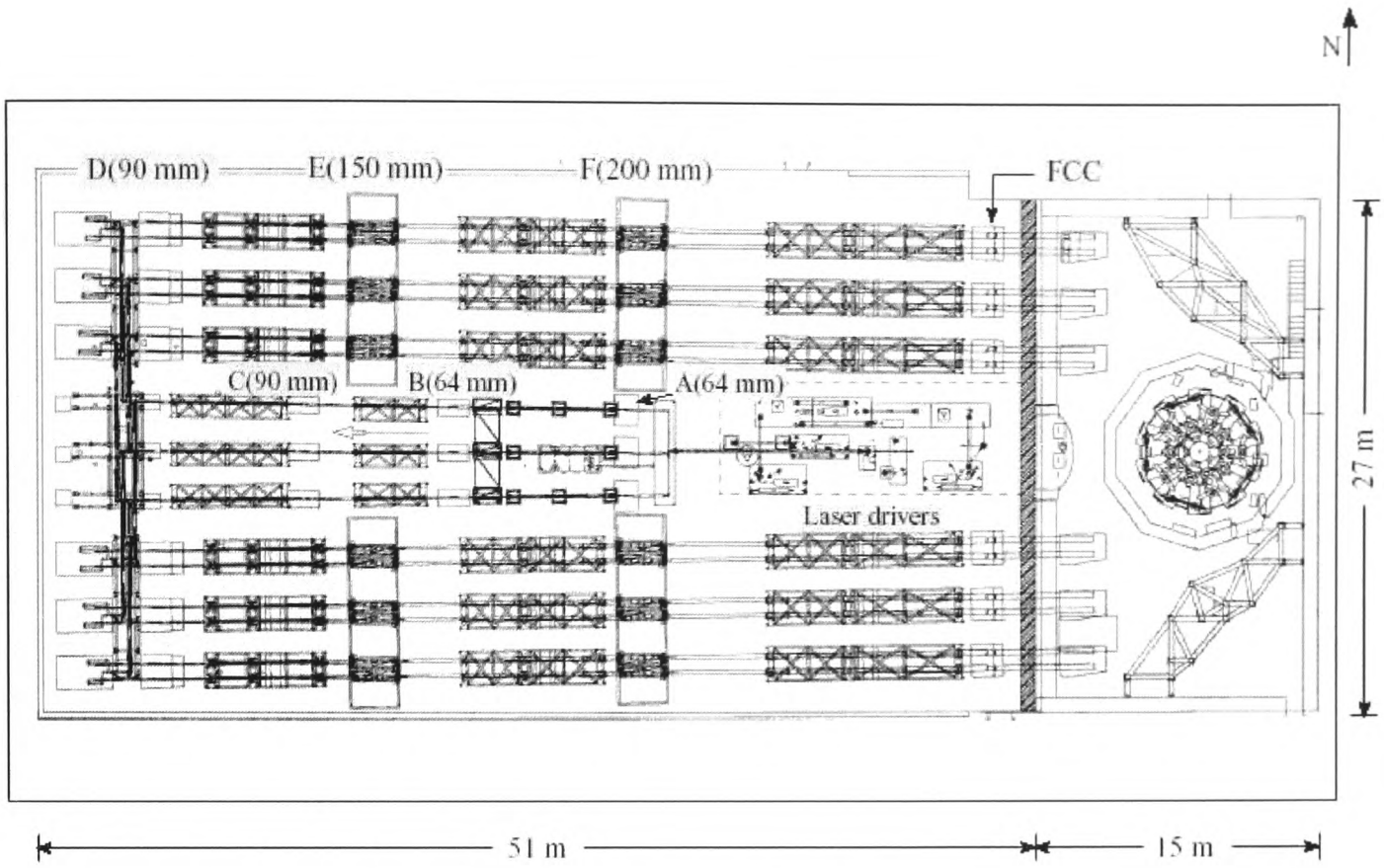


Figure 5.11: Layout of the OMEGA laser system [115]. The laser drivers in the centre of the laser bay inject the initial pulse. The four stages of rod amplifiers are labeled A-D. The further two stages of disk amplifiers are labeled E, F. The numbers indicate the diameters of the amplifiers, in milimetres. The frequency-conversion crystals (FCC) tripling the IR frequency to UV are indicated.

equipped with 60 lens ports and 32 primary diagnostic ports. A number of specialised staff are trained to operate various aspects of an experiment. This includes laser beam alignment into the target chamber centre and target and diagnostic positioning in the chamber.

5.5.1 Beam Geometry and Set-up for OMEGA

Between 2–4 beams, each with a pulse length of 3.0 ns, were used to shock the crystal. These were focused onto the target chamber centre. Their spot-size was 2.5 mm, i.e. large enough for most of the surface of the crystal to be irradiated. Either side of the crystal could be shocked; in the experiments described in this thesis, the side of the crystal which was shocked was the same one from which X-rays were diffracted.

In order to prolong the shock drive in the crystal, the beams could be arranged in such a way that the trailing edge of one laser pulse coincided with the leading edge of the following one, so as to form a longer driving pulse. The energy per shocking beam (in UV) was in the range 10–100 J.

To drive the backlighter target, between 4–6 beams were used. The pulse length was 1.0 ns, and the spot-size was 0.5 mm. The energy per beam (in UV) was ~ 300 J, giving the total irradiance on the backlighter of $\sim 10^{15}\,\mathrm{Wcm}^{-2}$. The backlighter beams' delay with respect to the crystal driving beams, measured from the leading edges of the pulses, varied from 1.4 to 6.4 ns.

The beam pointing precision and stability on OMEGA have been measured to be $\pm 16\,\mu$m [115].

5.6 Targets for OMEGA

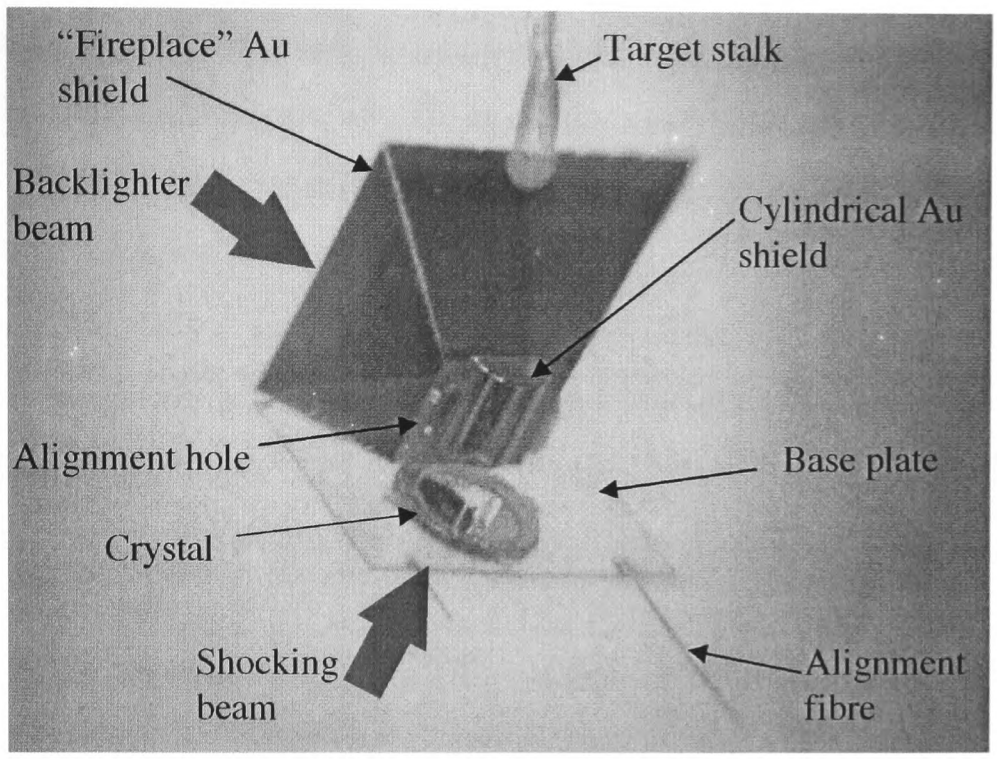


Figure 5.12: A schematic diagram of the combined crystal and backlighter target used on OMEGA experiments. It should be noted that the shocking beam can be applied from the bottom (as illustrated), as well as from the top. In the latter case, diffraction occurs from the driven side of the crystal.

The target is illustrated in Fig. 5.12. The crystal and the backlighter were parts of one assembly. The crystal was of circular shape, 3 mm in diameter, with thicknesses varying between 40–200 μm. A Gold shield in the shape of a fireplace was also attached to the base. This held a metal foil which was the X-ray backlighter. The thicknesses of the backlighter foils used were 5 μm or 12 μm. The size of the X-ray source was defined by the 200 μm aperture in the Au shield, through which the crystal was illuminated. Above this aperture was a cylindrical shield (also Au) which, along with the "fireplace" shield, was designed to prevent direct X-ray exposure of the diagnostic from the backlighter.

The coatings on the crystals for these experiments are shown in Fig. 5.13. Each crystal was coated with a 16 μm layer of lead-doped plastic or mylar, on top of which was a 1000 Å thick Aluminium coating. It can be seen that the order of the

two coatings on the crystal is swapped in comparison with the Vulcan experimental arrangement. The Al plasma created by the laser irradiation is not confined. Its ablation results in a shock wave propagating through the CH layer. This becomes steeper as it travels through the plastic and approaches the crystal surface, resulting in a sharper shock incident on the target. The laser intensity is, however, attenuated by the plastic layer prior to reaching the crystal surface. When sufficient laser intensities are available, this arrangement is more advantageous in comparison with the one described in section 5.2, since a sharper shock results in clearer diffraction lines from the crystal.

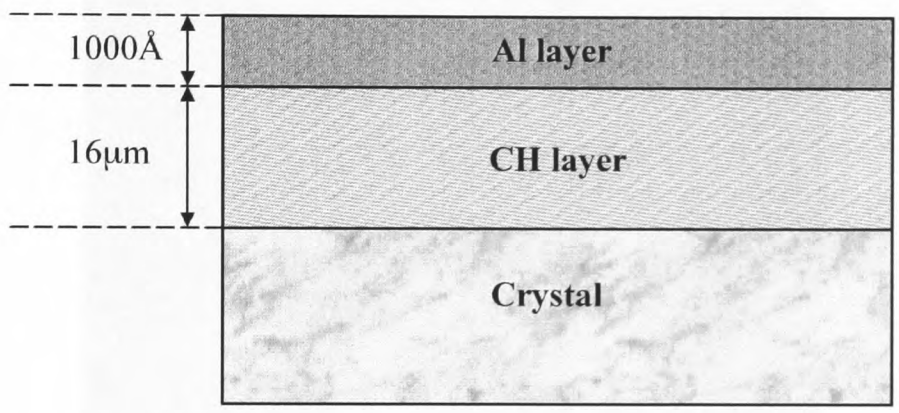


Figure 5.13: Coatings on crystal targets used for the OMEGA experiment. Ablation of the Al plasma drives a shock wave into the plastic coating. The shock steepens in the plastic before reaching the crystal target, resulting in sharper diffracted X-ray lines.

For alignment purposes, two thin stalks were attached to the base of the target assembly. Also to aid target alignment, two 200 μm holes were drilled on either side of the cylindrical Au shield. The target was placed into the chamber in such a way that the crystal was in the chamber centre and the backlighter was in the focal point of the backlighter-driving beams. Correct positioning of targets in the chamber was done using the standard OMEGA target positioner system, and target viewing system, both of which were externally controlled.

Detailed photographs of the targets are shown in Fig. 5.14.

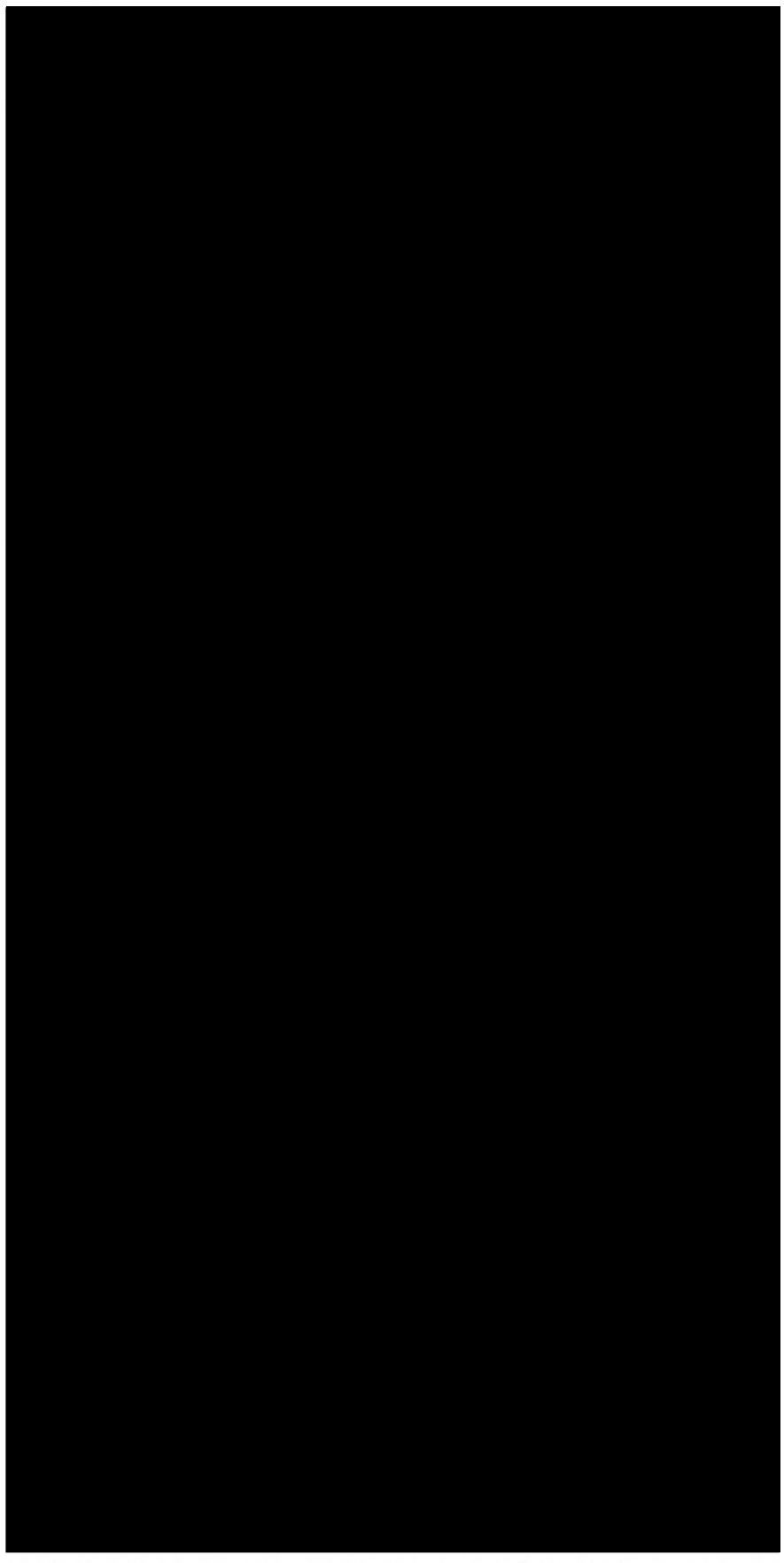


Figure 5.14: Detailed photographs of the target viewed from the top (top), at an angle (centre), and from the front (bottom). The alignment fibres are clearly seen in the top two diagrams, whilst the front view shows the detail of the two alignment holes drilled on each side of the Au cylindrical shield.

5.7 Diagnostics for OMEGA

In the experiments conducted on the OMEGA laser, the primary diagnostic was a large angle film detector, as used on the Vulcan laser and described in section 5.4. Instead of image plates, Kodak Direct Exposure Film (DEF) was used as the X-ray sensitive diagnostic. It was cut to fit the film holders and two pieces were places in each part of the film-pack, with the one closer to the backlighter partially acting as a further filter. On some of the shots, both Laue and Bragg film-packs were used. However, on shots using relatively thick crystal targets (200 μm), only the Bragg film-pack was used. The thickness of the crystal exceeded its X-ray attenuation length, so diffraction in Laue (transmission) geometry could not occur.

In the OMEGA target chamber, the detector was correctly positioned and held so that it surrounded the target chamber centre by using a Ten-Inch Manipulator. This is a steerable, air-locked, re-entrant platform, with a pointing accuracy of $<1\,\mu$m [115].

Chapter 6

Experimental Analysis and Results

This chapter presents the results, and their analysis, of the experiments described in Chapter 5. One of the aims of the experiments was to obtain X-ray diffraction evidence from multiple crystal planes of shock-induced hydrostatic compression of Copper occurring on nanosecond time-scales. The other main goal was to detect, for the first time by using *in situ* X-ray diffraction, the $\alpha - \epsilon$ phase transition in Iron, also induced by a shock wave on nanosecond time-scales.

The findings presented here are compared with previous experimental results (Cu), as well as the post-processing of MD simulations presented in Chapter 4.

6.1 Data Reduction

The software used to analyse the data was developed by Dr. James Hawreliak. The program enables the overlay of theoretically predicted diffraction lines with experimentally obtained ones. The modelling takes into account the shape and position of the wide-angle detector, as well as the precise location of the crystal with respect to the backlighter and the diagnostic. Also, any possible rotations of the crystal can be adjusted. In this way, the theoretical modelling uses the same parameters as those used in the experiments. Both Bragg and Laue geometries can be studied.

By making the appropriate adjustments, the theoretical lines are overlaid with the experimental ones, and fitted. Compression of the lattice along the three principal directions ([001], [010], and [100]) can then be simulated, until agreement between the theoretical lines and the experimental data is reached. Lattice strain in any of the three principal directions can thus be found.

The software is capable of simulating diffraction from FCC, BCC, and HCP lattices, as well as the diamond structure. This feature allows the user to detect any phase transition which may occur. This was particularly useful for the analysis of the Iron data.

An example of the theoretically predicted diffraction lines generated by the program is shown in Fig. 6.1. Lines corresponding to diffraction from a number of planes can be seen.

The software was written in C programming language.

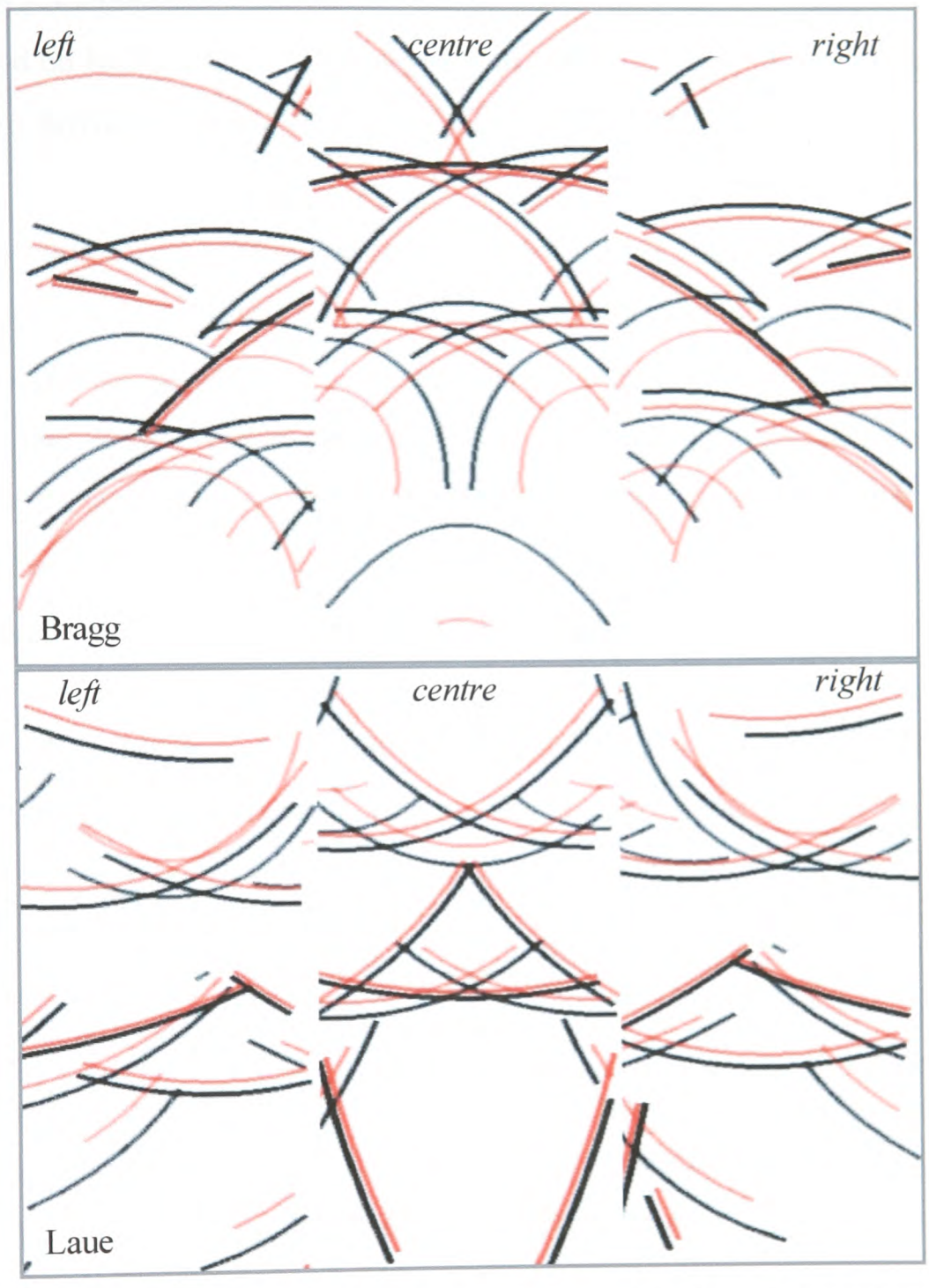


Figure 6.1: Illustration of the diffraction pattern used for line fitting of experimental data. Both Bragg (top) and Laue (bottom) geometries are modeled. Diffraction from a perfect Cu crystal is simulated in black. The red pattern corresponds to a Cu crystal compressed by 5% along all three principal directions, [001], [010], and [100]. The cutoff of some of the diffraction lines reflects the finite size of the crystal.

6.2 Copper Diffraction Results

The Copper data presented here was obtained at the Rutherford Appleton Laboratory and recorded on Image Plates. The recorded data was in digital form and immediately amenable to further analysis. The files could be opened using ImageJ or Photoshop software.

The experimental conditions were as follows: The crystal was 10 μm thick, with a 300 Å thick layer of Aluminium on its shocked side, overlaid with a further 1 μm layer of CH plastic, as detailed in section 5.2. It was grown and positioned in such a way that the shock traveled along the [001] direction. The intensity profile of the shocking beam is explained in detail in section 5.2 and illustrated in Fig. 5.6. As a result of this arrangement, a small part of the lattice in the centre of the crystal remained unshocked, whilst the top and bottom parts were shocked with 100% and 20% of the shocking beam energy, respectively.

The shocking beam had a pulse length of 2 ns and deposited 26 J onto a spot ~ 3 mm in diameter on the crystal surface. The pressure generated by the laser beam is related to these quantities by the following relationship due to Lindl [116],

$$P_{\mathrm{Mbar}} \simeq 40 \left[\frac{I_{15}}{\lambda_{\mu m}} \right]^{2/3}, \tag{6.1}$$

where I_{15} is the incident laser beam intensity in units of $10^{15}\,\mathrm{Wcm}^{-2}$, $\lambda_{\mu m}$ is the laser wavelength in μm, and P_{Mbar} is the resultant pressure, in Mbar.

Using the above formula, the approximate peak pressure generated at the target surface was found to be ~ 12 GPa. The attenuation of the laser intensity by the plastic coating is negligible, since its thickness is only 1 μm. The net pressure incident on the crystal exceeds the HEL of Copper, which is known to be in the range ~ 0.01–2.6 GPa [27].

The X-ray pulse used for diffraction was delayed by 1.7 ns with respect to the shocking beam, and had a length of 1 ns, determined by the laser pulse which irradiated the backlighter foil. The diffraction was from the far side of the crystal not

directly exposed to the shocking beam.

The diagnostic captured both Bragg and Laue diffraction geometries, covering a solid angle of nearly 2π with respect to the crystal surface. The raw data recorded on the film detector is presented in Fig. 6.2. Diffraction from multiple planes is shown, highlighting the main advantage of this diagnostic method. It can be seen that some lines visible in Fig. 6.1 are not seen here. Higher diffraction orders are not as easily discernible as lower orders (e.g. diffraction from (002) planes). This is due to the variations in the atomic form factor, the Debye-Waller factor, absorption and extinction of X-rays in the crystalline material, as well as the orientation of the crystal with respect to to the detector.

The lattice compression due to the shock wave was inferred from the central parts of the film-packs, as these recorded most of the relevant diffraction information and had the least exposure to diffuse X-rays. The theoretical diffraction lines were overlaid with the experimental data, and fitted.

Detailed diagrams of the central parts of the film-packs are shown in Fig. 6.3 for both Bragg and Laue geometries. The Miller indices of the relevant planes are labeled. Theoretical X-ray diffraction lines fitted to experimental data are shown on the right-hand-side of the figure.

It can be seen that certain diffraction lines are partially broadened, corresponding to a lattice compression, whilst other parts of the diffraction signal from the same set of atomic planes remain unbroadened. Also, diffraction signals from certain sets of planes show no lattice compression evidence, in particular (022) and $(\bar{1}13)$ planes in the Bragg geometry, and $(\bar{3}\bar{1}\bar{1})$ and $(\bar{1}1\bar{1})$ planes in the Laue geometry. This is due to the experimental arrangement mentioned above, wherein the size of the detector and its position were such that some recorded X-rays were scattered from the unshocked parts of the crystal only. In both figures, the evidence of lattice compression is highlighted in red, and diffraction lines from unshocked material are indicated in black.

The Bragg diffraction geometry in Fig. 6.3 shows a clear compression of the

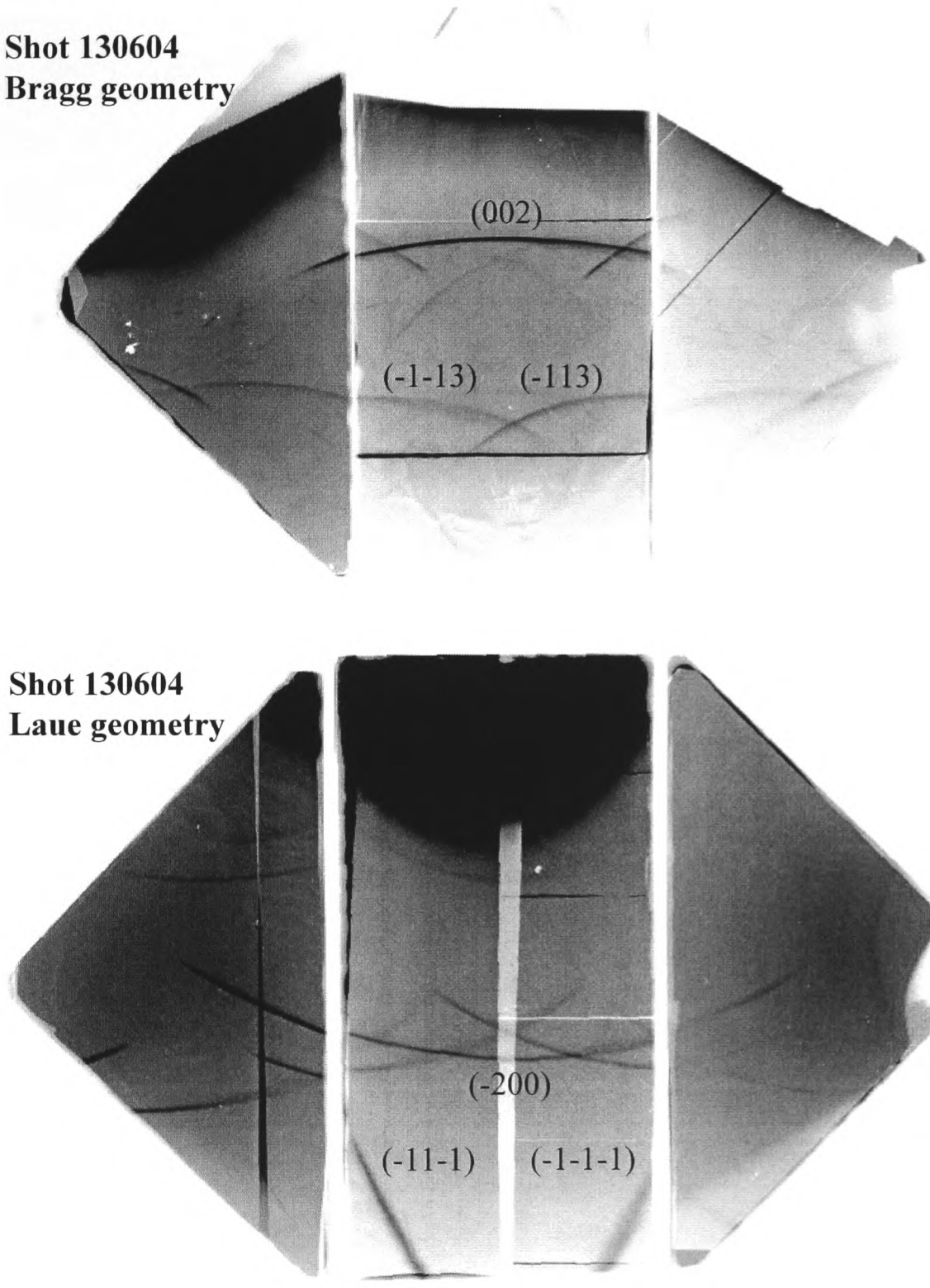
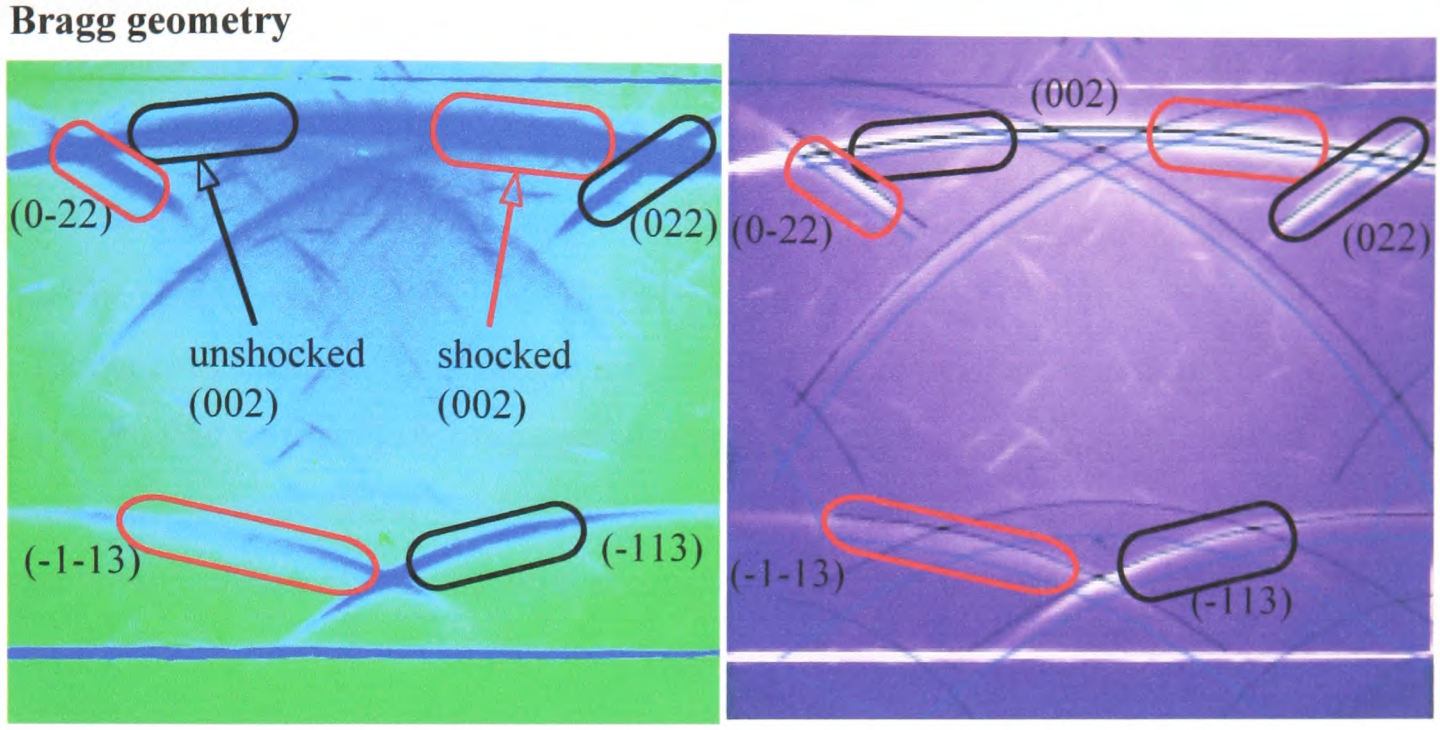


Figure 6.2: Shot 130604: raw diffraction data captured on the wide-angle film detector in both Bragg (top) and Laue (bottom) geometries. The diffraction lines from multiple crystal planes can be seen. Low orders of diffraction are most easily discernible, due to the high atomic form factors associated with them, and relatively small susceptibility to thermal vibrations in the crystal.

Shot 130604
Bragg geometry



Shot 130604
Laue geometry

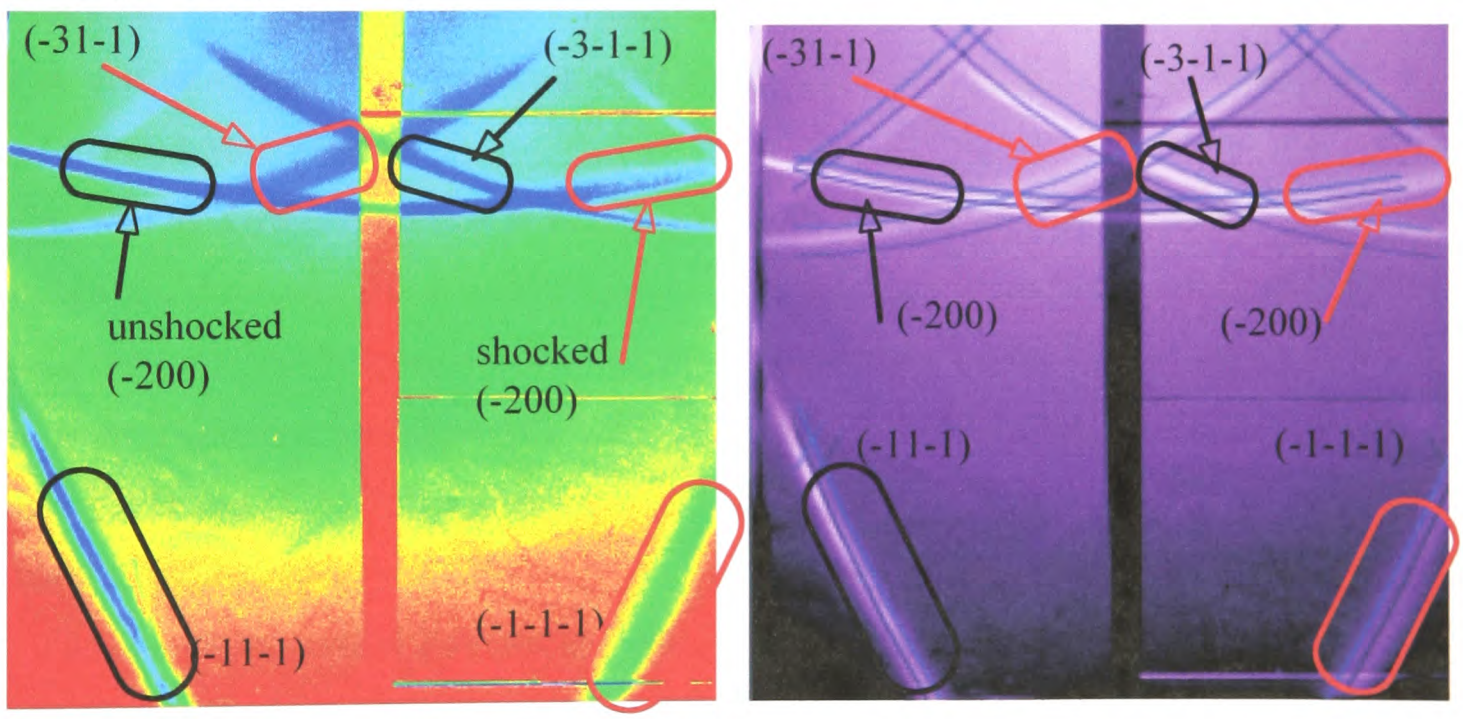


Figure 6.3: Shot 130604: diffraction from multiple planes in the Bragg (top) and Laue (bottom) geometries. Broadening of multiple diffraction lines (highlighted in red) is clear X-ray diffraction evidence of 3-D lattice compression. Theoretical lines fitted to experimental data are shown on the right side of the figure. Black = unshocked crystal; blue = shocked crystal.

(002) planes on one side of the crystal (seen on the right side of the figure), and no compression on the other side of the crystal (left side of the figure). Although the experimental set-up allowed $\sim 20\%$ of the full shocking beam energy onto the target, this was insufficient to cause any discernible lattice compression. The broadened line caused by shock-compression of the lattice corresponds to a strain of $\sim 3.0\% \pm 0.7\%$ along the shock propagation direction [001] (z).

Evidence of lattice compression is also seen in the Laue geometry in Fig. 6.3. $(\bar{2}00)$ planes, parallel to the shock propagation direction, are compressed in one part of the crystal, and uncompressed in another part (indicated in the figure in red and black, respectively). Here, the broadening corresponds to a compression of $\sim 2.7\% \pm 0.6\%$ along [100] (x), normal to the shock propagation direction.

The lineouts from the diffraction lines from (002) and $(\bar{2}00)$ planes are shown in Fig. 6.4. The broadening of the diffraction lines from the shocked parts of the crystal corresponds to a reduction of the spacing of the corresponding planes. This quantitative measurement is in agreement with the experiments carried out by Loveridge *et al.* [7] and Meyers *et al.* [8].

As well as X-ray diffraction from planes directly normal, or parallel, to the shock propagation direction, the results presented here show additional evidence of plastic lattice deformation from planes with various orientations to the shock propagation direction. These include planes $(0\bar{2}2)$ and $(\bar{1}\bar{1}3)$ detected in the Bragg geometry, and planes $(\bar{3}1\bar{1})$ and $(\bar{1}\bar{1}\bar{1})$ in the Laue geometry. Evidence of crystal lattice compression is highlighted in red.

The overall theoretical line fitting yielded strains of $3.0\% \pm 0.7\%$ along z direction, and $2.7\% \pm 0.6\%$ along x and y, resulting in a total volumetric compression of $\sim 8.4\%$. This is in excellent agreement with previous experimental data [7, 8], indicating that plasticity in Copper occurs on nanosecond time-scales.

A comparison of the data presented above with an existing experimental Hugoniot of Copper [117] is shown in Fig. 6.5. A fractional change in the volume, V/V_0, is plotted against the applied shock pressure. Errors in the experimental measurement

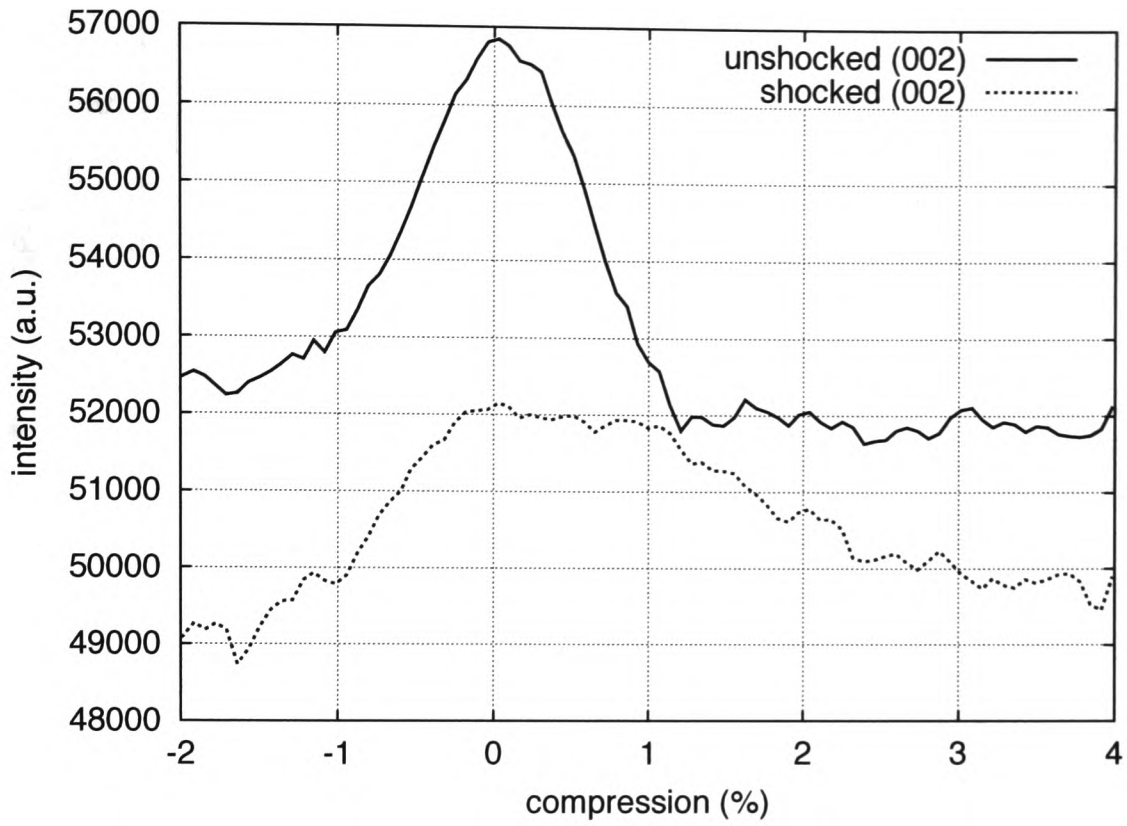


Figure 6.4: Lineouts of the diffraction lines corresponding to planes (002) (top) and ($\bar{2}00$) (bottom), from both unshocked and shocked parts of the crystal. The range of compressions the lattice is subjected to in both directions is indicated on the horizontal axes. (The intensity units on the vertical axes are arbitrary, and the positions of the lineouts with respect to the vertical axes are irrelevant.)

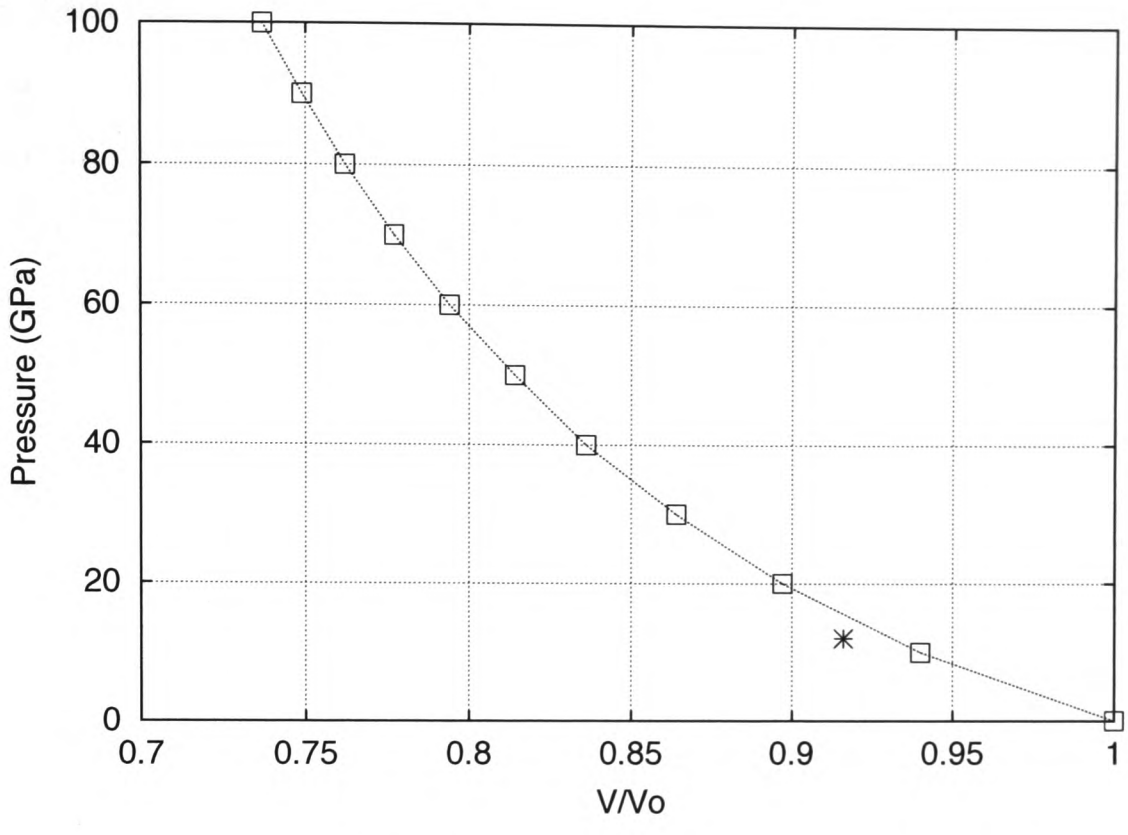


Figure 6.5: Comparison of the experimental result presented in this chapter (marked by an asterisk) with a Hugoniot for shock-compressed Copper. The reference data are taken from [117].

of strains in a shock-compressed material have to be accounted for, as well as the fact that eqn. (6.1) provides only an approximate value of the incident pressure. With these factors taken into account, one can see that good agreement between the current experiment and the reference data is reached.

The results were also compared with those of the MD simulations presented in Chapter 4. Analysis in section 4.1.3 showed that a modeled single crystal of Copper subjected to a pressure of $\sim 34\,\mathrm{GPa}$ on the time-scale of $\sim 100\,\mathrm{ps}$ undergoes a compression of $\sim 6\%$ along the shock propagation direction, and $\sim 4.6\%$ in the two lateral directions.

It can be seen that the MD simulation favours compression in the direction of the shock propagation within $\sim 130\,\mathrm{ps}$, whereas experimentally, an almost complete 3-D compression occurs on nanosecond time-scales, despite the shocking pressure being almost three times smaller.

This discrepancy is believed to be due to the scalar deficiency of the MD simulations; the time-scale of $\sim 130\,\text{ps}$, and spatial dimension of $\sim 0.6\,\mu\text{m}$ are still an order of magnitude lower than the scales of the experiment presented here. It is believed that further plasticity in the lattice could occur on time-scales exceeding $\sim 130\,\text{ps}$. Nonetheless, the MD model presented in section 4.1.3 is a significant improvement of previous modelling, an example of which is shown and analysed in section 4.1.1.

It is expected that MD simulations using longer temporal and spatial dimensions should yield a fuller 3-D compression of the lattice, as is observed in laser-induced shock experiments. Conversely, improving the temporal resolution in shock experiments would allow a more detailed understanding of the time-scales involved in the plastic yield of a crystalline material to a shock wave.

6.3 Iron Diffraction Results

The Iron data was obtained at the University of Rochester, USA, and recorded on an X-ray sensitive DEF film. This was digitised at the LLNL prior to analysis, using a densitometer, and received by the author in a form amenable to further study. Digitisation of raw data consists of transforming the optical density of the film into intensity. The relationship between these two quantities for Kodak DEF film used in these experiments is described for a range of wavelengths in [118].

Two shots are presented (36185 and 36194). The results from shot 36185 are analysed in detail, and those from shot 36194 are used for reference and comparison.

The crystal targets were 200 μm thick, cut and aligned to allow the shock propagation direction to be along [001]. In both cases, there were two shocking beams, each with a 3 ns pulse, with the leading edge of one coinciding with the tailing edge of the other so that combined, they formed a 6 ns long pulse incident on the target. The total energy of the two shocking beams was 184 J and 177 J for shots 36185 and 36194, respectively. The energy was deposited onto a 2.5 mm spot on the crystal surface. Using eqn. (6.1), the pressure generated at the plastic coating of the targets on the two shots was thus $\sim$59 GPa and $\sim$57 GPa, respectively. It has to be noted that these values are only approximate and also that the net pressure on the crystal was lowered, owing to the decay of the shock wave inside the 16 μm thick plastic coating.

There were two X-ray generating beams, both producing 1 ns pulses which were also stacked in sequence. For shot 36185, their leading edges were separated by 2 ns, leaving a 1 ns interval between the two pulses during which no X-ray diffraction measurement was made, however allowing a larger time-evolution of the crystal to be probed. For shot 36194, the leading edge separation was 1 ns, effectively forming a single 2 ns long probing pulse. The delay of the leading edge of the first X-ray generating pulse with respect to the leading edge of the shocking beams was 1.4 ns and 1.5 ns for shots 36185 and 36194, respectively. A diagram illustrating the beam timing for shot 36185 is shown in Fig. 6.6.

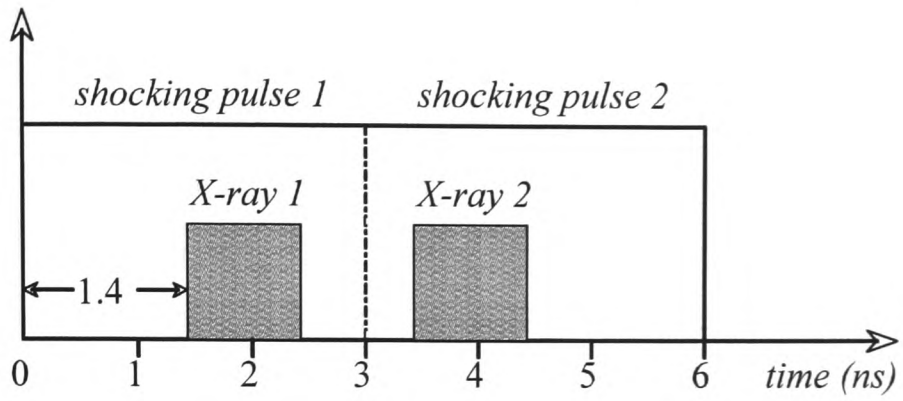


Figure 6.6: Beam timing for shot 36185. The two shocking pulses form one, 6 ns in length. "X-ray 1" and "X-ray 2" denote the two X-ray probe pulses, each 1 ns long, separated by 1 ns.

X-rays diffracted from the shocked side of the crystal, and information was recorded in the Bragg geometry only. One of the side parts of the film detector had to be removed from the target chamber for ease of target and diagnostic alignment. The raw data is shown in Fig. 6.7.

Data from both shots clearly display diffraction lines in the central part of the film-pack. The sharpest lines correspond to uncompressed BCC lattice. Diffraction from (002) planes is particularly clear in both shots. Both data sets also show a second line above this feature, corresponding to uniaxially compressed (002) planes. This is labeled "shocked (002)". Above this line lies a third, broader feature, marked "phase change". This is believed to be evidence of the $\alpha - \epsilon$ phase transition in Iron. Both the compressed (002) line and the evidence of the phase transformation are seen more clearly in the data from shot 36185. This data set is analysed in detail below.

Even a cursory glance at the figure will draw one's attention to the apparent rotation of the lines corresponding to BCC planes $(\bar{1}12)$ and $(\bar{1}\bar{1}2)$, in comparison with the same lines in data set 36194. It will be shown later that an accidental rotation of the crystal in its plane resulted in the appearance of an extra feature in the lower part of the central film-pack of 36185, crossing the BCC-diffracted (011) line. This feature will be shown to be a line diffracted from the new (ϵ) phase, and is therefore labeled "phase change".

Using the crystallographic relationship between the α and ϵ phases in Iron de-

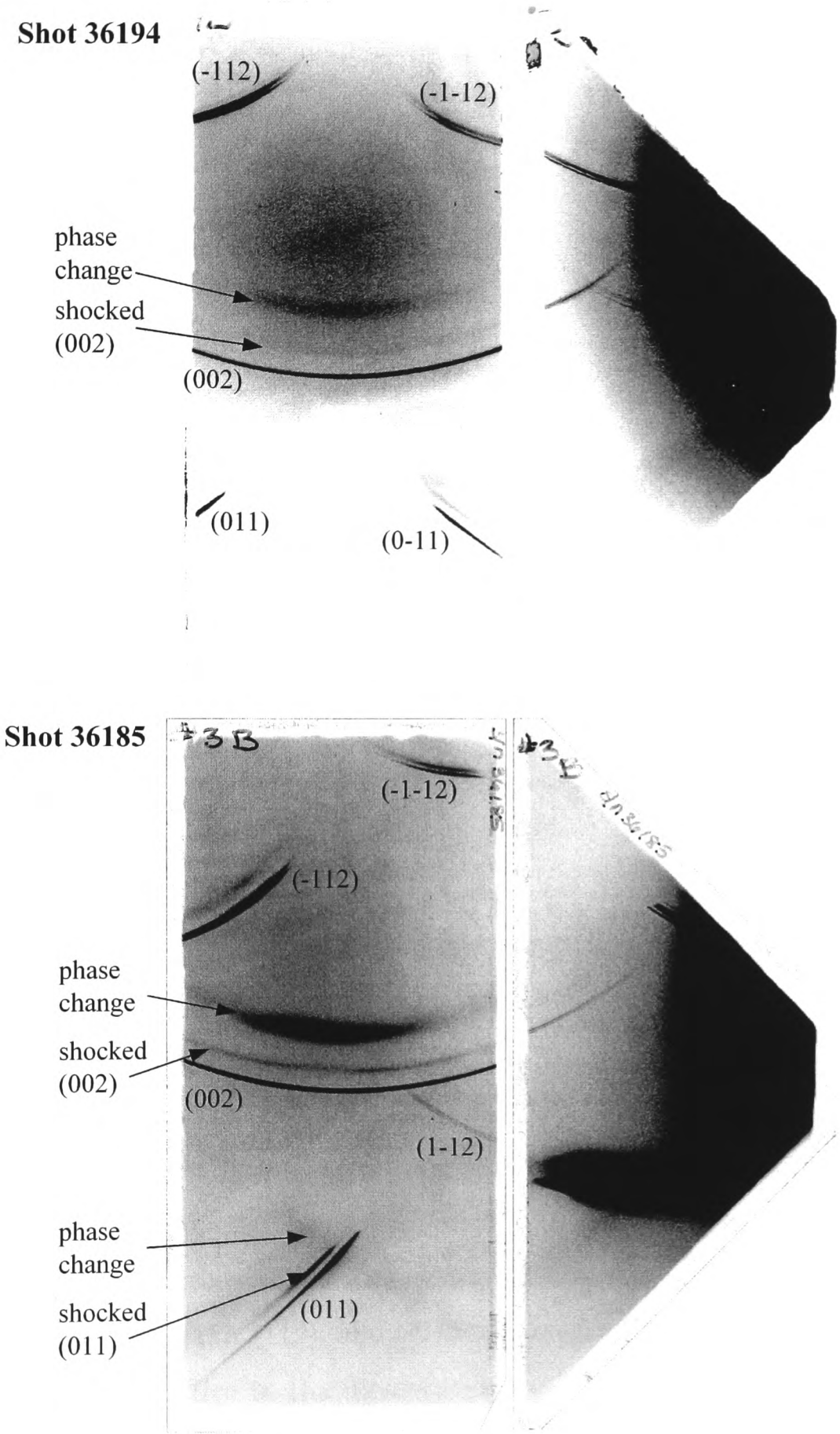


Figure 6.7: Shots 36194 and 36185: raw diffraction data. For shot 36185, the crystal has been rotated in its plane with respect to the film detector. An extra diffraction line labeled "phase change" appears as a result, crossing the diffraction signal scattered from BCC (011) planes.

scribed in section 2.6, it can be shown that a compression of 18.35% along the [001] direction of the BCC lattice is required in order for the (110) (or $(1\bar{1}0)$) planes to transform into *perfectly* hexagonal (0001) planes, forming the bases of the new phase. If this transformation takes place, the side of the hexagon in the new ϵ phase, $\tilde{a}$, will equal $\sqrt{2/3}\,a$, where a is the original unit cell size of the cubic α phase. This transformation results in the $c:\tilde{a}$ ratio to equal $\sqrt{3}$, with the c axis of the new phase corresponding to the original $[1\bar{1}0]$ (or [110]) directions.

Theoretical diffraction lines were fitted to the data from shot 36185 under this assumption, using the in-house tailored software. The result is shown in Fig. 6.8 and discussed in detail below.

Compression of BCC (002) planes, corresponding to a uniaxial strain along the [001] direction, was found to be $\sim 6\%$. It should be noted that the experimentally measured threshold pressure for the $\alpha-\epsilon$ transformation in Iron is $\sim 13\,\text{GPa}$ [21, 34], and was therefore significantly exceeded by the applied pressure in this experiment. Despite this, the uniaxial compression in the purely elastic wave in the BCC phase did not exceed $\sim 6\%$ (indicated in purple in the figure). This result is in very good agreement with the findings from the MD simulations discussed in section 4.2. In the MD study, four different applied pressures resulted in approximately constant uniaxial compression of the parent lattice, although the compression of the new phase gradually increased with pressure.

In this experiment, diffraction measurement in the Laue geometry was not performed, so no X-ray data from planes parallel to the shock propagation direction, (200) or (020), were obtained. The recorded data in the Bragg geometry do, however, contain lines diffracted from planes with various orientations to the shock propagation direction, such as $(\bar{1}12)$, $(\bar{1}\bar{1}2)$, and (011), which also provide information about the behaviour of the lattice in the directions normal to the shock. The fit of the theoretical lines with the experimental data is extremely good, indicating that only uniaxial compression of $\sim 6\%$ occurred in the BCC phase, and no lateral compression of the parent lattice took place. This is also in agreement with the results of the MD

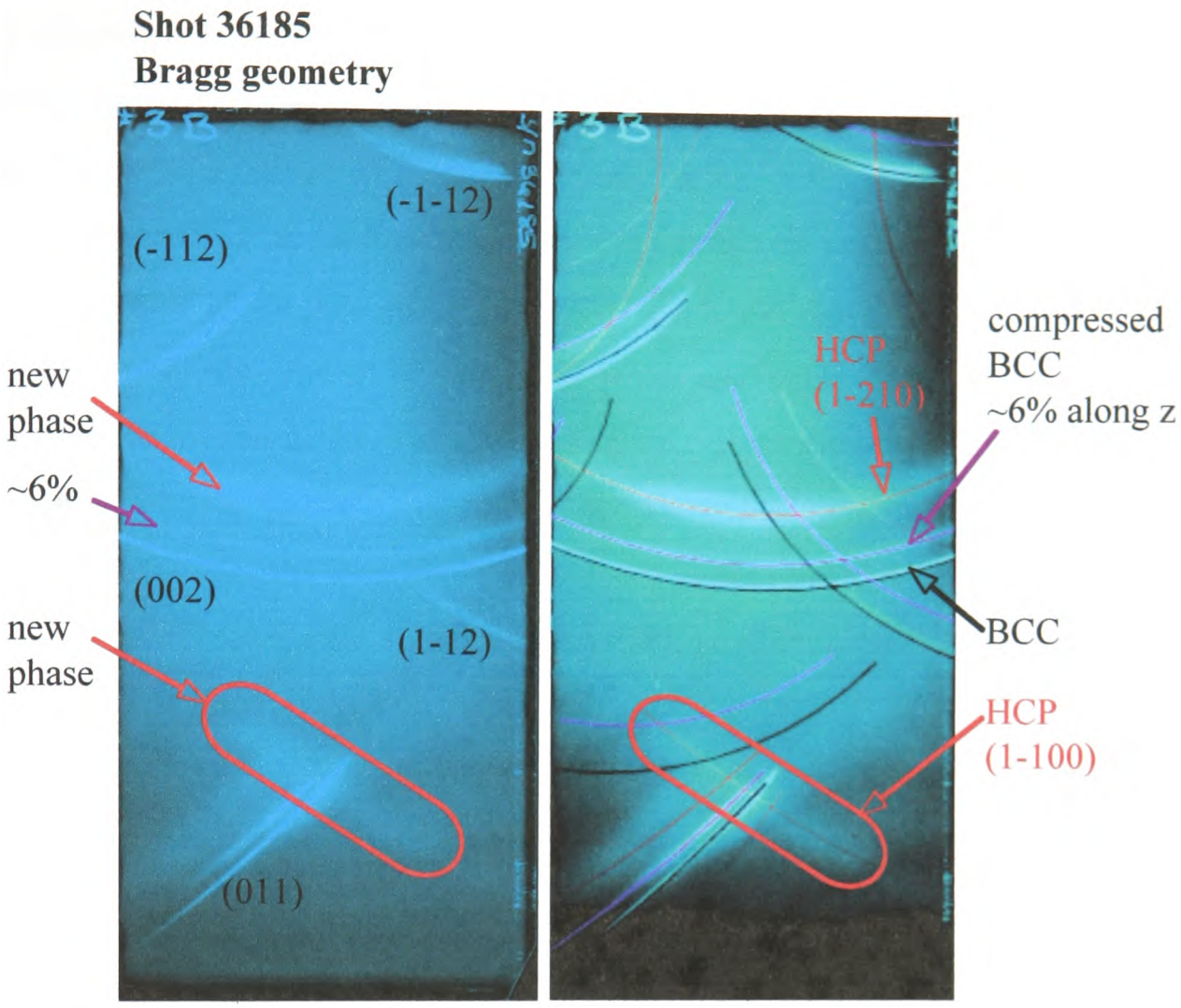


Figure 6.8: Shot 36185: theoretical fit (shown on the right) to experimental diffraction data. Black = uncompressed BCC; purple = compressed BCC; red = quasi-HCP phase. The weak line crossing the BCC-diffracted (011) line coincides with the $(1\bar{1}00)$ diffraction from the HCP phase.

post-processing described in section 4.2.

Analysis of the lines corresponding to BCC $(\bar{1}12)$ and $(\bar{1}\bar{1}2)$ planes from shot 36185 showed that the crystal was rotated by $\sim -20°$ around the normal to its surface. It was this new orientation of the sample which caused the additional signal from the new phase to be recorded, as can be seen in Fig. 6.8. This extra feature crossing the diffraction line from BCC (011) planes corresponds to diffraction from HCP $(1\bar{1}00)$ planes (using the four-index convention defined in section 2.1.4). The other HCP-diffracted line, appearing above the BCC-diffracted (002) lines, corresponds to the HCP $(1\bar{2}10)$ planes.

A transition from BCC (110) and $(1\bar{1}0)$ planes into *perfect* HCP (0001) planes was not expected to take place. Indeed, the z axis of the new phase was found to be compressed by only 15.0±0.5%. The pressure regime of this experiment corresponds most closely to MD simulation **D**, where the applied piston pressure was $\sim 53\,\mathrm{GPa}$. The compression of the phase-transformed lattice found there was $\sim 17.3\pm0.9\%$. Taking into account the line widths and the errors associated with the measurements, the agreement between the two results is good. Notwithstanding the difference in time-scales between the MD simulations and the experiment of approximately three orders of magnitude, the discrepancy could also be due to the particular choice of potential in the MD simulations, which might not model the behaviour of Iron faithfully enough at all pressures.

It is notable that the lines corresponding to what is believed to be the evidence of the $\alpha-\epsilon$ phase change in Iron display similar features to the simulated diffraction lines obtained from X-ray diffraction post-processing of MD models of Iron, presented in section 4.2. They are much less sharp and broader than the diffraction lines from either the unshocked BCC material, or the uniaxially compressed BCC material. This is to be expected: the phase transition does not result in a perfect HCP crystal, and X-ray diffraction lines will be broadened due to the presence of grain boundaries, as well as the duality of the orientation of the new phase.

One should note that such very good quantitative agreement between the MD simulations and experiments was reached despite the fact that the MD modelling was performed on picosecond time-scales, whilst the experimental temporal scale was several nanoseconds. Evidence from recent experiments by Sano *et al.* suggests that the $\alpha-\epsilon$ phase transition in Iron occurs on even shorter (femtosecond) time-scales [119]. Polycrystalline Iron was irradiated with 120 fs long laser pulses, and the quenched ϵ phase was detected in the recovered material using electron diffraction. Such short time-scales of the phase transition would explain the agreement between the MD simulation results and the experimental results presented in this chapter.

As mentioned in Chapter 4, the two-atom basis of the HCP phase results in the

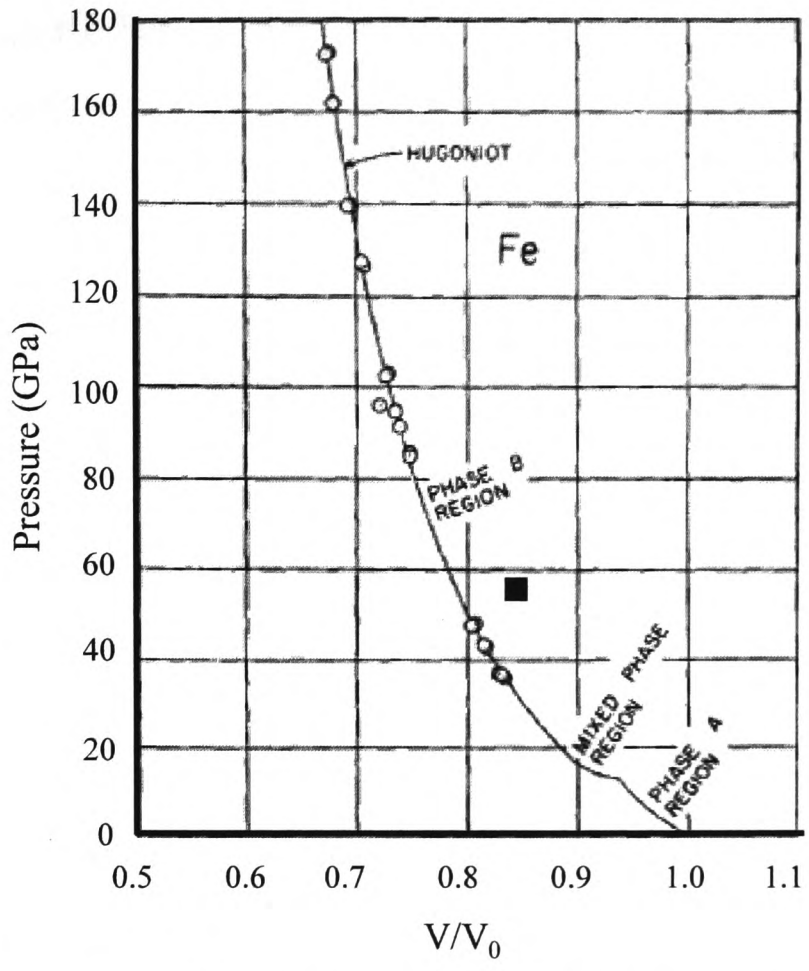


Figure 6.9: Comparison of the experimental result presented here (marked by a full square) with existing Hugoniot for shock-compressed Iron. The graph is taken from [117], and phases A and B refer to α and ϵ phases, respectively.

doubling of the number of points per unit volume in k-space in comparison with the parent BCC phase. This is also reflected in the experimental data presented here; the central film-pack recorded additional diffraction lines from the new phase, corresponding to an increase in the number of points in the inverse space.

A comparison of the results with an existing empirical Hugoniot for Iron [117] is shown in Fig. 6.9. The result from shot 36185 is represented by a full square. As mentioned earlier, the actual peak pressure incident on the crystal was lower than the calculated value of $\sim 59\,\mathrm{GPa}$, owing to the $16\,\mu\mathrm{m}$ thick plastic coating which attenuated the laser radiation. Taking into account this factor, as well as the errors on the experimental measurement, one can conclude that good agreement is achieved with existing experimental data.

Based on the results presented here, an experiment was conducted on the Vulcan

laser facility at the Rutherford Appleton Laboratory. The aim was to investigate the additional feature appearing in the data from shot 36185 (Fig. 6.8). The crystal samples studied in this experiment were deliberately rotated, so that their alignment with respect to the diagnostic would yield this diffraction line.

The results [120] are in excellent agreement with those presented in this chapter. A uniaxial compression of $\sim 6\%$ of the BCC lattice along the shock propagation direction was found, as well as a compression of ~ 15–18% of the ϵ phase. Furthermore, the diffraction signal recorded in the Laue geometry showed additional lines exclusively due to the ϵ phase of Iron, which are disallowed by the symmetry of the cubic α phase. This provides further evidence that the $\alpha - \epsilon$ phase transition in Iron occurs on extremely short (nanosecond or lower) time-scales of laser-induced shock-compression.

6.4 Summary

Plasticity occurring on nanosecond time-scales in laser-shocked single crystal Copper has been shown using a static wide-angle diagnostic. X-ray diffraction from multiple planes was recorded, enabling the detection of hydrostatic compression of the lattice from planes with several sets of (hkl) Miller indices. The results are in excellent agreement with previous experiments [7, 8].

Comparison of the experimental results with those of the MD simulations post-processing presented in Chapter 4 shows that the lattice compression detected experimentally on nanosecond time-scales is more hydrostatic. This discrepancy is believed to be caused by the shortage in scales (both temporal and spatial), by over an order of magnitude, of the MD models with respect to the experiments. Fuller 3-D compression of the lattice is believed to occur on the time-scales exceeding $\sim 100\,\text{ps}$.

The readiness of experimental Copper to undergo near-3-D compression under shock loading conditions is believed to be related to the defects in the material, both pre-existing and those generated by the shock wave. These are thought to play a crucial role in the relaxation of the lattice towards the hydrostat upon shock-compression. Experimental Copper crystals contain dislocations with densities ranging between $\sim 10^6$–$10^8\,\text{cm}^{-2}$, known to reduce the HEL to ~ 0.01–$2.6\,\text{GPa}$ and allow plastic flow of the material under shear stress [8,27]. A quantitative knowledge of dislocation densities *during* shock loading would be a significant step in our understanding of these processes; however, this has to date not been experimentally accomplished. Employing the method described in section 4.1, which could enable such a measurement, is clearly called for.

In situ X-ray diffraction experiments performed on shock-compressed (pressure $> 50\,\text{GPa}$) single crystal Iron yielded first-time diffraction evidence of the $\alpha - \epsilon$ phase transition in Iron on nanosecond time-scales, thus proving the onset of one of the most well-known phase transitions in material science under shock conditions. Two diffraction lines believed to correspond to the HCP phase in Iron were recorded, corresponding to $\sim 15\%$ compression along the shock propagation direction. Further

experiments performed since have confirmed these findings.

The experimental results are in very good agreement with the post-processing analysis of MD models of shock-compressed Iron. A uniaxial compression of the parent BCC lattice, as well as the $\alpha - \epsilon$ phase transition, were detected both experimentally on nanosecond time-scales, and computationally on picosecond time-scales. This agreement suggests that the time-scales of the phase transition may be much shorter than a nanosecond. This conclusion is also supported by recent experiments [119], where quenched ϵ phase in polycrystalline Iron was detected after a 120 fs-long laser irradiation. Improving the temporal resolution of X-ray diffraction experiments would lead to a precise determination of the time-scales of this phase transition.

Remarkably, neither the MD simulation results, nor the experimental data, detected any lateral lattice compression which would indicate plasticity of the material. The uniaxial compression of the BCC lattice does not appear to exceed a certain value regardless of the applied pressure in both the MD simulations and the experiment. On the other hand, in both cases the compression of the new phase along the shock propagation direction increased with pressure.

The difference between the responses of Iron and Copper to shock wave conditions is striking. Whilst Copper subjected to only ~ 12 GPa clearly displayed plastic behaviour, wherein compression along all three principal directions was $\sim 3\%$, Iron subjected to much higher pressures (> 50 GPa) was uniaxially compressed to $\sim 6\%$, but showed no sign of plasticity.

It is clear that the behaviour of Iron under shock conditions differs significantly from that of Copper. The detected plastic deformation in Copper is due to the high velocities of the dislocations generated in this material, since plastic flow on pico- and nanosecond time-scales crucially depends on the high mobility of dislocations. Previous experimental measurements have shown an increase, by two orders of magnitude, in screw dislocation density in Iron as a result of shock wave passage for applied pressures even below the $\alpha - \epsilon$ transition threshold of ~ 13 GPa [11]. The lack

of plasticity detected in the experiments presented in this thesis suggests, however, that dislocation mobilities in Iron are lower than in Copper. It is therefore possible that shear stress release in shock-compressed Iron only occurs on considerably longer time-scales (e.g. microseconds) than those probed in the experiments presented here.

As mentioned in section 6.2, the high mobility of dislocations in Copper subjected to the given pressure enables apt shear stress release on nanosecond (or lower) time-scales. However, a lower mobility and hence velocity of dislocations under similar shock wave conditions would result in shear stress release on longer time-scales, e.g. microseconds. If this is the case in Iron, experiments performed on nanosecond time-scales, such as those presented here, cannot detect any plastic flow, and longer temporal scales would be required. It remains an experimental challenge to determine whether this is the cause of the lack of plasticity in α Iron on nanosecond time-scales.

Chapter 7

Summary and Further Work

This thesis investigates the behaviour of Copper and Iron under the influence of shock-compression. The diagnostic method employed is *in situ* X-ray diffraction. This was applied both as a simulation on computer MD models of shocked crystals, and experimentally on laser-shocked single crystals.

7.1 Computational Work

7.1.1 Copper

Detailed X-ray diffraction analysis was performed on two MD simulations of Cu. The first one contained 2×10^6 atoms, employed a zero rise-time pulse and spanned < 10 ps. These scales reflect the size of most MD models conducted to date. The crystal was a perfect FCC material, containing no embedded defects. Post-processing showed predominantly uniaxial compression of the lattice, with the strain along the shock propagation direction ~ 3.5 times larger than strains along the two lateral directions.

X-ray diffraction post-processing also has enabled the calculation of dislocation concentrations generated homogeneously by the shock wave. This was done by conducting both the second and fourth order diffraction calculations from $(h00)$, $(0k0)$, and $(00l)$ planes in the sample, and taking into account the shifts of the diffraction peaks caused by the presence of stacking faults and dislocations. This feature of the X-ray diffraction diagnostic technique offers the possibility of measuring dislocation

densities *during* shock wave passage through a material—a measurement which has not been conducted to date, yet one which could resolve a very fundamental question related to plastic flow in materials subjected to a shock load.

Very high dislocation densities ($\sim 3\times10^{13}\,\mathrm{cm}^{-2}$) were found in the shocked region of the crystal. Since the generation and movement of dislocations is believed to be the key mechanism leading to plastic flow in crystalline solids, this finding was in contradiction with the lack of a fuller 3-D compression of the lattice. It is assumed that the dislocation mobility was hindered by their large densities, when generated homogeneously in the shocked region of the crystal. An impedance of dislocation mobilities can prevent thorough shear stress release and plastic flow in the sample.

These results inspired large-scale MD modelling of shocked FCC crystals. The second Cu MD simulation studied in this thesis consisted of 256×10^6 atoms, and its temporal and spatial dimensions represented an increase by more than an order of magnitude in comparison with the first one. Additionally, some realistic features were incorporated in the model. These included a 50 ps ramp on the shock wave, and the presence of pre-existing prismatic loops, mimicking the defects present in experimental samples.

X-ray diffraction post-processing showed a more 3-D-like compression of the shocked lattice in all regions of the sample. The finite ramp on the shock wave resulted in more hydrostatic-like compression even in the homogeneous regions of the crystal where no embedded defects were located; the compression along the shock propagation direction was only ~ 1.7 times larger than in the lateral directions. In the regions adjacent to and containing the prismatic loops, this ratio decreased further to ~ 1.3.

The calculated dislocation densities were $\sim 10^{13}\,\mathrm{cm}^{-2}$ in the homogeneous crystal regions, and $\sim 3\times10^{12}\,\mathrm{cm}^{-2}$ in the heterogeneous regions containing the prismatic loops. Crystal regions with pre-existing defects, which contained lower densities of dislocations after the shock wave passage, displayed clearly more 3-D-like compression than those where higher dislocation densities were generated. It is believed that the

mobility of dislocations increased in regions with lower dislocation concentrations where their movement was not obstructed, resulting in more successful shear stress release and plastic flow.

X-ray diffraction post-processing of MD simulations of shock-compressed Copper presented in this thesis thus resulted in a significant improvement in the modelling of shock-induced processes in FCC metals on nanosecond time-scales.

7.1.2 Iron

Four MD simulations of shock-compressed single crystals of Iron with increasing piston pressures were post-processed. The aim was to detect, using X-ray diffraction, the $\alpha - \epsilon$ phase transition in Iron.

At lower piston pressures, the phase transformation wave was preceded by a faster elastic wave, wherein the uniaxial compression of the BCC lattice was $\sim$6.6–7.1%$\pm$0.3%. For higher pressures, the speed of the phase transition wave increased and overtook the elastic wave, resulting in the region subjected to the shock wave to undergo the $\alpha - \epsilon$ phase transition.

Detailed 2-D FT analysis of the samples verified that, above the threshold pressure of ~ 15 GPa, the BCC phase changed into the HCP phase, with both (110) and $(1\bar{1}0)$ planes in the parent lattice transforming into (0001) planes of the new phase.

3-D post-processing showed that, with increasing piston pressure, the compression of the phase-changed lattice along the shock propagation direction gradually increased. Despite this, no lateral compression was detected for pressures up to ~ 53 GPa, indicating that no plastic deformation of the lattice occurred. This shows that the behaviour of Iron differs significantly from that of Copper under similar shock loading conditions.

It is assumed that the mobility of dislocations in Iron may not be as high as it is in Copper. This would result in a lowering of their mean velocity, and hence slow down the shear stress release in the material. Consequently, plastic flow could be occurring on much longer time-scales than those studied in the MD simulations.

7.2 Experimental Work

The experimental work conducted for this thesis was performed with very powerful lasers employed to generate short, high intensity X-ray pulses to diagnose shock-compressed crystals. In addition, a novel diagnostic method of a wide-angle film-pack [47] was used to capture the diffracted radiation from *multiple* planes in both Bragg and Laue geometries.

Near-hydrostatic compression of Copper on nanosecond time-scales was confirmed, with strains of $\sim 3\%$ both along and normal to the shock propagation direction detected. For the first time, diffraction was also recorded from multiple planes with a range of orientations with respect to the shock propagation direction.

Furthermore, first-time direct *in situ* X-ray diffraction evidence of the onset of the $\alpha - \epsilon$ phase transition in Iron was shown. As such, the experimental results presented in this thesis provide the first direct observation at the atomic level of one of the most important phase transformations in shock wave physics. The static film diagnostic recorded diffraction from various planes corresponding to the BCC phase of Iron, as well as the HCP phase. Compression of the phase-changed lattice of $\sim 15\%$ along the shock propagation direction was detected, whilst the BCC lattice was uniaxially compressed by $\sim 6\%$.

The lack of lateral compression in BCC Iron found experimentally is in very good agreement with the MD simulations post-processing results, despite the difference, of three orders of magnitude, in the time-scales of the two methods. Very good agreement was also found in the magnitude of the uniaxial compression of the parent BCC lattice. It is clear that in the pressure and temporal range covered here, BCC Iron undergoes the $\alpha - \epsilon$ phase transition into HCP lattice, but no plastic deformation of the parent lattice.

7.3 Future Research

The current fast advance of supercomputers offers vast possibilities to Molecular Dynamics modelling of shock-induced processes in crystals. In order to model more accurately and faithfully the response of materials to shock waves, a further increase in the scales of the simulations is called for. Other improvements might include thorough incorporation of realistic features into the models, such as defects and grains, wherein their densities would be equal to those present in real experimental samples.

Future channels for X-ray diffraction post-processing might include 3-D Fast Fourier Transforms of extremely large MD simulations. An increase in computer power will also enhance the quality of post-processing, enabling the use of finer resolution, and sampling of ever-increasing crystals.

Experimentally, using a thicker layer of plastic coating and a further thin layer of Al on crystal samples has proved advantageous, especially when laser intensities are not a limiting experimental factor. This arrangement ensures a steeper shock entering the crystal, resulting in clear diffraction lines.

An obvious challenge for experimental X-ray diffraction is the detection of stacking faults and dislocations in FCC metals. It has been shown that dislocations, embedded as well as those generated by the shock wave, are crucial in relieving shear stress and enabling plastic flow in a crystalline material. The method employed in the computational post-processing of MD simulations in this thesis uses the difference in the shifts of the second and fourth order diffraction peaks to calculate dislocation concentrations in the shocked material. This feature of X-ray diffraction can also be exploited experimentally. Large, high resolution detectors would be required for these experiments, as well as bright X-ray sources allowing the diffraction of the weaker fourth order. If successful, such a measurement of dislocation densities could elucidate one of the most fundamental processes related to plastic deformation of materials under shock loading conditions.

The next step in experimental studies of shock-compressed Iron could be increas-

ing the applied shock pressure, as well as the temporal scales of the experiments. This would clarify whether plastic deformation of the material occurs at higher pressures and/or on longer time-scales. Conversely, improving the temporal resolution of X-ray diffraction experiments to the femtosecond regime should enable the determination of the ultimate time-scale of the $\alpha - \epsilon$ phase transition. Such high temporal resolution could be attained by a free electron laser.

It can be concluded that whilst the results presented in this thesis answer some important questions related to the processes in a crystalline medium subjected to a shock wave, they also pose new ones, and consequently open up further challenges, both computational and experimental, in the field of shock wave physics.

Although the inconclusiveness of the findings shown here may seem somewhat frustrating, one can only concede that this is the very nature of scientific research, where the limits of our understanding are constantly expanded.

Bibliography

[1] McLean A., 'www.levity.com/alchemy',

[2] 'www.answers.com',

[3] Meyers M.A., *Dynamic Behaviour of Materials* (John Wiley and Sons, Inc., 1994)

[4] Swegle J.W. and Grady D.E. (1985), 'Shock Viscosity and the Prediction of Shock Wave Risetimes', *J Appl Phys*, **58**: 692

[5] Holian B.L. and Lomdahl P.S. (1998), 'Plasticity Induced by Shock Waves in Non-Equilibrium Molecular Dynamics Simulations', *Science*, **280**: 2085–2088

[6] Kadau K., Germann T.C., Lomdahl P.S. and Holian B.L. (2002), 'Microscopic View of Structural Phase Transitions Induced by Shock Waves', *Science*, **296**: 1681–1684

[7] Loveridge-Smith A., Allen A.M., Belak J., Boehly T., Hauer A., Holian B., Kalantar D., Kyrala G., Lee R.W., Lomdahl P., Meyers M.A., Paisley D., Pollaine S., Remington B., Swift D.C., Weber S. and Wark J.S. (2001), 'Anomalous Elastic Response of Silicon to Uniaxial Compression on Nanosecond Time Scales', *Phys Rev Lett*, **86** (11): 2349–2352

[8] MEYERS M.A., GREGORI F., KAD B.K., SCHNEIDER M.S., KALANTAR D.H., REMINGTON B.A., RAVICHANDRAN G., BOEHLY T. and WARK J.S. (2003), 'Laser-Induced Shock Compression of Monocrystalline Copper: Characterisation and Analysis', *Acta Mater*, **51**: 1211–1228

[9] SMITH C.S. (1958), 'Metallographic Studies of Metals after Explosive Shock', *Trans Metal Soc AIME*, **212**: 574–589

[10] MEYERS M.A. (1978), 'A Mechanism for Dislocation Generation in Shock-Wave Deformation', *Scripta Metal*, **12** (1): 21–6

[11] HORNBOGEN E. (1962), 'Shock Induced Dislocations.', *Acta Met*, **10**: 978–980

[12] BRIDGMAN P.W., in 'Collected Experimental Papers', (Harvard University Press, Cambridge, Mass., 1964)

[13] RANKINE W.J.M. (1870), *Trans Roy Soc*, **160**: 277

[14] HUGONIOT H. (1889), *J Ec Polytech*, **58**: 1

[15] TSUKERMANN V.A. and ANDEENKO A.I. (1942), *Zh Tekh Fiz*, **12**: 185

[16] AL'TSHULER L.V. (1943), *Zh Eksperim i Teor Fiz*, **13**: 11–12

[17] JOHNSON Q., MITCHELL A.C., KEELER R.N. and EVANS L. (1969), 'Nanosecond X-ray Diffraction: Study of Solids under Shock Compression', *Trans Amer Crystallogr Ass*, **4**: 133

[18] JOHNSON Q., MITCHELL A., KEELER R.N. and EVANS L. (1970), 'X-ray Diffraction During Shock-Wave Compression', *Phys Rev Lett*, **25**: 1099–1101

[19] JOHNSON Q. and MITCHELL A.C. (1972), 'First X-Ray Diffraction Evidence for a Phase Transition during Shock-Wave Compression', *Phys Rev Lett*, **29** (20): 1369–1372

[20] WALSH J.M. (1954), *Bull Am Phys Soc*, **29**: 28

[21] BANCROFT D., PATTERSON E.L. and MINSHALL S. (1956), 'Polymorphism of Iron at High Pressure', *J Appl Phys*, **27**: 291

[22] JAMIESON J.C. and LAWSON A.W. (1962), 'X-Ray Diffraction Studies in the 100 Kbar Pressure Range', *J Appl Phys*, **33**: 776

[23] MAO H.K., BASSETT W.A. and TAKAHASHI T. (1966), 'Effect of Pressure on Crystal Structure and Lattice Parameters of Iron up to 300kbar', *J Appl Phys*, **38** (1): 272

[24] LIVINGSTON J.D. (1962), *Acta Metal*, **10**: 229

[25] GREENMAN W.F., VREELAND T. and WOOD D.S. (1967), *J Appl Phys*, **38**: 3595

[26] GILLIS P.P., GILMAN J.J. and TAYLOR J.W. (1969), 'Stress Dependence of Dislocation Velocities', *Phil Mag*, **20**: 279

[27] JONES O.E. and MOTE J.D. (1969), 'Shock-Induced Dynamic Yielding in Copper Single Crystals', *J Appl Phys*, **40** (12): 4920–8

[28] JOHNSON J.N., JONES O.E. and MICHAELS T.E. (1970), 'Dislocation Dynamics and Single-Crystal Constitutive Relations: Shock-Wave Propagation and Precursor Decay', *J Appl Phys*, **41**: 2330

[29] JOHNSON J.N. (1971), 'Shock Propagation Produced by Planar Impact in Linearly Elastic Anisotropic Media', *J Appl Phys*, **42**: 5522

[30] JOHNSON J.N. (1972), 'Calculation of Plane-Wave Propagation in Anisotropic Elastic-Plastic Solids', *J Appl Phys*, **43**: 2074

[31] POPE L.E. and JOHNSON J.N. (1975), 'Shock-Wave Compression of Single-Crystal Beryllium', *J Appl Phys*, **46**: 720

[32] GUPTA Y.M. (1975), 'Stress Dependence of Elastic-wave Attenuation in LiF', *J Appl Phys*, **46**: 3395

[33] GUPTA Y.M. (1977), 'Effect of Crystal Orientation on Dynamic Strength of LiF', *J Appl Phys*, **48**: 5076

[34] BARKER L.M. and HOLLENBACH R.E. (1974), 'Shock Wave Study of the Alpha-Epsilon Phase Transition in Iron', *J Appl Phys*, **45**: 4872

[35] FORBES J.W. (1976), Ph.D. thesis, Washington State University

[36] DUVALL G.E. and GRAHAM R.A. (1977), 'Phase Transitions under Shock-Wave Loading', *Rev Mod Phys*, **49**: 523

[37] BOETTGER J.C. and WALLACE D.C. (1997), 'Metastability and Dynamics of the Shock-Induced Phase Transition in Iron', *Phys Rev B*, **55**: 2840

[38] WARK J.S., WHITLOCK R.R., HAUER A., SWAIN J.E. and SOLONE P.J. (1987), 'Shock Launching in Silicon Studied with Use of Pulsed X-ray Diffraction', *Phys Rev B*, **35** (17): 9391–5

[39] WARK J.S., WHITLOCK R.R., HAUER A.A., SWAIN J.E. and SOLONE P.J. (1989), 'Subnanosecond X-ray Diffraction from Laser-Shocked Crystals', *Phys Rev B*, **40** (8): 5705–5714

[40] WOOLSEY N.C., WARK J.S. and RILEY D. (1990), 'Sub-nanosecond X-ray Powder Diffraction', *J Appl Cryst*, **23**: 441–3

[41] WARK J.S., RILEY D., WOOLSEY N.C., KEIHN G. and WHITLOCK R. (1990), 'Direct Measurements of Compressive and Tensile Strain during Shock Breakout by Use of Subnanosecond X-ray Diffraction', *J Appl Phys*, **68**: 4531–4

[42] WARK J.S., WOOLSEY N.C. and WHITLOCK R.R. (1992), 'Novel Measurements of High-Dynamic Crystal Strength by Picosecond X-Ray Diffraction', *Appl Phys Lett*, **61**: 651–3

[43] WHITLOCK R.R. and WARK J.S. (1995), 'Orthogonal Strains and Onset of Plasticity in Shocked LiF Crystals', *Phys Rev B*, **52**: 8–11

[44] RIGG P.A. and GUPTA Y.M. (1998), 'Real-time X-ray Diffraction to Examine Elastic-Plastic Deformation in Shocked Lithium Fluoride Crystals', *Appl Phys Lett*, **73**: 1655–7

[45] KALANTAR D.H., CHANDLER E.A., COLVIN J.D., LEE R., REMINGTON B.A., WEBER S.V., HAUER A., WARK J.S., LOVERIDGE A., FAILOR B.H., MEYERS M.A. and RAVICHANDRAN G. (1999), 'Transient X-ray Diffraction Used to Diagnose Shock Compressed Si Crystals on the Nova Laser', *Rev Sci Inst*, **70** (1): 629–632

[46] ZARETSKY E. (2003), 'Multipeak Pulse X-ray Diffraction Study of Shocked Single Crystals', *J Appl Phys*, **93** (5): 2496–2506

[47] KALANTAR D.H., BELAK J., BRINGA E.M., BUDIL K., CATURLA M., COLVIN J., KUMAR M., LORENZ K.T., RUDD R.E., STOLKEN J., ALLEN A.M., ROSOLANKOVA K., WARK J.S., MEYERS M.A. and SCHNEIDER M. (2003), 'Multiple Film Plane Diagnostic for Shocked Lattice Measurements', *Rev Sci Inst*, **74** (3): 1929–1934

[48] KALANTAR D.H., BELAK J., BRINGA E., BUDIL K., CATURLA M., COLVIN J., KUMAR M., LORENZ K.T., RUDD R.E., STOLKEN J., ALLEN A.M., ROSOLANKOVA K., WARK J.S., MEYERS M.A. and SCHNEIDER M. (2003), 'High-Pressure, High-Strain-Rate Lattice Response of Shocked Materials', *Physics of Plasmas*, **10** (5): 1569–1576

[49] WARREN B.E., *X-ray Diffraction* (Dover Publications, Inc., 1969)

[50] KITTEL C., *Introduction to Solid State Physics* (John Wiley and Sons., Inc., 1953), 7th edition

[51] DARWIN C.G. (1914), 'The Theory of X-ray Reflection', *Phil Mag*, **27**: 315

[52] DARWIN C.G. (1914), 'The Theory of X-ray Reflection, Part II', *Phil Mag*, **27**: 675

[53] WOOLSEY N.C., *Time Resolved, in situ X-ray Diffraction from Laser Shocked Crystals* (DPhil Thesis, University of Oxford, 1994)

[54] LOVERIDGE A., *Quantitative Analysis of Shock Propagation in Crystals by Use of Time Resolved X-ray Diffraction* (DPhil Thesis, University of Oxford, 2000)

[55] YOUNG F.W. and SAVAGE J.R. (1964), *JAppl Phys*, **35**: 1917

[56] HULL D. and BACON D.J., *Introduction to Dislocations* (Butterworth Heinemann, 2002), fourth edition

[57] NYE J.F., *Physical Properties of Crystals* (Oxford University Press, Oxford, 1957)

[58] LANDAU L.D. and LIFSHITZ E.M., *Fluid Mechanics* (Pergamon Press, 1959)

[59] ZELDOVICH Y.B. and RAIZER Y.P., *Physics of Shock Waves and High-Temperature Hydrodynamic Phenomena* (Academic Press, Inc., New York, U. S. A., 1966-67)

[60] SWEGLE J.W. and GRADY D.E., in 'Shock Waves in Condensed Matter', (Edited by Y.M. GUPTA), (page 353) (Plenum, New York, 1985)

[61] TAYLOR J.W. (1965), 'Dislocation Dynamics and Dynamic Yielding', *J Appl Phys*, **36**: 3146–3150

[62] FRENKEL J. (1926), *Z Phys*, **37**: 572

[63] OROWAN E. (1934), *Z Phys*, **89**: 605–634

[64] TAYLOR G.I. (1934), *Proc Roy Soc*, **A145**: 362

[65] POLANYI M. (1934), *Z Phys*, **89**: 660

[66] HIRTH J.P. and LOTHE J., *Theory of Dislocations* (Krieger Publishing Company, 1982), 2nd edition

[67] OROWAN E. (1940), 'Problems of Plastic Gliding', *Proc Phys Soc*, **52**: 8–22

[68] ASAY J.R., HICKS D.L. and HOLDRIDGE D.B. (1975), 'Comparison of Experimental and Calculated Elastic-Plastic Wave Profiles in LiF.', *J Appl Phys*, **46** (10): 4316–4322

[69] MEYERS M.A. and MURR L.E. (1978), 'A Model for the Formation of Annealing Twins in FCC Metals and Alloys', *Acta Metal*, **26** (6): 951–962

[70] MURR L.E., 'Residual Microstructure—Mechanical Properties Relationships in Shock-Loaded Metals and Alloys', in 'Shock Waves and High Strain Rate Phenomena in Metals', (Edited by M.A. MEYERS and L.E. MURR), (pages 607–673) (Plenum, New York, 1981)

[71] ZARETSKY E. (1995), 'Dislocation Multiplication behind the Shock Front', *J Appl Phys*, **78** (6): 3740–7

[72] ZARETSKY E. (1998), 'Dislocation Mechanism and Kinetics of Shock-Induced Phase Transformation in KCl', *J Phys Chem Solids*, **59** (2): 253–9

[73] WANG F.M. and INGALLS R. (1998), 'Iron BCC-HCP Transition: Local Structure from X-ray-Absorption Fine Structure', *Phys Rev B*, **57** (10): 5647

[74] BHADESHIA H.K.D.H. (1987), 'Worked Examples in the Geometry of Crystals', Institute of Materials, London

[75] BASSETT W.A. and HUANG E. (1987), 'Mechanism of the Body-Centred Cubic-Hexagonal Close-Packed Phase Transition in Iron', *Science*, **238** (4828): 780–3

[76] ALLEN M.P. and TILDESLEY D.J., *Computer Simulation of Liquids* (Clarendon Press, Oxford, 1987)

[77] HOOVER W.G. and ASHURST W.T., 'Non-Equilibrium Molecular Dynamics', in 'Theoretical Chemistry: Advances and Perspectives', (Edited by H. EYRING and D. HENDERSON), volume 1, (pages 1–51) (1975)

[78] HOLIAN B.L., HOOVER W.G., MORAN B. and STRAUB G.K. (1980), 'Shock Wave Structure via Non-Equilibrium Molecular Dynamics and Navier-Stokes Continuum Mechanics', *Phys Rev A*, **22**: 2798–2808

[79] BRINGA E.M., WIRTH B.D., CATURLA M.J., STOLKEN J. and KALANTAR D. (2003), 'Metals Far from Equilibrium: From Shocks to Radiation Damage', *Nuc Inst and Methods Phys Res B*, **202**: 56

[80] 'http://bifrost.lanl.gov/MD/MD.html',

[81] 'http://www.llnl.gov/asci/purple/benchmarks/limited/mdcask/',

[82] DAW M.S. and BASKES M.I. (1983), 'Semiempirical, Quantum Mechanical Calculation of Hydrogen Embrittlement in Metals', *Phys Rev Lett*, **50**: 1285–8

[83] DAW M.S. and BASKES M.I. (1984), 'Embedded-Atom Method: Derivation and Application to Impurities, Surfaces, and Other Defects in Metals', *Phys Rev B*, **29**: 6443–6453

[84] ALDER B.J. and WAINWRIGHT T.E. (1957), 'Phase Transition for a Hard Sphere System', *J Chem Phys*, **27**: 1208–9

[85] DICKEY J.M. and PASKIN A. (1969), 'Computer Simulation of the Lattice Dynamics of Solids', *Phys Rev*, **188**: 1407–1418

[86] PASKIN A. and RAHMAN A. (1966), 'Effects of a Long-Range Oscillatory Potential on the Radial Distribution Function and the Constant of Self-Diffusion in Liquid Na', *Phys Rev Lett*, **16**: 300–3

[87] TSAI D.H. and BECKETT C.W. (1966), *J Geophys Res*, **71**: 2601

[88] PASKIN A. and DIENES G.J. (1972), 'Molecular Dynamics Simulations of Shock Waves in a Three-Dimensional Solid', *J Appl Phys*, **43**: 1605–10

[89] HOLIAN B.L. and STRAUB G.K. (1979), 'Molecular Dynamics of Shock Waves in Three-Dimensional Solids: Transition from Nonsteady to Steady Waves in

Perfect Crystals and Implications for the Rankine-Hugoniot Conditions', *Phys Rev Lett*, **43** (21): 1598–1600

[90] MOGILEVSKY M.A., 'Mechanisms of Deformation under Shock Loading', in 'Shock Waves and High Strain Rate Phenomena in Metals', (Edited by L.E. MURR and M.A. MEYERS), (page 531) (1981)

[91] MOGILEVSKY M.A. (1983), 'Mechanisms of Deformation Under Shock Loading', *Phys Rep*, **97** (6): 357–93

[92] MOGILEVSKY M.A. (1988), *Impact Loading and Dynamic Behaviour of Materials*, (page 957)

[93] HOLIAN B.L. (1988), 'Modeling Shock-Wave Deformation via Molecular Dynamics', *Phys Rev A*, **37**: 2562–8

[94] HOOVER W.G., GROOT A.J.D., HOOVER C.G., STOWERS I.F., KAWAI T., HOLIAN B.L., BOKU T., IHARA S. and BELAK J. (1990), 'Large-Scale Elastic-Plastic Indentation Simulations via Non-Equilibrium Molecular Dynamics', *Phys Rev A*, **42**: 5844–5853

[95] HOLIAN B.L., VOTER A.F., WAGNER N.J., RAVELO R.J., CHEN S.P., HOOVER W.G., HOOVER C.G., HAMMERBERG J.E. and DONTJE T.D. (1991), 'Effects of Pairwise versus Many-Body Forces on High-Stress Plastic Deformation', *Phys Rev A*, **43**: 2655–2661

[96] HOLIAN B.L. and RAVELO R. (1995), 'Fracture Simulations Using Large-Scale Molecular Dynamics', *Phys Rev B*, **51**: 11275–11288

[97] DE LA RUBIA T.D. and GUINAN M.W., in 'Mat. Res. Forum 174', (page 151) (1990)

[98] BRINGA E.M., 'private communication',

[99] MISHIN Y., MEHL M.J., PAPACONSTANTOPOULOS D.A., VOTER A.F. and KRESS J.D. (2001), 'Structural Stability and Lattice Defects in Copper: Ab Initio, Tight-Binding, and Embedded-Atom Calculations', *Phys Rev B*, **63** (224106)

[100] ROSOLANKOVA K., KALANTAR D.H., BELAK J.F., BRINGA E.M., CATURLA M.J., HAWRELIAK J., HOLIAN B.L., KADAU K., LOMDAHL P.S., GERMANN T.C., RAVELO R., SHEPPARD J. and WARK J.S., 'X-Ray Diffraction from Shocked Crystals: Experiments and Predictions of Molecular Dynamics Simulations', in 'Shock Compression of Condensed Matter', (pages 1195–8) (AIP, 2003)

[101] KELCHNER C.L., PLIMPTON S.J. and HAMILTON J.C. (1998), 'Dislocation Nucleation and Defect Structure during Surface Indentation', *Phys Rev B*, **58** (17): 11085–8

[102] BRINGA E.M., DUCHAINEAU M., ROSOLANKOVA K., RUDD R.E., KALANTAR D.H., REMINGTON B.A., WARK J.S. and BELAK J. (2005), 'Shock Deformation of FCC Metals on Sub-Nanosecond Timescales', *Nature Materials, submitted*

[103] HARRISON R.J., VOTER A.F. and CHEN S.P., *Atomistic Simulation of Materials Beyond Pair Potentials*, (page 219) (Plenum, New York, 1989)

[104] MEYER R. and ENTEL P. (1998), *Phys Rev B*, **57**: 5140

[105] SONDHAUSS P.K., 'private communication',

[106] DANSON C.N., BARZANTI L.J., CHANG Z., DAMERELL A.E., EDWARDS C.B., HANCOCK S., HUTCHINSON M.H.R., KEY M.H., LUAN S., MAHADEO R.R., MERCER I.P., NORREYS P., PEPLER D.A., RODKISS D.A., ROSS I.N., SMITH M.A., SMITH R.A., TADAY P., TONER W.T., WIGMORE K.W.M., WINSTONE T.B., WYATT R.W.W. and ZHOU F. (1993), 'High Contrast Multi-Terawatt Pulse Generation Using Chirped Pulse Amplification on the VULCAN Laser Facility', *Opt Comm*, **103**: 392–7

[107] PHILLION D.W. and HAILEY C.J. (1986), *Phys Rev A*, **34**: 4886

[108] 'http://www-cxro.lbl.gov/',

[109] GRANT I.P., MCKENZIE B.J., NORRINGTON P.H., MAYERS D.F. and PYPER N.C. (1980), 'An Atomic Multiconfigurational Dirac-Fock Package', *Comput Phys Commun*, **21**: 207

[110] MOORE C.E. (1970), 'Ionisation Potentials and Ionisation Limits Derived from the Analysis of Optical Spectra', NBS Pub., NSRDS-NBS 34

[111] TAKAHASHI K., KOHDA K. and MIYAHARA J. (1984), *J Lumin*, **31**: 266–8

[112] VON SEGGERN H. (1989), *Cryst Latt Def Amorph Mater*, **18**: 399–417

[113] SCHLAPP M., BULUR E. and VON SEGGERN H. (2003), 'Photo-Stimulated Luminescence of Calcium Co-Doped BaFBr:Eu2+ X-ray Storage Phosphors', *J Phys D*, **36**: 103–8

[114] TEMPLER R.H. (1991), *Nucl Instr and Meth*, **A300**: 357

[115] 'National Laser Users' Facility Users' Guide', University of Rochester, Laboratory for Laser Energetics

[116] LINDL J. (1995), 'Development of the Indirect-Drive Approach to Inertial Confinement Fusion and the Target Physics Basis for Ignition and Gain', *Physics of Plasmas*, **2**: 3933–4024

[117] MCQUEEN R.G. and MARSH S.P. (1960), 'Equation of State for Nineteen Metallic Elements from Shock-Wave Measurements to Two Megabars', *J Appl Phys*, **31** (7): 1253–1269

[118] HENKE B.L., UEJIO J.Y., STONE G.F., DITTMORE C.H. and FUJIWARA F.G. (1986), 'High-Energy X-ray Response of Photographic Films: Models and Measurement', *J Opt Soc Am B*, **3** (11): 1540–1550

[119] SANO T., MORI H., OHMURA E. and MIYAMOTO I. (2003), 'Femtosecond Laser Quenching of the Epsilon Phase of Iron', *Appl Phys Lett*, **83** (17): 3498–3500

[120] KALANTAR D.H., BELAK J., COLLINS G., COLVIN J., EGGERT J., GERMANN T., HAWRELIAK J., KADAU K., LOMDAHL P., LORENZANA H., MEYERS M., ROSOLANKOVA K., SCHNEIDER M., STOLKEN J. and WARK J.S., 'Direct Observation of the alpha-epsilon Transition in Shock-Compressed Iron via Nanosecond X-ray Diffraction', *Science, submitted*

~

The End.

~